

# Dynamics of Trapped Ions Near the Linear–Zigzag Structural Phase Transition

by

**Sara Ejtemaee**

M.Sc., Simon Fraser University, 2010

B.Sc., University of Tehran, 2007

Dissertation Submitted in Partial Fulfillment of the  
Requirements for the Degree of  
Doctor of Philosophy

in the  
Department of Physics  
Faculty of Science

© Sara Ejtemaee 2015  
SIMON FRASER UNIVERSITY  
Fall 2015

All rights reserved.

However, in accordance with the *Copyright Act of Canada*, this work may be reproduced without authorization under the conditions for “Fair Dealing.” Therefore, limited reproduction of this work for the purposes of private study, research, criticism, review and news reporting is likely to be in accordance with the law, particularly if cited appropriately.

# Approval

**Name:** Sara Ejtemaee  
**Degree:** Doctor of Philosophy (Physics)  
**Title:** *Dynamics of Trapped Ions Near the Linear-Zigzag Structural Phase Transition*  
**Examining Committee:** **Chair:** Dr. Eldon Emberly  
Associate Professor

**Dr. Paul C. Haljan**  
Senior Supervisor  
Associate Professor

---

**Dr. Mohammad Amin**  
Supervisor  
Adjunct Professor

---

**Dr. Jeffrey McGuirk**  
Supervisor  
Associate Professor

---

**Dr. Malcolm Kennett**  
Internal Examiner  
Associate Professor  
Physics Department

---

**Dr. Boris Blinov**  
External Examiner  
Associate Professor  
Physics Department  
University of Washington

---

**Date Defended:** 14 Dec 2015

# Abstract

Laser-cooled ions held in a linear Paul trap with strong transverse confinement organize into a one-dimensional (1-D) linear crystal. If the transverse confinement is relaxed, the linear ion crystal undergoes a continuous, structural phase transition to a 2-D zigzag configuration. We study the dynamics near the critical point of the linear-zigzag transition. In the first part of this thesis, we study the spontaneous nucleation and dynamics of topological kink defects, formed as a result of a rapid quench across the linear-zigzag transition. The experimental results are compared to the Kibble-Zurek mechanism, which provides an intuitive model of defect formation and predicts a power-law scaling for the number of defects formed as a function of transition quench rate. The second part of this thesis is focused on one of the key requirements for investigations of the near-transition dynamics in the quantum regime. To achieve an efficient ground state cooling of the zigzag vibrational mode, we demonstrate 3-D polarization-gradient cooling of strings of 1–4 trapped ions as an intermediate step between Doppler and sideband cooling, and study the polarization-gradient cooling rate and cooling limit as a function of the cooling beam intensity in and near the Lamb-Dicke regime. The results of this thesis pave the way towards our future experiments aimed at assessing the coherence time of a zigzag superposition state through measurements of tunneling oscillations.

**Keywords:** Ion trap, Linear-zigzag phase transition, Polarization-gradient cooling, Kibble-Zurek mechanism

# Dedication

To Maman, Baba and Setareh.

# Acknowledgements

Pursuing a physics degree has been a long dream of mine, and countless people helped me to make the dream come true. I will not be able to list them all here, but I am grateful to every single one of them.

First, and foremost I would like to thank my supervisor, Paul Haljan for his guidance, encouragement and support. Running an ion trapping experiment in a single-person sized group could have been challenging, but amazingly Paul was able to turn that into an advantage for me and taught me a wide range of skills. Thank you Paul. I am proud to be your first Masters and Ph.D. student.

Thanks also to Jeffrey McGuirk and Mohammad Amin, my committee members, who have been very encouraging and have provided helpful suggestions and advice throughout my Ph.D. degree.

Thanks to the physics department's wonderful staff, Joan Cookson, Rose Evan, Stephen Flach, and Ayako Nagasawa who provide every possible help when required to ease your path.

Thanks to the past and present members of the Haljan group, specially the newest member, Jie Zhang, who arrived one month ago but has already provided lots of help with reading and discussing the thesis.

Thanks to Bernice, for providing a true home since the first days of my arrival to Canada. She gave me an opportunity that turned into an interesting valuable life experience, and a huge financial help during my student life. Thanks to my roommates, who were very considerate during the thesis writing time, and special thanks to Dan who was always there to help regardless of the request.

Thanks to my dance troop, who always saved me a spot despite all the missed practices, and special thanks to Amadea for her cheerful support.

Thanks to Laleh, for being the perfect friend she is, Parisa and Simin, my friends and first physics companions, Payam for his friendship and tremendous helps during the transition times, Hamed for the delicious foods he cooks and for forcing me to stick with the "early-morning" schedule in the past two months, and Dorna, Azadeh, Alireza, Mercedeh, Fereydoun, Kamyar, Amir, Mohammad, Defne and Chessie for their friendship.

I would also like to thank Mahboubeh Ziyabari, my first physics teacher, who had a life-long impact on me and set me on my way.

Last, but not the least, thanks to my parents, sister, aunts and Ana. Their continuous unlimited love and support amaze me and lighten up my life. Shimin bala mi sar.

# Table of Contents

Approval	ii
Abstract	iii
Dedication	iv
Acknowledgements	v
Table of Contents	vii
List of Figures	x
<b>1 Introduction</b>	<b>1</b>
<b>2 The Kibble – Zurek Mechanism</b>	<b>5</b>
2.1 Introduction to the Kibble – Zurek mechanism . . . . .	5
2.2 Theory of Kibble – Zurek mechanism . . . . .	7
2.3 A historical review of experiments designed to test the KZM . . . . .	10
2.3.1 Liquid Crystals: . . . . .	10
2.3.2 Superfluid He: . . . . .	11
2.3.3 Liquid Crystal Light Valve: . . . . .	12
2.3.4 Superconductors: . . . . .	13
2.3.5 Multiferroics . . . . .	16
2.3.6 Landau-Zener transition and the KZM . . . . .	17
2.3.7 Ultracold trapped atoms and ions . . . . .	18
2.3.8 Ion trapping . . . . .	20
2.3.9 Conclusion . . . . .	21
<b>3 The Kibble–Zurek Mechanism for Trapped Ions</b>	<b>22</b>
3.1 Ion – trap system . . . . .	22
3.2 Inhomogeneous linear equilibrium structure . . . . .	25
3.3 The structural transition from linear to zigzag structure . . . . .	28
3.4 Calculation of the critical point of the linear–zigzag transition: approach I.	28

3.5	Calculation of the critical point of the linear-zigzag transition: approach II.	32
3.6	Beyond the zigzag structure . . . . .	35
3.7	Characteristics of the linear-zigzag "phase transition" . . . . .	35
3.8	Kibble – Zurek mechanism in ion-trap systems . . . . .	39
3.8.1	Homogenous KZM (HKZM) for trapped ions . . . . .	40
3.8.2	Inhomogeneous KZM (IKZM) for trapped ions . . . . .	42
<b>4</b>	<b>Experimental Setup for KZM Studies</b>	<b>47</b>
4.1	Ytterbium ion . . . . .	47
4.1.1	Ytterbium Isotopes . . . . .	48
4.1.2	Energy levels of $^2S_{1/2} - ^2P_{1/2}$ transition in $^{174}\text{Yb}^+$ . . . . .	49
4.2	Fluorescence theory . . . . .	50
4.3	Doppler cooling . . . . .	53
4.3.1	Doppler cooling of a single free atom . . . . .	53
4.3.2	Doppler cooling of a single trapped ion . . . . .	54
4.3.3	Doppler cooling of a string of trapped ions . . . . .	58
4.4	Efficient loading of a large pure ion crystal . . . . .	62
4.5	Ramp across linear-zigzag transition . . . . .	63
4.6	Imaging setup and data collection . . . . .	66
4.7	Laser setup . . . . .	67
<b>5</b>	<b>Experimental Results on KZM in Ion Trap Systems</b>	<b>71</b>
5.0.1	Summary of the experimental setup . . . . .	71
5.0.2	The effect of a central non-fluorescing ion . . . . .	72
5.1	Different types of kinks . . . . .	75
5.2	Probability of kink generation vs. quench rate . . . . .	80
5.2.1	Experimental measurement of number of kinks vs. quench rate . . . . .	80
5.2.2	Determining the effect of losses from simulation . . . . .	81
5.2.3	Comparison to the IKZM predictions . . . . .	83
5.3	Kink dynamics . . . . .	84
5.4	Comparison to other experiments and conclusion . . . . .	87
<b>6</b>	<b>Dynamics Near the Linear-Zigzag Transition in the Quantum Regime</b>	<b>91</b>
6.1	Introduction to the L-Z transition in the quantum regime . . . . .	91
6.2	Zigzag double-well potential and tunneling rate . . . . .	92
6.3	Outline of the proposed experiment . . . . .	96
6.3.1	Preparing the setup for a zigzag tunneling measurement and outline of potential challenges . . . . .	97
<b>7</b>	<b>Laser Cooling to Near Ground State of Motion</b>	<b>99</b>



7.1	Introduction and motivation . . . . .	99
7.2	Theoretical models of Sisyphus cooling . . . . .	101
7.3	Theoretical models of P-G cooling of a trapped $^{171}\text{Yb}^+$ . . . . .	103
7.3.1	Energy levels of $^{171}\text{Yb}$ ion . . . . .	103
7.3.2	P-G cooling of a free atom– semiclassical approach . . . . .	104
7.3.3	P-G cooling of a bound ion – semiclassical approach . . . . .	109
7.3.4	Semiclassical simulations of P-G cooling . . . . .	117
7.3.5	P-G cooling of a bound ion– quantum approach . . . . .	118
7.3.6	Quantum simulation of P-G cooling . . . . .	120
7.4	Comparison between analytical theoretical models and simulations . . . . .	121
7.4.1	Perfect assumptions, excellent match . . . . .	121
7.4.2	The effect of the Lamb-Dicke regime: . . . . .	123
7.4.3	The effect of ground state coherences: . . . . .	124
7.4.4	The effect of phase modulation: . . . . .	125
7.5	Motion–sensitive stimulated Raman transitions . . . . .	128
7.6	Thermometry using stimulated Raman transitions: . . . . .	133
7.7	Experimental setup for Sisyphus cooling . . . . .	135
7.7.1	Sisyphus beams . . . . .	135
7.7.2	Raman beams . . . . .	138
7.7.3	The cooling experiment setup . . . . .	141
7.8	Experimental results of the Sisyphus cooling of a single ion . . . . .	146
7.8.1	Sisyphus cooling rate measurement: . . . . .	146
7.8.2	Sisyphus cooling limit: . . . . .	149
7.8.3	Comparison between experimental results and simulations . . . . .	150
7.9	Resolved sideband cooling using two-photon stimulated Raman transitions .	153
7.10	Raman transition and thermometry of multiple ions . . . . .	154
7.10.1	Thermometry: . . . . .	156
7.11	Experimental results of sideband cooling . . . . .	157
7.11.1	Sideband cooling of a single ion: . . . . .	157
7.11.2	Sisyphus and sideband cooling of a four-ion string . . . . .	159
7.12	Conclusion . . . . .	161
<b>8</b>	<b>Conclusion</b>	<b>163</b>
	<b>Bibliography</b>	<b>165</b>

# List of Figures

Figure 2.1	Schematic description of how the relaxation time $\tau$ and the characteristic time of changes, $ \epsilon/\dot{\epsilon} $ , vary over time. The relaxation time is very small far from the critical point and it becomes significantly large as we approach the critical point at $t = 0$ . For a linear change of the reduced order parameter $\epsilon$ , the characteristic time of changes varies linearly with time. The time when these two times meet ( $ \frac{\epsilon}{\dot{\epsilon}}  = \tau$ ) is called the freeze-out time. According to the adiabatic-impulse approximation, dynamics of the system is considered non-adiabatic or impulsive in between the two freeze-out times, while adiabatic elsewhere. . . . .	9
Figure 2.2	Time evolution of two strings defects, showing the crossing, then reconnecting in the other way. From [1]. Reprinted with permission from AAAS. . . . .	10
Figure 2.3	The time evolution of nematic bubbles at different times of (a) 2 s, (b) 5 s, (c) 11 s, and (d) 23 s, showing the process of domain formation and coalescence, and ultimately the formation of defects, following a quench. From [2]. Reprinted with permission from AAAS.	11
Figure 2.4	Intensity patterns in a liquid crystal light valve (LCLV) experiment, showing a number of defects (for example the circled one) 0.5 s after an intensity quench over a time of $\tau_Q = 0.41$ s. Reprinted figure with permission from [3]. Copyright (1999) by the American Physical Society. . . . .	13
Figure 2.5	(a), (b) The AFM (atomic force microscopy) images of stripe patterns and vortex-antivortex domain patterns in $\text{ErMnO}_3$ crystals. Large domains of a single order-parameter polarization are separated by narrow (dark) domains of the opposite polarization. (c) The density of vortices as a function of cooling rate for slow cooling rates (red triangles, Chae <i>et al.</i> results [4]) and fast cooling rates (blue circles, Griffin <i>et al.</i> results [5]). Reprinted figure with permission from [4]. Copyright (2012) by the American Physical Society. . . .	16

Figure 2.6	Images of BECs in a harmonic trap with a single vortex (left, center) and two vortices (right) nucleated by a quench of the normal-BEC transition. Reprinted by permission from Macmillan Publishers Ltd: [Nature] [6], copyright(2008). . . . .	18
Figure 2.7	a-d, Sample time of flight pictures of BEC containing 0, 1, 2, and 3 solitons. The vertical direction corresponds to the strong-confinement direction in the trap. Reprinted by permission from Macmillan Publishers Ltd: [Nature Physics] [7], copyright(2013). . . . .	19
Figure 3.1	The linear rf Paul trap used in our experiment is composed of four rods held in a square configuration of the side of 1.27 mm and two needles separated by 2.5 mm. The rods confine the ion in the transverse direction. Two opposing rods are grounded (shown in red) and the other two are connected to rf and dc voltage of $V_0 \cos(\Omega_T \cdot t) + U_{rod}$ (shown in olive green). Two needles confine the ion in the axial direction and are connected to a dc voltages of $U_0$ . . . . .	23
Figure 3.2	The oscillatory motion of a trapped ion as a function of secular period. The motion consists of two parts: secular motion shown in black with a low frequency $\omega$ and larger amplitude $x_0$ , and micro-motion shown in red with a high frequency $\Omega_T = 20\omega$ and smaller amplitude $x_0 \cdot q/2 = 0.1x_0$ , where $q = 0.2$ in this plot. . . . .	25
Figure 3.3	(a) An experimental CCD image 42 $^{174}\text{Yb}$ ions in a 1-D linear structure taken by an intensified CCD camera for $\alpha = 17$ with $\omega_z = 38$ kHz and $\omega_y = 660$ kHz. (b) The numerical calculation results of ions positions in a string of 42 ions with the same $\alpha$ value. (c) The axial density of ions vs. scaled ion position. The points are extracted from the numerically calculated ion positions shown in (b). The red dashed line is the LDA theory as described in Eq. 3.13. The black line is a fit to the points for which $n(0)$ and $L$ are considered as free parameters. Distances scaled to $a_0 = 24.4 \mu\text{m}$ . . . . .	27

Figure 3.4	(a) Experimental images of the equilibrium structures of a string of 41 $^{174}\text{Yb}$ ions for different trap anisotropy values. Distances scaled to $a_0 = 24.4 \mu\text{m}$ . After passing the critical point ( $\alpha_c \simeq 16$ ) the zigzag configuration starts to form in the center. As the trap anisotropy decreases further, the transverse displacement of the central ions becomes larger and more ions join the zigzag configuration. In the laser image, the white line indicates the scale of $10 \mu\text{m}$ , and the transverse separation of central ions ( $\Delta y_{pp0}$ ) is shown by two arrows. (b): Numerical calculations of the transverse displacement vs. axial position for a series of $\alpha$ values in a range of 9-16, shown by different colors. . . . .	29
Figure 3.5	The transverse separation (peak to peak zigzag amplitude) of the two center ions at $z = 0$ as a function of trap anisotropy. The points are the experimental data for a string of 41 $^{174}\text{Yb}$ ions (see Fig. 3.4). The line shows $\Delta y_{pp}$ obtained from numerically determined equilibrium configurations for a range of $\alpha$ values. The critical point is $\alpha_c \simeq 16$ . . . . .	30
Figure 3.6	The connected blue points are derived from minimizing the potential energy to find the onset of zigzag structure using MAPLE. The red line is the power-law dependence of $\alpha_{0c}$ in terms of $N$ as described by Eq. 3.18. The good agreement between the two lines indicates that the power-law dependence (Eq. 3.18) is a fair approximation of the central ion's critical point. . . . .	31
Figure 3.7	The numerical calculation results of the eigenvectors of normal modes in a string of 4 ions on the linear (left column) and zigzag (right column) side of the L-Z transition. On the linear side, the eigenvector components of a mode are the same in the axial and transverse directions. It can also be seen that the axial and transverse motions are totally decoupled on the linear side. On the zigzag side, only for the center of mass mode are the axial and transverse motions decoupled. . . . .	34
Figure 3.8	Numerical calculation of frequencies of 8 normal modes of Fig. 3.7 with the same color code. All frequencies are scaled with respect to the transverse trap frequency $\omega_y$ . The frequency of the transverse zigzag mode goes to zero at $\alpha = 2.04$ , which defines the critical point of the linear-zigzag transition. . . . .	35
Figure 3.9	Numerical calculations of the 2-D equilibrium structure for four different values of $\alpha$ in a string of 41 ions. (a) A zigzag structure. (b) A 3-row structure formed at the center of the zigzag configuration. (The critical point of the 3-row structure is at $\alpha_c \simeq 5.8$ ) (c) A deep 3-row structure. (d) A 4-row structure. . . . .	36

Figure 3.10	The axial and transverse normal modes of three trapped ions, along with the tables showing the eigenvectors of $i^{th}$ ion and $k^{th}$ normal mode $\psi_{ik}$ for each direction. . . . .	38
Figure 3.11	The ratio of front to sound velocity is shown for the left half of a 42-ion chain, for different quench times in the range of 10-70 $\mu$ s. The transverse trap frequency $\omega_y$ changes from $2\pi \cdot 657$ to $2\pi \cdot 412$ kHz, while the axial trap frequency $\omega_z = 2\pi \cdot 37.6$ kHz remains constant.	44
Figure 3.12	Simulation results from Pyka <i>et al.</i> of the density of defects as a function of quench rate in a string of 30 ions. The quench rate is varied by a factor of 150, and the string is in the under-damped regime. All three regimes of defect nucleation can in principle be accessed over this range. Reprinted by permission from Macmillan Publishers Ltd: [Nature Communications] [8], copyright(2013). . . .	45
Figure 4.1	$\text{Yb}^+$ energy levels, involved in Doppler cooling and fluorescence detection. The primary transition is $^2S_{1/2} - ^2P_{1/2}$ at 369 nm. The 935 nm transition is used to clear out the small leakage from the excited state $^2P_{1/2}$ to $^2D_{3/2}$ state. An additional low lying state of $^2F_{7/2}$ can be populated via collision process, and is depopulated through the 638 nm transition. . . . .	48
Figure 4.2	Zeeman resolved structure of the $^2S_{1/2} - ^2P_{1/2}$ transition for $^{174}\text{Yb}^+$ . Zeeman splittings due to the magnetic field $B$ are indicated in terms of $\delta_B = \mu_B B / \hbar$ . Laser detuning, $\Delta$ is defined relative to the $B = 0$ transitions. The polarization resolved branching ratios are 1/3 for $\pi$ and 2/3 for $\sigma$ transitions. . . . .	50
Figure 4.3	The excited state $^2P_{1/2}$ population of $^{174}\text{Yb}^+$ is shown as a function of saturation parameter (laser intensity) for three different detuning values, $\Delta/2\pi = \{0, -10, -33\}$ MHz, and an optimized $\theta_{BE} = 0^\circ$ . The Zeeman shift is $\delta_B/2\pi = 8.2$ MHz and $\gamma/2\pi = 19.6$ MHz. . . . .	52
Figure 4.4	The effect of micro-motion on (a) scattering rate, (b) cooling rate, and (c) cooling limit, for three cases of, no micro-motion ( $\beta = 0$ ), medium micro-motion ( $\beta = 0.75$ ) and large micro-motion ( $\beta = 3$ ). In these plots, parameters used are rf trap frequency $\Omega_T/2\pi = 11.75$ MHz, Zeeman frequency $\delta_B/2\pi = 8.24$ MHz, $\theta_{BE} = 6^\circ$ , effective saturation parameter $s_{0eff} = 2.7$ , $\gamma/2\pi = 19.6$ MHz, and wavevector projection $k_i = 1/2$ i.e. for a transverse trap axis so the vertical axes of all the three plots are normalized to their optimum values. . . . .	59

Figure 4.5	Samples of fluorescence measurements as a function of detuning $\Delta$ for (a) an ion in the middle of a 51-ion string, and (b) an ion close to the edge of the string. Fitting the fluorescence rate of an ion to Eq. 4.24 gives the value of $\beta$ at the position of that ion. (c) The modulation index $\beta$ as a function of axial position. An image of a 43-ion string is overlapped on the x-axis for reference. . . . .	60
Figure 4.6	The simulation results of (a) normalized cooling rate and (b) normalized steady-state kinetic energy across a crystal of 42 ions for a detuning of $\Delta/2\pi = -32.6$ MHz, $s_{0eff} = 2.7$ at the center, and a laser beam FWHM=280 $\mu\text{m}$ . The other parameters are similar to Fig 4.4. The estimated cooling rate is uniform to a factor of 2 or better across the crystal. The cooling rate is normalized to $\Gamma_{c,max}$ given by Eq. 4.22 and the steady-state energy is normalized to minimum $E_{k-ss}$ given by Eq. 4.23. . . . .	61
Figure 4.7	(a) To quench across the linear-zigzag transition, we change the transverse trap frequency by changing the voltage of the rods linearly over a quench time of $2\tau_Q$ . (b) The single-ion calibration of the secular transverse trap frequency $\omega_y$ with the applied dc rod voltage $V_{dc}$ . The line indicates the fit to Eq. 4.25. (c) The transverse quadrupole potential is produced by applying $+V(t)$ and $-V(t)$ to each pair of opposing rods. . . . .	63
Figure 4.8	(a) The front panel of the Labview program for the dc voltage setup used at the start of the experiment to null the micro-motion. (b) The front panel of the Labview program for implementing a voltage ramp. The micro-motion correction is added to the start- and end-point of the ramp in the two-step ramp setup. (c) The circuit diagrams of the Bessel filter and the current-booster circuit of the four rods, and two endcaps. The resonator is only shown schematically . . . . .	65
Figure 4.9	The effect of adding a Bessel filter to the board output for $5\mu\text{s}$ ramps over 0-400 mV (a) and 0-4 V (b). The yellow line is the output of the board (input of the Bessel filter), and the blue line is the output of the Bessel filter. The Bessel filter smoothens the shape of the ramp. For fast quenches, the low current output of the board cannot charge up the final capacitor of the Bessel filter fast enough to support fast quenches. . . . .	66
Figure 4.10	Typical result of the added current-booster, and Bessel filter along with the partially smoothed residual distortion for 0-5 V ramps over quench times of (a) $2\tau_Q = 10 \mu\text{s}$ and (b) $2\tau_Q = 70 \mu\text{s}$ . The maximum distortion in voltage is $V_{pp} \sim 100$ mV. . . . .	67

Figure 4.11	The simplified schematic of the laser-beam paths to the trap for the cooling/detection laser beam at 369 nm, the D-state and F-state repump laser beams at 935 nm and 638 nm, and the photo-ionisation laser beam at 399 nm. . . . .	69
Figure 5.1	Experimental CCD images of 42 $^{174}\text{Yb}$ ions. (a) A linear structure. (b) A zig configuration, in which the odd-numbered ions shift up and the even-numbered ions shift down. (c) A zag configuration, in which the even-numbered ions shift up and the odd-numbered ions shift down . . . . .	73
Figure 5.2	(a) Orientation (sign) of the zigzag structure and (b) number of dark ions present for a sample sequence of successive quenches. A zigzag sign of 0 corresponds to an indeterminate case in image analysis. (c)–(g) Images of the ion crystal corresponding to selected runs in the quench sequence. Each pair of images shows the ion crystal before and after the quench. The locations of dark ions in the initial linear crystal are indicated by arrows.(h) The central dark-ion exclusion region. The runs with dark ion(s) in this region are excluded from analysis. Note that the horizontal axis is in pixels, and 1 pixel $\simeq$ 0.7 $\mu\text{m}$ . . . . .	74
Figure 5.3	(a) The run-to-run autocorrelation of the zigzag orientation. A clear positive autocorrelation between adjacent sites can be observed in the files with dark ion(s). (b) The run-to-run autocorrelation after excluding the dark-ion contaminated runs in each file. . . . .	75
Figure 5.4	(a)-(c): Images of crystals of 42 $^{174}\text{Yb}$ ions in zigzag configurations with (a) a single discrete kink (indicated by arrow) and (b), (c) a single extended kink. The axial trap frequency for all images is $\omega_z/2\pi = 37.6$ kHz, while the weak transverse frequency $\omega_y/2\pi$ is (a) 414 kHz, (b) 380 kHz, and (c) 342 kHz. Starting at 0 V the corresponding quench end points $V_f$ are (a) 4.8, (b) 5.3, and (c) 5.8 V. The imaging system looks at $45^\circ$ to the transverse y axis where the zigzag displacement occurs. (d) Two discrete kinks (kink and antikink) in a string of 42 ions. (e) Two extended kinks in a string of 51 ions. In the lower panel, the zigzag domains are traced with dotted yellow lines to accentuate the location of the kinks in the crystal structure. . . . .	76

Figure 5.5	Observed axial position distribution of (a) discrete and (b) extended kinks versus quench end-point. All data taken at a quench rate of $0.19 \text{ V}/\mu\text{s}$ . Simulation results of axial position distribution of (c) discrete and (d) extended kinks at the same quench rate as experiment. (e) Average number per run of discrete kinks (red circles) and extended kinks (blue squares) for distributions in (a) and (b). Data points, for 41-43 ions, include 1000-2200 runs. Errors calculated assuming binomial statistics. Lines are a simulation for 42 ions with no free parameters, and shown 2 ms after the quench, $2/3$ of the camera exposure time. Statistical uncertainties in simulation comparable to experimental ones shown. . . . .	77
Figure 5.6	Simulation: The axial kinetic energy (red) and transverse kinetic energy (blue) as a function of time in a (a) fast $2\tau_Q = 10 \mu\text{s}$ quench and (b) a slow $2\tau_Q = 70 \mu\text{s}$ quench. Only for the fast quench can a large spike and fast oscillations in the kinetic energy be seen starting at 1.8 ms, where the quench occurs. The energy is primarily added to the axial direction via excitations of the axial breathing mode. In the zigzag phase, the average kinetic energy along both dimensions approach the same value. . . . .	78
Figure 5.7	Simulation frames showing nucleation of a discrete kink, and the evolution after nucleation into an extended kink, and migration of the extended kink to the center. Simulation is at $V_f = 5.8 \text{ V}$ ( $\omega_y/2\pi = 342 \text{ kHz}$ ). . . . .	79
Figure 5.8	Experiment: (a): Average number of kinks observed per run vs. scaled quench rate for standard trap with $\omega_z/2\pi = 37.6 \text{ kHz}$ (triangles). Data for 41-43 ions include 1000-5000 runs. Error bars are calculated binomial, approximately consistent with fluctuations. Solid line is a molecular dynamics simulation with parameters including $\omega_z/2\pi = 38.2 \text{ kHz}$ (see text), and shown 2 ms after the quench. Statistical uncertainties of simulation less than or equal to the experiment. (b)-(d): Observed position distributions of kinks for 42 ions (red, upper) and 43 (blue, lower) in standard trap at quench time $2\tau_Q$ of (b) 20, (c) 15, and (d) $12 \mu\text{s}$ with simulations (lines) for comparison. . . . .	80



Figure 5.9	Simulation: The selected kinks at early times after (a) a fast quench ( $2\tau_Q = 10 \mu\text{s}$ ) and (b) a slow quench ( $2\tau_Q = 70 \mu\text{s}$ ). The quench begins at $t = 0$ Color-coded points show identified trajectories. The blue points are potential kinks rejected by the filtering process. The grey lines show the edges of the zigzag region for individual simulation runs. The black line indicates the averaged zigzag edge defined by $0.15a_y$ used to window the valid kinks. The outer 9 ion-sites on each edge are also excluded. (c): The density of kinks as a function of time for different quench rates. . . . .	82
Figure 5.10	Simulation: The effect of a delay in counting on the maximum number of counted kinks as a function of quench time. We chose a $7\mu\text{s}$ delay time. The plots are shown for a threshold on zigzag amplitude of $0.15a_y$ . . . . .	83
Figure 5.11	Experiment: (a): Average number of kinks observed per run vs. scaled quench rate for standard trap with $\omega_z/2\pi = 37.6 \text{ kHz}$ (black circles), and for one with secular frequencies reduced by 2 (orange triangles) with quench changed accordingly. The solid black line is a molecular dynamics simulation with parameters including $\omega_z/2\pi = 38.2 \text{ kHz}$ (see text), and shown 2 ms after the quench. The dashed black line is the same simulation with "early counted" kinks. Dotted and dash-dotted lines (green) show kink number 2 ms after quench and shortly after nucleation, respectively, for a simulation of 84 ions with optimized Doppler cooling (detuning $-11.3 \text{ MHz}$ , $s_0 = 2.0$ ) and with $\omega_z/2\pi = 20.6 \text{ kHz}$ , chosen to match the transverse critical frequency for 42 ions at crystal center. The simulation plot is scaled using $\omega_z/2\pi = 38.2 \text{ kHz}$ for direct comparison to 42 ions. (b): The blue region, $\log_2(1/2\omega_z\tau_Q) = [-3.1, -2.1]$ , divides the plot into three octaves of quench rate. Shown are linear fits in each of the three octaves for a string of 42 ions to extract power-law scaling. The linear fit to the experimental measurements at $\omega_z/2\pi = 37.6 \text{ kHz}$ in the middle octave gives a power-law exponent of $3.3(2)$ (c): Table of slopes obtained from linear fits to early-counted simulations of 42-ion (shown in b) and 84-ion strings (not shown). . . . .	85

Figure 5.12	(a), (b): Axial trajectories of discrete kinks in zigzag crystals ( $V_f = 4.8$ V) with (a) 42 and (b) 43 ions for three different initial positions: center and four sites away on both sides. The number of trajectories for each case is 11 with fewer for $z < 0$ . (c), (d): Exponential lifetime of kinks (filled circles) vs. initial position in crystals of (c) 42 and (d) 43 ions. Lifetimes and their uncertainties obtained from a maximum likelihood estimate including binning due to camera frame rate. Also shown are axial position distributions at $t = 0$ ms (filled gray bars) and $t = 400$ ms (open red bars). . . . .	86
Figure 5.13	Images of a crystal of 43 ions. The separation between frames is 40 ms. (a) A typical departure of a kink through the edges of the ion crystal. (b) An unusual motion of a kink with back- and forth-motion before departure. . . . .	89
Figure 5.14	(a) A crystal of 42 ions with two discrete kinks. The one on the left, leaves the crystal within 5 frames (200 ms), while the kink on the right remains on the same site for 8 frames (320 ms) and is gone on the 9 <sup>th</sup> frame. (b) Departure of an extended kink in a crystal of 50 ions (Extended like this one are not part of the presented data of post nucleation dynamics and lifetime). . . . .	90
Figure 6.1	The scaled effective potential $V(\phi_{zz})$ and the level structure of the first five motional energy levels of a string of four $^{171}\text{Yb}$ ions for different deviations from the critical point. Each plot shows the scaled potential over the extent of the embedding square well used to solve for the energy levels (see text). For quantitative results, see Fig. 6.2. Plot (a) and (b) are on the linear side, where the effective potential is quadratic far from the critical point and has a single-well form. Plot (c) is right at the critical point (c.p.), where the effective potential is quartic. Plot (d) is slightly after the c.p., where the double well is starting to shape. Plot (e) is a double well that embeds only the first energy level ( $n = 0$ ). Plot (f) is when the second energy level ( $n = 1$ ) is just below the barrier (the point with the highest tunneling frequency). Plots (g) and (h) show how the two lowest energy levels approach degeneracy further past the critical point. Plot (e) is even deeper into zigzag, where the third and fourth energy levels are approaching degeneracy as well. . . . .	94

Figure 6.2	(a) The well separation and (b) classical local frequency (soft mode frequency)(green), quantum local frequency (proportional to energy separation between $n = 2$ and $n = 0$ )(blue) and the separation between the first two energy levels (corresponding to tunneling frequency) (red) in kHz, as a function of transverse frequency deviation from the critical point. (c) Same as plot (b) on the zigzag side, where the tunneling frequency is the right axis and the local frequencies are the left axis. The calculations are for a string of four $^{171}\text{Yb}$ ions, at a fixed axial trap frequency $\omega_z = 2\pi \cdot 370$ kHz. . . . .	95
Figure 6.3	The four stages of the proposed experiment for measuring the tunneling oscillations between the zig and zag configurations near the critical point of the L-Z transition. . . . .	97
Figure 7.1	The Zeeman-resolved energy levels of the $^2S_{1/2}$ and $^2P_{1/2}$ states of $^{171}\text{Yb}^+$ and the main $S_{1/2}(F = 1) \rightarrow P_{1/2}(F = 0)$ transition used for Doppler cooling, P-G cooling, and fluorescence detection. The size of Zeeman shifts are exaggerated. The polarization resolved branching ratios for the three $S_{1/2}(F = 1)$ sub-levels are all the same and equal to $1/3$ . Two of the hyperfine levels of the ground state, $S_{1/2} F = 0, m_F = 0\rangle \equiv  \uparrow\rangle$ and $S_{1/2} F = 1, m_F = 0\rangle \equiv  \downarrow\rangle$ , form an effective spin-1/2 system used for microwave and two-photon Raman transitions. . . . .	104
Figure 7.2	A polarization-gradient configuration formed by the superposition of two linearly polarized counter-propagating beams. The typical "Lin- $\perp$ -Lin" configuration corresponds to $\theta = \pi/2$ . . . . .	105
Figure 7.3	The sketch of the Sisyphus cooling process for a free $^{171}\text{Yb}$ ion moving in a Lin- $\perp$ -Lin configuration. The ac Stark shifts (potentials) of the effective $m_F = \pm 1$ state, shown in green, and of the $m_F = 0$ state, shown in red, are plotted using Eq. 7.15 and 7.16, assuming $\Delta > 0$ . The probability of the optical pumping is highest at the maximum point of a potential; the atom tends to end up in the state with a lower potential after pumping, and so loses an amount of kinetic energy lost to "climbing the hill". See also [9] . . . . .	108
Figure 7.4	The comparison between (a) optical pumping rates and (b) steady-state populations for both $ 0\rangle$ and $ \pm 1\rangle$ states as a function of position for the Lin- $\perp$ -Lin case. . . . .	111

Figure 7.5	<p>The Sisyphus cooling process of a single trapped <math>^{171}\text{Yb}</math> ion. (a) An ion in the <math> \pm 1\rangle</math> state is oscillating in the <math>U_{[\pm 1]}</math> potential. At the point <math>x_{o.p.}</math>, displaced by <math>\Delta x_{\pm 1}</math> from the ion's potential center, an optical pumping event transfers the ion into the other state. As a result of optical pumping, the ion is brought closer to the center of its new potential <math>U_{[0]}</math> and loses energy. Samples of a (b) heating event and (c) a cooling event through optical pumping from the <math> \pm 0\rangle</math> to the <math> \pm 1\rangle</math> state. . . . .</p>	113
Figure 7.6	<p>Illustration of the transition rates between the three Fock states using the rate coefficients <math>A_+</math> and <math>A_-</math>. . . . .</p>	119
Figure 7.7	<p>The calculation results of laser intensity dependence of the cooling rate (a and c) and cooling limit (b and d) in the axial (a and b) and transverse (c and d) directions. Calculations shown are the 3-D semiclassical simulation (filled circles), 1-D semiclassical simulation (open circles), analytical semiclassical model (black lines), and analytical quantum model (green line). The semiclassical analytical plots show a model with both ac Stark shift and scattering due to the <math>P_{1/2}(F = 1)</math> state (black dashed line) and with the scattering effect omitted (black solid line). The related parameters are <math>\{\eta_y, \eta_z\} = \{0.031, 0.052\}</math>, <math>\delta_B/2\pi = 18.2</math> MHz, <math>\Delta/2\pi = 310</math> MHz, <math>\theta = \pi/2</math>, and <math>\phi = \pi/4</math>. . . . .</p>	122
Figure 7.8	<p>The results of the (a) cooling rate and (b) steady-state <math>\bar{n}</math> as a function of the axial trap frequency for two laser saturation parameters of <math>s_0 = 20.3</math> and <math>s_0 = 36.1</math>. The open circles are the results of 1-D semiclassical simulations and the dashed lines are the 1-D semiclassical analytical model (derived for the LD regime). Also, the squares represent the results of 1-D quantum simulations for <math>s_0 = 20.3</math>, and starting with an initial state of <math>n_i = 8</math> (green) and an initial Doppler thermal distribution (red). (c): The condition for the LDL is investigated in a plot of <math>\eta_z\sqrt{2\bar{n} + 1}</math> vs. axial frequency for the range of Doppler-cooled to Sisyphus-cooled average energies. The operation point of our experiment at <math>\omega_z/2\pi = 0.525</math> MHz is indicated. Other parameters are; <math>\delta_B/2\pi = 18.2</math> MHz, <math>\Delta/2\pi = 310</math> MHz, <math>\theta = \pi/2</math>, and <math>\phi = \pi/4</math>. . . . .</p>	123
Figure 7.9	<p>(a) Cooling rate and (b) steady-state <math>\bar{n}</math> as a function of the Zeeman shift, calculated using the 1-D quantum analytical model. Parameters used for the plots are an axial trap frequency <math>\omega_z/2\pi = 0.525</math> MHz, transverse trap frequency <math>\omega_y/2\pi = 0.766</math> MHz, <math>s_0 = 15</math>, <math>\theta = \pi/2</math>, and <math>\phi = \pi/4</math>. . . . .</p>	125

Figure 7.10	(a) Cooling rate, (b) heating rate, and (c) steady-state $\bar{n}$ as a function of phase $\phi$ . The calculations are for the transverse direction with $\omega_y/2\pi = 0.766$ MHz and at a saturation parameter of $s_0 = 20.3$ . The other parameters are similar to the ones used in the experiment: $\delta_B/2\pi = 8.2$ MHz, $\Delta/2\pi = 310$ MHz, and $\theta = \pi/2$ . The blue circles show the 3-D (filled circle) and 1-D (open circle) semiclassical simulations. The lines represent the analytical models, where the black dashed line is a semiclassical model and the green line is a quantum model. The discrepancy in $\bar{n}_{ss}$ between simulation and analytical models in (c) is due to the omission of the $P_{1/2}(F = 1)$ state's pumping effect in the simulations. . . . .	126
Figure 7.11	Phase averaged (a) cooling rate and (b) steady-state $\bar{n}$ as a function of $s_0$ . The effect of slow (red line) and fast (purple line) modulation is compared to the static case at the optimum point (black dashed line). Also, the 3-D/1-D semiclassical simulation (blue circles) and 1-D quantum simulation (green square) for a lattice modulation of $\omega_m/2\pi = 0.08$ MHz, are shown for comparison. The shaded region indicates the standard deviation of the $\bar{n}$ fluctuations in steady state for the quantum simulation. The uncertainty in $\bar{n}_{ss}$ value is similar. These plots are calculated for the transverse direction with $\omega_y/2\pi = 0.766$ and $\delta_B/2\pi = 8.2$ MHz, $\Delta/2\pi = 310$ MHz, and $\theta = \pi/2$ . . . . .	127
Figure 7.12	The $P_{1/2}(F = 1)$ state pumping correction to 3-D semiclassical simulations of $\bar{n}_{ss}$ vs. $s_0$ for the (a) axial and (b) transverse directions. The green squares are 1-D quantum simulation and blue filled circles are 3-D semiclassical simulation without any correction (same as Fig. 7.11(b)). The open blue triangles are 3-D semiclassical simulations considering the effect of the $P_{1/2}(F = 1)$ scattering. . . . .	127
Figure 7.13	(a) The first red-sideband transition and (b) blue-sideband transition driven by a single laser beam. . . . .	130
Figure 7.14	The scaled Rabi frequencies of carrier and blue-sideband transitions for the Lamb-Dicke parameters of (a) $\eta = 0.2$ and (b) $\eta = 0.02$ . . . . .	131
Figure 7.15	The first blue-sideband transition driven by a pair of laser beams in a stimulated two-photon Raman process. . . . .	132
Figure 7.16	The optical path of the north and south Sisyphus beams along with the Doppler cooling/detection beam. . . . .	135

Figure 7.17	The pulse sequence of the microwave Ramsey experiment to measure the differential ac Stark shift of a single Sisyphus beam. Ramsey oscillations are obtained by varying the exposure time $\Delta t$ of the Sisyphus beam. . . . .	137
Figure 7.18	Polarization calibration of south (blue) and north (red) Sisyphus beams. The points show the measure values and the lines show the fit results. . . . .	138
Figure 7.19	The simplified optical path of the three perpendicular Raman beams entering the trap from south, west, and east sides. The south and east beams are used for the axial thermometry and sideband cooling, while the south and west beams are used for the transverse direction.	140
Figure 7.20	(a) The circuit diagram of the noise-eater. (b) The noise-eater setup used to stabilize the laser power of the Raman beams. (c) The performance of the noise-eater showing the laser power with and without the servo active. . . . .	142
Figure 7.21	(a) All the laser beams used in our experiment and their entry directions into the trap. (b) The $\Delta \vec{k}$ (compared to the trap axis) of south/west and south/east Raman beams applied for the transverse and axial thermometry (or sideband cooling). . . . .	143
Figure 7.22	The sequence of pulses used for the Sisyphus cooling experiments. The optical transitions that are driven with each pulse are also depicted with Zeeman structures suppressed for clarity. The sequence starts with a long Doppler cooling period, followed by a variable number $N$ of Sisyphus pulses. Each Sisyphus pulse includes a short ( $10 \mu s$ ) optical pumping pulse, followed by a microwave $\pi$ -pulse. These two pulses initialize the ion into the $S_{1/2} F = 1, m_F = 0\rangle$ state, ready for the Sisyphus beams. The Sisyphus cooling sequence is followed by a $50\text{-}\mu s$ optical pumping pulse that prepares the ion in the $S_{1/2} F = 0, m_F = 0\rangle$ state for a two-photon Raman carrier transition for thermometry. The sequence ends with a detection pulse. During spin-sensitive fluorescence detection, the fluorescence cycle is active for the $S_{1/2}(F = 1)$ state but is closed to the $S_{1/2}(F = 0)$ state.	144
Figure 7.23	The measurement for the rate of pumping to the dark $S_{1/2}(F = 0)$ state in the presence of two Sisyphus beams at $s_0 = 11$ . A pumping time of $\tau = 0.3$ ms is found from an exponential fit, and the single-pulse cooling time is set to $1/3$ of that value (0.1 ms) for all the measurements at that power. . . . .	146

Figure 7.24	A selection of carrier scans vs. cooling time for the transverse direction and at a saturation parameter of $s_0 = 11$ . The scans are fit to a thermally averaged Rabi oscillation (red line) to derive $\bar{n}$ for each cooling time. . . . .	147
Figure 7.25	(a) Transverse $\bar{n}$ and (b) axial $\bar{n}$ as a function of Sisyphus cooling time at a single beam laser intensity corresponding to saturation parameter $s_0 = 11$ . The plots are fit to an exponential decay to find the cooling rates at that laser intensity. (c) The complete data set of cooling rate over a range of laser intensities for both the axial and transverse directions. Note that the error bars for the $\bar{n}$ values are from the carrier fits and the error bars for the cooling rates are from the exponential fits. The green line shows $s_0^2$ scaling as a guide to the eye. . . . .	148
Figure 7.26	Measured steady-state $\bar{n}$ vs. laser intensity, in terms of the single-beam on-resonant saturation parameter $s_0$ , for the axial (red) and transverse (blue) directions. A minimum of $\bar{n}_{ss} \simeq 1 - 2$ is observed at an optimum value of $s_0 = 10 - 20$ , depending on the axis. . . . .	149
Figure 7.27	The cooling rate ((a) and (c)) and steady-state quantum number $\bar{n}$ ((b) and (d)) as a function of laser intensity for the axial ((a) and (b)) and transverse ((c) and (d)) directions. The experimental measurements (black open circles) are compared to 3-D semiclassical simulations (solid blue line), 1-D semiclassical simulations (dashed blue line), and 1-D quantum simulations (red). The quantum simulations include those with an initial thermal state with $\bar{n}_i = 22$ (red open circles), and an initial state of $n_i = 8$ (red dotted line). The shaded region indicate the standard deviation of the $\bar{n}$ fluctuations in steady state for the quantum simulation. The uncertainty in the $\bar{n}_{ss}$ values obtained from the simulation is smaller. . . . .	152
Figure 7.28	The ground-state cooling process is performed in two steps: first, a red-sideband transition driven by two Raman beams transfers the ion into a lower motional state: $ \downarrow, n\rangle \rightarrow  \uparrow, n - 1\rangle$ . Second, an optical pumping step resets the spin state: $ \uparrow, n - 1\rangle \rightarrow  \downarrow, n - 1\rangle$ . The two steps are repeated until the ion reaches the ground state, which is decoupled from the red-sideband transition. . . . .	153

Figure 7.29	(a), (b) Simulation results of red-sideband Rabi oscillations for the transverse center-of-mass mode, starting from the $ \downarrow\downarrow\downarrow\downarrow\rangle$ state (red line) or the $ \uparrow\uparrow\uparrow\uparrow\rangle$ state (blue line) in a four-ion string with (a) $\bar{n} = 1$ or (b) $\bar{n} = 2$ . The sideband asymmetry for each pair of sideband oscillations is found by locating the maximum and minimum points of oscillations (shown by black points in (a), (b)). (c) The sideband asymmetry vs. $\bar{n}$ (green line). This plot can be fit to a linear function (black dashed line) to obtain the approximate correction factor of 2.32(2) relating the sideband asymmetry to $\bar{n}$ for the transverse COM mode of a four-ion string. . . . .	157
Figure 7.30	Rabi time scans used for the thermometry of a single sideband-cooled $^{171}\text{Yb}$ ion. Both axial (a, b) and transverse $y$ directions (c, d) are shown. The top panels (a, c) show the red sideband starting in the $ \uparrow\rangle$ state and the bottom panels (b, d) show the red sideband starting in the $ \downarrow\rangle$ state. The suppression of the red sideband oscillations in the later case indicates cooling to near the ground state of motion. . . . .	158
Figure 7.31	The measured frequencies of the normal modes of a four-ion string along the three axes of motion, and the estimated sideband asymmetry correction factor for each mode. . . . .	159
Figure 7.32	Sideband Rabi oscillations for three vibrational modes of a four-ion string following (a, b and c) Sisyphus cooling and (d, e and f) Raman sideband cooling for: (a and d) The transverse bending mode, (b and e) the transverse zigzag mode, and (c and f) the axial zigzag mode. Note that no discrimination between photon count levels is used in our four-ion detection, and so the vertical axes show the total number of counted photons in 0.4 ms. Black lines show fits including corrections for experimental imperfections (see text). Dotted lines show the ideal model with contrast envelope removed. Average vibrational number $\bar{n}$ from the Sisyphus fits are (a) 1.60(4) for the transverse bending mode, (b) 1.95(4) for the transverse zigzag mode, and (c) 1.11(4) for the axial zigzag mode. The fits to the sideband cooled data constrain $\bar{n} \leq 0.05$ . . . . .	160



# Chapter 1

## Introduction

The first observation of a crystal of trapped charged particles was reported in 1959 by Wuerker et al. [10]. Using Paul traps, they demonstrated ordered configurations of aluminium micro-particles cooled via buffer gas. Repeated melting-crystallization events were also obtained by variation of the confining potential and the cooling force. Despite this demonstration of an easily controlled order-disorder transition, as experiments for trapping atomic ions developed in sophistication, the research was mainly focused on utilizing single trapped ions for high resolution spectroscopy and frequency standards [11]. It took a number of years before the applicability of ion-trapping experiments to exploring "few-body phase transitions" was realized.

Indeed, it was the motivation to improve the high-resolution spectroscopy of trapped ions that led Wineland and Dehmelt [12], and Hänsch and Schawlow [13] to come up with schemes for laser cooling in 1975. In 1978, laser cooling of trapped ions was successfully implemented for an ensemble of trapped ions [14, 15]. Within two years, Neuhauser et al. had demonstrated the localization of single cooled trapped ions [16]. Finally, in 1987 the first observation of the crystallization of laser-cooled, trapped ions into an ordered structure was shown by the group at the Max Planck Institute in Germany [17], and the NIST group in the USA [18]. The NIST group was interested in probing the motional spectroscopy of this pseudo-molecule [19,20], which led to stimulated Raman transitions [20] and sideband cooling [21,22]. These techniques, which had ready application to single-ion atomic clocks [23], were ultimately adapted to quantum information applications [20, 24]. The Max-Planck group was interested in the system as a condensed matter analog for studying mesoscopic phase transitions, and they made early studies of the order-disorder and then structural phase transitions [25-27]. The achievements of these two pioneer groups were widely used afterwards.

Since the first experimental realizations of Coulomb crystals through laser cooling of trapped ions [17,18], there has been growing experimental [25,28-36] and theoretical [37-49] interest in studying the structural and dynamic properties of various ion crystal configura-

tions in different trap setups. Many of the theoretical studies have used molecular dynamics simulation to bridge between pure theory and real experiments and to make direct comparisons to experiment. In fact there was already theoretical interest predating the first experiments [50], and perhaps one should say that the history of the subject goes all the way back to the first theoretical investigations by Wigner of crystals of electrons [51].

This thesis is focused on the specific case of ion crystals in a linear Paul trap. The equilibrium crystal structure of the trapped ions in a linear Paul trap with strong transverse confinement is a 1-D linear configuration [52]. The next structure encountered when the transverse confinement is reduced is a 2-D zigzag structure [49]. The linear-zigzag (L-Z) structural phase transition is categorized as a second-order phase transition in thermodynamics limit [53], and has the potential to be characterized as a classical phase transition, described by the Landau model [54], or a quantum phase transition, belonging to the universality class of a one-dimensional transverse field Ising model [55, 56]. The interesting properties of this transition along with the high controllability existing in ion-trapping systems has motivated a number of intriguing proposals to explore different aspects of the transition in both classical and quantum regimes in recent years [54, 57–63].

A number of these works, prompted by the intrinsic non-linearity of the L-Z transition, are focused on exploring both static and dynamic effects in non-linear physics (see [64] for a review). One of the main non-linear effects that has attracted significant attention is the nucleation of topological kink-defects. The dynamics involved are essentially classical and kinks can be formed as a result of a fast quench across this second-order phase transition. At least two applications have been proposed for these kinks including a test of the Kibble-Zurek mechanism (KZM) of defect nucleation (see below) [61], and the use of the internal modes of the kink to store and process quantum information [59].

The first part of this thesis is focused on exploring dynamics near the critical point of the L-Z transition in classical regime. In particular, this includes the nucleation of kink-defects and a test of the KZM. The KZM was originally proposed by Kibble in 1976 [65] as a theory to describe the formation of topological structures (such as cosmological strings) in the early universe. He proposed that as the universe cooled, the cosmological symmetries were broken and the universe was divided into independent domains, topological structures could have subsequently been formed on the boundary of domains with different symmetries. In 1985, Zurek [66] brought up the analogy between cosmic strings and vortex lines in a superfluid, and suggested an experiment in liquid Helium to verify the key elements of the Kibble theory. He reformulated Kibble’s theory for the superfluid system and showed that the density of the formed defects is related to the quench rate by a power-law dependence. Nowadays, these two proposals are merged into the universal Kibble-Zurek mechanism describing the formation of defects across any second-order phase transition and predicting the same scaling behavior for all systems fitting within the same universality class. Since Zurek’s first proposal, there have been many theoretical proposals for testing the KZM in

a broad range of physical systems, and many experimental attempts to do so. Following a theoretical proposal for testing the KZM in ion-trap systems [61], we have measured the density of defects as a function of quench rate and have studied a range of post-nucleation dynamics in a string of  $\sim 42$   $^{174}\text{Yb}$  ions.

Building on the experience and techniques we acquired for that experiment, and following a theoretical proposal [57], our group decided to investigate the near-transition dynamics in a string of four  $^{171}\text{Yb}$  ions at low temperature in the quantum regime. The goal of this experiment is to manipulate and assess quantum coherences by tunneling between the two configurations of the zigzag structure near the critical point of the transition. This experiment requires a high level of control and stability, and there are a number of techniques that need to be developed and technical problems to be addressed in order to realize a successful tunneling measurement. One of the key requirements for investigating the L-Z transition in the quantum regime is the ability to cool the zigzag vibrational mode of the string to the ground-state of motion with a high probability. In addition, given the relatively high Doppler average energy in our trap we expect it be necessary to cool the other modes of the string with a sub-Doppler cooling technique to a few quanta of vibration, or better. Motivated to resolve these issues, we implemented 3-D Sisyphus cooling in the form of polarization-gradient cooling [67] to obtain simultaneous near-ground state cooling of all vibrational modes and to allow a more efficient ground-state cooling of the zigzag mode. The Sisyphus cooling technique is widely used in laboratory experiments to cool down neutral atomic gasses of a variety of species [68], in optical lattice experiments [69–72] and for individual atoms in optical tweezers or optical cavities [73–75]. However, the Sisyphus cooling of trapped ions has been reported only once, for the case of one and two particles [76]. Based on the efficiency and simplicity of this cooling technique, we believe that it can be very useful in experiments with moderately sized ion crystals.

Following this introduction, we provide an overview in Chapter 2 of the theory of the Kibble-Zurek mechanism and survey most of the physical systems in which an attempt to test the KZM was made. In Chapter 3, we show how the KZM can be applied in ion-trapping systems. Starting with the equilibrium configurations in linear Paul traps, we explain the theory of the linear-zigzag transition and show how the scaling law of the defect formation is obtained for the ion-trap system. In Chapter 4, we focus on the experimental setup required to test the KZM and describe the complications encountered with using a large string of ions. The experimental results on spontaneous nucleation and dynamics of kinks are presented in Chapter 5. The experimental results are accompanied by molecular dynamics simulations used to assess the dynamics of kinks at the transition point and shortly after, which is hard to access experimentally. The second part of the thesis starts at Chapter 6, where we describe the details of a proposed experiment to measure the tunneling rate near the transition. We also point out the experimental challenges that need to be addressed to make the coherence assessment of zigzag superposition states possible. In Chapter 7, we provide

a detailed theoretical description of Sisyphus cooling in trapped-ion systems, experiments to assess the cooling performance, and comparison to simulation results. We also present Sisyphus cooling of all vibrational modes of a 4-ion string followed by ground-state cooling of any given mode. Finally, the conclusion of the thesis appears in Chapter 8.

## Chapter 2

# The Kibble – Zurek Mechanism

This chapter begins with a historical overview of the Kibble-Zurek Mechanism (KZM). Starting with Kibble's proposal to explain the formation of domains and topological defects in the early universe, we discuss how Zurek extended Kibble's idea to condensed matter systems. We then review the Kibble-Zurek mechanism as a "universal" theory describing the spontaneous nucleation of topological defects in any system that is rapidly brought ("quenched") across a continuous phase transition. In particular, we discuss a key prediction of the KZM, namely a universal power-law scaling for the density of defects as a function of the quench rate. Finally, we survey most of the physical systems used to test the predictions of the KZM since the first experiments were performed in 1991. Since then, Kibble, Zurek and others have provided a series of updated reviews of the experimental tests of the KZM and commented on their degree of success [77–79].

### 2.1 Introduction to the Kibble – Zurek mechanism

In the 1970's, after the successful theoretical unification of electromagnetic and weak interactions, researchers tried to expand the electro-weak theory into a grand unified theory of the electro-weak and strong interactions. They suggested a larger underlying symmetry exists at high energies which relates the carriers of these three interactions. Evidence shows that the strengths of these three interactions approach a common value at energy scales of about  $10^{16}$  GeV, suggesting that the underlying symmetry was somehow broken around those energy scales [77]. Accordingly, it was natural to propose that after the big-bang, as the universe cooled and expanded, it went through some early symmetry breaking phase transitions around a critical temperature corresponding to those energy scales. The question that followed this proposal was whether these symmetry breaking phase transitions have led to the formation of any topological defects in the early universe. In 1974, Zeldovich *et al.* first discussed this question [80]. They pointed out the cosmological consequences of

the formation of a specific cosmic structure known as a planar domain wall that could have been formed as a result of a spontaneously broken discrete symmetry.

In 1976, Kibble broadened the discussion by studying the possibility of the formation of different topological structures that could have appeared in the early universe and their evolution over time [65]. He assumed that the universe could be described by a spontaneously broken gauge symmetry exhibiting a phase transition at a critical temperature of  $T_c$ . At earlier times and above  $T_c$ , the universe was assumed to be in a normal phase, in which the expectation value of the complex "order parameter" field was zero  $\langle\phi\rangle = 0$ . As the universe cooled and reached  $T_c$ , the fluctuations in  $\phi$  rose, and as it passed through  $T_c$ , the expectation value of  $\phi$  settled into a non-zero value. Since the size of the universe is very large, due to causality, largely separated regions in space could independently choose randomly different expectation values of  $\phi$ . The mean size of these widely separated regions (domains) was estimated to be the same order as the correlation length at a time when fluctuations in  $\phi$  diminish significantly or freeze out. Beyond this time, known as the "freeze-out" time, regions of normal and ordered phases, and also the ordered phases of different domains are distinct. He then examined the topology of structures in the boundaries of domains and showed a variety of topological structures could have been formed when different numbers of domains meet. For example, at the boundary of two domains, planar domain walls could appear, at the boundary of three domains, linear cosmic strings; and finally at the boundary of four domains, pointlike monopoles. He studied the evolution of domain walls and strings under the effects of tension and interaction with the surrounding matter and found both of these defect structures evolved similarly, and their sizes grew with time and eventually could become comparable to the universe size. Domain walls were found to have a large gravitational effect and could be ruled out observationally. In this first paper, Kibble also concluded that it is unlikely to expect strings to survive on a small scale until the present time to be directly visible. Later on, after the introduction of inflation into the cosmology, researchers concluded that if the strings were formed after the inflation period, a sufficient number of them could have survived to have interesting effects on the evolution of universe.

In 1985, Zurek brought up the analogy between cosmic strings and vortex lines in superfluids, and suggested an experiment using  $^4\text{He}$  to verify the key elements of the Kibble mechanism describing cosmic string formation. He proposed that a fast pressure quench across the normal to superfluid phase transition in bulk  $^4\text{He}$  leads to the appearance of vortex lines [81], and proposed a related experiment for spontaneous formation of quantized rotation in an annulus of superfluid [66]. The title of the latter well-known paper inspired the term "cosmology in the lab" used so often later. A vortex, analogous to a cosmic string, is a thin tube around which the phase of  $\phi$  varies by  $2n\pi$  ( $n$  being a non-zero integer). The order parameter  $\phi$  of the  $^4\text{He}$  superfluid corresponds to the Bose condensate wavefunction, and vortex lines are quantized circulations of the superfluid. Zurek replaced the speed of light in the Kibble's theory with the relevant characteristic speed in the  $^4\text{He}$  system, which

is the speed of "second sound", and used equilibrium concepts such as correlation length and relaxation time to assess the non-equilibrium dynamics of this phase transition. He estimated the density of vortex lines formed using the correlation length of the system at the "freeze-out" time and showed the density of defects is related to the quench time by a power-law relation.

Nowadays, the theoretical results of these two scenarios are merged into one universal mechanism known as the Kibble-Zurek-mechanism (KZM) and describes the non-equilibrium dynamics of any system going through a second-order phase transition. The KZM proposes an intuitive model of domain and defect formation, and predicts a power-law scaling for the number of defects formed as a function of transition quench rate.

## 2.2 Theory of Kibble – Zurek mechanism

A second-order phase transition induced by the change of a control parameter  $\lambda$  can be described by Landau-Ginzburg theory in which the potential energy is: [65, 82, 83]

$$V = \alpha(\lambda - \lambda_c)|\phi|^2 + \frac{\beta}{2}|\phi|^4, \quad (2.1)$$

where  $\alpha$  and  $\beta$  are constants and  $\phi$  is the order parameter field. In this case, both of the *equilibrium* correlation (or healing) length  $\xi$  and the *equilibrium* relaxation (response) time  $\tau$  diverge in a power-law relation as a function of reduced order parameter or dimensionless distance from the critical point  $\epsilon = \frac{\lambda - \lambda_c}{\lambda_c}$  :

$$\xi(\epsilon) = \frac{\xi_0}{|\epsilon|^\nu}, \quad (2.2)$$

$$\tau(\epsilon) = \frac{\tau_0}{|\epsilon|^\mu}. \quad (2.3)$$

In these equations,  $\nu$  and  $\mu$  are critical exponents defined by the universality class of the transition, while  $\xi_0$  and  $\tau_0$  are constants defined based on the microphysics of the system in use. The divergence in the response time of the system to external perturbations, as described by Eq. 2.3, is given the name "critical slowing down".

To understand the non-equilibrium dynamics of a second-order phase transition near the critical point, we assume the control parameter is changed uniformly over a finite time:

$$\epsilon(t) = t/\tau_Q \quad , \quad t \in [-\tau_Q, \tau_Q], \quad (2.4)$$

where  $\tau_Q$  is the quench time of the symmetric quench around the critical point. Following the KZM argument, if we start far from the critical point, ( $\epsilon \ll 1$ ), where the relaxation time  $\tau(\epsilon)$  is short, the adjustment rate to the imposed changes is fast compared to the

rate of changes induced by the quench. Consequently, the system follows the changes adiabatically and remains in equilibrium. As we approach the critical point ( $\epsilon \rightarrow 0$ ), as a result of the critical slowing down, the response time of the system becomes too long to keep up with the imposed changes. Consequently, the dynamics of the system become non-equilibrium and the system ceases to react to the quench-induced changes (it freezes). When we are well past the critical point ( $\epsilon \gg 1$ ), the dynamics of the system become adiabatic again. The KZM divides the dynamics into three separate regions: adiabatic, frozen, and adiabatic again. This simplification is referred to as the adiabatic-impulse approximation. In this approximation, the non-equilibrium region is assumed to be effectively frozen and the transition between the adiabatic (quasi-equilibrium) and frozen (non-equilibrium) regions is effectively shrunk to a point in time. This point, known as the freeze-out point (see Fig. 2.1), is the point when the relaxation time of the system becomes comparable to the time remaining to reach the critical point (or equivalently the time elapsed after crossing the critical point):

$$\tau(t) \approx \left| \frac{\epsilon}{\dot{\epsilon}} \right| = t. \quad (2.5)$$

Equating Eqs. 2.3 and 2.5, and assuming a linear quench (Eq. 2.4), one can find the "freeze-out" time  $\hat{t}$ :

$$\hat{t} \sim \left( \tau_0 \tau_Q^\mu \right)^{\frac{1}{1+\mu}}, \quad (2.6)$$

which corresponds to the reduced order parameter

$$\hat{\epsilon} \sim \hat{t} / \tau_Q = \left( \frac{\tau_0}{\tau_Q} \right)^{\frac{1}{1+\mu}}. \quad (2.7)$$

The correlation length at the "freeze-out" time can be derived by substituting Eq. 2.7 into the divergence equation of the correlation length (Eq. 2.2):

$$\hat{\xi} = \xi_0 \left( \frac{\tau_Q}{\tau_0} \right)^{\frac{\nu}{1+\mu}}. \quad (2.8)$$

The correlation length,  $\xi(\epsilon)$ , is related to the scale of fluctuations in the system. In other words, the correlation length defines the extent of the system over which the order parameter returns to its equilibrium value following quench induced changes. The information about the state choice propagates with a finite speed that is a characteristic of the system (for example, the speed of light in cosmological cases and second-sound speed in superfluids). Near the freeze-out time  $\hat{t}$ , the size of the correlation length becomes of the same order as the distance over which the information about the state choice is spread. Assuming that the size of system is sufficiently larger than the correlation length at  $\hat{t}$ , then the system can contain regions (domains) with an average size of  $\hat{\xi}$  at this time. These domains are causally disconnected and have independent, randomly chosen, broken states. The



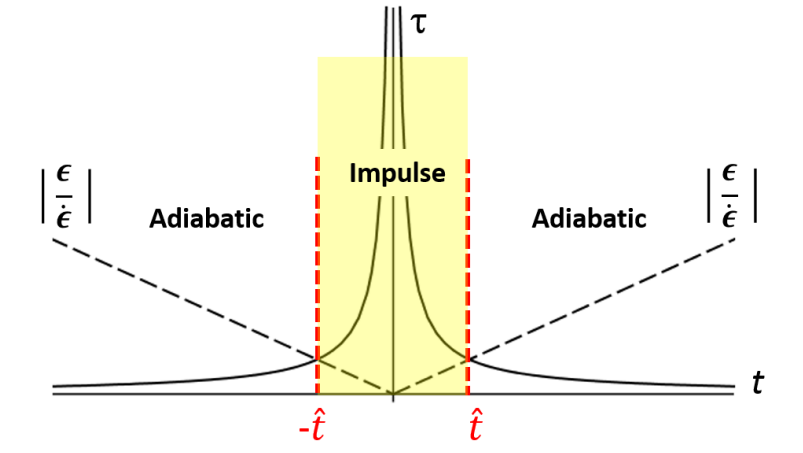


Figure 2.1: Schematic description of how the relaxation time  $\tau$  and the characteristic time of changes,  $|\epsilon/\dot{\epsilon}|$ , vary over time. The relaxation time is very small far from the critical point and it becomes significantly large as we approach the critical point at  $t = 0$ . For a linear change of the reduced order parameter  $\epsilon$ , the characteristic time of changes varies linearly with time. The time when these two times meet ( $|\frac{\epsilon}{\dot{\epsilon}}| = \tau$ ) is called the freeze-out time. According to the adiabatic-impulse approximation, dynamics of the system is considered non-adiabatic or impulsive in between the two freeze-out times, while adiabatic elsewhere.

topological defects can form on the boundary of domains with different broken states and the density of these defects is related to the number of domains *i.e.* the correlation length at freeze-out time:

$$d \sim \frac{1}{\hat{\xi}} = \frac{1}{\xi_0} \cdot \left( \frac{\tau_0}{\tau_Q} \right)^{\frac{\nu}{1+\mu}}. \quad (2.9)$$

The density of defects follows a power-law relation as a function of quench time, for which the power-law exponents depend only on the universality class of the transition. This is the key prediction of the KZM. As is often noted by Zurek, the power-law which describes the non-equilibrium dynamics is determined by equilibrium properties of the system near critical point. From the opposite perspective, assuming the KZM holds, sufficiently good measurements of the power-law exponent in principle would provide a constraint on  $\nu$  and  $\mu$  for a system.

Checking the universal KZM's power-law scaling requires a measurement of the number of defects over a reasonable range of quench rates. In the next section we provide an overview of different experiments designed to investigate the Kibble-Zurek Mechanism and to test the power-law dependence of the density of defects on the quench time.

## 2.3 A historical review of experiments designed to test the KZM

Since the first experiment in 1991, many experiments have been performed to test KZM predictions, and have been reviewed many times. The founders of the KZM, Tom Kibble and Wojciech H. Zurek, (and others) have reviewed the outcome of experimental tests of the KZM and commented on their degree of success [77–79]. The most recent review was written by A. del Campo and W. H. Zurek in 2014, for the occasion of Tom Kibble’s 80<sup>th</sup> birthday, and provides a complete review of all the experimental attempts at testing the KZM power-law prediction so far [79].

### 2.3.1 Liquid Crystals:

The first experimental attempt to test KZM predictions was on nematic liquid crystals by Chuang *et al.* in 1991 [1]. Nematic liquid crystals (NLC) are rod-like molecules in which isotropic-nematic transitions from a randomly oriented to an aligned phase occur by changing the temperature (or pressure). As the KZM predicts, it was demonstrated that rapid pressure and temperature quenches across isotropic-nematic transitions lead to the spontaneous formation of defects. The advantage of using NLC is the feasibility of simultaneous formation of various types of defects, including strings, monopoles and textures, that can be seen directly. Chuang *et al.* also studied the dynamical evolution of defects (see Fig. 2.2) and showed that the decay rate of defects matches the theoretical predictions.

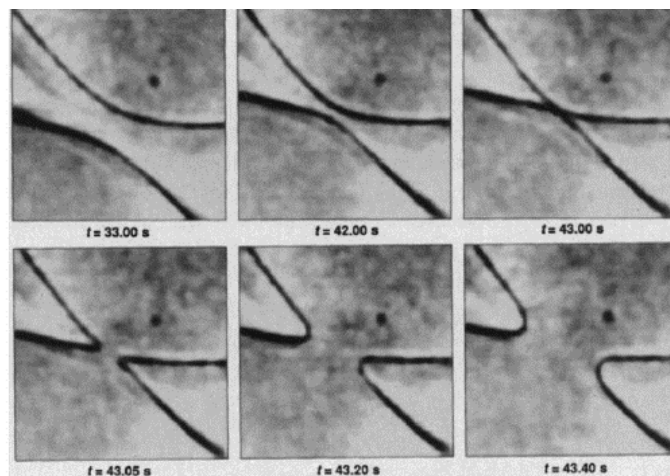


Figure 2.2: Time evolution of two strings defects, showing the crossing, then reconnecting in the other way. From [1]. Reprinted with permission from AAAS.

Following this experiment, Bowick *et al.* studied the nucleation, growth, and coalescence of nematic domains after a quench and how this leads to string-defect formation (see Fig. 2.3) [2]. They measured the number of string defects formed per domain after a quench

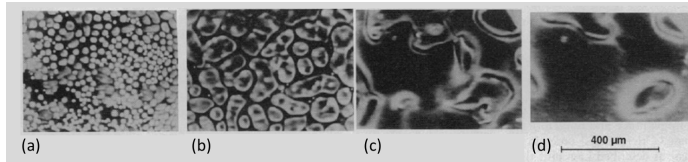


Figure 2.3: The time evolution of nematic bubbles at different times of (a) 2 s, (b) 5 s, (c) 11 s, and (d) 23 s, showing the process of domain formation and coalescence, and ultimately the formation of defects, following a quench. From [2]. Reprinted with permission from AAAS.

and compared it to simulations based on the Kibble mechanism. The measurement result was about a factor of two smaller than simulations, which they related to the losses of strings before the measurement time. The isotropic-Nematic transition studied in this and the prior experiment is a 1<sup>st</sup>-order phase transition, for which the theory of domain nucleation is different than that described above for the 2<sup>nd</sup>-order phase transition [78]. Neither group attempted to investigate the power-law dependence of the number of defects on the quench time for NLC.

### 2.3.2 Superfluid He:

At about the same time that Bowick *et al.* were studying defect formation in liquid crystals, Hendry *et al.* were pursuing an experiment more directly in line with Zurek's original proposal, in which they investigated the spontaneous formation of vortex defects in liquid <sup>4</sup>He after a rapid temperature reduction across the normal-superfluid transition [84]. Unlike NLC, liquid <sup>4</sup>He has a simpler order parameter, a scalar corresponding to the wavefunction associated with the superfluid. Nevertheless, as noted by Zurek in his original paper, the choice of phase for the superfluid order parameter provides a close analogy to the symmetry breaking associated with the quantum vacuum in relevant cosmological models, and the quantized vortex lines are the analog of cosmological strings. In comparing their <sup>4</sup>He system to NLC, Hendry *et al.* pointed out that while their experiment requires the added complication of cryogenics and does not allow direct observation of defects, the low viscosity of the liquid <sup>4</sup>He and the purity of their samples provides perhaps a cleaner cosmological analog. In their initial publication, Hendry *et al.* reported evidence of spontaneous nucleation of vortices after a fast quench across the normal-superfluid transition, but the occurrence of vortices was found later to be caused by imperfections in the experiment [85]. With an improved set-up, there was no sign of vortices from a quench [85], and it is believed that they disappear too quickly to be observed.

Following the <sup>4</sup>He experiment, two groups in 1996 reported observations of spontaneously nucleated vortices in superfluid <sup>3</sup>He [86, 87]. In both cases a neutron-induced nuclear reaction was used to locally heat small regions of superfluid <sup>3</sup>He to form bubbles of normal liquid. As the bubble cooled down to the superfluid state, vortex formation was

investigated. Although superfluid  $^3\text{He}$  experiments need yet more sophisticated cryogenic technology due to the ultralow temperatures involved, the system has some novel features compared to  $^4\text{He}$  and liquid crystals. As noted by both Bauerle *et al.* [86] and Ruutu *et al.* [87], during the normal to superfluid transition in  $^3\text{He}$  more symmetries are broken, which together with the types of symmetries involved, make for a closer analogy to what is believed to have happened in the early universe. Compared to  $^4\text{He}$ , superfluid  $^3\text{He}$  exhibits more phases and allows for a wider range of defects including points, vortex lines and domain walls, as well as excitations associated with the underlying fermionic system.

Ruutu *et al.* used a continuously rotating container of superfluid  $^3\text{He}$  to allow vortex rings nucleated in the bubble to expand into stable vortex lines in the container. An NMR technique was used to monitor the number of vortices formed during the  $0.1\text{-}\mu\text{s}$  cooling time of the bubbles as a function of normalized super-fluid velocity due to rotation. Spontaneously nucleated vortices were observed, and the experimental results, when plotted in terms of the normalized superfluid velocity, followed a dependence in favor of the KZM of defect formation.

In a complimentary experiment, Bauerle *et al.* used the same nuclear reaction to create bubbles of normal fluid, but measured the amount of energy kept in the fluid in the form of a vortex tangle after the bubble re-cooled. Their experiments were performed well below the critical temperature ( $0.1 T_c$ ). Knowing the thermal energy of a vortex per unit length, they could infer the typical spacing between vortices for three different ambient pressures *i.e.* three different quench rates. They found a pressure-independent value of about 8 for the ratio of vortex separation to correlation length, while an estimate based on the KZM predicted a value between 4-7 depending on the pressure through a weak power-law of  $\tau_Q^{1/4}$ . Although the value of the measured vortex density was close to the estimated range, it was constant and the reason for this discrepancy in pressure dependence was unclear.

In conclusion, both the experiment by Ruutu *et al.* [87] and Bauerle *et al.* demonstrated vortex formation during a quench of a second-order phase transition, but due to the small range of achievable quench rates and the weak  $\tau_Q^{-1/4}$  scaling, the experiments could not provide definitive evidence in support of the KZM power-law prediction for the vortex density as a function of quench rate.

### 2.3.3 Liquid Crystal Light Valve:

The first experiment to directly test the power-law dependence of the KZM was performed by Ducci *et al.* in a nonlinear optical system consisting of a liquid crystal light valve [3]. The transitions in these types of systems are not a typical phase transition between equilibrium states, but still can be described in terms of an effective field theory. The liquid crystal light valve (LCLV), which acts as a Kerr medium, was placed in an optical feedback loop and illuminated by a laser beam. Due to the Kerr effect, the reflected beam from the front face of the LCLV undergoes a phase retardation proportional to the light intensity at the

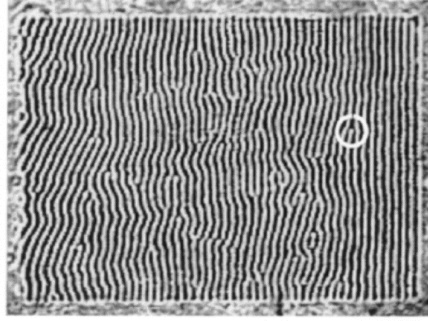


Figure 2.4: Intensity patterns in a liquid crystal light valve (LCLV) experiment, showing a number of defects (for example the circled one) 0.5 s after an intensity quench over a time of  $\tau_Q = 0.41$ s. Reprinted figure with permission from [3]. Copyright (1999) by the American Physical Society.

rear face. The intensity of this light (the control parameter) can be varied linearly from below to above a threshold value for optical pattern formation in the profile of the reflected beam. This experiment was set to obtain stripe patterns, and as they ramped the intensity of the light, defects were formed in the stripes (see Fig. 2.4). The density of defects was expected to follow a scaling law proportional to  $\tau_q^{-1/2}$ . For quench times between 5 and 100 ms, after correcting for effects of defect drift, a scaling law was found to be consistent with the theoretical prediction.

The ease with which the laser intensity, and so the quench, can be controlled was one of the advantages that allowed this system to achieve a power-law measurement. However, as noted in a recent review by del Campo and Zurek [79], more recent experiments and theory suggest that for such systems, involving switching between non-equilibrium states, renormalization theory may not be applicable. As a result the KZM scaling may apply only approximately or not at all in these cases.

### 2.3.4 Superconductors:

Another broad class of experiments used to investigate the KZM involves superconductor systems. The presence of an evolving gauge field, *i.e.* the electromagnetic field, that evolves with time across the transition complicates the description of the quench dynamics in superconductor transitions [88].

The first attempt to test the KZM in a normal-superconductor phase transition was performed at the Technion-Israel institute of Technology in 1999, using high temperature superconductor films [88]. A thin superconductor film held in a cell was heated to the normal state using a quartz lamp. The thin film was then cooled down to superconducting state via a helium exchange gas that linked the cell to liquid nitrogen. Following a temperature quench, the appearance of vortex-like defects, known as fluxons, was searched for. Based on KZM predictions, the number of defects is proportional to the inverse of correlation

length. The correlation length of a high temperature superconductor is much smaller than a conventional one. As a result, more defects are expected to form in a high temperature superconductor, but due to the low quench rate of 20 K/s in this experiment, no evidence of defect formation was observed at that time.

Four years later, the same group with an improved experiment reported the observation of flux lines in high temperature superconductor thin films, following a much faster quench rate of  $\sim 10^8 K/s$  [89]. It is interesting to note that the  $\sim 10^7$  times faster cooling rate was achieved by using a pulsed laser to provide a local heating of the thin film, and a transparent cold substrate as a heat sink for cooling. In these experiments only the net flux could be measured which is proportional to the difference between the number of fluxons and antifluxons. One down-side to this indirect measurement of flux formation is that the power-law scaling is very weak,  $\Delta N \sim \tau_Q^{-1/8}$ , compared to a direct measurement,  $N \sim \tau_Q^{-1/2}$ . The weak scaling law was verified over a small quench-rate range of  $2 \times 10^7 - 1 \times 10^8 K/s$ . However, as a result of a small range of changes in the measured flux values and large error bars, the exponent could not be extracted. It was also shown that the sign of net flux changes totally randomly from one quench to another, which is on par with KZM predictions.

In 2001, Hindmarsh and Rajantie proposed an additional mechanism (HRM) of defect formation for cases like superconductors, in which a local gauge symmetry breaking is involved rather than a global symmetry breaking [90]. They pointed out that in superconductors, in addition to fluctuations of the order parameter, leading to defect formation through the KZM, fluctuations of the magnetic field can also lead to the formation of clusters of fluxons of the same sign. The number of HRM defects is independent of quench rate, and their contribution to the total number of nucleated defects varies in different experiments [91,92]. In almost all the superconductor experiments described here, the KZM has the main role in defect formation, but in 2003 Kirtley *et al.* verified the HRM over five orders of magnitude of quench range [93]. They used specifically chosen thin film superconductor rings with a high magnetic field penetration depth and inductance, which make the activation of fluctuations in ring vortex number not too costly energetically at temperatures relatively far from  $T_c$ . As a result, they could show that thermal fluctuations in the magnetic flux can activate spontaneous formation of defects [92,93].

In 2010, the Technion group performed another experiment to study the spontaneous generation of fluxons in superconductors, but this time with the ability to image the defects in the sample [94]. They performed the experiment for two different quench rates. They found a higher density of fluxons for faster quench rates, but their measured values were two orders of magnitude smaller than KZM predictions. They also measured the spatial correlation between the fluxons and found both short- and long-range correlations. While the short-range correlation agrees with the KZM prediction, the long-range correlations are unexplained so far.

Another superconductor experiment was performed by the same Technion group in 2000 using a high-temperature superconductor loop made of 214 Josephson junctions in series [95]. During a thermal quench, as the loop cools down, each segment between the junctions would be expected to choose an independent random phase as the segment becomes superconducting. At lower temperature when the junctions coherently link the segments, the random walk in phase around the loop can resolve into a net integer phase winding, *i.e.* a net non-zero flux, around the loop. They indeed observed spontaneous formation of flux in the loop and found the sign and magnitude of the flux to be random from one quench to another in accordance with the KZM. However, due to the constant distance between the Josephson junctions that sets the size of domains, the number of domains are fixed and independent of quench rate in this experiment. As a result the power-law dependence of defect formation on quench rate cannot be tested.

Lastly, a series of more sophisticated experiments was performed by Monaco *et al.* using small, annular, low-temperature superconductor systems between 2001-2009. These experiments were the most elaborate effort to that point to specifically test the KZM power-law prediction [96–101], and were the second direct KZM power-law scaling measurement after the experiments by Ducci *et al.* using a liquid crystal light valve [3]. Monaco *et al.* used small annular Josephson tunnel junctions (JTJ) and small superconducting loops, where the size of the system is much smaller than the correlation length at freeze-out time (*i.e.* typical domain size). Therefore, the number of trapped fluxon defects during a thermal quench will be either 0 or 1. The probability of spontaneous formation of a single fluxon was measured by inspecting  $I$ - $V$  curves in which the presence of a fluxon is revealed by current peaks. At first, the probability of finding a fluxon in a small annular JTJ or loop as a function of quench time was predicted to follow a power-law scaling of  $P \propto \tau_Q^{-1/4}$ , and a verification of this power-law was reported in 2002 over three orders of magnitude of quench time in annular JTJs [96]. In 2006, a similar but much improved experiment with better magnetic field shielding, more statistics, and a wider quench range of four orders of magnitude, found a power-law exponent of  $0.51 \pm 0.06$  [99]. The factor of 2 discrepancy in power-law exponent was attributed at that time to flaws in the fabrication of the junction barrier. However, in 2009, a similar "doubled" power-law exponent of  $0.62 \pm 0.15$  was also measured in small loops [101].

Monaco *et al.* explained this by using a calculation to propose a doubling of the power-law due to a change in the dispersion of winding numbers for small annuli.<sup>1</sup> In fact, a doubling in the KZM power-law was already noted in theoretical studies of atomic Bose-Einstein condensate systems [102, 103] and has figured in the interpretation of the recent KZM experiments in trapped ions (see discussion below).

---

<sup>1</sup>For a more recent interpretation of these experiments that does not invoke fabrication flaws, and that discusses the power-law doubling among other effects, see the recent review by del Campo and Zurek [79].

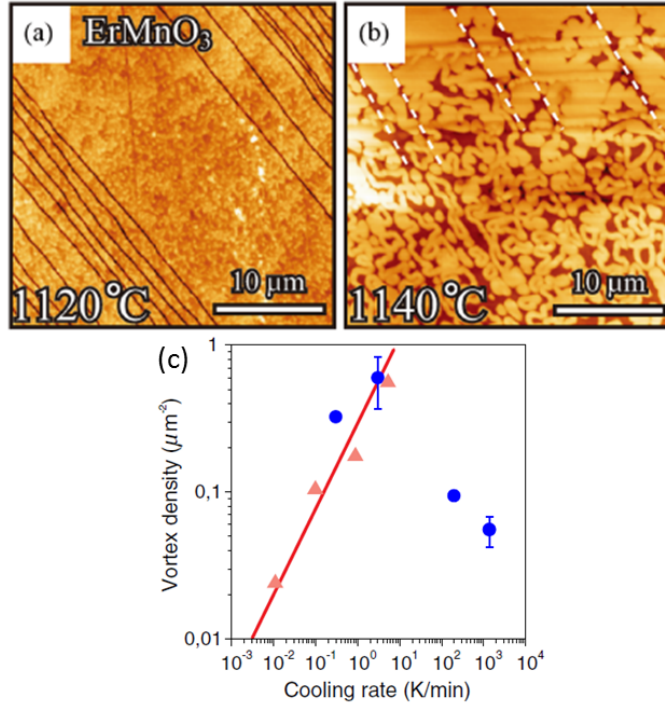


Figure 2.5: (a), (b) The AFM (atomic force microscopy) images of stripe patterns and vortex-antivortex domain patterns in ErMnO<sub>3</sub> crystals. Large domains of a single order-parameter polarization are separated by narrow (dark) domains of the opposite polarization. (c) The density of vortices as a function of cooling rate for slow cooling rates (red triangles, Chae *et al.* results [4]) and fast cooling rates (blue circles, Griffin *et al.* results [5]). Reprinted figure with permission from [4]. Copyright (2012) by the American Physical Society.

### 2.3.5 Multiferroics

The Kibble-Zurek mechanism has also been studied in multiferroic materials. These materials exhibit more than one primary ferroic order parameter in a single phase [104]. For example, hexagonal (h-) manganites, h-REMnO<sub>3</sub> (RE:Rare Earth, e.g. Er, Y, Yb), are one type of multiferroics that possess ferroelectric and ferromagnetic behaviour simultaneously. In h-REMnO<sub>3</sub>, ferroelectricity appears as a result of a structural phase transition which is induced by the size mismatch between RE and Mn-O layers. The interplay between structural and ferroelectric order parameters leads to the formation of domains that can have different configurations [4].

In 2012, Chae *et al.* investigated the growth of various REMnO<sub>3</sub> crystals. They first showed that ErMnO<sub>3</sub> crystals, grown with stripe patterns (see Fig. 2.5), transformed into ones with vortex-antivortex patterns when the sample was annealed above a characteristic temperature of 1200°C and then cooled to room temperature. Once formed, the vortex-antivortex structures were observed to persist (*i.e.* did not change back to stripes), and the



size of the domains varied with the cooling rate. Comparing the characteristic temperature of  $\text{RE}\text{MnO}_3$  crystals with different rare earth atoms, including Y, Ho, Er, Tm, Yb and Lu, it was found that the characteristic temperature increases almost linearly with decreasing size of RE atoms used, which suggested this temperature to be the same as the critical temperature ( $T_c$ ) of the structural phase transition. Starting slightly above  $T_c$  and changing the cooling rate for a set of  $\text{ErMnO}_3$  samples, they measured the average distance of vortex-antivortex pairs and showed a power-law dependence of vortex density on the quench rate. A power-law exponent of 0.23 was extracted from four data points over a range of 3 orders of magnitude of cooling rate, while the KZM prediction is 0.29 based on subsequent numerical calculations of the critical exponents performed by Griffin *et al.* [5]. In addition to the good agreement in the power-law exponent, the absolute density of defects itself is also reasonably well predicted by these calculations. All put together, Griffin *et al.* suggest that this provides strong confirmation of KZM behaviour. However, as noted by del Campo and Zurek in their recent review [79], some caution is in order. As first pointed out by Chae *et al.*, the critical temperatures of h- $\text{RE}\text{MnO}_3$  are very high and can be determined only approximately. Moreover, very little is known about the critical behaviour of these materials experimentally. As a result, this leaves some uncertainty in the comparison of the measurements to the KZM, which in the end relies on the details of the dynamics of the system in the vicinity of the critical point. Finally, in the same year as the work by Chae *et al.*, Griffin *et al.* extended the cooling rates in another experiment using  $\text{YMnO}_3$  and showed a suppressed defect formation at higher cooling rates (see Fig. 2.5c) that is opposite to KZM predictions and unexplained so far [5].

### 2.3.6 Landau-Zener transition and the KZM

The probability of a non-adiabatic transition between two quantum states at an avoided level crossing has been known since the 30's [105–108]. It has been shown that when the energy difference of the two states changes linearly with time, the excitation probability decays exponentially with the "quench" time  $\tau_Q$  (Landau-Zener formula). Recently, Damski has pointed out [109] that the average excitation probability can be correctly predicted up to 3rd order in quench time  $\tau_Q$  by applying the adiabatic-impulse approximation. The importance of this result is that it provides a direct route to extend the KZM to the dynamics of quantum phase transitions. The connection between the Landau-Zener formula and KZM has been demonstrated experimentally in a nine stage Mach-Zender interferometer [110] and subsequently in a semiconductor electron charge qubit system [111]. Note that these are not extended systems, and a test of the power-law scaling of the defect density (i.e. inverse of the domain size) is not achievable.

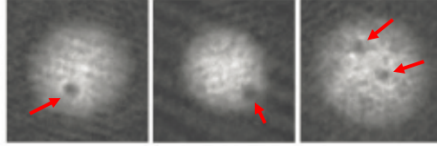


Figure 2.6: Images of BECs in a harmonic trap with a single vortex (left, center) and two vortices (right) nucleated by a quench of the normal-BEC transition. Reprinted by permission from Macmillan Publishers Ltd: [Nature] [6], copyright(2008).

### 2.3.7 Ultracold trapped atoms and ions

In addition to all the condensed matter systems described above, atomic systems are also found to be a good testbed for investigating the KZM. The atomic systems include ultracold trapped atoms and ions. These systems are well-controlled and theoretically simple, and provide the possibility of investigating the KZM in an inhomogeneous system. The inhomogeneity of these systems is a result of the external trapping potential. The inhomogeneous KZM (IKZM) will be discussed in more detail in the next chapter in the context of trapped ions.

In 2006 Sadler *et al.* first demonstrated the formation of topological defects, including walls, textures, and vortices, as a result of spontaneous symmetry breaking across a quantum phase transition near zero temperature [112]. For this type of situation, the structure of the quantum ground state undergoes a discontinuous change as a function of some external control parameter. In their experiments, Sadler *et al.* used a spinor BEC gas held in an optical dipole trap [112], and quenched the quantum phase transition from an un-magnetized to a ferromagnetic ground state by reducing the magnetic field by a factor of 100.

In 2007, Scherer *et al.* demonstrated vortex formation during a controlled merging of multiple uncorrelated BECs in a harmonic trap in an experiment reminiscent of that in a superconducting system discussed above [113]. Two years later, the same group reported spontaneous formation of vortices following a quench of the normal-BEC transition in an ultracold trapped gas of Rb atoms [6] (see Fig. 2.6). They showed spontaneous vortex formation after a fast quench in both a toroidal and a 2-D pancake shaped trap. In the latter case, they demonstrated a factor of  $\sim 2$  increase in vortex formation between two different temperature quenches. The cooling was performed using forced evaporative cooling. As the authors note, one challenge in extending these experiments to a power-law measurement is to obtain sufficient control and range for the evaporative cooling rate. Due to limited statistics, the power-law scaling of KZM could not be tested in this experiment and it remains un-tested to date.

In 2011, Chen *et al.* [114] studied the spontaneous formation of defects across the Mott insulator-superfluid (MI-SF) transition, a quantum phase transition. Like Sadler *et al.*, they also demonstrated the formation of defects as a result of a rapid quench across a quantum

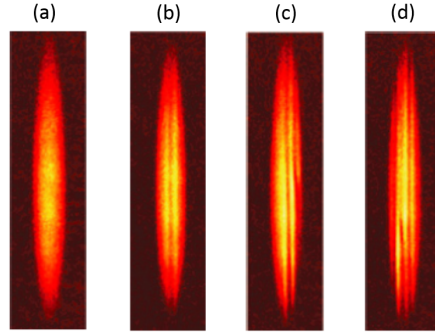


Figure 2.7: a-d, Sample time of flight pictures of BEC containing 0, 1, 2, and 3 solitons. The vertical direction corresponds to the strong-confinement direction in the trap. Reprinted by permission from Macmillan Publishers Ltd: [Nature Physics] [7], copyright(2013).

phase transition, but they also went on to investigate the possibility of extending KZM predictions to a quantum phase transition by measuring the power-law scaling. The experiments of Chen *et al.* used ultracold Rb atoms trapped in a 3-D optical lattice, which can be described by the inhomogeneous Bose-Hubbard model (For a recent review of these systems in the context of non-equilibrium dynamics, see [115]). The quench across the MI-SF quantum phase transition is attained by varying the ratio of tunneling to interaction energy. In the actual experiment, this ratio is controlled by the optical intensity, which adjusts the depth of optical lattice potential. For quench rates across two orders of magnitude, vortices were found in the final BEC state. They used time of-flight density profiles to measure the amount of excitations, and the energy produced during quenches, as a function of  $\tau_Q$ , and found a KZM-like power-law behaviour with an exponent of  $0.32 \pm 0.02$ . Chen *et al.* point out that the exponent does not match the theoretical prediction value of  $3/4$  for 3-D homogeneous systems but it was not clear at that time if the deviations could be explained by known effects such as inhomogeneity or the 10% thermal fraction present in samples. In a subsequent theory paper, Dziarmarga *et al.* [116] found the scaling law to be quite insensitive to trapping potential, and the same scaling value of  $1/3$  for a 1-D chain also holds in 3-D. This is in reasonable agreement with the Chen *et al.* power-law exponent, indicating no obvious discrepancy from the KZM prediction. However, the recent review of del Campo and Zurek [79] places caveats on the direct connection between the KZM and Chen *et al.*'s results. For instance, the trap-induced inhomogeneity gives rise to an initial state of MI layers separated by SF layers. Consequently as the transition is crossed, different layers cross at different times, which is a more complicated scenario compared to the inhomogeneous KZM. Moreover, the small system size and finite temperature of the initial cloud along with other complications makes it unclear whether this scaling agreement is a coincidence or not.

In 2013, following ion-trap KZM experiments including the one reported in this thesis, Lamporesi *et al.* studied spontaneous formation of soliton defects across the normal-BEC phase transition of ultracold sodium atoms in a cigar-shaped magnetic trap [7]. This experiment was in fact the original system proposed by Zurek as a testbed for the study of the Inhomogeneous KZM (IKZM) [117]. In this experiment, the temperature is quenched by evaporative cooling and domains of condensate with different phases form. As the BEC grows, neighboring condensates merge and the phase mismatch can lead to the formation of (non-topological) solitonic defects.

The solitons were detected using time-of-flight density profiles (see Fig. 2.7) and a power-law dependence with an exponent of  $1.38 \pm 0.06$  was measured over a quench range of about a factor of 10. They also demonstrated that the power law is insensitive to a change in atom number by about a factor of 6 from 25 to 4 million atoms which could suggest a universal behaviour with some caution (see [7] for details). Based on the IKZM predictions a power-law exponent of  $7/6$  can be expected in this system. The authors suggest that the discrepancy may arise from the non-uniform axial temperature in the BEC, atom losses in fast quenches and soliton decays during slow quenches.

### 2.3.8 Ion trapping

In 2010, del Campo *et al.* proposed that trapped ions could be an ideal testbed for KZM studies, and in particular could be used to investigate the inhomogeneous KZM where the propagation of a transition front across the inhomogeneous sample would lead to a steepening of the KZM power-law [61]. This proposal motivated this experimental thesis work, as well as simultaneous work by two other groups [8, 118], which will be discussed in Chapter 5.

Ion trapping systems are highly controllable, simple enough to make direct comparison to theory, and efficient in that the defects are imaged in situ and the trapped sample can be recycled repeatedly across the transition. In ion-trap systems, the symmetry-breaking phase transition in use is a structural transition between linear and zigzag configurations. Laser-cooled ions held in a linear Paul trap with strong transverse confinement organize into a one-dimensional (1-D) linear crystal with an inhomogeneous axial density. If the transverse confinement is relaxed slowly, the linear ion crystal undergoes a continuous, structural phase transition to a 2-D zigzag configuration, beginning at the center of the crystal. Two broken-symmetry states (zig and zag) are possible. Rapidly quenching the transverse confinement across the transition can lead to crystal structures containing spontaneously nucleated topological defects (kinks), which are formed by the interface between domains of opposite symmetry. In our experiment we study the spontaneous nucleation of defects, and the power-law scaling of the number of defects as a function of quench time in a string of 41-43  $^{174}\text{Yb}$  ions. As a natural extension of the nucleation studies, we also

explore the dynamics of the defects. The results of these studies are presented in Chapter 5.

### **2.3.9 Conclusion**

It seems by now clear that a quench does indeed lead to spontaneous nucleation of defects, as has been demonstrated in a wide range of systems. Also the early work has shown many of the features of domain coalescence involved in the Kibble mechanism for defect formation, including the number of defects formed per domain. The status of the power-law measurements and confirmation of KZM has been most recently evaluated by del Campo and Zurek in their 2014 review [79]. In a nutshell, their conclusion is that there has been much progress, particularly recently, in making power-law measurements, but in each case (including ions as will be discussed later) there are caveats that leave work to be done before one can say the definitive test of the KZM has been done.

## Chapter 3

# The Kibble–Zurek Mechanism for Trapped Ions

In this chapter, we present the KZM predictions for the specific system of trapped ions. First, the linear rf Paul trap setup and an ion’s motion in the resulting confining potential are discussed. Then, the equilibrium structure of trapped laser-cooled ions is found as a function of trap anisotropy and it is shown that the linear structure of ions in a linear Paul trap is spatially inhomogeneous with an axial ion spacing (ion density) that varies across the ion chain. As the trap anisotropy is changed, the equilibrium structure transits into a zigzag configuration. The behaviour of the linear-zigzag transition and the effects of inhomogeneity on this transition are explained and the critical anisotropy of the phase transition is derived through two different approaches. Next, it is discussed how the linear-zigzag structural transition is a second-order phase transition and can be used for KZM studies. Finally, the KZM prediction of power-law scaling for the number of defects nucleated as a function of quench time is discussed, considering the cases of a homogeneous and inhomogeneous ion chain in two cooling limits of over-damped and under-damped.

### 3.1 Ion – trap system

The ion-trap setup used in our experiment is a linear radio frequency (rf) Paul trap composed of four rods and two endcap needles (see Fig. 3.1). Four 0.48-mm diameter tungsten rods are held in a square configuration by ceramic spacers at either end. The distance between the trap axis and rods’ surfaces is  $R_0 = 0.7$  mm. Two opposing rods are grounded and the other two are connected to a combined rf and dc voltage,  $V_0 \cos(\Omega_T \cdot t) + U_{rod}$ , that generates (combined) oscillating (and static) quadrupolar potentials in the transverse

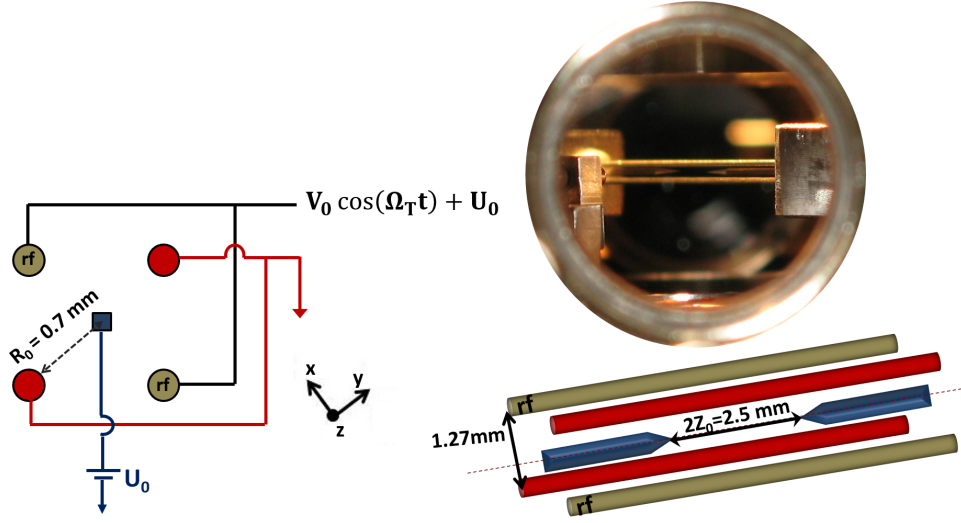


Figure 3.1: The linear rf Paul trap used in our experiment is composed of four rods held in a square configuration of the side of 1.27 mm and two needles separated by 2.5 mm. The rods confine the ion in the transverse direction. Two opposing rods are grounded (shown in red) and the other two are connected to rf and dc voltage of  $V_0 \cos(\Omega_T \cdot t) + U_{rod}$  (shown in olive green). Two needles confine the ion in the axial direction and are connected to a dc voltages of  $U_0$ .

direction<sup>1</sup>. The electric potential can be approximated near the trap axis as follows [20,119]:

$$\Phi \simeq \frac{(V_0 \cos(\Omega_T \cdot t) + U_{rod})}{2} \left[ 1 + \frac{(x^2 - y^2)}{R^2} \right], \quad (3.1)$$

where  $R \simeq R_0$ .

Two tungsten needles connected to dc voltages of  $U_0$  confine the ion in the axial  $\hat{z}$  direction and are separated by  $2Z_0 = 2.5$  mm. The needles provide the static harmonic well potential in the axial direction and their effect can be described by the following potential for points near the center of the trap:

$$\Phi_s = \kappa U_0 \left[ z^2 - \frac{1}{2}(x^2 + y^2) \right], \quad (3.2)$$

where  $\kappa$  is a geometrical factor. In both of the above equations, experimental imperfections such as anharmonicities, asymmetries, external stray fields, and the leakage of rf electric field into the axial direction are neglected.

<sup>1</sup>In the actual experiment separate dc voltages are applied to all rods for maximum flexibility in design of the potential.

The equations of motion of a single ion of mass  $M$  and charge  $Q$ , in the combined potential of Eq. 3.1 and Eq.3.2 can be found using Newton's second law:

$$M\ddot{x}_i = -Q \cdot \frac{\partial(\Phi + \Phi_s)}{\partial x_i}, \quad i = \{1, 2, 3\}. \quad (3.3)$$

The above equation results in a Mathieu equation for each direction as follows:

$$\frac{d^2 x_i}{d\zeta^2} + [a_i + 2q_i \cos(2\zeta)] x_i = 0, \quad (3.4)$$

where  $\zeta = \Omega_T t/2$  and

$$a_x = \frac{4Q}{M\Omega_T^2} \left( \frac{U_{rod}}{R^2} - \frac{\kappa U_0}{Z_0^2} \right), \quad a_y = -\frac{4Q}{M\Omega_T^2} \left( \frac{U_{rod}}{R^2} + \frac{\kappa U_0}{Z_0^2} \right), \quad a_z = \frac{8Q\kappa U_0}{M\Omega_T^2 Z_0^2}, \quad (3.5)$$

and

$$q_x = -q_y = \frac{2QV_0}{M\Omega_T^2 R^2}, \quad q_z \cong 0. \quad (3.6)$$

The Mathieu equations (Eq. 3.4) can be solved using Floquet solutions [20,120]. Assuming  $a_i < q_i \ll 1$ , the position of an ion to first order in  $a_i$  and  $q_i$  is

$$x_i(t) \approx x_{0i} \cos(\omega_i t + \phi_i) \left[ 1 + \frac{q_i}{2} \cos(\Omega_T \cdot t) \right], \quad (3.7)$$

where the amplitude  $x_{0i}$  and phase  $\phi_i$  are determined by the initial conditions, and  $\omega_i$  is the secular trap frequency in the  $i^{th}$  direction defined as

$$\omega_i \cong \frac{1}{2} \Omega_T \sqrt{a_i + \frac{1}{2} q_i^2}. \quad (3.8)$$

In the transverse direction, the secular frequency is associated with a simple harmonic oscillation in a time-averaged pseudopotential, while in the axial direction a harmonic oscillator potential is generated directly by the dc endcap voltages  $U_0$  (see Eq. 3.2).

As Eq.3.7 shows, the motion of a trapped ion consists of two oscillatory components:

1 – A low-frequency motion called secular motion, oscillating with a secular trap frequency of  $\omega_i \simeq (2\pi \cdot 0.35 - 0.8)$  MHz for our setup. The amplitude of secular motion is  $x_{0i}$  and can be reduced by laser cooling methods (see "Doppler cooling" section in Chapter 4).

2 – A high-frequency motion of relatively small amplitude, known as micromotion, oscillating with the rf trap frequency of  $\Omega_T = (2\pi \cdot 12 - 17.5)$  MHz. The amplitude of micromotion is  $x_{0i} \cdot q_i/2$ . Considering  $q_i \sim 0.12 - 0.16 \ll 1$ , the amplitude of micromotion is smaller than that of secular motion.

The two oscillatory components of a trapped ion's motion in a transverse direction are shown in Fig. 3.2 for  $q_i = 0.2$ . The ratio of the micromotion to secular motion frequency in this figure is  $\Omega_T/\omega = 20$ , which is comparable to our experimental values.



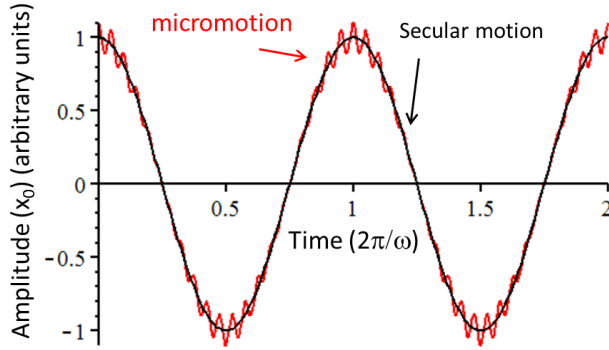


Figure 3.2: The oscillatory motion of a trapped ion as a function of secular period. The motion consists of two parts: secular motion shown in black with a low frequency  $\omega$  and larger amplitude  $x_0$ , and micromotion shown in red with a high frequency  $\Omega_T = 20\omega$  and smaller amplitude  $x_0 \cdot q/2 = 0.1x_0$ , where  $q = 0.2$  in this plot.

In an ideal linear trap, the micromotion vanishes for an ion at rest along the axial rf null. However, in a non-ideal situation, in addition to the intrinsic micromotion accompanying the secular motion, an excess micromotion can arise due to different causes. For instance, a phase difference between the ac potentials applied to the rods will give a non-zero minimum rf field value on the trap axis. This is not a significant effect in our trap. Of more importance are external stray dc electric fields on the electrodes and patch potentials which cause the ion-trap center to shift from the rf field null in the transverse direction [120]. Micromotion in our non-ideal linear trap and the detrimental effects of the excess micromotion on laser cooling will be discussed in Chapter 4. The detection of excess micromotion and its minimization through the use of shim electric fields are also discussed in that chapter. For multiple ions in a linear string, the excess micromotion can be minimized by placing them along the rf null along the trap’s axial axis of a linear Paul trap. On the other hand, when the ions are in a 2-D configuration such as the zigzag structure, the excess micromotion is unavoidable. For typical trap conditions and as long as the trapped ions are not too far from the rf null, it is typical to neglect the micromotion as a first approximation.

### 3.2 Inhomogeneous linear equilibrium structure

To find the equilibrium structure of trapped laser-cooled ions in a linear Paul trap, we consider  $N$  identical ions with mass  $M$  and charge  $Q$ . The classical Hamiltonian of this system includes kinetic and potential energy terms:

$$H = \sum_{i=1}^N \frac{p_i^2}{2M} + V(\{\vec{r}_i\}), \quad (3.9)$$

where the potential term accounts for the harmonic confining pseudo-potential and the ion-ion Coulomb interaction. In 2-D, the potential energy is

$$V(\{\vec{r}_i\}) = \frac{M}{2} \sum_{i=1}^N (\omega_y^2 y_i^2 + \omega_z^2 z_i^2) + \frac{1}{2} \cdot \frac{1}{4\pi\epsilon_0} \sum_{i=1}^N \sum_{i \neq j}^N \frac{Q^2}{|\vec{r}_i - \vec{r}_j|}, \quad (3.10)$$

where  $\omega_y$  is the transverse and  $\omega_z$  is the axial secular trap frequency. The position of the  $i^{\text{th}}$  ion is denoted by  $\vec{r}_i$ . If the ions' positions are re-scaled in terms of the axial Coulomb length  $a_0 = (Q^2/4\pi\epsilon_0 M\omega_z^2)^{1/3}$  as  $\vec{r}/a_0 \rightarrow \vec{r}'$ , then the potential energy simplifies to

$$V(\{\vec{r}'_i\}) = V_0 \left( \frac{1}{2} \sum_{i=1}^N (\alpha^2 y_i'^2 + z_i'^2) + \frac{1}{2} \sum_{i=1}^N \sum_{i \neq j}^N \frac{1}{|\vec{r}'_i - \vec{r}'_j|} \right), \quad (3.11)$$

where  $V_0 = M\omega_z^2 a_0^2$ . In the above equation,  $\alpha$  denotes the trap anisotropy<sup>2</sup>:

$$\alpha \equiv \frac{\omega_y}{\omega_z}. \quad (3.12)$$

When trapped ions are sufficiently laser cooled, the ions crystalize into an array and the equilibrium position of each ion can be found by minimizing the potential  $V$  (Eq. 3.11) with respect to all coordinates [44]. By writing the potential in this way we see that the minimum-energy equilibrium structure in linear Paul traps depends only on trap anisotropy  $\alpha$ .

When  $\alpha \gg 1$ , which means the transverse confinement is much stronger than the axial confinement, the equilibrium structure is a one-dimensional linear structure. Figure 3.3(a) shows an experimental CCD image of a linear string of 42  $^{174}\text{Yb}$  ions in our trap for  $\alpha \simeq 17$  with  $\omega_z = 2\pi \cdot 38$  kHz and  $\omega_y = 2\pi \cdot 660$  kHz. In Fig. 3.3(b), the numerical solution for the equilibrium positions of 42 ions, obtained from minimizing the potential energy of Eq. 3.11 for the same  $\alpha$  value, is plotted using MAPLE software. The comparison of the two images of experiment and numerical calculations (Fig. 3.3(a),(b)) indicates that the theory provides a fair description of the system.

As can be seen in this figure, the axial ion spacing of the linear structure is inhomogeneous. The axial density which is proportional to the inverse separation between neighboring ions, is highest at the center and decreases towards the edges. In Fig. 3.3(c) the axial density variation along the string of 42 ions is shown. The points are extracted from the numerically calculated ion positions shown in Fig. 3.3(b) using the inverse of adjacent ions' separation,  $n_i = \frac{1}{z_{i+1} - z_i}$ .

---

<sup>2</sup>The trap anisotropy  $\alpha$  can be defined in different ways. For instance  $\alpha = \omega_z^2/\omega_y^2$  is one of the commonly used alternative definition [44,49]. In our experiment, we vary the trap anisotropy by changing the transverse trap frequency while the axial frequency remains constant. As a result  $\alpha = \omega_y/\omega_z$  definition is more convenient than other possibilities.

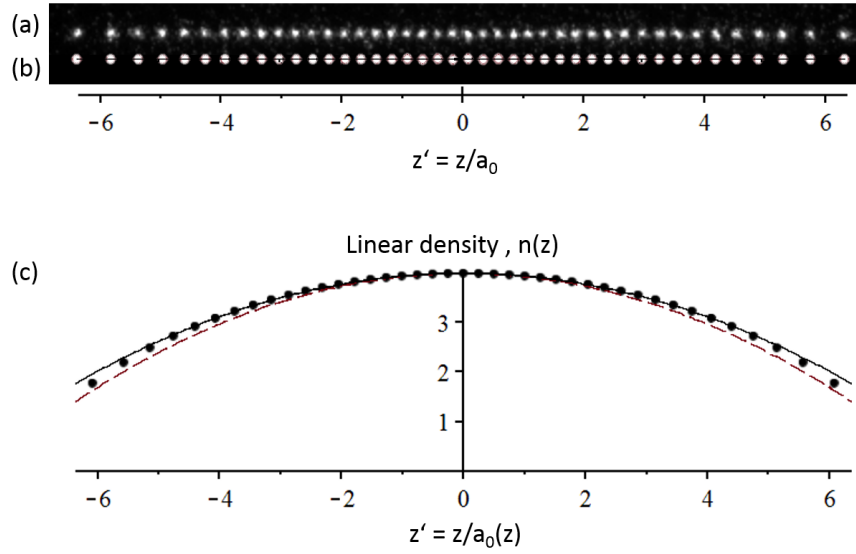


Figure 3.3: (a) An experimental CCD image 42  $^{174}\text{Yb}$  ions in a 1-D linear structure taken by an intensified CCD camera for  $\alpha = 17$  with  $\omega_z = 38$  kHz and  $\omega_y = 660$  kHz. (b) The numerical calculation results of ions positions in a string of 42 ions with the same  $\alpha$  value. (c) The axial density of ions vs. scaled ion position. The points are extracted from the numerically calculated ion positions shown in (b). The red dashed line is the LDA theory as described in Eq. 3.13. The black line is a fit to the points for which  $n(0)$  and  $L$  are considered as free parameters. Distances scaled to  $a_0 = 24.4 \mu\text{m}$ .

Alternatively, for a large number of ions, it is reasonable to consider a local density approximation (LDA) to find a description of the axial density. This approximation works best in homogenous cases; hence it is expected to work better in the center of large strings compared to the edges. Using the LDA, for a string with a half-length  $L$ , the axial density is reasonably well approximated by:

$$n(z) = n(0) \left(1 - \frac{z^2}{L^2}\right), \quad n(0) = \frac{3N}{4L}. \quad (3.13)$$

This functional form for a string of 42 ions is shown in Fig. 3.3(c) by the dashed red line. As expected, it works better at the center compared to the edges. If  $n(0)$  and  $L$  are treated as free adjustable parameters, the functional form in Eq. 3.13 can match the density across the crystal even better, with the central density unchanged and  $L$  replaced by an effective length  $L' = 1.07L$ .

### 3.3 The structural transition from linear to zigzag structure

The 1-D linear structure remains as the equilibrium structure as long as the transverse confinement stays considerably stronger than the axial confinement. As the transverse confinement is relaxed, or equivalently the axial confinement is strengthened, the anisotropy of the trap potential decreases. Below a threshold value of the trap anisotropy ( $\alpha_c$ ), the linear structure will no longer have the lowest energy, and a structural phase transition into a 2-D zigzag structure occurs<sup>3</sup>. The 2-D zigzag structure lies in the plane of the axial direction,  $\hat{z}$ , and the weakest transverse direction, which we call  $\hat{y}$ . When the inward transverse trapping force becomes equal to the net outward Coulomb force due to the surrounding ions, the linear structure breaks for points infinitesimally away from the axial axis. In a finite string with an inhomogeneous linear structure, the density (*i.e.* Coulomb pressure) is highest in the center, so the central ions break into the zigzag, or reach the critical point, first. As the trap anisotropy decreases further, the transverse displacements of the central ions (*i.e.* zigzag amplitude) grow while ions closer to the edges join the zigzag configuration. Figure. 3.4 shows some experimental snapshots of this transition from linear to zigzag structure in a string of 41 ions. The  $\alpha$  is reduced from 17 to 9 with the critical point being at  $\alpha_c \simeq 16$ . In the same figure, the numerical calculations of the transverse separation of adjacent ions  $\Delta y_{pp}$  vs. the ions' axial position is shown for different  $\alpha$  values. It can be seen that as the critical point is crossed,  $\Delta y_{pp}$  starts to grow at the center while the outer ions are still in the linear structure ( $\Delta y_{pp} = 0$ ). As  $\alpha$  passes further below the critical point, more ions join the zigzag structure. Figure 3.5 shows the transverse separation of the two central ions,  $\Delta y_{pp0}$  (peak to peak zigzag amplitude at  $z = 0$ ) as a function of trap anisotropy. The points are derived from the experimental measurements of a string of 41  $^{174}\text{Yb}$  ions (see Fig. 3.4). The line is the numerical calculations in MAPLE obtained from minimizing the potential  $V$  to find the equilibrium positions of central ions at each value of  $\alpha$ . The rapid onset of the zigzag transition, near the critical point can be seen clearly in this figure.

### 3.4 Calculation of the critical point of the linear–zigzag transition: approach I.

In the thermodynamic limit, the critical point of a string of  $N \rightarrow \infty$  ions can be found by equating the trapping and outward Coulomb forces in the transverse direction. Assuming that no axial confinement exists, *i.e.*  $\omega_z \rightarrow 0$ , and so the axial ion spacing  $d$  is constant,

---

<sup>3</sup>The term of "phase transition" in condensed matter systems is only used in the thermodynamic limit for which  $N \rightarrow \infty$ . However, in this thesis we follow the atomic physics literature on this topic [44, 49, 121] and use this term for the structural transition in a system of  $N = 3 - 43$  trapped ions.

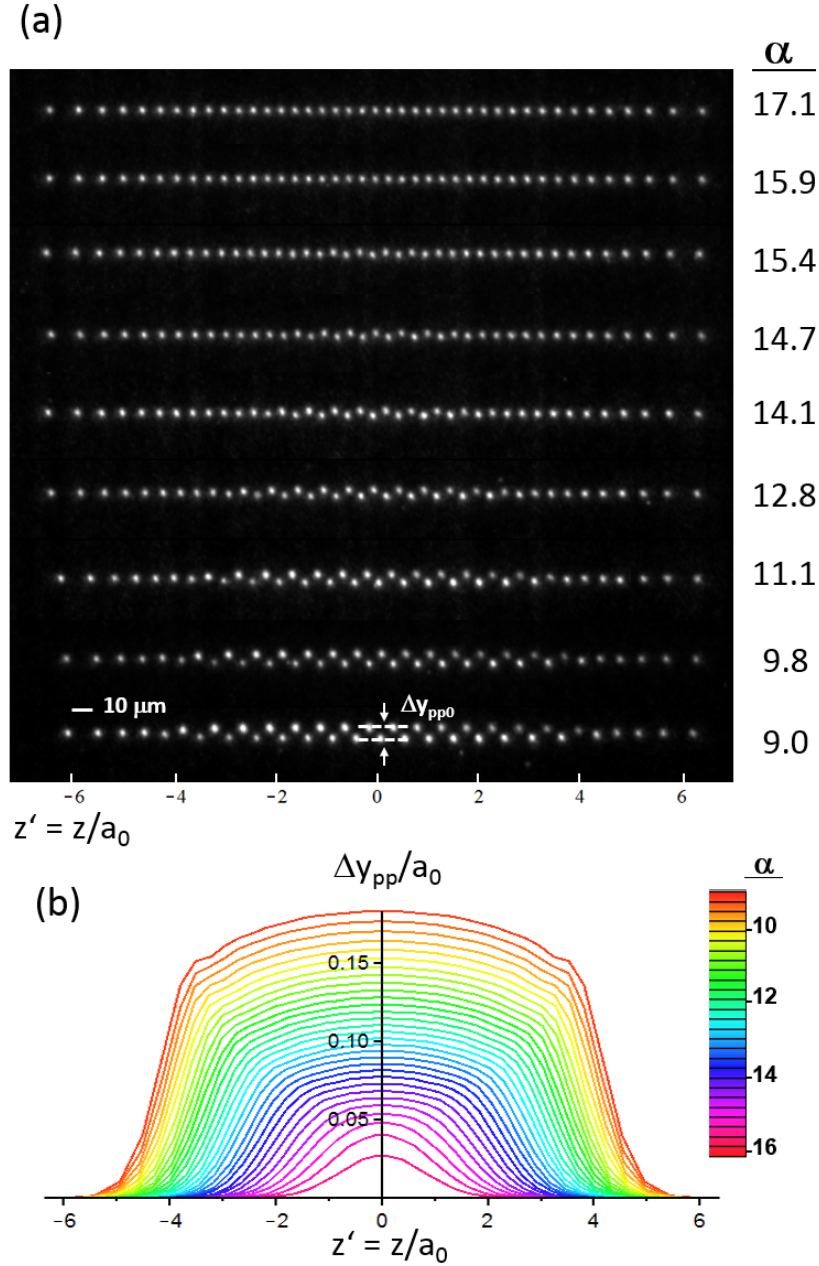


Figure 3.4: (a) Experimental images of the equilibrium structures of a string of 41  $^{174}\text{Yb}$  ions for different trap anisotropy values. Distances scaled to  $a_0 = 24.4 \mu\text{m}$ . After passing the critical point ( $\alpha_c \simeq 16$ ) the zigzag configuration starts to form in the center. As the trap anisotropy decreases further, the transverse displacement of the central ions becomes larger and more ions join the zigzag configuration. In the laser image, the white line indicates the scale of  $10 \mu\text{m}$ , and the transverse separation of central ions ( $\Delta y_{pp0}$ ) is shown by two arrows. (b): Numerical calculations of the transverse displacement vs. axial position for a series of  $\alpha$  values in a range of 9-16, shown by different colors.

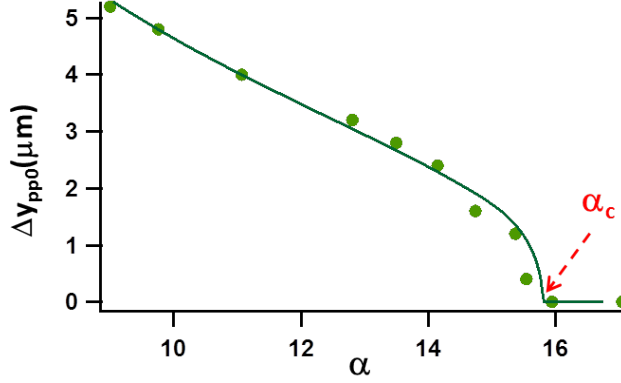


Figure 3.5: The transverse separation (peak to peak zigzag amplitude) of the two center ions at  $z = 0$  as a function of trap anisotropy. The points are the experimental data for a string of 41  $^{174}\text{Yb}$  ions (see Fig. 3.4). The line shows  $\Delta y_{pp}$  obtained from numerically determined equilibrium configurations for a range of  $\alpha$  values. The critical point is  $\alpha_c \simeq 16$ .

the critical transverse frequency in an infinite homogenous string is [20]

$$\omega_{y,c}^2 = \frac{7}{8\pi\epsilon_0} \zeta(3) \frac{Q^2}{md^3}, \quad (3.14)$$

where  $\zeta$  is the Riemann zeta function. This critical point applies to all points in the ion chain simultaneously, unlike in the inhomogeneous case. Nevertheless, Eq. 3.14 can be used to approximate the critical trap anisotropy  $\alpha_c$  for the central ions of a finite inhomogeneous string. In this case, the constant ion spacing  $d$  is replaced by the central ion-ion separation  $d_0$  in the linear configuration. Eq. 3.14 can be re-written in terms of the axial Coulomb length  $a_0$  as :

$$\omega_{0y,c}^2 = \frac{7}{2} \zeta(3) \omega_z^2 \left( \frac{a_0}{d_0} \right)^3. \quad (3.15)$$

Equivalently, the critical trap anisotropy can be written as :

$$\alpha_{0c}^2 = \frac{7}{2} \zeta(3) \left( \frac{a_0}{d_0} \right)^3. \quad (3.16)$$

According to the numerical calculations reported in [122], the central ion-ion spacing in a linear string of  $N$  ions follows a power-law scaling as a function of  $N$ :

$$d_0 = a_0 \cdot \frac{2.018}{N^{0.559}}. \quad (3.17)$$

Finally, substituting the above equation into Eq. 3.16 results in a power-law relation for  $\alpha_{0c}$  in terms of  $N$  as follows:

$$\alpha_{0c} = 0.7155 N^{0.8385}. \quad (3.18)$$

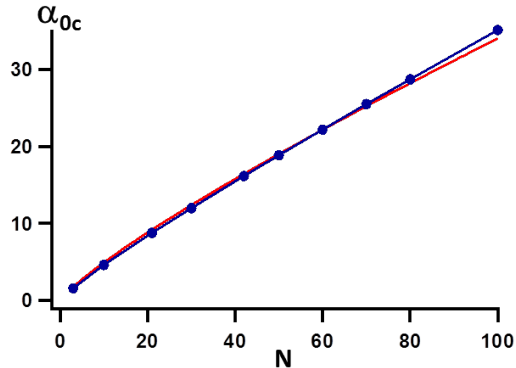


Figure 3.6: The connected blue points are derived from minimizing the potential energy to find the onset of zigzag structure using MAPLE. The red line is the power-law dependence of  $\alpha_{0c}$  in terms of  $N$  as described by Eq. 3.18. The good agreement between the two lines indicates that the power-law dependence (Eq. 3.18) is a fair approximation of the central ion’s critical point.

A power-law dependence of  $\alpha_c$  on  $N$  was first theoretically predicted by Schiffer [44] and Dubin [45], and subsequently confirmed experimentally by Enzer *et al.* [49]. The calculated and measured power-law coefficient and exponent are slightly different in these reports, but ultimately the values for  $\alpha_c$  are in good agreement for moderate number of ions. As the power-law relation suggests, when the string gets larger,  $\alpha_c$  increases. In other words, when the number of ions increases, the Coulomb pressure becomes stronger, and it requires less of a decrease in trap anisotropy to transit from the linear to zigzag configuration. In Fig. 3.6, the power-law dependence of  $\alpha_c$  on  $N$  as predicted by Eq. 3.18 (shown by the red line) is compared to the numerical calculations of  $\alpha_c$  for ten different  $N$  values between 3 and 100 (shown by the connected blue points). The latter points are obtained by finding the onset of the zigzag structure in numerically obtained  $\Delta y_{pp}$  vs.  $\alpha$  plots (see Fig. 3.5). The two results are in a good agreement over the range shown, which suggests that for the central ions the power-law dependence of Eq. 3.18 is a good approximation for the onset of linear-zigzag transition. It is also convenient for predicting the critical asymmetry for  $N$  values of experimental interest, including  $N = 41 - 43$  used in our KZM measurements. In an experiment with a string of  $N = 42$  ions, we have measured  $\alpha_c = 16.5(1)$ , while the power-law predicts  $\alpha_c = 16.43$  which is within the error bar of the measured value.

As pointed out earlier, the central ions cross the critical point of the linear-zigzag transition first, and so the zigzag configuration forms first at the center and spreads to the edges of the ion crystal as  $\alpha$  reduces. In other words,  $\alpha_c$  is a function of the axial position, and is highest for the central ions and lower for the outer ions. The value of  $\alpha_c$  across the crystal can be approximated by replacing  $1/d$  in Eq. 3.16 by the axial density  $n(z)$  (Eq. 3.3). The resulting critical point as a function of axial position  $\alpha_c(z)$  is as follows:

$$\alpha_c(z) = \alpha_{0c} \cdot \left(1 - \frac{z^2}{L^2}\right)^{3/2}. \quad (3.19)$$

### 3.5 Calculation of the critical point of the linear-zigzag transition: approach II.

Another approach to understand the linear-to-zigzag structural transition and the value of the critical anisotropy is through studying the vibrational normal modes of the system. This is a very common approach in studying the structural phase transitions in condensed matter systems. It was suggested by Cochran [123] in 1960 (although commented on earlier by Raman, Anderson and others [124]) that the structural phase transition of some ferroelectric materials is associated with a dynamical instability against a particular normal mode, called the "soft mode". Later on, the concept of a soft mode was expanded to explain a wide range of structural phase transitions (for a list of these phase transitions see [125]).

*The soft mode concept:* When a material is cooled from above  $T_c$ , the frequency of a vibrational normal mode decreases to zero and the crystal becomes unstable against excitations of this "soft mode". In an extension of the Landau theory, it was predicted that the frequency of the soft mode behaves as [124]:

$$\omega^2 \propto \left| \frac{T}{T_c} - 1 \right|. \quad (3.20)$$

Similarly, the linear-to-zigzag structural transition in trapped ions occurs when the frequency of the transverse zigzag mode (the "soft" mode) goes to zero [49]. Hence, the critical point of the transition can be determined through an analysis of the frequency of the transverse zigzag mode as a function of the trap anisotropy. To find the vibrational modes in a string of  $N$  ions, the potential  $V$  (Eq. 3.10) can be expanded to second order in displacement about the equilibrium configuration:

$$V = V^{(0)} \Big|_{y_{eq}, z_{eq}} + V^{(1)} \Big|_{y_{eq}, z_{eq}} + V^{(2)} \Big|_{y_{eq}, z_{eq}}. \quad (3.21)$$

The first-order term is zero at equilibrium. Assuming that the ions' oscillations about their equilibrium positions,  $\delta z_i = z_i - z_{i,eq}$  and  $\delta y_i = y_i - y_{i,eq}$ , are small, the second-order term will be [126]

$$V^{(2)} = \frac{m}{2} \sum_{i=1}^N (\omega_y^2 \delta y_i^2 + \omega_z^2 \delta z_i^2) - \frac{1}{8} \sum_{i=1}^N \sum_{i \neq j}^N K_{i,j} \left[ (\delta y_i - \delta y_j)^2 - 2(\delta z_i - \delta z_j)^2 \right], \quad (3.22)$$



where  $K_{i,j} = \partial^2 V / \partial z_j \partial z_i |_{z_{eq}}$  is

$$K_{i,j} = \frac{1}{4\pi\epsilon_0} \cdot \frac{2Q^2}{|z_{i,eq} - z_{j,eq}|^3}. \quad (3.23)$$

Using Eq. 3.22 for the potential, the equations of motion and normal modes can be derived from Lagrange's equations. For a linear equilibrium structure where  $\{y_{i,eq} = 0\}$ , the axial and transverse motions are decoupled for small oscillations. For up to 3 ions in the linear regime the normal modes in the axial and transverse directions can be found algebraically. For  $N \geq 4$ , the normal modes can be found numerically (see [122] for convenient tables of axial eigenfrequencies and eigenvectors of up to 10 ions in a linear array). On the other hand, for ions in the equilibrium zigzag structure, the axial and transverse motions are coupled, which leads to more complicated mode structures.

The results of a numerical calculation of the eigenvectors of all 8 normal modes of 4 trapped ions in 2-D and on both the linear and zigzag sides of the transition are shown in Fig. 3.7. It can be seen that on the linear side, the transverse and axial motions are decoupled, and the corresponding modes in the two directions (*e.g.* the axial zigzag and the transverse zigzag modes) have matching eigenvectors. On the other hand, on the zigzag side only for the center of mass mode are the axial and transverse motions decoupled.

The results of a numerical calculation of the frequencies of these normal modes as a function of trap anisotropy  $\alpha$  is shown in Fig. 3.8. It can be seen that the frequency of the transverse zigzag mode goes to zero at  $\alpha \simeq 2.04$ . This point marks the onset of the linear-zigzag transition where the linear structure becomes unstable against the excitations of the transverse zigzag mode. This value matches the critical point obtained from the numerical analysis of the equilibrium structure in the previous section. Also, Fig. 3.8 shows that on the linear side, the frequency ordering of transverse modes is opposite to that of axial modes. For instance, in the transverse direction the zigzag mode is the lowest frequency and the center-of-mass (COM) mode is the highest frequency, while in the axial direction it is the opposite: the zigzag mode is the highest frequency and the COM mode is the lowest frequency.

From the small oscillation analysis it can be shown that the frequency of the soft mode (zigzag mode) on the linear side depends on  $\alpha$  as follows [127]:

$$\omega_{yzz} = \omega_y \sqrt{1 - \left(\frac{\alpha_c}{\alpha}\right)^2}, \quad (3.24)$$

which is an analogous expression to Eq. 3.20.

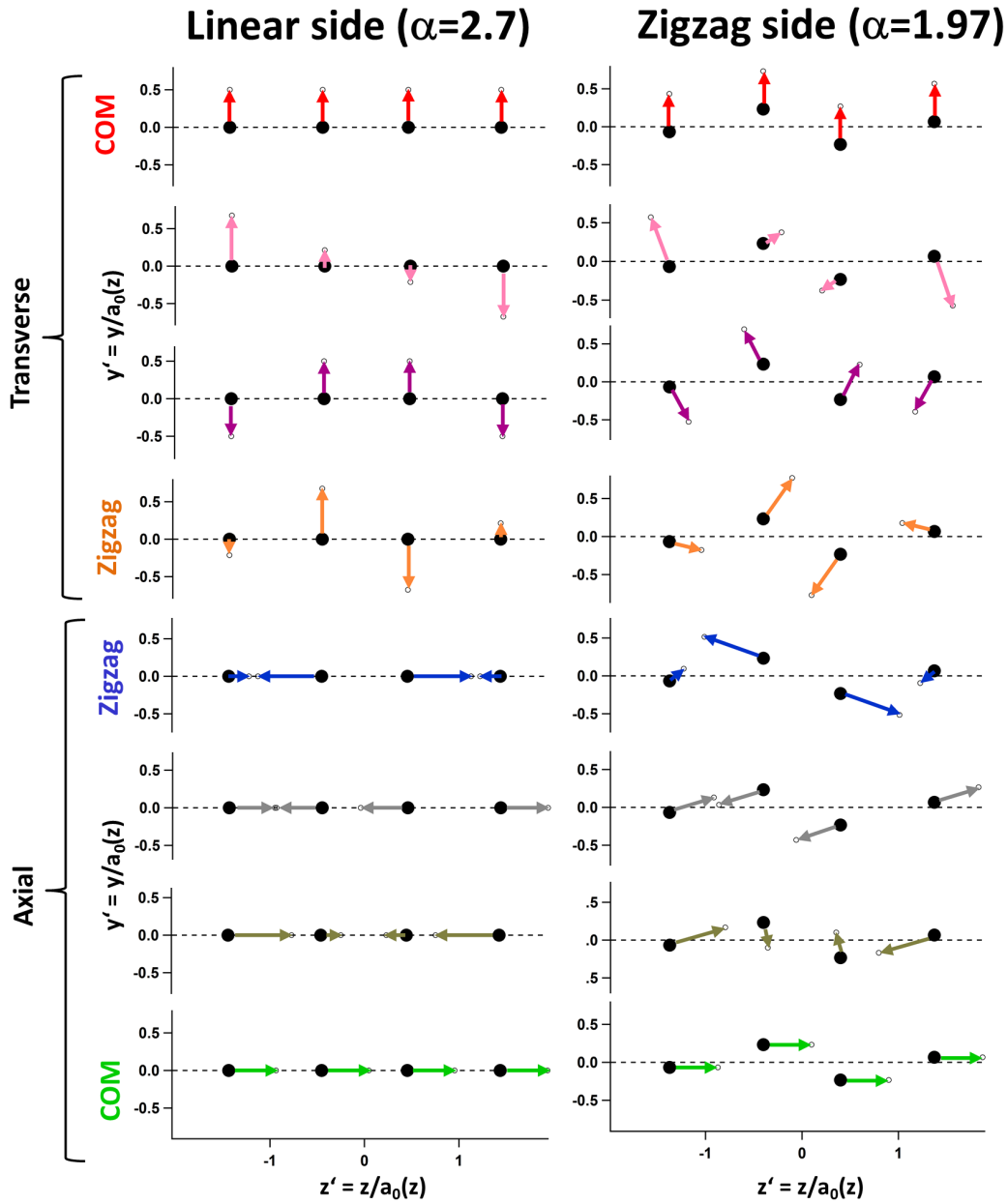


Figure 3.7: The numerical calculation results of the eigenvectors of normal modes in a string of 4 ions on the linear (left column) and zigzag (right column) side of the L-Z transition. On the linear side, the eigenvector components of a mode are the same in the axial and transverse directions. It can also be seen that the axial and transverse motions are totally decoupled on the linear side. On the zigzag side, only for the center of mass mode are the axial and transverse motions decoupled.

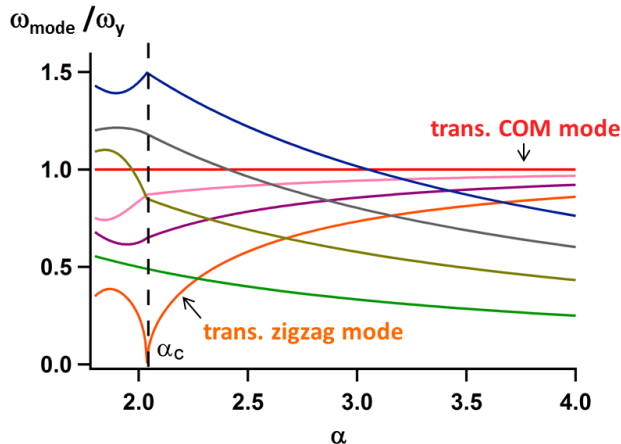


Figure 3.8: Numerical calculation of frequencies of 8 normal modes of Fig. 3.7 with the same color code. All frequencies are scaled with respect to the transverse trap frequency  $\omega_y$ . The frequency of the transverse zigzag mode goes to zero at  $\alpha = 2.04$ , which defines the critical point of the linear-zigzag transition.

### 3.6 Beyond the zigzag structure

As  $\alpha$  decreases below  $\alpha_c$ , the amplitude of the zigzag structure increases, but there is an upper limit for the transverse separation of ions. At sufficiently low values of  $\alpha$ , further transitions in 2-D into multi-row structures occur at a succession of critical values [44]. In Fig. 3.9, the results of numerical calculations of equilibrium structures at lower  $\alpha$  values are presented for a string of 41 ions in 2-D (relevant to our experimental setup). Figure 3.9(a) shows a zigzag structure at  $\alpha = 6$ . The transition to a 3-layer structure happens at  $\alpha \simeq 5.8$  and Fig. 3.9(b) shows the 3-row structure in the center of the zigzag configuration at  $\alpha = 5.6$ . As  $\alpha$  decreases further, the 3-row structure expands to the edges (Fig. 3.9(c)), and ultimately turns into a 4-row structure (Fig. 3.9(d)). However in our experiment, we normally observe the ions to de-crystallize shortly after forming a 3-row structure presumably due to micromotion heating and weak transverse confinement.

### 3.7 Characteristics of the linear-zigzag "phase transition"

The classification of the linear-zigzag transition in ion traps was first investigated by Piacente *et al.*. They consider an infinite number of identical charges interacting through a screened Coulomb potential (Yukawa potential)<sup>4</sup> and trapped in a transverse parabolic

<sup>4</sup>The screened Coulomb potential is defined as  $V(r) = \frac{Q}{4\pi\epsilon_0} \cdot \frac{e^{-r/\lambda}}{r}$ , where the exponential term is the screening factor and its strength is controlled by the screening length  $\lambda$ .

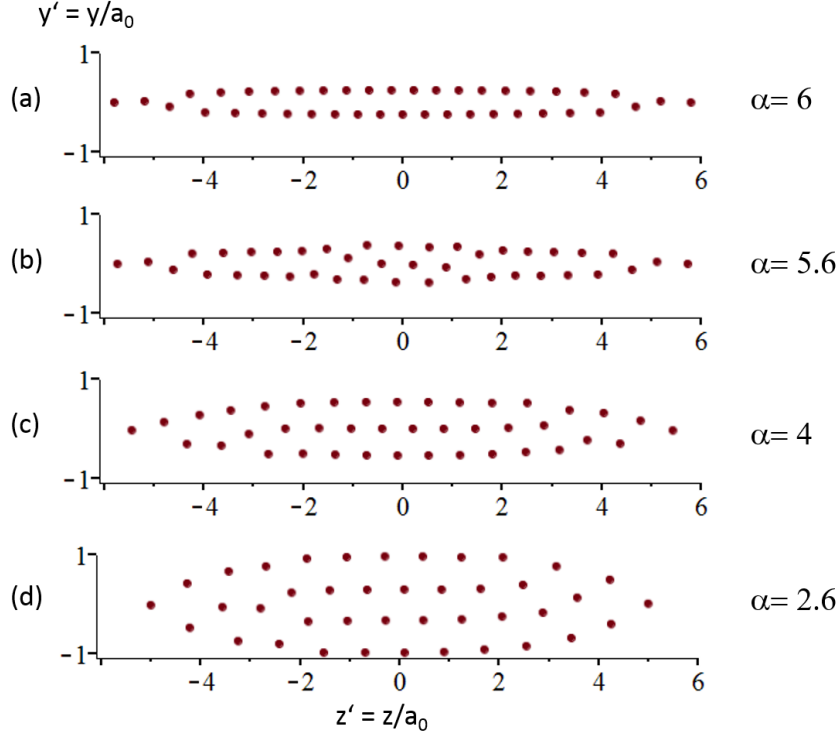


Figure 3.9: Numerical calculations of the 2-D equilibrium structure for four different values of  $\alpha$  in a string of 41 ions. (a) A zigzag structure. (b) A 3-row structure formed at the center of the zigzag configuration. (The critical point of the 3-row structure is at  $\alpha_c \simeq 5.8$ ) (c) A deep 3-row structure. (d) A 4-row structure.

confining potential [53]. Using a combination of analytical calculations and Monte Carlo simulations, they find the minimum energy structures as a function of the density (or trap potential) and screening length of the Yukawa potential, and show that the linear-zigzag transition is a second-order (continuous) phase transition. In a later study, Fishman *et al.* use mean field approaches to derive a classical model describing the system's behaviour in the vicinity of the critical point, and demonstrate that the linear-zigzag transition is second-order. Fishman *et al.* consider  $N$  identical charges in the thermodynamic limit with a fixed inter-particle separation  $d$  and no axial confinement [54]. They expand the potential  $V$  (Eq. 3.10) to fourth order around the equilibrium positions of the linear crystal, and re-write the potential in terms of the normal-mode coordinates. In the vicinity of the critical point, they study the dynamics of the transverse zigzag mode and the coupling of the zigzag mode to other quasi-degenerate modes with a small wave-vector difference compared to the zigzag mode ( $|\delta k|d \ll 1$ ). In zeroth order of expansion in terms of  $|\delta k|d$ , the third order term  $V^{(3)}$  containing axial-transverse coupling vanishes, while the remaining fourth order term  $V^{(4)}$  involves only the coupling between transverse modes. For the

latter couplings, in the vicinity of the critical point, where the frequency of the transverse zigzag mode approaches zero, a frequency gap opens up between the zigzag mode and all the quasi-degenerate modes. Therefore, close to the critical point the dynamics is controlled by the transverse zigzag mode alone and the effective potential reduces to:

$$V = \frac{1}{2} (\omega_y^2 - \omega_{y,c}^2) \phi_{zz}^2 + \frac{1}{4} A \phi_{zz}^4, \quad (3.25)$$

where the coefficient  $A$  is

$$A = \frac{93}{16} \zeta(5) \frac{Q^2}{m d^5}, \quad (3.26)$$

in which  $\zeta$  is the Riemann-zeta function. Equation 3.25 has the same form as for any other second-order phase transition. Above the critical point where  $\omega_y^2 - \omega_{y,c}^2 > 0$ , the potential has a single minimum at  $\phi_{zz} = 0$  and the minimum-energy configuration is linear. When the critical point is passed,  $\omega_y^2 - \omega_{y,c}^2 < 0$ , the potential has a double-well form with two degenerate minima corresponding to the "zig" and "zag" configurations.

Both of the above references demonstrate that in the thermodynamic limit, the linear-zigzag transition is a second-order type phase transition. However, Fishman *et al.* also comment on the experimentally relevant situation of a finite number of ions in a trap that provides both transverse and axial confinements. They note that in the vicinity of the critical point, their theory is expected to provide qualitatively reasonable predictions (though not quantitatively detailed). They point out two effects that arise from the axial confinement in particular. First, the axial inter-particle separation  $d$  is not constant anymore, which makes the transition inhomogeneous across the ion crystal, as already discussed above. Second, the axial spacing will change in going from the linear to zigzag structure as the ions move inward under the influence of the axial confinement. We next investigate briefly the consequences of the small coupling of the zigzag mode to the axial motion.

Following a similar approach as Fishman *et al.*, we approximate the effective potential of the transverse zigzag mode near the critical point, for the smallest possible trapped ion system consisting of only three ions. Expanding the 2-D potential  $V(y_i, z_i)$  (Eq. 3.11) to fourth order around the equilibrium positions of the three ions on the linear side, we re-write  $V(y_i, z_i)$  in terms of the linear normal mode coordinates  $\phi_k$  using the transformation:

$$X_i = \sum_{k=1}^{2N} \psi_{ik} \cdot \phi_k. \quad (3.27)$$

Here,  $X_i$  are the 6 coordinates of  $N=3$  ions in 2-D, and  $\psi_{ki}$  are the normalized eigenvector components of normal modes on the linear side as shown in the tables of Fig. 3.10. Finally, we use  $V(\phi_k)$  to derive the dynamical equations for the normal modes, including the nonlinear coupling. At first the set of equations appear complicated, but in the vicinity of critical point the fast oscillating nonlinear coupling terms between the low-frequency zigzag

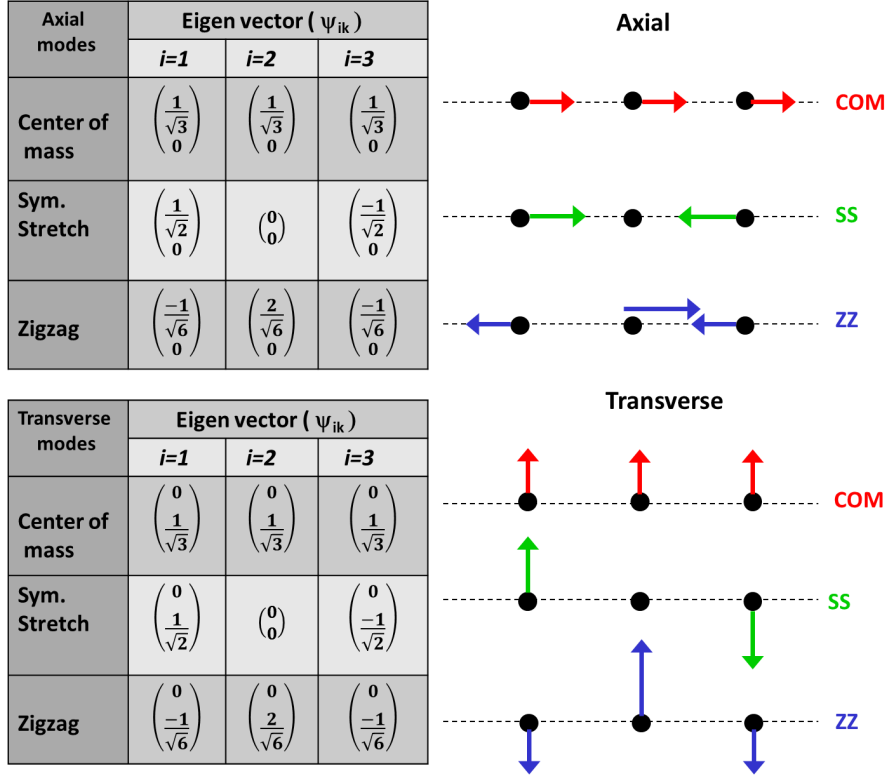


Figure 3.10: The axial and transverse normal modes of three trapped ions, along with the tables showing the eigenvectors of  $i^{th}$  ion and  $k^{th}$  normal mode  $\psi_{ik}$  for each direction.

mode and the other modes can be discarded.<sup>5</sup> With this approximation, the dynamics of the transverse zigzag mode can be viewed as due to the following effective potential:

$$V = \frac{1}{2} \left[ (\alpha_c^2 - \alpha^2) + \sum_{k \neq yzz} c_k \langle \phi_k^2 \rangle - c_1 \langle \phi_{zss} \rangle \right] \phi_{yzz}^2 + \frac{1}{4} A \phi_{yzz}^4. \quad (3.28)$$

Two coupling terms survive the averaging over the fast oscillations:

1– The coupling term related to the amplitudes of all the normal modes  $\langle \phi_i^2 \rangle$  excluding  $\phi_{yzz}$ . This term leads to a weak thermal shift in the critical point  $\alpha_c$ , which can be accounted for through the definition of a new critical value  $\alpha_c'^2 = \alpha_c^2 + \sum c_k \langle \phi_k^2 \rangle$ . The effect of thermal fluctuations on the linear-zigzag transition, including the effect of thermal fluctuations of the transverse zigzag mode itself, is considered more rigorously elsewhere [60].

2– The other term is the coupling to the axial symmetric stretch (breathing) mode  $\phi_{zss}$ . This term accounts for the fact that due to the axial confinement, ions move closer axially as the zigzag structure grows. On the linear side,  $\alpha > \alpha_c'$ , the axial correction is zero,

<sup>5</sup>It is well-known that at certain specific trap asymmetries it is possible to hit nonlinear resonance coupling of several modes, but these are not relevant here.

$\langle \phi_{zss} \rangle = 0$ , so it does not affect the situation on the linear side, including the determination of the critical point. The breathing mode acquires a non-zero dc component as the transition is crossed. The average over fast oscillations implicitly assumes that the fast axial breathing mode adiabatically follows the slow zigzag evolution. From the equations of motion and assuming adiabatic following, we find  $\langle \phi_{zss} \rangle \propto \phi_{yzz}^2$ , which shows that the change in axial spacing is a higher order correction, and only affects the size of order parameter, but not the soft mode frequency. The effect of the axial correction can be accounted for through the definition of a new quartic coefficient  $A'$ . The effective potential in terms of  $\alpha'_c$  and  $A'$  has the same form as Eq. 3.25:

$$V = \frac{1}{2}(\alpha'_c{}^2 - \alpha^2)\phi_{yzz}^2 + \frac{1}{4}A'\phi_{yzz}^4. \quad (3.29)$$

In addition to thermal shifts, micromotion can also lead to small shifts in  $\alpha_c$  that depends on rf trap frequency  $\Omega_T$ . In a trap like ours, this shift is about 1% for three ions [128]. Also note that the adiabatic following of the breathing mode will break down for fast quenches across the transition. Far past the critical point, as the order parameter grows quickly it will excite the breathing mode impulsively, which can lead to defect losses and will be discussed in Chapter 5.

By way of conclusion to this section, we note that like in any other second-order phase transition, as we pass through the linear-zigzag transition, the potential changes from a single-well to a double-well, which means there are two possible symmetry broken configurations. In our case, these two configurations, "zig" and "zag", are differentiated by the sign of the transverse displacement for even and odd numbered ions in a linear array. In one configuration, the even numbered ions shift up and the odd numbered ions shift down, and in the other configuration they shift oppositely. For a linear array of Doppler cooled ions confined in a symmetric trap, when the linear-zigzag transition is crossed, thermal fluctuations lead ions into one of the two configurations with equal probability. The presence of these two equally probable configurations is a key feature of the linear-zigzag transition for the studies of the Kibble-Zurek mechanism that will be described next.

### 3.8 Kibble – Zurek mechanism in ion–trap systems

The theory of KZM in ion-trap systems was first investigated by del Campo *et al.* in 2010 [61]. Along the lines of a more detailed follow-on paper by De Chiara *et al.* [129], we now investigate the theoretical scaling of the number of defects with the quench rate across the transition, and demonstrate a power-law dependence using the KZM. We derive the power-law exponents in the two limits of under-damped and over-damped regimes for the homogeneous and inhomogeneous scenarios.

### 3.8.1 Homogenous KZM (HKZM) for trapped ions

With a similar approach as Fishman *et al.* [54], del Campo *et al.* expand the potential  $V$  of a homogeneous ion chain to fourth order and re-write the potential in terms of the transverse normal modes. By assuming that ions are pinned in the axial direction, they discard the axial-transverse couplings ( $V^{(3)} = 0$ ). Considering the effects of the quasi-degenerate modes with a small wave-vector difference compared to the zigzag mode  $|\delta kd| \ll 1$ , the effective potential near the critical point is

$$V = \frac{1}{2} \left[ (\omega_y^2 - \omega_{y,c}^2) + h^2 \delta k^2 \right] \phi_{zz}^2 + \frac{1}{4} A \phi_{zz}^4. \quad (3.30)$$

This equation is valid for up to second order of expansion in terms of  $|\delta k|d \ll 1$ , which assumes the amplitude of transverse oscillations is much smaller than the inter-particle separation  $d$ . In the limit of  $|\delta kd| \ll 1$ , they transformed  $\phi_{zz}$  into a continuum field  $\phi_{zz}(z)$  by a Fourier transform, and obtained the Lagrangian  $L = \int dz \mathcal{L}(z)$ , in which the Lagrangian density  $\mathcal{L}(z)$  has the same form of a Ginzburg-Landau theory:

$$\mathcal{L}(z) = \frac{1}{2} \rho \left[ (\partial_t \phi_{zz}(z))^2 - h^2 (\partial_z \phi_{zz}(z))^2 - (\omega_y^2 - \omega_{y,c}^2) \phi_{zz}^2(z) - 2A \phi_{zz}^4(z) \right]. \quad (3.31)$$

The coefficient  $h = \omega_0 d \sqrt{\log 2} \simeq \omega_0 d / 2$  with  $\omega_0 = \sqrt{Q^2 / 4\pi\epsilon_0 M d^3}$ , can be interpreted as the speed with which a transverse perturbation propagates along the chain. The coefficient  $A$  influences the value of the order parameter on the zigzag side and is a similar form to that in Eq. 3.26. As usual in the KZM theory, it is assumed that the control parameter, in this case the difference  $\omega_y^2 - \omega_{y,c}^2$ , changes in a time interval of  $[-\tau_Q, \tau_Q]$  as follows:

$$\omega_y(t)^2 - \omega_{y,c}^2 = \delta(t), \quad (3.32)$$

in which  $\delta(t)$  is taken to be a linear function of time,

$$\delta(t) = -\delta_0 \frac{t}{\tau_Q}, \quad 0 < \delta_0 \ll \omega_{y,c}. \quad (3.33)$$

In this notation, the frequency of the transverse zigzag mode (soft mode) can be expressed as  $\sqrt{\delta}$  near the transition.

To add the effect of the laser cooling, it was assumed that the ion chain is in contact with a thermal bath at a low temperature  $T$ , so the evolution of the energy distribution of the modes satisfies the same form of a Fokker-Planck equation [130]. In this case, the equation of motion of the field can be written in equivalent Langevin form as:

$$\partial_t^2 \phi_{zz} - h^2 \partial_z^2 \phi_{zz} + \eta \partial_t \phi_{zz} + \delta(t) \phi_{zz} + 2A \phi_{zz}^3 = \vartheta(t), \quad (3.34)$$



in which  $\eta$  is the damping rate proportional to the laser cooling rate (see Section 4.3) and  $\vartheta(t)$  is the Langevin force associated with the thermal bath.

The first step in deriving the power-law scaling of the number of defects as a function of quench time is to find the correlation length and relaxation time. Having the relaxation time, the freeze-out time can be found, and finally the density of defects can be derived from the size of correlation length at the freeze-out.

**Correlation length:** Based on the Ginzburg-Landau theory, the correlation function evaluated for the linear-zigzag transition decays exponentially with a correlation length of  $\xi = h/\sqrt{\delta}$  [61]. Near the critical point, the correlation length can be approximated in terms of the reduced control parameter  $\epsilon$  as follows:

$$\epsilon = \frac{\omega_{y,c}^2 - \omega_y^2}{\omega_{y,c}^2}, \quad (3.35)$$

$$\xi \simeq \left( \frac{1}{\sqrt{8}} \frac{d\omega_0}{\omega_{y,c}} \right) \frac{1}{|\epsilon|^{1/2}}. \quad (3.36)$$

In trapped ion systems, the critical exponent of the correlation length  $\xi$  is therefore  $\nu = 1/2$ .

**Freeze-out time:** The freeze-out time  $\hat{t}$  is the instant at which the the time remaining to reach the critical point (or the time elapsed after crossing the critical point), is the same as the relaxation time  $\tau$ :

$$\left| \frac{\delta(\hat{t})}{\dot{\delta}(\hat{t})} \right| = \hat{t} = \tau(\hat{t}). \quad (3.37)$$

Using the expression of the relaxation time  $\tau$  (Eq. 3.39), and the linear variation of the control parameter  $\delta$  (Eq. 3.33), the following freeze-out time can be obtained in the over-damped and under-damped regimes:

$$\begin{aligned} \text{Over-damped :} \quad \hat{t}_o &= \left( \frac{\tau_Q \eta}{\delta_0} \right)^{1/2}; \\ \text{Under-damped :} \quad \hat{t}_u &= \left( \frac{\tau_Q}{\delta_0} \right)^{1/3}. \end{aligned} \quad (3.38)$$

**Relaxation time:** Unlike the correlation length, the relaxation time depends on the strength of the damping rate and can be evaluated in two limits of over-damped and under-damped [131]. In the over-damped limit,  $\eta \gg \sqrt{\delta(\hat{t})}$ , the damping overcomes the oscillations at freeze-out, while in the under-damped limit,  $\eta \ll \sqrt{\delta(\hat{t})}$ , the damping is weak and the response of the system is determined by the soft mode frequency. In these two limits, the

relaxation time  $\tau$  is

$$\begin{aligned}
\text{Over-damped : } \quad \tau_o &\simeq \frac{\eta}{\delta} \simeq \left( \frac{\eta}{2\omega_{y,c}^2} \right) \frac{1}{\epsilon}; \\
\text{Under-damped : } \quad \tau_u &\simeq \frac{1}{\sqrt{\delta}} \simeq \left( \frac{1}{\sqrt{2}\omega_{y,c}} \right) \frac{1}{\epsilon^{1/2}}.
\end{aligned} \tag{3.39}$$

Note that in the under-damped case, the response time of the system is independent of the system's damping  $\eta$  and is governed only by the soft mode frequency  $\sqrt{\delta}$ .

In trapped ion systems, the critical exponent of the relaxation time,  $\tau$ , is  $\mu_o = 1$  in the over-damped, and  $\mu_u = 1/2$  in the under-damped regime.

**Density of defects:** As noted in Chapter 2, the inverse of the correlation length at freeze-out,  $\hat{\xi}$ , sets the typical domain size at that point, and is proportional to the density of defects formed. For the homogeneous trapped ion system, the density of defects in the two cooling limits of over-damped and under-damped is therefore

$$\begin{aligned}
\text{Over-damped : } \quad n_o &\sim \frac{1}{\hat{\xi}_o} = \frac{2}{\omega_0 d} \left( \frac{\delta_0 \eta}{\tau_Q} \right)^{1/4}; \\
\text{Under-damped : } \quad n_u &\sim \frac{1}{\hat{\xi}_u} = \frac{2}{\omega_0 d} \left( \frac{\delta_0}{\tau_Q} \right)^{1/3}.
\end{aligned} \tag{3.40}$$

As expected, the density of defects follows a power-law scaling as a function of quench time  $\tau_Q$ . For the homogeneous trapped ion system, the exponent of the power-law scaling is 1/4 in the over-damped, and 1/3 in the under-damped regime.

### 3.8.2 Inhomogeneous KZM (IKZM) for trapped ions

The homogeneous KZM description provided so far can be used to describe the dynamics of uniformly arranged ions in a ring trap, or for the central ions of a sufficiently large string in a linear Paul trap, for which the inter-particle separation stays (reasonably) constant. As we discussed earlier in this chapter, the homogeneous case is not a good description in general for ions confined in a linear Paul trap where the density of the ion chain is inhomogeneous with the inter-particle separation,  $d(z)$ , varying along the chain. When the ions' spacing is position-dependent, all the related parameters of the equation of motion (Eq. 3.34) become position-dependent as well and the equation of motion can be written as:

$$\partial_t^2 \phi_{zz} - h(z)^2 \partial_z^2 \phi_{zz} + \eta \partial_t \phi_{zz} + \delta(z, t) \phi_{zz} + 2A(z) \phi_{zz}^3 = \vartheta(t). \tag{3.41}$$

Using the local density approximation for axial density, the position-dependent coefficients can be found in terms of the coefficient value at the center of the trap ( $z = 0$ ). For instance in an inhomogeneous ion string with half-length  $L$ , the critical transverse trap frequency as a function of axial position is

$$\omega_{y,c}^2(z) = \omega_{0y,c}^2 \left(1 - \frac{z^2}{L^2}\right)^3. \quad (3.42)$$

A position-dependent critical point means that in an inhomogeneous linear ion string, as we reduce the transverse trap frequency, the critical point is crossed at different times along the chain. The center of the chain with the highest  $\omega_{y,c}$  value reaches the critical point first and the outer ions follow afterward. In other words, the transition front propagates from the center towards the edges with a position-dependent velocity known as the "front velocity".

**Front velocity vs. sound velocity:**

Knowing the time dependence of the transverse trap frequency (Eq. 3.32), and the position dependence of the critical frequency  $\omega_{y,c}$ , (Eq. 3.42), one can find the time  $t_f$  at which an ion in the position  $x$  reaches the critical point, or equivalently the time at which the front reaches that position:

$$t_f(z) = \frac{\tau_Q \omega_{0y,c}^2}{\delta_0} \left[1 - \left(1 - \frac{z^2}{L^2}\right)^3\right]. \quad (3.43)$$

The front velocity can therefore be defined as:

$$v_f(z) = \left(\frac{dt_f(z)}{dz}\right)^{-1}. \quad (3.44)$$

In order for it to be possible to nucleate a defect, causality dictates that at the freeze-out time, the front velocity should be greater than the sound velocity in the ion chain. In other words, the front velocity should be faster than the speed with which perturbations or information of the selected symmetry propagates to have causally disconnected domains formed. The sound velocity at the freeze-out time can be approximated as the ratio between the correlation length and the relaxation time at freeze-out:

$$\hat{v}_s \sim \frac{\hat{\xi}}{\hat{\tau}}. \quad (3.45)$$

Using the expression for the correlation length,  $\hat{\xi} = h(z)/\sqrt{\delta(z, \hat{t})}$ , and the freeze-out time given by Eq. 3.39, the sound velocity at the freeze-out can be found.

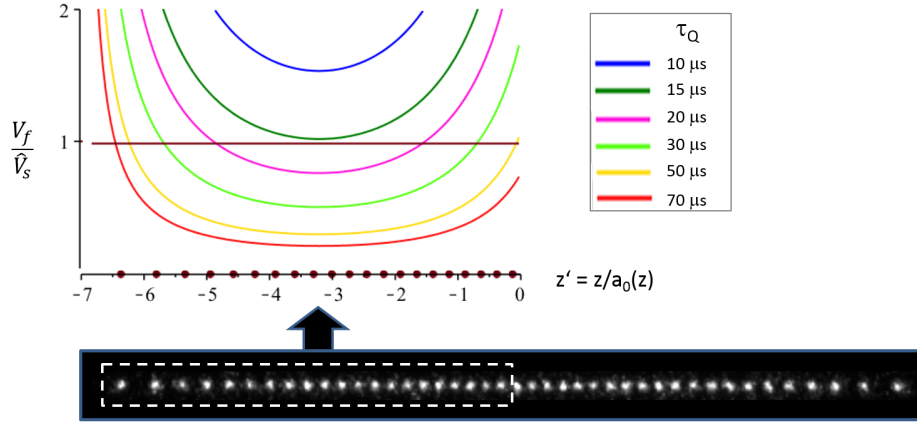


Figure 3.11: The ratio of front to sound velocity is shown for the left half of a 42-ion chain, for different quench times in the range of 10-70  $\mu\text{s}$ . The transverse trap frequency  $\omega_y$  changes from  $2\pi \cdot 657$  to  $2\pi \cdot 412$  kHz, while the axial trap frequency  $\omega_z = 2\pi \cdot 37.6$  kHz remains constant.

### Nucleation region and density of defects:

In a homogeneous ion chain all the ions reach the critical point at the same time, *i.e.* the front velocity is infinite. This means that the front velocity is always greater than the sound velocity and defects can be nucleated anywhere along the ion chain. In an inhomogeneous ion chain, the front velocity is finite and position-dependent, and the nucleation of defects is only possible in the regions where  $v_f > \hat{v}_s$ .

In Fig. 3.11, the ratio of the front velocity to sound velocity is shown for the left half of a 42-ion string for different quench times  $\tau_Q$ . It can be seen that for fast quenches ( $\tau_Q = 10, 15 \mu\text{s}$ ),  $v_f/\hat{v}_s > 1$  across the whole crystal, so nucleation is possible anywhere across the ion chain, like a homogeneous case. For the slower quenches, the condition of  $v_f/\hat{v}_s > 1$  is satisfied in two separate regions around the center and near the edges of the ion string. When the size of the nucleation region is being estimated, due to the high loss rates of defects at the edges, the outer edges are ignored and only the central region is considered. The size of the nucleation region  $2Z^*$ , can be estimated by finding the boundary point for which  $v_f(Z^*)/\hat{v}_s(Z^*) = 1$ . The density of defects in the nucleation region of an inhomogeneous ion chain can then be estimated for the limit of  $Z^* \ll L$ , in the over-damped and under-damped regimes as follows:

$$\begin{aligned}
 \text{Over-damped :} \quad n_o &\sim \frac{1}{\hat{\xi}_o} \frac{2Z^*}{L} = \frac{4L}{3\omega_{0y,c}^2 \omega_0^2 d^2} \left( \frac{\delta_0 \eta}{\tau_Q} \right). \\
 \text{Under-damped :} \quad n_u &\sim \frac{1}{\hat{\xi}_u} \frac{2Z^*}{L} = \frac{4L}{3\omega_{0y,c}^2 \omega_0^2 d^2} \left( \frac{\delta_0}{\tau_Q} \right)^{4/3}.
 \end{aligned} \tag{3.46}$$

For the inhomogeneous trapped ion system, the exponent of the power-law scaling is 1 in the over-damped, and  $4/3$  in the under-damped regime. Compared to the homogeneous case, the density of defects is reduced in an inhomogeneous ion string, but the power-law dependence on the quench rate is strengthened, and so should be easier to measure.

### Homogeneous KZM, Inhomogeneous KZM and Doubled IKZM:

The ratio between the density of defects in the IKZM and HKZM is:

$$\frac{n_{IKZM}}{n_{KZM}} = \frac{2Z^*}{L}. \quad (3.47)$$

What the applicable scaling is -HKZM, IKZM or otherwise- in fact depends on the quench rate, which controls the size of the nucleation region ( $2Z^*$ ) In the limit of very fast quenches, the front velocity ( $v_f \propto \tau_Q^{-1}$ ) is sufficiently fast that the size of the nucleation region becomes the same as the crystal length. In ion crystals that are large enough to contain several domains, the IKZM scaling therefore breaks down for fast quenches, and the HKZM describes the situation best. In the other limit, for slow quenches or simply for small ion crystals, the nucleation region is so small that it becomes of the same order, or smaller than the domain size at freeze out  $2Z^* \leq \hat{\xi}$ . As a result, after the quench at most one defect is nucleated and a doubling of the IKZM power-law is expected [79]. This is similar to the doubling behaviour that has already been predicted in other systems including BECs [102, 103], and reported in experiments with small annular Josephson tunnel junctions [101]. In between these two limits, the IKZM scaling holds.

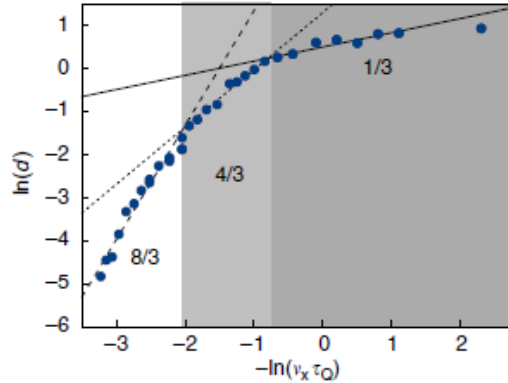


Figure 3.12: Simulation results from Pyka *et al.* of the density of defects as a function of quench rate in a string of 30 ions. The quench rate is varied by a factor of 150, and the string is in the under-damped regime. All three regimes of defect nucleation can in principle be accessed over this range. Reprinted by permission from Macmillan Publishers Ltd: [Nature Communications] [8], copyright(2013).

Simulation results reported by Pyka *et al.* [8] show that in a string of 30 ions when the quench rate is varied by a factor of 150, all three of the regimes of HKZM, IKZM and

DIKZM (Doubled IKZM) will be spanned (see Fig. 3.12). (Pyka *et al.* were one of the other two groups studying the KZM in ion trap systems at the same time as us). The power-law scaling in the under-damped regime, changes from  $1/3$  in the HKZM regime to  $4/3$  in the IKZM regime as the quench rate is slowed, and for much slower quench rates a doubling of power-law scaling to  $8/3$  can be expected. As will be shown in Chapter 5, for strings of 10's of ions and the range of quench rates used in our experiment and those performed by two other groups at the same time, the experiments lie in or near the DIKZM regime.

The source of the damping mechanism in KZM studies with ion traps is laser cooling, the strength of which defines if the system is in the over-damped or under-damped regime. In the next chapter, we focus on the Doppler cooling mechanism for a string of 10's of ions. We also focus on the experimental details and complications that can arise in a larger string of trapped ions.

## Chapter 4

# Experimental Setup for KZM Studies

In this chapter, we give an overview of different aspects of the ion trapping experimental setup used for KZM studies. We start with the ytterbium ion and focus on the specific isotope of  $^{174}\text{Yb}$  used in the KZM studies. A summary of the energy levels for the main fluorescence/Doppler cooling transition and the fluorescence theory of the isotope are given. Then, we explain the mechanism of Doppler laser cooling needed to crystallize the trapped ions. The Doppler cooling is also the source of the damping mechanism in the KZM studies with trapped ions. We note the complications that arise in Doppler cooling of large strings of trapped ions in our setup. We also include a description of photo-ionization as an effective technique for loading the isotopically pure ion crystals necessary for KZM studies. We then describe the ramp setup used to quench rapidly across the linear-zigzag transition. Lastly, we focus on the imaging system used for the defect detection, and the laser setup used in the experiment.

### 4.1 Ytterbium ion

Trapped ion systems currently have many different applications, including quantum information and quantum simulation [20, 24, 132–138], precision spectroscopy for time and frequency metrology [139–142], studies of interactions with ultra-cold atoms [143, 144], and studies of few-body "phase transitions" including the study of the non-equilibrium dynamics [8, 64, 118, 145]. Depending on the application, different ions or isotopes of an ion can be used in the ion trapping experiments. Commonly used ions include  $\text{Ba}^+$ ,  $\text{Be}^+$ ,  $\text{Ca}^+$ ,  $\text{Cd}^+$ ,  $\text{Mg}^+$ ,  $\text{Sr}^+$  and  $\text{Yb}^+$ . In this thesis, we use different isotopes of ytterbium ions,  $\text{Yb}^+$ . A more detailed study of the energy levels of  $\text{Yb}^+$ , including hyperfine structure, and the fluorescence theory is provided in my M.Sc. thesis and the associated publication [146, 147]. Only a summary of those results is reported here.

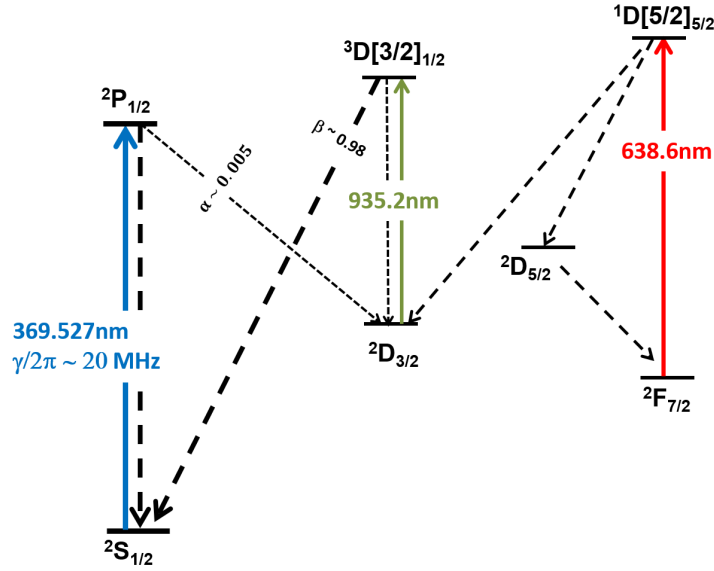


Figure 4.1: Yb<sup>+</sup> energy levels, involved in Doppler cooling and fluorescence detection. The primary transition is  $^2S_{1/2} - ^2P_{1/2}$  at 369 nm. The 935 nm transition is used to clear out the small leakage from the excited state  $^2P_{1/2}$  to  $^2D_{3/2}$  state. An additional low lying state of  $^2F_{7/2}$  can be populated via collision process, and is depopulated through the 638 nm transition.

Like other ions used in laser cooled trapped-ion experiments, Yb<sup>+</sup> has a single active electron which ensures that the ion has a simple level structure. This allows, in particular, a relatively simple closed transition for laser cooling and fluorescence detection. Partial energy levels of Yb<sup>+</sup> are shown in Fig. 4.1. The primary transition used for Doppler cooling and fluorescence detection is  $^2S_{1/2} - ^2P_{1/2}$  at 369.5 nm with a natural linewidth of  $\gamma/2\pi 19.60(5)$  MHz [148, 149]. A small leak from the  $^2P_{1/2}$  excited state to the low lying  $^2D_{3/2}$  state occurs with a branching ratio of  $\alpha = 0.005$  [133] and requires the use of a repump laser to maintain fluorescence. Clear-out of the  $^2D_{3/2}$  state is achieved via a 935.2-nm transition to the  $^3D[3/2]_{1/2}$  excited state. The ion returns to the ground state with a calculated branching ratio of  $\beta = 0.98$  [150]. We assume the remainder of the branching ratio is back to the  $^2D_{3/2}$  state. There is also a low lying and long-lived metastable  $^2F_{7/2}$  state that can be populated via collisional processes [151–153]. An additional repump laser at 638.6 nm is necessary to depopulate the  $^2F_{7/2}$  state via a  $^1D[5/2]_{5/2}$  state from where it can return to the cooling cycle.

#### 4.1.1 Ytterbium Isotopes

Ytterbium has seven stable isotopes with different natural abundances, shown in Table. 4.1. Of the isotopes listed in the table,  $^{174}\text{Yb}^+$  and  $^{171}\text{Yb}^+$  were used for the experiments



Isotope	Natural Abundance(%)	Atomic Nuclear Spin	Hyperfine Splitting [GHz]
$^{168}\text{Yb}$	0.13	0	-
$^{170}\text{Yb}$	3.04	0	-
$^{171}\text{Yb}$	14.28	1/2	12.6
$^{172}\text{Yb}$	21.83	0	-
$^{173}\text{Yb}$	16.13	5/2	10.5
$^{174}\text{Yb}$	31.83	0	-
$^{176}\text{Yb}$	12.76	0	-

Table 4.1: Different isotopes of ytterbium atoms [154].

presented in this thesis. To study the Kibble-Zurek mechanism in ion trapping systems, we used a string of 41-43 Doppler-cooled  $^{174}\text{Yb}$  ions. Doppler cooling of all the  $\text{Yb}^+$  isotopes is easily achievable, but we choose to work with  $^{174}\text{Yb}^+$  for two main reasons. First and most importantly, the  $^{174}\text{Yb}$  isotope has the highest abundance which makes the isotope-selective loading process of the 41-43 ions fast and easy in practice. Second, for this type of experiment which involves only Doppler cooling,  $^{174}\text{Yb}^+$  has the added advantage that it has no nuclear spin and so lacks the complication of hyperfine structure. This simplifies the experimental setup.

As a note in passing, for other experiments in the quantum regime, *i.e.* involving significant motional ground state occupation, we will take advantage of the hyperfine structure in  $^{171}\text{Yb}^+$  to achieve resolved sideband cooling. A description of the energy levels of  $^{171}\text{Yb}^+$  and effects associated with the hyperfine structure are left to Chapter 7, where we discuss Sisyphus cooling and resolved sideband cooling mechanisms. This chapter is focused on  $^{174}\text{Yb}^+$  and the KZM experiment.

#### 4.1.2 Energy levels of $^2S_{1/2} - ^2P_{1/2}$ transition in $^{174}\text{Yb}^+$

The primary  $^2S_{1/2} - ^2P_{1/2}$  transition of  $^{174}\text{Yb}^+$  is used for Doppler cooling and fluorescence detection. Both the ground and excited states of this transition have a half-integer angular momentum of  $J = 1/2$  and two sublevels,  $m_J = \pm 1/2$ . All of our experiments are performed in the presence of a magnetic field that defines the quantization axis. The energy shift of sublevels due to the magnetic field is known as a Zeeman shift. The Zeeman shift of a  $|J, m_J\rangle$  state at low fields is linearly proportional to the magnetic field strength  $B$  as follows [68]:

$$\Delta E_B(J, m_J) = g_J \cdot m_J \cdot (\mu_B \cdot B) = g_J \cdot m_J \cdot (\hbar \delta_B), \quad (4.1)$$

where  $\mu_B$  is the Bohr magneton and  $\delta_B = \mu_B B / \hbar$  is the Zeeman frequency-shift. The Lande g-factor  $g_J$  is  $g_J = 2$  for the  $^2S_{1/2}$  state and  $g_J = 2/3$  for the  $^2P_{1/2}$  state. As a result, the Zeeman splitting for the ground-state sublevels are three times larger than for the excited state sublevels. The Zeeman resolved structure of the  $^2S_{1/2} - ^2P_{1/2}$  transition of

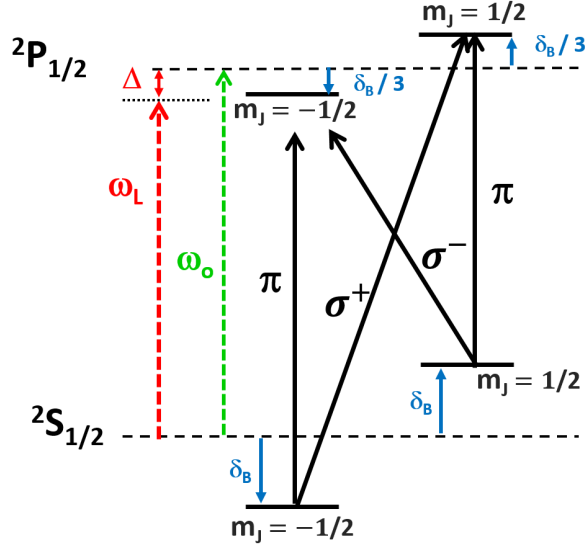


Figure 4.2: Zeeman resolved structure of the  ${}^2S_{1/2} - {}^2P_{1/2}$  transition for  ${}^{174}\text{Yb}^+$ . Zeeman splittings due to the magnetic field  $B$  are indicated in terms of  $\delta_B = \mu_B B/\hbar$ . Laser detuning,  $\Delta$  is defined relative to the  $B = 0$  transitions. The polarization resolved branching ratios are  $1/3$  for  $\pi$  and  $2/3$  for  $\sigma$  transitions.

${}^{174}\text{Yb}^+$  is shown in Fig. 4.2. In this figure,  $\omega_o$  is the frequency of the  ${}^2S_{1/2} - {}^2P_{1/2}$  atomic transition in the absence of magnetic field, and  $\omega_L$  is the frequency of the laser. Laser detuning is defined as  $\Delta = \omega_L - \omega_o$ . For efficient fluorescence and to make sure that the ion is not optically pumped dark into one of the ground-state sublevels, one should avoid pure circularly polarized light. In practice we use a linear polarization, which depending on its orientation can drive a  $\pi$  transition or an equal combination of  $\sigma^+$  and  $\sigma^-$ .

## 4.2 Fluorescence theory

The basis of Doppler laser cooling (and detection) relies on efficient fluorescence scattering. The fluorescence theory of a single Yb ion is studied and reported in our previous works [146, 147]. In this section, I present a summary of our previous results to describe the fluorescence behaviour of  ${}^{174}\text{Yb}^+$  and the requirements for achieving an optimum fluorescence rate.

The fluorescence rate on the  ${}^2S_{1/2} - {}^2P_{1/2}$  transition is defined as  $\gamma\mathcal{P}_p$ , in which  $\mathcal{P}_p$  is the total population of the excited state  ${}^2P_{1/2}$ , and  $\gamma$  is the natural linewidth of the transition. To find the excited-state population, we calculated the steady-state solution of the Liouville equation, describing the time evolution of the density matrix, as follows:

$$\frac{d\rho}{dt} = -\frac{i}{\hbar}[H, \rho]_{kl} + \mathcal{L}\rho, \quad (4.2)$$

where  $\rho$  is the density matrix, in which the diagonal terms represent the population of the states, and the off-diagonal terms represent the coherences between different states. The Hamiltonian  $H$  includes the interaction of the atom with the laser field and external magnetic field. The last term,  $\mathcal{L}_\rho$ , represents the damping effects, which are exclusively due to spontaneous emission in our case and may be calculated from Clebsch-Gordan coefficients (see for example [155]).

Finding the steady-state solution of the Liouville equation analytically is in general complicated for  $^{174}\text{Yb}^+$ . To simplify the solution, we assumed the coherence terms between the excited-state Zeeman levels, as well as between the ground state levels, are zero. (Numerical simulation shows that these numbers are in fact very small and this assumption is valid over a wide range of parameters). As long as the magnetic field is not too large ( $\delta_B \lesssim \gamma/2$ ), to a good approximation theoretically, the excited-state population can be simplified to a saturation form analogous to a two-level system as follows [146, 147]:

$$\mathcal{P}_p = \sum_{M_J=-1/2}^{1/2} \mathcal{P}_p(M_J) = \frac{1}{2} \cdot \frac{\frac{\Omega_0^2}{6}}{\Delta^2 + \left(\frac{\Gamma_{174}}{2}\right)^2}. \quad (4.3)$$

In this equation,  $\Omega_0$  is the laser Rabi frequency, which is a function of laser power,  $\Delta$  is the laser detuning, and  $\Gamma_{174}$  is the effective linewidth.

**Rabi frequency  $\Omega_0$ :** The Rabi frequency and associated "on-resonant saturation parameter"  $s_0$  are defined in terms of the bare  $^2S_{1/2} - ^2P_{1/2}$  fine-structure transition as follows:

$$\Omega_0 \equiv \sqrt{\frac{s_0}{2}} \gamma, \quad s_0 = \frac{I}{I_{sat}}, \quad I_{sat} = \frac{\pi hc}{3\lambda^3} \gamma. \quad (4.4)$$

In this equation, the natural linewidth  $\gamma/2\pi = 19.60(5)$  MHz [148, 149], and  $I$  is the laser intensity. The saturation intensity  $I_{sat}$  is only a function of the natural linewidth  $\gamma$  and wavelength  $\lambda$  of the transition, which to a very good approximation are the same for different isotopes. The saturation intensity of the  $^2S_{1/2} - ^2P_{1/2}$  transition of  $\text{Yb}^+$  is  $I_{sat} = 51$  mW/cm<sup>2</sup>.

**Effective linewidth  $\Gamma_{174}$ :** The effective linewidth for a linearly polarized laser field is extracted in the limit of large detuning  $\Delta \rightarrow \infty$ , and is a function of Rabi frequency  $\Omega_0$ , Zeeman shift  $\delta_B$ , natural linewidth  $\gamma$ , and  $\theta_{BE}$ . The latter is the angle between the laser's electric field and the external magnetic field. The effective linewidth is approximated as follows<sup>1</sup>:

$$\left(\frac{\Gamma_{174}}{2}\right)^2 = \frac{\Omega_0^2}{6} + \frac{\gamma^2}{4} \cdot \frac{\left(1 + \frac{16\delta_B^2}{9\gamma^2}\right) \left(1 + \frac{64\delta_B^2}{9\gamma^2}\right)}{1 + \frac{16\delta_B^2}{9\gamma^2} \cdot (3 \cos^2 \theta_{BE} + 1)} \quad (4.5)$$

---

<sup>1</sup>The effective linewidth is extracted at large detunings, but the shape of the polarization dependence is not well modeled at high detunings. The absolute systematic error however remains small, below 10% over the magnetic field range used. The approximated form coincides with the exact solution at  $\theta_{BE} = 0^\circ, 90^\circ$ . In our experiment,  $\theta_{BE} \approx 0^\circ$ .

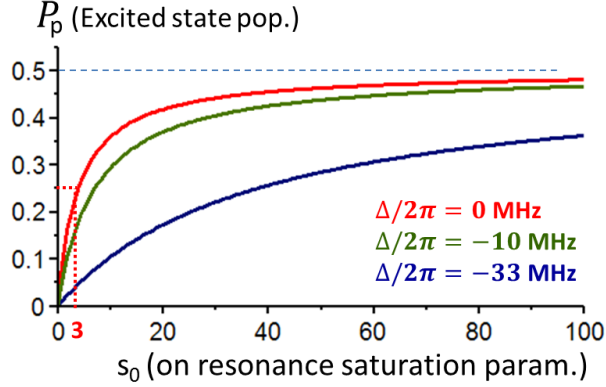


Figure 4.3: The excited state  ${}^2P_{1/2}$  population of  ${}^{174}\text{Yb}^+$  is shown as a function of saturation parameter (laser intensity) for three different detuning values,  $\Delta/2\pi = \{0, -10, -33\}$  MHz, and an optimized  $\theta_{BE} = 0^\circ$ . The Zeeman shift is  $\delta_B/2\pi = 8.2$  MHz and  $\gamma/2\pi = 19.6$  MHz.

The peak of the excited-state population, and so the maximum fluorescence, occurs at  $\theta_{BE} = 0^\circ$ , which corresponds to a  $\pi$ -polarized laser field. At this optimum point the effective linewidth simplifies to:

$$\left(\frac{\Gamma_{174}(\theta_{BE} = 0)}{2}\right)^2 = \frac{\Omega_0^2}{6} + \frac{\gamma^2}{4} + \frac{4\delta_B^2}{9} \quad (4.6)$$

The behaviour of the excited-state population  $\mathcal{P}_p$  as a function of saturation parameter  $s_0$ , for three different detuning values  $\Delta/2\pi = \{0, -10, -33\}$  MHz and an optimized  $\theta_{BE} = 0^\circ$  is shown in Fig. 4.3. In this plot, the Zeeman shift is set to  $\delta_B/2\pi = 8.2$  MHz, which is equivalent to a magnetic field of  $B = 5.9$  G that is used in our KZM experiment. As can be seen in the figure, increasing the saturation parameter, or equivalently the laser intensity, increases the fluorescence until saturation is reached. The maximum achievable population is 0.5, in which the population of excited and ground states are equal. On resonance, the ion reaches half the maximum value at saturation parameter  $s_0 = 3$ , or an effective value of  $s_{0eff} = s_0/3 = 1$ , where  $s_{0eff}$  is equivalent to the on-resonance saturation parameter of a two-level system.

Note that the leakage to the low lying  ${}^2D_{3/2}$  state is ignored in the calculation of the excited state population  $\mathcal{P}_p$ . For a saturated UV transition ( $\mathcal{P}_p = 0.5$ ), and near-optimal 935.2-nm laser parameters, numerical simulations indicate that repump effects comprise a maximum of  $\sim 5\%$  correction to the fluorescence, which can be neglected.

The UV fluorescence that we measure experimentally,  $\eta_{eff} \cdot \gamma\mathcal{P}_p$ , is proportional to the fluorescence (scattering) rate  $\gamma_{sc} = \gamma\mathcal{P}_p$  of the excited state and the collection efficiency of our imaging system, which is about  $\eta_{eff} \simeq 3 \times 10^{-3}$ . The imaging setup in this experiment is described as a part of the experimental setup at the end of this chapter.

## 4.3 Doppler cooling

Doppler cooling is a laser-cooling technique that applies light scattering from a laser beam to slow down the motion of atoms through a velocity resisting force. We start with the simple case of Doppler cooling of a free atom, and then expand the idea to the case of a single trapped ion. Finally we point out the complications that arise in Doppler cooling of a large string of ions.

### 4.3.1 Doppler cooling of a single free atom

A free atom with an atomic transition of frequency  $\omega_0$  and moving with a constant velocity  $\vec{v}$  is irradiated by a laser beam of frequency  $\omega_l$ . In the reference frame of the atom, the laser's frequency is Doppler shifted by  $\omega_l - \vec{k}_l \cdot \vec{v}$ , in which  $\vec{k}_l$  is the laser beam's wave vector. Doppler cooling can be achieved when  $\omega_l + k_l v$  is near resonance with the atomic transition. In this case, photons moving in the opposite direction to the particle, and with frequencies tuned below the atomic resonance (red detuned), will be absorbed. During the absorption-emission process, the atom first receives a momentum kick (recoil) of  $\hbar \vec{k}_l$  from the absorbed photon, followed by another recoil from the spontaneously emitted photon. However, the angular distribution of spontaneous emission has symmetry, such that the total recoil momenta over a large number of spontaneous emission processes averages to zero. Averaged over a large number  $N$  of scattering events, the atom loses a net momentum of  $N \hbar \vec{k}_l$  due to the total momentum kicks from absorbed photons moving in the opposite direction to the atom.

The absorption-emission process occurs at the scattering rate  $\gamma_{sc} = \gamma \mathcal{P}_e$ , given by the decay rate  $\gamma$  (natural linewidth), and the probability of being in the excited state  $\mathcal{P}_e$  (excited state population). Momentum kicks are received at the same rate, and on average the atom experiences a force as follows:

$$\left\langle \frac{\Delta p}{\Delta t} \right\rangle \approx F = \pm \hbar k_l \cdot \gamma_{sc}, \quad (4.7)$$

where the  $+(-)$  sign refers to an atom moving along (opposite to) the laser's propagation direction. For small atom velocities, where the Doppler broadening is low ( $k_l v \ll \gamma$ ), the average force can be approximated as [68]:

$$F \approx F_0(1 + \kappa v); \quad F_0 = \hbar k_l \cdot \gamma_{sc0}. \quad (4.8)$$

In this equation,  $F_0$  is the averaged radiation-pressure force exerted on a stationary atom ( $v = 0$ ). The damping coefficient  $\kappa$  is proportional to detuning  $\Delta$ , and its sign follows that of the detuning. For negative detunings, the force becomes velocity resisting (damping), leading to a loss in kinetic energy (*i.e.* the atom cools). To ensure cooling of a free atom in

1-D, two laser beams are required to provide damping forces for both positive and negative directions. Even when the two laser beams are provided, the atom cannot be cooled down to zero energy through Doppler cooling. Although the recoil momenta average to zero in the spontaneous emission process, the recoil energies that the atom receives,  $E_r = \hbar^2 k_l^2 / 2M$ , do not average to zero. The atom goes through a random walk in momentum space with each step being equal to the momentum of the emitted photon, and there is a diffusion of  $p$ , with  $\langle \Delta p \rangle = 0$  while  $\langle \Delta p^2 / 2M \rangle \neq 0$ . In addition to the emitted photons, absorbed photons also contribute to the recoil energy, and the atom gains a kinetic energy of  $\langle \Delta p^2 / 2M \rangle = 2NE_r$  (*i.e.* it heats) after  $N$  absorption-emission processes <sup>2</sup>. When the heating and cooling effects balance, an equilibrium state will be attained with the lowest achievable energy called the Doppler cooling limit. The minimum Doppler energy is a function of linewidth and detuning, and is optimized when the detuning is set to half a linewidth. In this case, the average kinetic energy, which for an ensemble of atoms can be expressed in terms of a temperature through  $\langle E_K \rangle = \frac{1}{2} k_B T_D$ , simplifies to :

$$T_D = \frac{\hbar \gamma}{2k_B}. \quad (4.9)$$

As an example, in an atomic sample with an atomic transition of linewidth  $\gamma = 2\pi \cdot 20$  MHz, a minimum Doppler temperature of  $T_D = 0.48$  mK can be expected.

### 4.3.2 Doppler cooling of a single trapped ion

The Doppler cooling of an ion confined in a harmonic trap has some differences compared to a free atom. For instance, due to the oscillatory motion of the trapped ion, a single near-resonant laser beam is sufficient to cool the ion. Moreover, depending on the strength of confinement, the cooling with a near resonant beam breaks up into two regimes: the weak and tight binding regimes [156]. The weak binding limit corresponds to  $\omega_i \ll \gamma$ , where  $\omega_i$  is the secular trap frequency along the  $i^{\text{th}}$  direction,  $i \in \{1, 2, 3\}$ . In this limit, the Doppler cooling can be modeled as if the ion was free during the scattering process, since the decay rate is much faster than the oscillatory motion of the trapped ion. In addition, the energies are high enough that the quantization of energy levels of the trap are not relevant and a semiclassical model is adequate. In the other limit, where the ion is bound very tightly,  $\omega_i \gg \gamma$ , the above free-atom picture is not applicable and the cooling can reach well below the Doppler limit, including ground-state cooling.

In our KZM experiments, we operate in the weak binding regime, where the transverse trap frequency  $\omega_t / 2\pi \simeq 0.6$  MHz is small compared to the linewidth  $\gamma / 2\pi = 19.6$  MHz. A detailed derivation of the Doppler cooling mechanism for a trapped ion is reported by Wineland and Itano [156, 157]. In this section, we present a summary of these results for the specific case of  $^{174}\text{Yb}^+$  in the weak binding limit.

---

<sup>2</sup>Properly, spontaneous recoil energy is distributed over three dimensions (see next section)

During an absorption-emission event, a single trapped ion with mass  $M$  absorbs a photon with a wave vector  $\vec{k}_l$  and frequency  $\omega_l$ , and emits another photon with a wave vector  $\vec{k}_s$  and frequency  $\omega_s$ , resulting in a velocity change from  $\vec{v}$  to  $\vec{v}'$ . The conservation of momentum and energy require:

$$M\vec{v}' + \hbar\vec{k}_s = M\vec{v} + \hbar\vec{k}_l, \quad (4.10)$$

$$\frac{1}{2}Mv'^2 + \hbar\omega_s = \frac{1}{2}Mv^2 + \hbar\omega_l. \quad (4.11)$$

In the non-relativistic limit and for near-resonant laser beams, after a scattering event, the change in kinetic energy associated with motion in the  $i^{\text{th}}$  direction can be approximated as<sup>3</sup>:

$$\Delta E_{ki} = \frac{1}{2}Mv_i'^2 - \frac{1}{2}Mv_i^2 = E_r(\hat{k}_{li}^2 - 2\hat{k}_{li}\hat{k}_{si} + \hat{k}_{si}^2) + \hbar(k_{li} - k_{si})v_i. \quad (4.12)$$

In this equation,  $E_r = (\hbar k_0)^2/2M$  is the recoil energy, and  $\hat{k}_{li}$  and  $\hat{k}_{si}$  are the  $i^{\text{th}}$  components of the unit vectors  $\hat{k}_l$  and  $\hat{k}_s$ . While  $\hat{k}_l$  has a fixed direction defined by the laser beam,  $\hat{k}_s$  changes randomly from one scattering event to another. The average of kinetic energy change in the  $i^{\text{th}}$  direction per scattering event is

$$\langle \Delta E_{ki} \rangle_s = E_r(f_{li} + f_{si}) + \hbar k_{li}v_i, \quad (4.13)$$

where  $f_{li}$  and  $f_{si}$  reflect the average components of the absorption and emission recoil kicks along the  $i^{\text{th}}$  direction, and are defined as:

$$f_{li} = \hat{k}_{li}^2 \quad f_{si} = \int P_s(\hat{k}_s) \hat{k}_{si}^2 d\Omega. \quad (4.14)$$

in which  $P_s(\hat{k}_s)$  is the probability of emitting a photon in the  $\hat{k}_s$  direction.

We briefly note in passing that the above derivation breaks up the cooling of the 3D motion of a trapped ion into three independent 1D cooling effects. This assumes that we can ignore correlations between motion along different axes. We will pursue a similar approach later when we consider a model for Sisyphus cooling for a trapped ion.

At this point we focus specifically on  $^{174}\text{Yb}^+$  and find the rate of kinetic energy change during Doppler cooling. This leads us to the definition of the cooling and heating rates, as well as the minimum steady-state energy or Doppler temperature. The change in kinetic energy occurs at the scattering rate  $\gamma_{sc} = \gamma\mathcal{P}_p$ , in which the population of  $^2P_{1/2}$  excited state,  $\mathcal{P}_p$ , is given in Eq. 4.3. Note that the detuning  $\Delta$  in that expression will be replaced by  $\Delta - \vec{k}_l \cdot \vec{v} - \omega_r$  to account for the first-order Doppler shift and recoil shift. The recoil frequency is defined as  $\omega_r = E_r/\hbar$ . Averaging over the velocity distribution of a trapped

<sup>3</sup>In this equation it is assumed  $(\hbar k_l)^2/2M = (\hbar k_s)^2/2M = (\hbar k_0)^2/2M = E_r$ , based on two approximations:

- 1- For near resonant laser beam,  $\Delta = |\omega_l - \omega_0| \sim \gamma \ll \omega_0$ , which leads to  $\omega_l \approx \omega_0$  or equivalently  $k_l \approx k_0$ .
- 2- In non-relativistic limit,  $|\omega_l - \omega_s| \sim \omega_r \ll \gamma$ , with  $\omega_r$  being the recoil frequency. As a result,  $k_l \approx k_s$ .

ion, one can find the following rate equation for the kinetic energy of a single  $^{174}\text{Yb}$  trapped ion:

$$\dot{E}_{ki} = \langle \gamma \mathcal{P}_p \langle \Delta E_{ki} \rangle_s \rangle_v = \frac{\gamma}{2} \cdot \frac{\Omega_0^2}{6} \left\langle \frac{E_r(f_{li} + f_{si}) + \hbar k_{li} v_i}{(\Delta - k_{li} v_i - \omega_r)^2 + (\frac{\Gamma_{174}}{2})^2} \right\rangle_v. \quad (4.15)$$

In the final stages of cooling, where the Doppler shift is much smaller than the linewidth, Eq. 4.15 simplifies to

$$\dot{E}_{ki} = \gamma_{sc0} \left( E_r(f_{li} + f_{si}) + \frac{2\hbar k^2 f_{li} \Delta \langle v_i^2 \rangle_v}{\Delta^2 + (\frac{\Gamma_{174}}{2})^2} \right), \quad (4.16)$$

in which the scattering rate at zero velocity  $\gamma_{sc0}$  is

$$\gamma_{sc0} = \frac{\gamma \Omega_0^2 / 12}{\Delta^2 + (\frac{\Gamma_{174}}{2})^2}. \quad (4.17)$$

Using the fact that  $E_{ki} = \frac{1}{2} M \langle v_i^2 \rangle_v$ , the right hand side of Eq. 4.16 can be re-written as a linear function of the energy, from which the cooling rate and steady-state energy can be derived:

$$\dot{E}_{ki} = -\Gamma_c E_{ki} + R_{Heat}, \quad (4.18)$$

$$E_{ki-ss} = \frac{R_{Heat}}{\Gamma_c}, \quad (4.19)$$

where

$$R_{Heat} = \gamma_{sc0} E_r(f_{li} + f_{si}), \quad (4.20)$$

$$\Gamma_c = \frac{8 f_{li} \omega_r (-\Delta s_{0_{eff}}) (\frac{\gamma}{2})^3}{\left( \Delta^2 + \left( \frac{\Gamma_{174}}{2} \right)^2 \right)^2}. \quad (4.21)$$

The heating term  $R_{Heat}$  arises from the recoil energy gained by the ion from absorbed and scattered photons. The cooling term of the energy is due to the velocity-resisting force  $F = -\kappa v$  associated with the Doppler effect. The damping rate  $\eta = \kappa/m$ , introduced in the KZM theory of Chapter 3, is related to the cooling rate as  $\eta = \Gamma_c/2$ . The maximum cooling rate is achieved when the detuning is set to half of the Zeeman broadened linewidth  $\Delta = -\Gamma_{174}^{(0)} = -\sqrt{(\frac{\gamma}{2})^2 + (\frac{2\delta_B}{3})^2}$ , and the effective saturation parameter is  $s_{0_{eff}} = 2 \left( \frac{\Gamma_{174}^{(0)}}{\gamma} \right)^2$ . At these optimum values, the cooling rate is:

$$\Gamma_{c,max} = \omega_r f_{li} \left( \frac{\gamma}{\Gamma_{174}^{(0)}} \right). \quad (4.22)$$



The minimum steady-state kinetic energy is achieved when  $\Delta = -\Gamma_{174}/2$ . At this optimum detuning, the minimum achievable average kinetic energy, *i.e.* the Doppler limit, will be:

$$E_{ik-ss} = (1 + f_{si}/f_{li}) \cdot \frac{\hbar\Gamma_{174}}{8}. \quad (4.23)$$

The Doppler limit depends on the laser direction and angular distribution of spontaneous emission relative to the trap direction being cooled through the values of  $f_{li}$  and  $f_{si}$ . For a  $J = 1/2 \rightarrow J' = 1/2$  transition, the angular distribution of spontaneous emission is isotropic, which means  $f_{si} = 1/3$  [158]. If the cooling beam is perpendicular to the  $i^{th}$  principal axis of the trap ( $f_{li} = 0$ ), there will be no cooling in that direction and the recoil heating will lead to an energy divergence in that direction ( $E_{ki-ss} \rightarrow \infty$ ). In order to have 3-D Doppler cooling, the cooling laser's wave vector needs to have components along all principal trap axes. In the case of isotropic emission, the optimum Doppler limit is obtained at  $f_{li} = f_{si} = 1/3$ , resulting in a minimum kinetic energy of  $E_{ki-ss} = \Gamma_{174}/4$  in each direction. At a low laser power ( $\Omega_0 \ll 1$ ) and small magnetic field ( $\delta_B \ll \gamma$ ), the effective linewidth approaches the natural linewidth ( $\Gamma_{174} \rightarrow \gamma$ ), and  $E_{ki-ss} = \hbar\gamma/4$ , which agrees with the typical Doppler-cooling limit discussed above. In ion trapping experiments it is more common to use the average vibrational quantum number  $\bar{n}$  in the harmonic trap rather than temperature to define how cold an ion is. The total energy  $E = 2E_k$  from equipartition can be used to estimate  $\bar{n}$  from  $E_i = \hbar\omega_i(\bar{n} + \frac{1}{2})$ .

### Doppler cooling parameters in our setup:

**Laser beam's direction:** The Doppler cooling beam lies in a horizontal plane at an angle of  $45^\circ$  with the axial direction so that  $\vec{k}_l = \{\frac{1}{2}, \frac{1}{2}, \frac{1}{\sqrt{2}}\}k_l$ , corresponding to  $f_{li} \in \{1/4, 1/4, 1/2\}$ . The direction of the beam, which is determined by optical access to the trap, ensures cooling along all trap axes.

**Trap frequencies:** The KZM experiment is performed at trap frequencies of:

$$\{\omega_x, \omega_y, \omega_z\} = 2\pi\{0.679, 0.658, 0.037\} \text{ MHz.}$$

**Doppler cooling limit:** In an optimum case of low laser power and no magnetic field, the minimum steady-state energy of a trapped  $^{174}\text{Yb}$  ion along each direction is  $E_{i-ss} \in \{0.6, 0.6, 0.4\}\hbar\gamma$ . For the given trap frequencies, the minimum steady-state  $\bar{n}$  achieved through Doppler cooling is  $\bar{n}_{i-ss} \in \{17, 18, 200\}$ , which clearly shows that a classical treatment of the motion is indeed appropriate.

**Damping (cooling) rate:** The optimum cooling rate according to Eq. 4.21, along each direction is:  $\Gamma_{ic,max} \in \{1/4, 1/4, 1/2\}\omega_r$  with the recoil frequency  $\omega_r/2\pi = 8.4$  kHz. The optimum damping time  $\eta^{-1}$  for each direction becomes  $\{38, 38, 19\} \mu\text{s}$ . In our KZM studies, the transverse frequencies are normally changed by  $\Delta\omega_y \simeq 2\pi \cdot 450$  kHz, over a quench time of  $2\tau_Q = 10 - 70 \mu\text{s}$ . The soft mode frequency at freeze out  $\sqrt{\delta(\hat{t})} = (\delta_0/\tau_Q)^{1/3}$  (see Chapter

3, Section 8) is  $(1 \mu\text{s})^{-1}$ , which compared to the optimum damping rate of  $(38 \mu\text{s})^{-1}$ , is much faster. This means that our experiment is in the under-damped regime. Note that the damping time of  $38 \mu\text{s}$  is obtained for the transverse motion of a single ion in the optimum cooling situation. The damping time in the context of the KZM is related to the damping of the transverse zigzag mode in a string of ions. In practice, considering the complications of the larger strings and experimental imperfections, the damping time is expected to be even longer.

### 4.3.3 Doppler cooling of a string of trapped ions

When a Doppler cooling beam illuminates an ion string uniformly, the recoil kicks from each ion are distributed throughout the crystal by the Coulomb interactions. Depending on the participation of an ion in a given vibrational mode, the cooling effect of a given ion will have different effects on each collective vibrational mode of the string. Morigi and Eschner [130] have studied the laser cooling of an ion string theoretically. For thermal energy in the Doppler cooling regime, the theory is not particularly simple but the conclusion is a Fokker-Planck equation for the energy distribution of the modes is derived and it is shown that the Doppler laser cooling of an ion string is essentially the same as for the single ion. For uniform illumination, the Doppler limit and cooling rate for the total energy of the crystal match that of the single-ion case. However, there are some practical complications that can arise as we Doppler cool a large string of ions. In this section, we investigate some of these complications and their possible effects on the cooling outcome.

In order to have a uniform cooling beam across the crystal, we use a combination of spherical and cylindrical lenses to make a beam that is focused transversely, but more extended axially, without excessive scatter on the endcaps. The full width at half maximum (FWHM) of the cooling beam is  $280 \mu\text{m}$  in the axial direction. We chose to limit our experiment to a string of maximum 43 ions, which has a similar length to the FWHM over the range of trap frequencies used in the experiment. Another practical complication of the large ion strings in a linear Paul trap is the presence of the excess micro-motion. For our trap design, the two needles used for endcaps result in non-negligible leakage of rf electric field into the axial direction with an amplitude that increases towards the endcaps. For a small crystal of a few ions, the micro-motion axially can be minimized by optimizing the position of the crystal. However, for larger crystals ( $N > 10$ ) that extend over significant axial distance, the micro-motion is unavoidable and the ions on the outer edges may end up with significant micro-motion. The excess micro-motion results in a linewidth broadening and reduction in scattering rate. The other parameters such as the cooling rate and cooling limit that depend on scattering rate are also affected. In the presence of micro-motion, whose amplitude is characterized by a modulation index  $\beta$ , the excited state population of

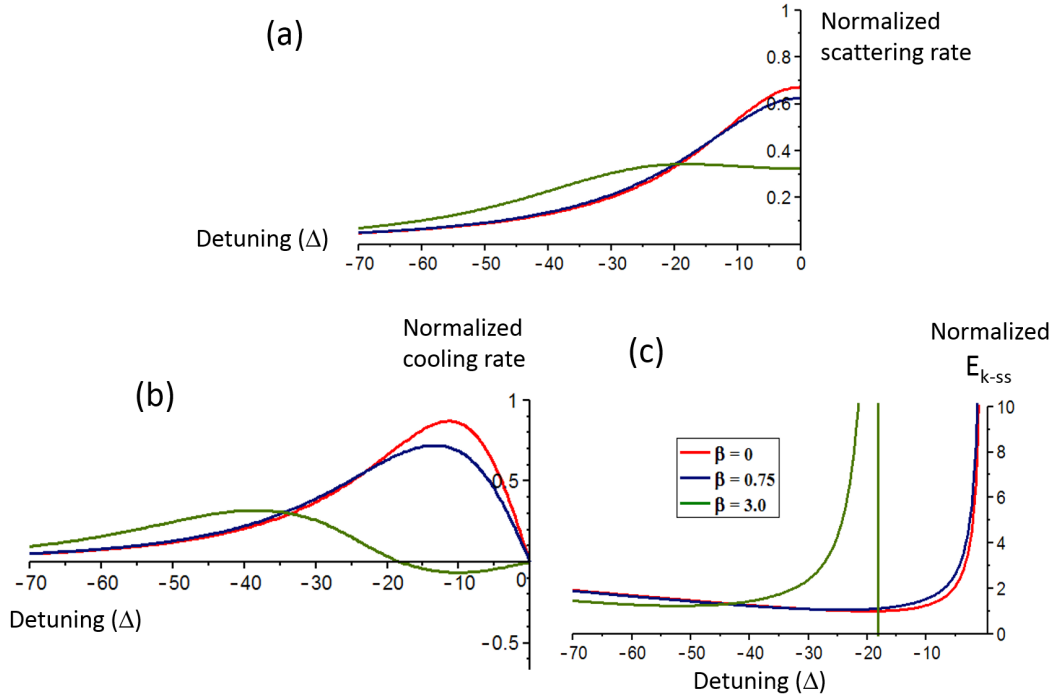


Figure 4.4: The effect of micro-motion on (a) scattering rate, (b) cooling rate, and (c) cooling limit, for three cases of, no micro-motion ( $\beta = 0$ ), medium micro-motion ( $\beta = 0.75$ ) and large micro-motion ( $\beta = 3$ ). In these plots, parameters used are rf trap frequency  $\Omega_T/2\pi = 11.75$  MHz, Zeeman frequency  $\delta_B/2\pi = 8.24$  MHz,  $\theta_{BE} = 6^\circ$ , effective saturation parameter  $s_{0eff} = 2.7$ ,  $\gamma/2\pi = 19.6$  MHz, and wavevector projection  $k_i = 1/2$  i.e. for a transverse trap axis so the vertical axes of all the three plots are normalized to their optimum values.

Eq. 4.3 changes to [120]:

$$\mathcal{P}_{p(mm)} = \frac{1}{2} \cdot \sum_{n=-\infty}^{n=\infty} \frac{(\Omega_0^2/6)J_n^2(\beta)}{(\Delta + n\Omega_T)^2 + (\Gamma_{174}/2)^2}, \quad (4.24)$$

where  $J_n$  is the Bessel function and  $\Omega_T$  is the rf trap frequency. Figure 4.4 shows the effect of micro-motion on scattering rate ( $\gamma_{sc} = \gamma\mathcal{P}_{p(mm)}$ ), cooling rate, and cooling limit for a transverse trap axis as a function of detuning. The numerical values of the parameters used in these plots are the same as the experimental values. The plots include three cases of no micro-motion ( $\beta = 0$ ), a medium micro-motion ( $\beta = 0.75$ ) and a large micro-motion ( $\beta = 3$ ). It can be seen in Fig. 4.4(a) that as the amplitude of micro-motion increases, the linewidth broadens and sidebands at  $\pm n\Omega_T$  ( $n = 1, 2, 3, \dots$ ) develop, while the carrier's strength decreases. (The sidebands are not resolved in Fig. 4.4(a)). The reduction in the

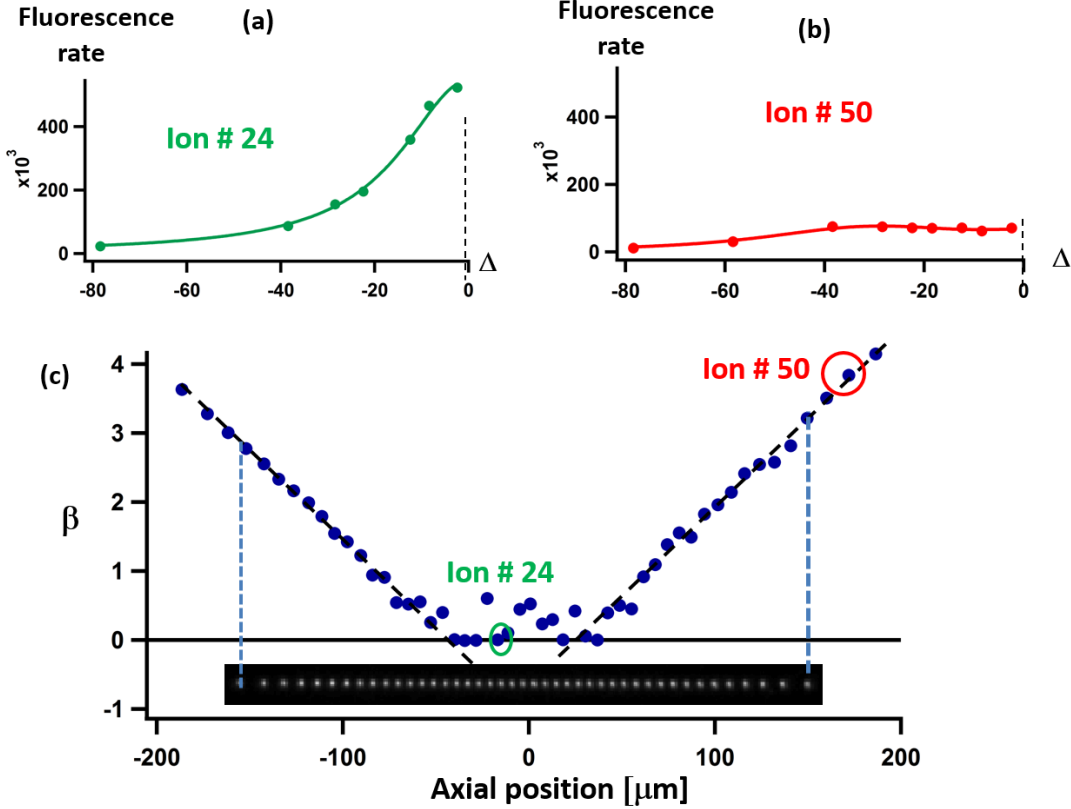


Figure 4.5: Samples of fluorescence measurements as a function of detuning  $\Delta$  for (a) an ion in the middle of a 51-ion string, and (b) an ion close to the edge of the string. Fitting the fluorescence rate of an ion to Eq. 4.24 gives the value of  $\beta$  at the position of that ion. (c) The modulation index  $\beta$  as a function of axial position. An image of a 43-ion string is overlapped on the x-axis for reference.

scattering rate leads to a reduction in cooling rate or even a heating effect at detunings \*below\* the transition resonance (see Fig. 4.4(b)). Figure 4.4(c) shows that when micro-motion is large, the minimum steady-state energy is not obtained at half a linewidth and larger detunings are needed.

To find out the magnitude of excess micro-motion amplitude across the crystal, we measured the fluorescence rate of individual ions with camera images as a function of detuning in a string of 51 ions. The values of modulation index  $\beta$  were obtained from fitting the fluorescence measurement to Eq. 4.24. The fits use a fixed value for the rf frequency ( $\Omega_T/2\pi = 11.75$  MHz), unmodulated linewidth ( $\Gamma_{174}/2\pi = 35$  MHz, determined by a separate measurement) and the resonance location. The laser power is at a low value to limit saturation and the only fit parameters are peak value and  $\beta$ . In Fig. 4.5, we show the variation of  $\beta$  as a function of axial position (or equivalently ion number). Two samples of fluorescence measurements for the central ion and the outer edge one is also shown in

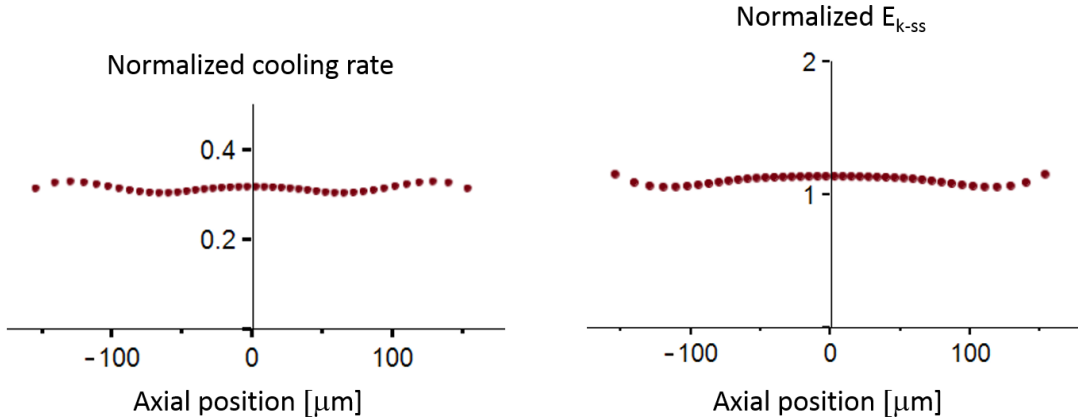


Figure 4.6: The simulation results of (a) normalized cooling rate and (b) normalized steady-state kinetic energy across a crystal of 42 ions for a detuning of  $\Delta/2\pi = -32.6$  MHz,  $s_{0eff} = 2.7$  at the center, and a laser beam FWHM=280  $\mu\text{m}$ . The other parameters are similar to Fig 4.4. The estimated cooling rate is uniform to a factor of 2 or better across the crystal. The cooling rate is normalized to  $\Gamma_{c,max}$  given by Eq. 4.22 and the steady-state energy is normalized to minimum  $E_{k-ss}$  given by Eq. 4.23.

this figure. The on-resonance scattering rate reduces by a factor of  $\sim 10$  as we go from the center to the edges. As can be seen in the  $\beta$  vs. position plot, micro-motion is nulled for the central 15 ions but starts to increase linearly for the ions farther out. The central value from fits is systematically sensitive to the unmodulated linewidth used in the fits. However, a separate measurement of micro-motion using a much more sensitive technique of photon correlation indeed shows that the ion at the center of crystal has a modulation index  $< 0.1$  (We did not use this technique for the plots since it would be more labor intensive and require using a single ion moved to different positions). The  $\beta$  vs. position plot can be used as a ruler to estimate the excess micro-motion on the edges of a 41-43 ion string. An image of a string of 43 ions is also included in Fig. 4.5, from which we can deduce that the index of modulation increases to a maximum of  $\beta \simeq 3$  for ions on the outer edge.

Based on the results of cooling rate and cooling limit shown in Fig. 4.4, and considering the maximum index of modulation of  $\beta \simeq 3$  on the edges of a 43-ion string, we chose to operate at a detuning of  $\Delta/2\pi = -32.6$  MHz to provide a reasonable and uniform cooling rate and steady-state energy across the crystal. The simulation results of the normalized cooling rate and steady-state energy across a crystal of 42 ions are shown in Fig. 4.6. With an effective saturation parameter of  $s_{0eff} = 2.7$  at crystal center, the estimated cooling rate is uniform to a factor of 2 or better across the crystal. Due to these adjustments, the cooling rate becomes slower by a factor of  $\sim 2.5$ , corresponding to a value of 200 – 400  $\mu\text{s}$  including estimated spatial variation of the cooling rate. So, we are a bit further in the under-damped regime. The decrease in cooling rate will also have some impact on losses of

kinks once formed. Having dealt with the damping rate and having identified the cooling limit in a string of 41 – 43 trapped ions, we next describe the loading process to achieve an isotopically pure crystal with a given number of ions.

## 4.4 Efficient loading of a large pure ion crystal

For the KZM experiments, it is very important to use an isotopically pure ion crystal, since the presence of even one non-fluorescing ion at the center of the crystal biases the zigzag into one of the symmetry broken states and thus reduces the rate of defect formation significantly (see Chapter 5). Also we aimed for tight control of the ion number in our experiment to limit its effect on our results. As a result, we require an efficient means to load an isotopically pure crystal of a known number of ions. This is done by photo-ionization loading of  $^{174}\text{Yb}^+$  from an effusive atomic beam. The details of the atomic beam production and photo-ionization process is provided in my M.Sc. thesis [146]. In summary, a 398.911-nm beam is used to resonantly excite neutral Yb atoms from the  $^1S_0$  to  $^1P_1$  state with reasonable selectivity (the isotope shifts are around hundreds of MHz). Then, an outer electron in the  $^1P_1$  state is directly excited to the continuum by absorbing a 369.5-nm photon. To improve the isotope selectivity of the photo-ionization process, the 399-nm beam is directed nearly perpendicular to the atomic beam to minimize Doppler shifts, and it is maintained at a relatively low power to limit saturation broadening of the  $^1S_0 \rightarrow ^1P_1$  transition. To obtain efficient loading, we use the 369-nm Doppler/detection beam and a beam with several mW of power from an additional Ti-Sapph beam to provide the second photon of the photo-ionization process.

To load a crystal of  $42 \pm 1$   $^{174}\text{Yb}$  ions, we set the trap's rod voltages to the onset of the zigzag transition for a slightly smaller string (such as  $\sim 38$  ions). Then we turn on the ytterbium oven that produces the effusive Yb atomic beam, and introduce the photo-ionization beam into the trap. A video-like monitor of the center of the trap is provided by our CCD camera in "focus" mode, running at maximum frame rate. The  $^{174}\text{Yb}$  ions loaded into the trap form a linear crystal whose length increases as more ions are added to the crystal. When the number of trapped ions surpasses  $N = 38$ , a zigzag structure appears. At that point, we stop the loading process by turning off the oven and blocking the photo-ionization beam, and wait for a few minutes to allow any extra loaded ions to cool down and join the crystal. We then count the number of ions. If the total number of ions is lower than 42-43 ions, we re-start the loading process with a reduced photo-ionization power to slow down the loading rate. This allows us to top up the number of ions to 42-43. On the other hand, if the number of loaded ions is slightly higher than 43, we found it convenient to "boil off" an ion or two by increasing the rod voltages close to the point where the trapping potential is lost. A pure 42-43 ion crystal can be used for 2-3 hours of experiment. However during this time, one or two trapped  $^{174}\text{Yb}$  ions from time to time will form a molecular ion

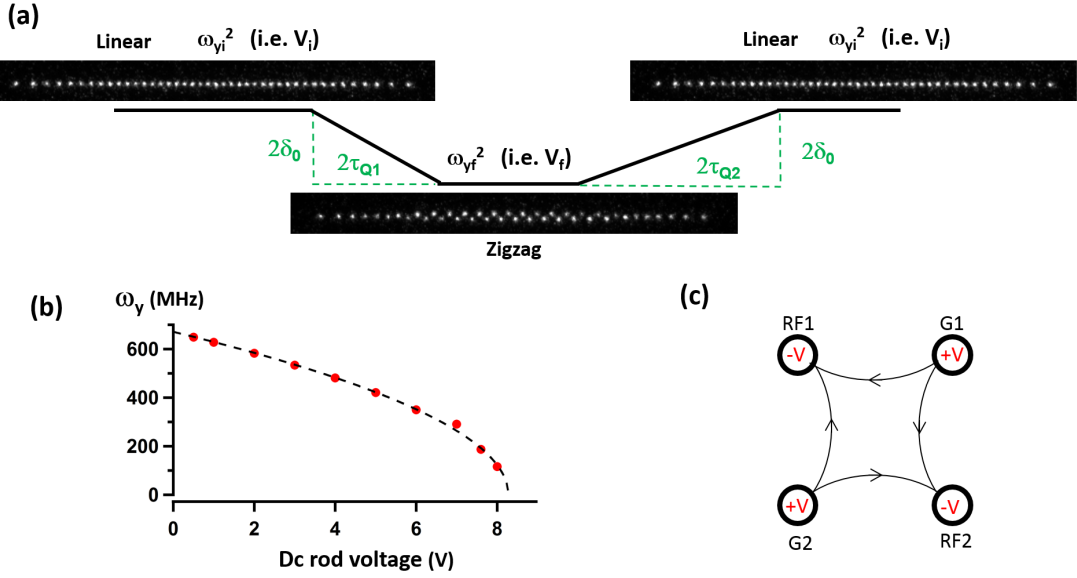


Figure 4.7: (a) To quench across the linear-zigzag transition, we change the transverse trap frequency by changing the voltage of the rods linearly over a quench time of  $2\tau_Q$ . (b) The single-ion calibration of the secular transverse trap frequency  $\omega_y$  with the applied dc rod voltage  $V_{dc}$ . The line indicates the fit to Eq. 4.25. (c) The transverse quadrupole potential is produced by applying  $+V(t)$  and  $-V(t)$  to each pair of opposing rods.

through collision with a background gas atom. We are able to use the high power Ti-Sapph beam to dissociate the molecule and recover the pure crystal. Additionally, ions leave the trap occasionally, in which case we re-load to top up the crystal.

Having loaded a pure ion crystal, the next step for performing a KZM experiment is the implementation of the quench across the linear-zigzag transition.

## 4.5 Ramp across linear–zigzag transition

To study the KZM in an ion-trap system, we start with a linear string of 41-43 Doppler cooled  $^{174}\text{Yb}$  ions, then rapidly quench across the linear-zigzag transition, and finally image the zigzag structure to see if any defect was formed. We then ramp back to the linear structure and repeat the process with the same ion string to accumulate more statistics. To quench across the linear-zigzag transition, the ratio between the transverse and axial confinement needs to be reduced ( $\alpha \equiv \omega_y/\omega_z$ ) to pass the critical point ( $\alpha_c$ ). This can be achieved by weakening the transverse confinement or equivalently strengthening the axial confinement. In keeping with the theoretical proposal [61], we chose to reduce the secular transverse trap frequency and keep the axial frequency constant to maintain a constant axial

spacing until the transition point. The transverse secular trap frequencies are controlled by applying a transverse dc quadruple potential via the trap rods. The transverse secular trap frequency along the  $y$  axis scales with the applied dc rod voltage as:

$$\omega_y^2(t) = \omega_{y0}^2 \left( 1 - \frac{V(t)}{V_0} \right), \quad (4.25)$$

where the constants  $\omega_{y0} = 658(1)$  kHz and  $V_0 = 7.95(2)$  V are obtained from a single-ion calibration measurement. (See a sample of these calibrations in Fig. 4.7(b)). In this case,  $\delta(t) = \omega_y^2(t) - \omega_{y,c}^2$  represents the time-dependent change of the control parameter (see theory of KZM Chapter 3, section 8) and is proportional to rod voltage. A linear voltage ramp is equivalent to a linear change in  $\delta(t)$  as assumed in the KZM theory. The transverse trap frequency along the  $x$ -axis,  $\omega_x$ , *increases* in an equivalent way to  $\omega_y$  with the dc rod voltage. To generate a transverse quadruple potential, it is sufficient to apply  $V_0$  to two opposing trap rods. Instead we make use of all four rods as shown in Fig. 4.7(c). In this way, we get twice the effect for the same voltage change, which extends the range of the voltage card we use. More importantly, the effect of the electric field leaking into the axial direction is eliminated to the lowest order, and the axial frequency stays almost constant. To correct the residual axial effect, we add some corrections to the endcap voltages during the ramp.

To obtain the necessary voltage ramps, we use a computer running LabView software to control the output of a National Instrument PCI-6733 board. The NI PCI-6733 has 8 high-speed analog outputs, which is enough number to control the voltages of all four trap rods and two endcaps independently. The voltage range of the board is -10 to 10 V, which is large enough to cover the range of required order parameter variations, an accuracy of 2.24 mV, and 16-bit resolution (300  $\mu$ V). The board has a clock rate of 10 MHz, and can be externally triggered.

For this setup, we write the ramp-up and ramp-down waveforms into the on-board buffer of the card, and use a pair of external triggers from the main experiment-control computer to control the output of the ramp-up and ramp-down waveforms, and the timing between them. The ramp waveform can be programmed to an arbitrary shape. The front panel of the Labview program is shown in Fig. 4.8 and contains both a dc panel and a two-step ramp panel. The dc panel is normally used at the start of the day when nulling the micro-motion for the start and end points of the ramp. The voltage corrections for nulling the micro-motion are incorporated into the ramp. In practice, we found the correction to be nearly independent of the voltage over the typical 0-5 V ramp. The two-step ramp panel allows for the choice of the ramp shape including linear, step function and tanh, but we exclusively use the linear form for the KZM experiments. The quench time of the ramp-up and ramp-down can be chosen independently. Typically we use a fixed ramp-down time of 200  $\mu$ s for resetting the crystal to a linear string. For the fastest ramps considered, on



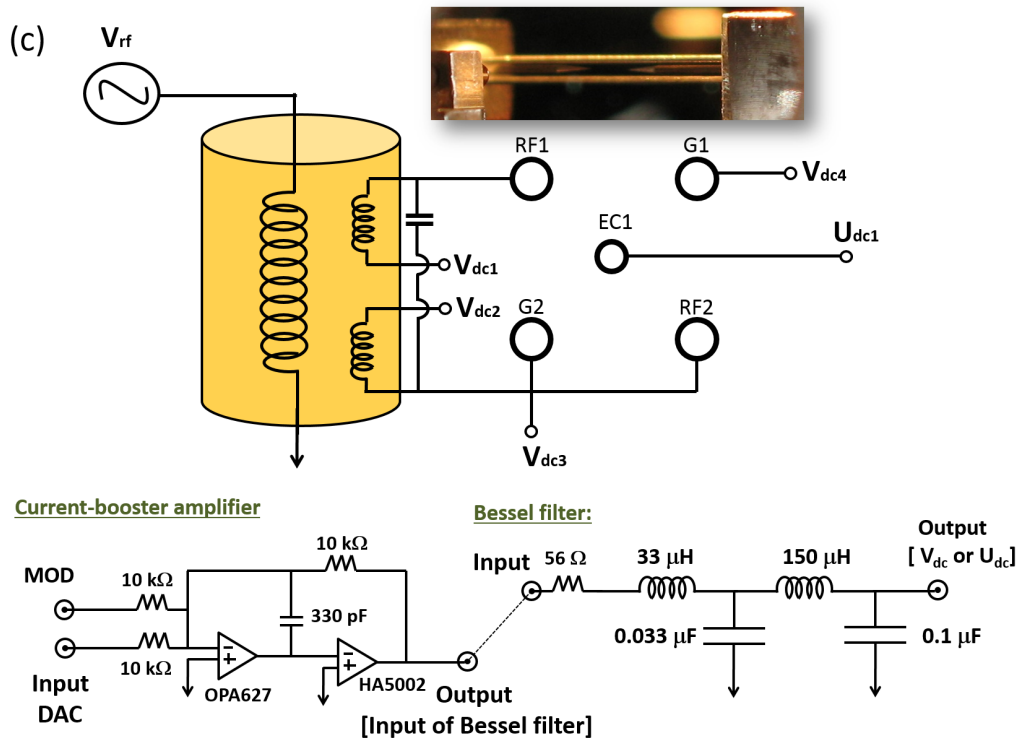
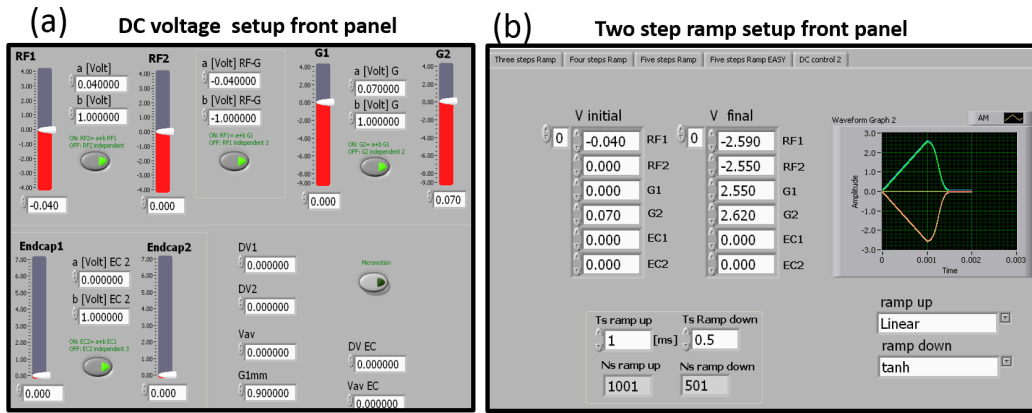


Figure 4.8: (a) The front panel of the Labview program for the dc voltage setup used at the start of the experiment to null the micro-motion. (b) The front panel of the Labview program for implementing a voltage ramp. The micro-motion correction is added to the start- and end-point of the ramp in the two-step ramp setup. (c) The circuit diagrams of the Bessel filter and the current-booster circuit of the four rods, and two endcaps. The resonator is only shown schematically

the order of  $0.5\text{-}2\text{ V}/\mu\text{s}$ , the discretization of the voltage steps in the DAC output is fairly obvious. In order to smooth the ramp shape, six Bessel filters are added between the analog output of the board and all four trap rods and two endcaps (The circuit diagram of the

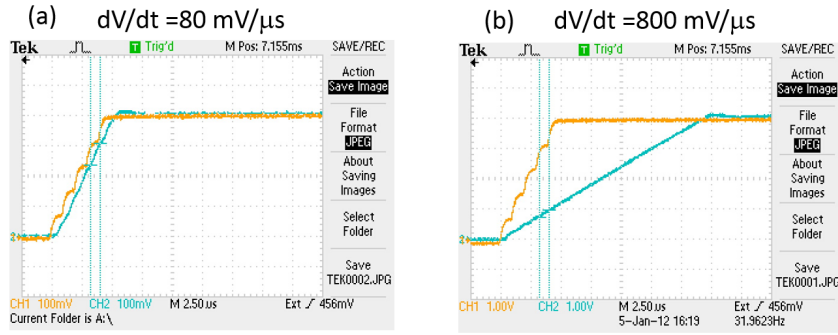


Figure 4.9: The effect of adding a Bessel filter to the board output for  $5\mu\text{s}$  ramps over 0–400 mV (a) and 0–4 V (b). The yellow line is the output of the board (input of the Bessel filter), and the blue line is the output of the Bessel filter. The Bessel filter smoothens the shape of the ramp. For fast quenches, the low current output of the board cannot charge up the final capacitor of the Bessel filter fast enough to support fast quenches.

Bessel filters can be found in Fig. 4.8). The Bessel filters are chosen to minimize distortion of the waveform. They are placed close to the trap, since they also serve the dual purpose of rf grounding their connection points. The smoothing effect of the Bessel filters on the waveform is shown in Fig. 4.9(a).

One limitation of the PCI-6733 board is its low 5-mA output current, which does not allow for the fast voltage changes required ( $\text{V}/\mu\text{s}$ ), when driving the Bessel filters (see Fig. 4.9(b)). The essential limitation is the charging of the final capacitor of the Bessel filter needed to hold the output at rf ground. To solve this problem, we added a current-booster amplifier for each output of the board (The circuit diagram of the booster-amplifier is shown in Fig. 4.8). For typical ramps of 0–5 V and ramp times of 10 – 70  $\mu\text{s}$  used in the experiment, the ramp performance after adding the current-boosters and Bessel filters is shown in Fig. 4.10 (top panel). A magnified view of the partially smoothed residual distortion is also shown in Fig. 4.10 (bottom panel), which indicates a maximum distortion of  $V_{pp} \sim 100$  mV after filtering. Having a large, pure crystal of trapped ions in hand, and being able to rapidly quench across the linear-zigzag transition, we next proceed to the defect detection technique in our ion-trap setup.

## 4.6 Imaging setup and data collection

The defects are detected and recorded by imaging the fluorescing trapped ions. The measured UV fluorescence,  $\eta\gamma_{sc}$ , is proportional to the scattering rate  $\gamma_{sc}$  and the collection efficiency of our imaging system,  $\eta_{eff} \simeq 3 \times 10^{-3}$ . The imaging setup in this experiment is similar to the one used previously in our group for fluorescence and hopping studies [127, 146, 147] with some modifications to reduce the total magnification from 140 to 16

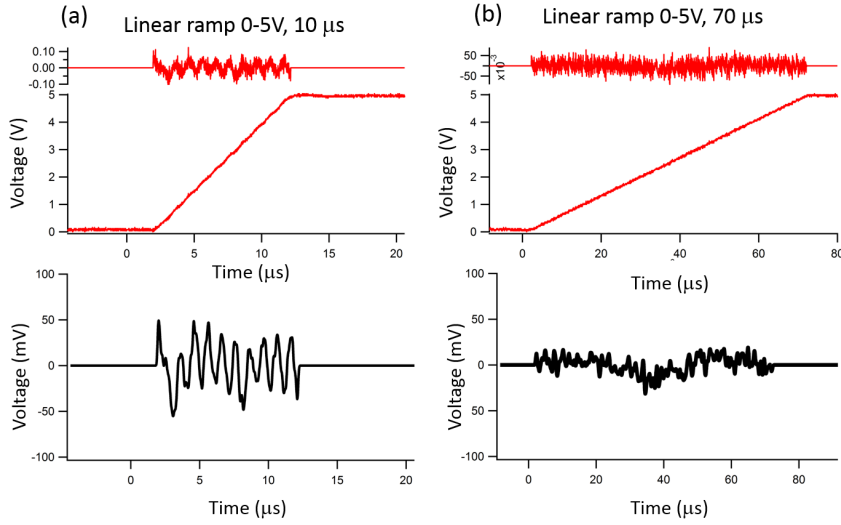


Figure 4.10: Typical result of the added current-booster, and Bessel filter along with the partially smoothed residual distortion for 0-5 V ramps over quench times of (a)  $2\tau_Q = 10 \mu s$  and (b)  $2\tau_Q = 70 \mu s$ . The maximum distortion in voltage is  $V_{pp} \sim 100 \text{ mV}$ .

in order to be able to see the larger strings. The scattered photons are collected with an anti-reflection-coated UV microscope objective lens with a focal length of 20 mm and a high numerical aperture ( $NA \approx 0.23$ ). An intermediate image of the ions is focused about 17 cm behind the objective where an adjustable slit, set to a width of  $450 \mu m$ , is used to suppress background scatter from electrodes. A back-to-back pair of  $f = 300 \text{ mm}$  lenses re-images the ions onto an intensified CCD camera (or onto a photo-multiplier-tube (PMT) for measurement of the ion fluorescence by photon counting, used for the Sisyphus cooling and Raman cooling data). The camera exposures are also triggered by the main experiment program. In a typical KZM experiment we acquire a single image of the initial linear string before the quench, and then one or more images after the quench to search for kinks or observe their dynamics in the zigzag structure. In order to limit the effect of loss of kinks before detection the exposure time of the camera is reduced to the minimum value of 3 ms that is required to obtain a good fluorescence image of the ions. However, the exposure time is still too long to capture any of the fast  $\mu s$  dynamics taking place shortly after the quench, including immediate kink loss from the crystal.

Having gone through the main aspects of a KZM experiment in our ion-trap system, we finish this chapter with a summary of the laser setup used in this experiment.

## 4.7 Laser setup

A detailed description of the all lasers used in this experiment and their lock setups is provided in my Masters' thesis [146]. Here, we provide a brief overview of the laser-beam

setup including the 369-nm beam tuned to the  $S_{1/2} \rightarrow P_{1/2}$  transition used for Doppler cooling and fluorescence detection, and the 935-nm and 638-nm repump beams needed to maintain the ion in the fluorescence/cooling cycle (see Fig. 4.1). All these three beams are continuously on during the experiment. We also include in the discussion below the 399-nm beam used for the photo-ionization. The simplified optical path of these laser beams is shown in Fig. 4.11.

**Doppler cooling/ detection beam:** The 369-nm beam used for Doppler cooling/fluorescence detection is produced by a frequency doubled diode-laser system at 739 nm. To ensure the short term stability of the detuning and to obtain a narrow laser linewidth, the 739-nm laser is short-term stabilized using its doubling resonator cavity as a reference. Long-term drifts are also suppressed by locking the laser to an iodine hyperfine feature using a saturated absorption setup. The laser system produces  $\sim 4$  mW of UV power, and  $\sim 2$  mW is fiber coupled to the experiment. About 90% of the fiber-coupled beam goes through a \*high-power\* path used for the KZM experiment with  $^{174}\text{Yb}^+$ , and the remaining 10% is directed to a \*low-power, frequency modulated\* path that is required for laser cooling and detection of  $^{171}\text{Yb}^+$  (see Chapter 7). The latter path is not relevant to the KZM experiment. Acousto-optic modulators (AOM) provide power (and frequency) control of the UV beams incident on the ion. The maximum power of the Doppler/detection beam (from the high-power path) reaching the trap is  $\sim 600 \mu\text{W}$ . The power used in this experiment is  $\sim 180 \mu\text{W}$ , which is equivalent to an effective saturation parameter of  $s_{0eff} = 2.7$ . Power drifts in the cooling laser are monitored during the experiment using the zeroth order of the AOM. The Doppler cooling beam is tuned to  $\Delta = 33$  MHz below resonance. The polarization of the 369-nm beams is initially linearly polarized by a polarizing beam splitter cube. A half-wave plate, placed near the beams' entrance to the trap is used to rotate the laser's polarization with respect to the magnetic field  $\vec{B}$ , and is set to  $\approx 0^\circ$  with respect to a 5.9 G magnetic field. The axial full width at half maximum (FWHM) of the beam is  $280 \mu\text{m}$  achieved with a cylindrical-spherical lens pair. The alignment and focus of the beams on the ion string are finely adjusted by a lens mounted on on  $XYZ$  translation stage.

**D-state repump beam:** The 935-nm beam which serves for  $^2D_{3/2}$ -state repumping, is produced by a stabilized external cavity diode laser. (For the  $^{171}\text{Yb}^+$  isotope, the beam is frequency modulated with a broadband fiber modulator at 3.07 GHz for hyperfine repumping). The 935-nm laser is stabilized against long-term drifts by a transfer lock setup consisting of a confocal Fabry-Perot cavity locked to the iodine-stabilized 739-nm laser. The lock setup was built as part of my Masters' thesis, and the details can be found in [146]. The power of the laser's output beam after a 30-dB isolator is  $\sim 40$  mW. Half of the power is fiber coupled to the experiment, from which  $\sim 6$  mW reaches the trap. About  $\sim 3$  mW reaches the lock setup through another fiber. The 935-nm beam is shaped with a spherical-

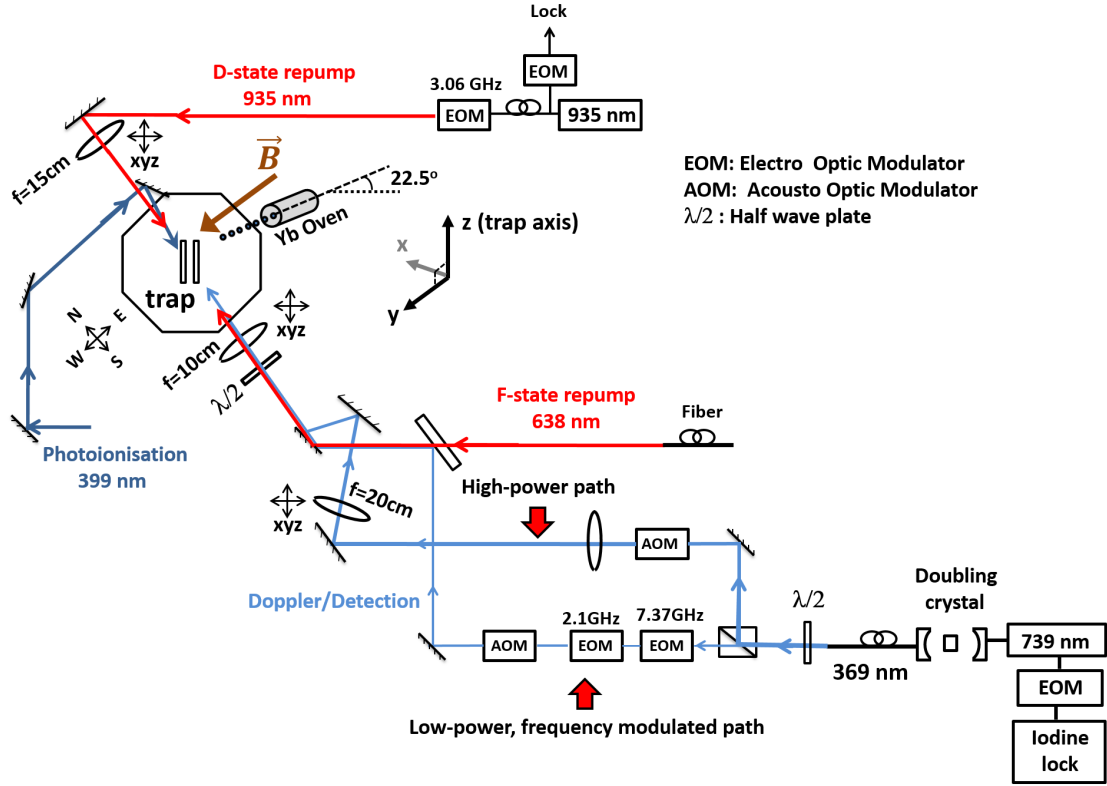


Figure 4.11: The simplified schematic of the laser-beam paths to the trap for the cooling/detection laser beam at 369 nm, the D-state and F-state repump laser beams at 935 nm and 638 nm, and the photo-ionisation laser beam at 399 nm.

cylindrical lens pair to cover the extent of the ion string. The alignment of the beam on the ion is fine tuned by a lens mounted on a  $XYZ$  translation stage.

**F-state repump beam:** The 638-nm beam used for the repumping of the metastable  $^2F_{7/2}$  state is produced by an external cavity diode laser and is fiber coupled to the experiment. The laser is not frequency locked, but a small amount of the laser power is directed to a wavemeter through a fiber beam splitter for wavelength monitoring. The beam reaching the trap has a power of  $\sim 2$  mW and a relatively large focused waist. The wavelength is ramped over  $\sim 0.01$  nm with a cycle time of 1 s to ensure resonance.

**Photo-ionisation beam:** The isotope-selective loading is achieved by a 399-nm photo-ionisation laser beam. The beam is produced by an external cavity diode laser and is only active during the loading process. The short-term passive stability of the laser system is adequate for the isotope selective photo-ionization. The wavemeter is used to monitor and set the wavelength to seven digits. The power of the laser's output beam after a 30-dB isolator is  $\sim 8$  mW, and 80% of that goes to the experiment through free space. The power

of the beam is attenuated using a manual optical attenuator. The beam enters from the north side of the trap and is nearly perpendicular to the atomic beam coming from the oven to minimize Doppler broadening. The beam is also only focused with a cylindrical lens in the vertical direction to reduce scatter from the trap rods. Note that a high-power UV beam produced by a frequency-doubled Titanium-Sapphire laser system is also used to assist the loading and maintenance of large ion strings. The high power UV beams from the Ti-Sapph. laser are mainly used in resolved sideband cooling and thermometry and are described in detail in Chapter 7.

As part of a daily routine, the output UV power of the 369-nm beam, and the output power of all the fiber couplers are optimized before the loading process. Once the ions are loaded, the 369-nm and 935-nm beams are aligned on the ions in preparation for experiments.

The next chapter is focused on the experimental results of the KZM studies, where we investigate the defect formation, the power law-dependence of the number of defects on the quench time, and the post nucleation dynamics of defects.

## Chapter 5

# Experimental Results on KZM in Ion Trap Systems

This chapter is focused on the experimental results of spontaneously nucleated kink-defects and their post-nucleation dynamics. We start with a brief summary of the experimental setup. Then, we show how the presence of non-fluorescing ion(s) in the ion crystal biases the linear-zigzag transition, and hence such cases are excluded from the analysis. We then proceed to the experimental results, starting with an exploration of the occurrence of two different forms of kink and the role of the quench end-point in configurational change and in kink survival probabilities. Then the number of kinks formed as a function of quench rate across the linear-zigzag transition is measured in the under-damped regime of the inhomogeneous Kibble-Zurek theory. We show that the experimental results agree well with molecular dynamics simulations, indicating how losses mask the intrinsic nucleation rate. Afterwards, the observation of a range of kink dynamics is presented including motion and lifetime, and behavioural sensitivity to ion number. Finally, we conclude with a comparison of our results with two other studies performed simultaneous to ours.

### 5.0.1 Summary of the experimental setup

We use a linear Paul trap, operating at a radio frequency (rf) of  $\Omega_T/2\pi = 12$  MHz. Photo-ionization is used to load a pure crystal of 42–43  $^{174}\text{Yb}$  ions, which arrange as a linear string in a trap with an axial secular frequency of  $\omega_z/2\pi = 37.6$  kHz, and transverse frequencies of  $\omega_x/2\pi = 679$  kHz and  $\omega_y/2\pi = 658$  kHz. A single laser beam at 369.5 nm (with axial FWHM of 280  $\mu\text{m}$ ) is used for fluorescence imaging of the ions and for Doppler cooling along all principal axes of the trap. The 369.5-nm laser is linearly polarized at  $6^\circ$  with respect to a 5.9-G magnetic field. A relatively large laser detuning of  $-33$  MHz (1.5 linewidths) is used to suppress the effects of micro-motion on fluorescence and cooling, arising from a non-zero component of the trap rf electric field along the axial direction (up to 2500 V/m at the edges of a 43-ion crystal). With an effective saturation parameter of  $s_{0eff} = 2.7$ , the

estimated cooling rate is uniform to a factor of 2 or better across the crystal with variation primarily at the edges, and the calculated damping time,  $\eta^{-1}$ , is 200–400  $\mu\text{s}$ . The damping rate places the experiment deeply in the under-damped regime for quench rates considered.

To quench the system through the linear-zigzag transition, we apply a transverse dc quadrupolar potential using the trap rods. The quench waveform is linear ( $V(t) = V_f \cdot t/(2\tau_Q)$ ) with a quench end-point of  $V_f = 4.2 - 5.8$  V, a ramp time of  $2\tau_Q = 10 - 70$   $\mu\text{s}$ , and a maximum distortion of 100 mV<sub>pp</sub> after filtering. The quench also incorporates small adjustments to the end-caps and rods to maintain a constant axial secular frequency and to maintain the center of the crystal at the rf null in all dimensions. The linear form of our quench in terms of  $\omega_y^2$  is exactly as assumed in the KZM theory [61], with the one modification that we use an asymmetric ramp across the critical point. For example, in a string of 42 ions with  $\omega_z/2\pi = 37.6$  kHz where the critical transverse frequency at the center of the crystal is  $\omega_{0y,c}/2\pi = 619(3)$  kHz (or equivalently,  $0.92(6)$  V)<sup>1</sup>. Our quench starts at 658 kHz ( $V_i = 0.0$  V), which ensures a sufficiently linear configuration, and continues further past the critical point, for example to 414 kHz ( $V_f = 4.8$  V) to involve about half of the crystal in the zigzag phase<sup>2</sup>.

Each experimental run begins with 53 ms of cooling in the linear configuration, followed by the quench. Images of the initial linear and subsequent zigzag configurations are recorded with an exposure time of 3 ms. A 200- $\mu\text{s}$  ramp recycles the crystal to the linear structure. Data is acquired in batches of 100–700 runs over 3 minutes. Our data sets contain 80% of runs approximately equally divided between 42 and 43 ions with 41 or fewer ions in the remainder. Image analysis is used to identify the locations of any kinks in the zigzag structure.

## 5.0.2 The effect of a central non-fluorescing ion

Having two equally probable symmetry-broken configurations is the key feature of the linear-zigzag transition that allows the formation of defects in ion-trap crystal. The two symmetry-broken configurations are differentiated by the sign of the transverse displacement for even and odd numbered ions in a linear array. We assume that in the "zig" configuration, assigned a zigzag symmetry sign of  $S = +1$ , the odd numbered ions shift up and the even numbered ions shift down (Fig. 5.1(b)), and in the "zag" configuration, assigned a zigzag symmetry sign of  $S = -1$ , the ions shift oppositely (Fig. 5.1(c)).

The presence of a non-fluorescing ("dark") ion in the center of the crystal, biases the zigzag into one of the symmetry-broken states. The dark ion could be a <sup>174</sup>Yb ion that has temporarily transitioned to a non-fluorescing low lying F-state, or it could be a molecular

<sup>1</sup>The observed value of  $\omega_{0y,c}$  is slightly higher than expected (1%), roughly consistent with measured axial anharmonicity vs. ion number, and is accounted for in simulations by a shift in  $\omega_z$

<sup>2</sup>We note that the soft-mode frequency at quench start is larger than the KZM freeze-out value. Simulations of quenches starting at higher transverse frequency (883 kHz) give quantitatively similar kink numbers to those observed.



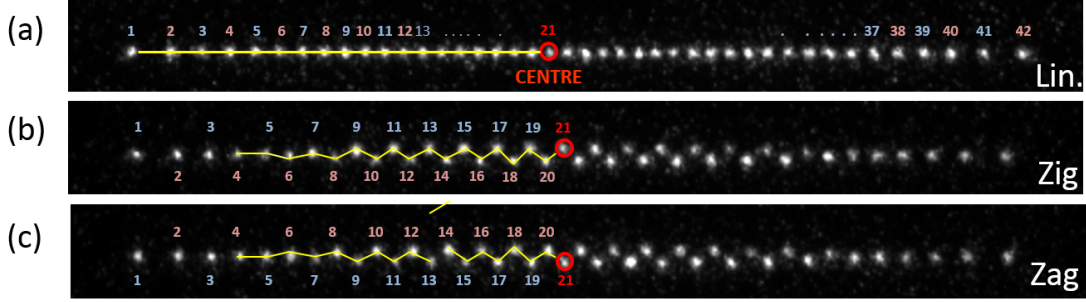


Figure 5.1: Experimental CCD images of 42  $^{174}\text{Yb}$  ions. (a) A linear structure. (b) A zig configuration, in which the odd-numbered ions shift up and the even-numbered ions shift down. (c) A zag configuration, in which the even-numbered ions shift up and the odd-numbered ions shift down

ion (e.g.  $\text{YbH}^+$ ) formed from a collision with a background gas atom. In either case, the primary cause of the bias in the zigzag structure is expected to be the differential laser radiation pressure force from the Doppler cooling beam. (As a separate effect a different mass ion in the center of the crystal will also cause the critical point to shift due to a pseudopotential effect.)

Figures 5.2(a) and (b) show a sample of time sequence of the zigzag orientation for 700 successive runs of a linear-zigzag quench, along with the number of dark ions present in the crystal. To understand the effect of dark ions on the zigzag structure, a selection of images for runs involving 1-2 dark ions (runs shown by red arrows in Fig. 5.2(a)) are presented in Figs. 5.2(c)–(g). Point (c) in Fig. 5.2(a) represents the case of a single dark ion that does not bias the zigzag orientation. Figure 5.2(c) shows that the dark ion is located closer to the edges of the crystal. Unlike point (c), at point (d) the presence of a single dark ion biases the zigzag structure into the zag configuration ( $S = -1$ ). Figure 5.2(d) shows that, in this case, the dark ion is located closer to the center of the crystal. Points (e) and (f) represent the cases of two dark ions in the crystal (see Figs. 5.2(b), (e) and (f)), resulting in a bias in the zigzag structure into the zag and zig configurations, respectively. Finally, point (g) shows another case of a single ion located close to the center of crystal, but this time leading to a bias into the zig configuration ( $S = 1$ ). Figures 5.2(c)–(g) indicate that the presence of the dark ion in the center of the crystal, where the zigzag structure is first born, results in a configuration in which the dark ion is shifted \*up\*. Depending on the site occupied by the dark ion, this preference can bias the structure into one of the two configurations (compare Figs. 5.2(d) and (g)). When the dark ion is farther from the center, it does not affect the configuration (see Figs. 5.2(a) and (d)). In the presence of two dark ions, the one closer to the center seems to dictate the preferred configuration (compare Figs. 5.2(e) and (g)).

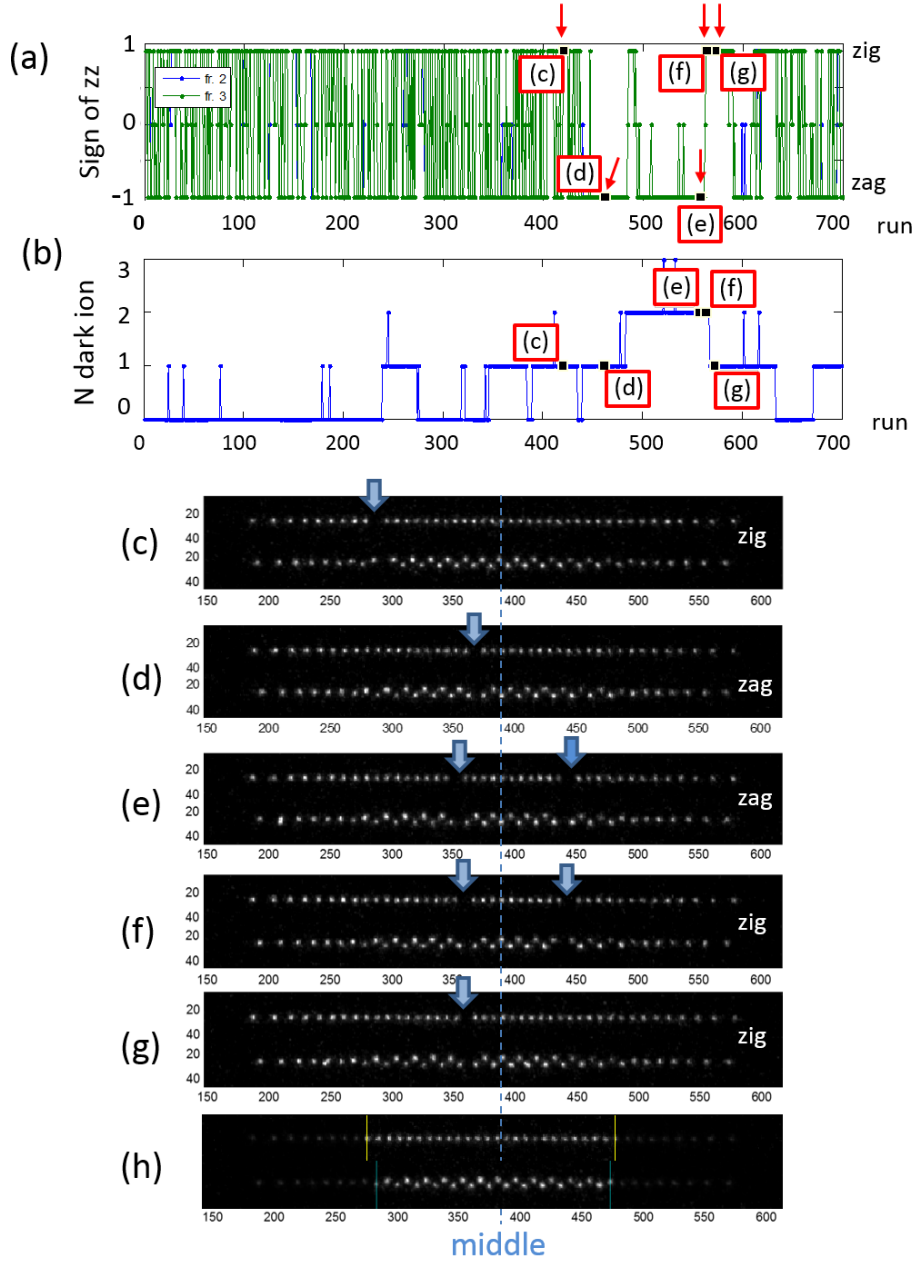


Figure 5.2: (a) Orientation (sign) of the zigzag structure and (b) number of dark ions present for a sample sequence of successive quenches. A zigzag sign of 0 corresponds to an indeterminate case in image analysis. (c)–(g) Images of the ion crystal corresponding to selected runs in the quench sequence. Each pair of images shows the ion crystal before and after the quench. The locations of dark ions in the initial linear crystal are indicated by arrows. (h) The central dark-ion exclusion region. The runs with dark ion(s) in this region are excluded from analysis. Note that the horizontal axis is in pixels, and  $1 \text{ pixel} \simeq 0.7 \mu\text{m}$ .

Due to hopping events, the site of the dark ion can change over time, resulting in a different bias. To assess effects of zigzag bias we check the deviations from run-to-run randomness by calculating the autocorrelation of the zigzag sign  $S$  for a time sequence of quenches:

$$c_k = \sum_j S_j S_{j+k}, \quad (5.1)$$

where  $j$  is the index of the run. Figure 5.3(a) shows the calculated normalized autocorrelation for all measurements on a given day. The files with dark ion(s) in the central part of the crystal have a significant positive temporal autocorrelation on adjacent runs. Only  $\sim 15\%$  of our data is contaminated with a dark ion in the zigzag region. The obvious bias in the zigzag configuration due to the dark ion suppresses the defect nucleation and can affect the statistics of the results. Therefore, in our analysis we exclude the runs with dark ions within the zigzag region ( $\pm 70\mu\text{m}$  around the center.) See Fig. 5.2(h) for the visualization of the dark-ion exclusion region. Excluding these cases, the temporal statistics of the two symmetry-broken phases is nominally random with a bias of  $\leq 1\%$  and a normalized binary autocorrelation on adjacent runs of  $\leq 1\%$  (see Fig. 5.3(b)).

Having a random distribution of the two possible configurations, we next investigate the types of defects and their axial distribution in the crystal as a function of the quench end-point.

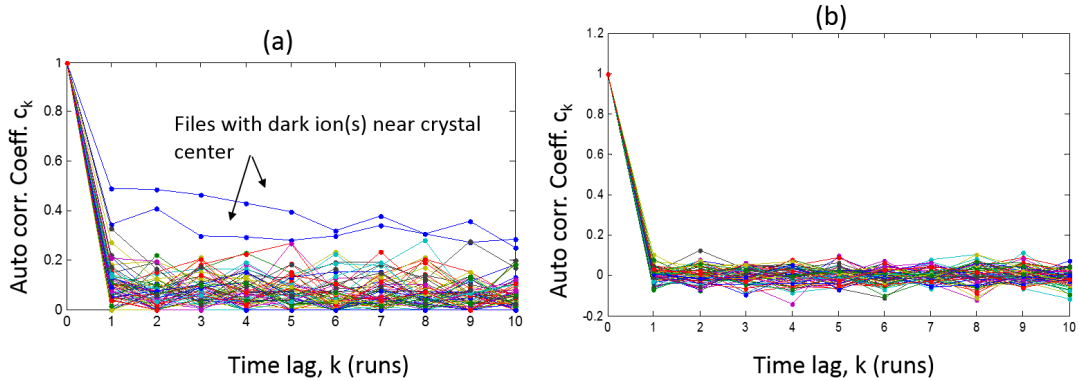


Figure 5.3: (a) The run-to-run autocorrelation of the zigzag orientation. A clear positive autocorrelation between adjacent sites can be observed in the files with dark ion(s). (b) The run-to-run autocorrelation after excluding the dark-ion contaminated runs in each file.

## 5.1 Different types of kinks

In the first experiment, we explore the formation of two types of kink [59]: discrete kinks, which are localized to about 3 ion-sites (see Figs. 5.4(a) and (d)), and extended ones, which involve more sites and occur in crystals brought far into the zigzag region (see Figs. 5.4(b),

(c), and (e)). The shape of the extended kink and the number of involved sites varies deeper into the zigzag (compare Figs. 5.4(b) and (c)). A sample of two discrete kinks and two extended kinks are also shown in Figs. 5.4(d) and (e). The occurrence of two discrete kinks is very rare in our results: In a crystal of the size of 42-43 ions and for the quench ranges we use, more than one kink is only observed after fast quenches ( $2\tau_Q \leq 15\mu\text{s}$ ). Two extended kinks were only observed when the size of crystal was increased to more than 50 ions, which is outside the range of data presented in subsequent sections.

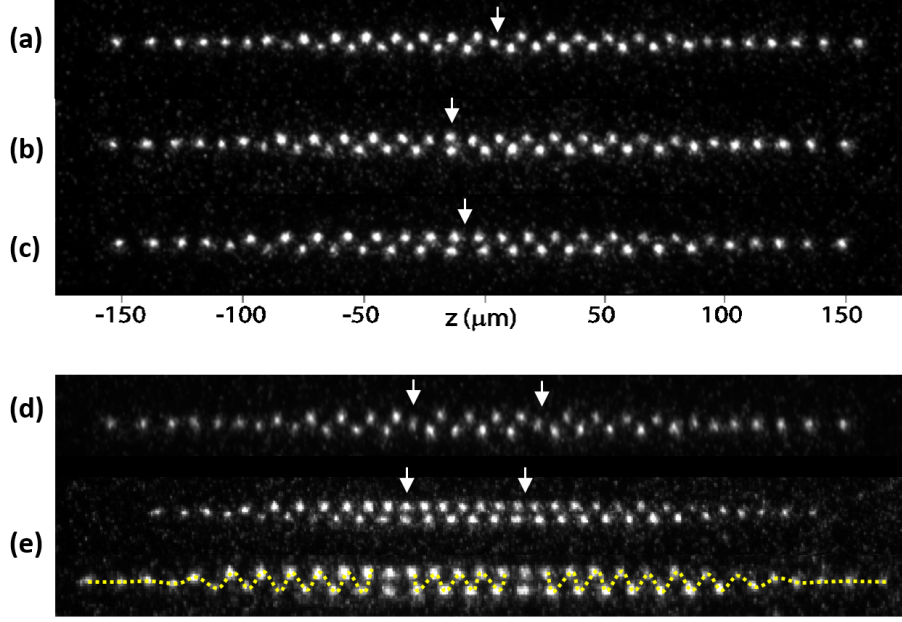


Figure 5.4: (a)-(c): Images of crystals of 42  $^{174}\text{Yb}$  ions in zigzag configurations with (a) a single discrete kink (indicated by arrow) and (b), (c) a single extended kink. The axial trap frequency for all images is  $\omega_z/2\pi = 37.6$  kHz, while the weak transverse frequency  $\omega_y/2\pi$  is (a) 414 kHz, (b) 380 kHz, and (c) 342 kHz. Starting at 0 V the corresponding quench end points  $V_f$  are (a) 4.8, (b) 5.3, and (c) 5.8 V. The imaging system looks at  $45^\circ$  to the transverse  $y$  axis where the zigzag displacement occurs. (d) Two discrete kinks (kink and antikink) in a string of 42 ions. (e) Two extended kinks in a string of 51 ions. In the lower panel, the zigzag domains are traced with dotted yellow lines to accentuate the location of the kinks in the crystal structure.

Figures 5.5(a)–(c) show the observed axial distribution of both kink types and their total numbers as a function of the quench end-point,  $V_f$ . The data, for 41–43 ions, is taken at a constant ramp rate of  $0.19$  V/ $\mu\text{s}$  so that the nucleation dynamics near the critical point is expected to be same. Any differences are due to post-nucleation dynamics during the remainder of the ramp through to detection. To understand the outcome of the experiment, we have performed molecular dynamics simulations with no free parameters. The ion trap is treated as an ideal harmonic potential limited to two dimensions. The

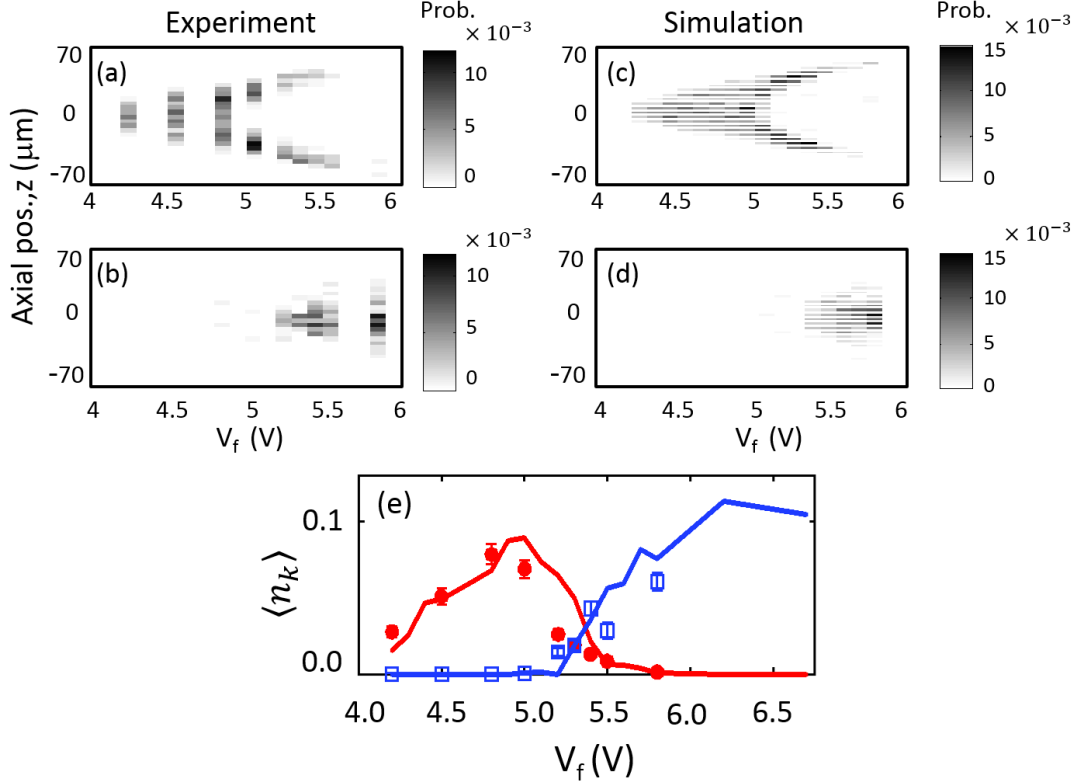


Figure 5.5: Observed axial position distribution of (a) discrete and (b) extended kinks versus quench end-point. All data taken at a quench rate of  $0.19 \text{ V}/\mu\text{s}$ . Simulation results of axial position distribution of (c) discrete and (d) extended kinks at the same quench rate as experiment. (e) Average number per run of discrete kinks (red circles) and extended kinks (blue squares) for distributions in (a) and (b). Data points, for 41-43 ions, include 1000-2200 runs. Errors calculated assuming binomial statistics. Lines are a simulation for 42 ions with no free parameters, and shown 2 ms after the quench,  $2/3$  of the camera exposure time. Statistical uncertainties in simulation comparable to experimental ones shown.

small axial anharmonicity in the experiment is modeled in an effective way by shifting the axial frequency from 37.6 to 38.2 kHz. The effect of the Doppler cooling laser is modeled explicitly [39] and includes the steady-state fluorescence behaviour of  $^{174}\text{Yb}^+$  and all laser calibrations [147]. Simulations for 42 ions reveal similar distributions (see Figs. 5.5(c) and (d)). There is also a good qualitative match in the numbers of discrete and extended kinks between simulation and experiment (see Fig. 5.5(e)). From the simulations, we find that discrete kinks are nucleated in the central 5-10 sites of the crystal shortly after the critical point is first crossed. Then, there is an outward motion and loss of the discrete kinks, propelled by the gradient in zigzag amplitude and axial density, and enhanced by the added kinetic energy due to the quench. Figure 5.6 shows the axial and transverse kinetic energy

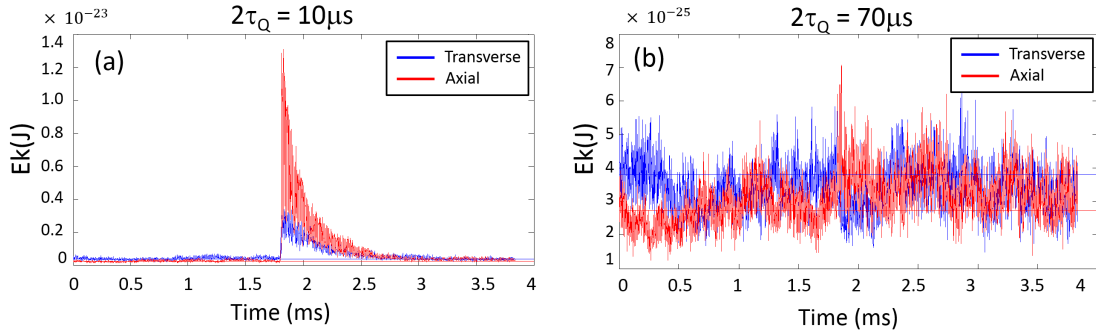


Figure 5.6: Simulation: The axial kinetic energy (red) and transverse kinetic energy (blue) as a function of time in a (a) fast  $2\tau_Q = 10 \mu s$  quench and (b) a slow  $2\tau_Q = 70 \mu s$  quench. Only for the fast quench can a large spike and fast oscillations in the kinetic energy be seen starting at 1.8 ms, where the quench occurs. The energy is primarily added to the axial direction via excitations of the axial breathing mode. In the zigzag phase, the average kinetic energy along both dimensions approach the same value.

for a fast  $10 \mu s$  and a slow  $70 \mu s$  quench. In the fast quench, a large spike in the kinetic energy can be seen at the time that the ramp starts. This is due to the effect of the impulsively excited zigzag mode and, more importantly, axial breathing mode that causes a modulation in the transverse zigzag structure as the crystal stretches and compresses. As the quench end-point increases towards 5.0 V, the mean number of discrete kinks and the width of their distribution increase since more of the dispersing kinks are trapped in a deeper and wider zigzag region. Above 5.0 V, the number of discrete kinks collapses when, as seen in the simulation, those at the center of the crystal distort to extended form (Fig. 5.7). Extended defects can also migrate to the center, leading to the well-centered distribution observed in the experiment (Fig. 5.5(b)). This is understood to be caused by a confining potential for the extended defect created by the inhomogeneous zigzag structure deep in the zigzag phase [159]. Due to reduced losses, the mean number per run of extended kinks in the simulation saturates at a value 1.4 times higher than the peak in the mean number of discrete kinks. The experiment data ends at 5.8 V, well before the  $\sim 7.1$ -V onset of another structural transition to a different 2-D configuration. As this transition is approached, we see an enhancement in (otherwise negligible) background kink nucleation, due to energy transfer events such as background-gas collisions.

Understanding the role of quench end-point sets the stage for our nucleation studies, which are as a function of the complementary variable of quench time. The results of Fig. 5.5 motivated the choice of quench end-point of  $V_f = 4.8$  V for nucleation studies with discrete kinks, presented in the next section.

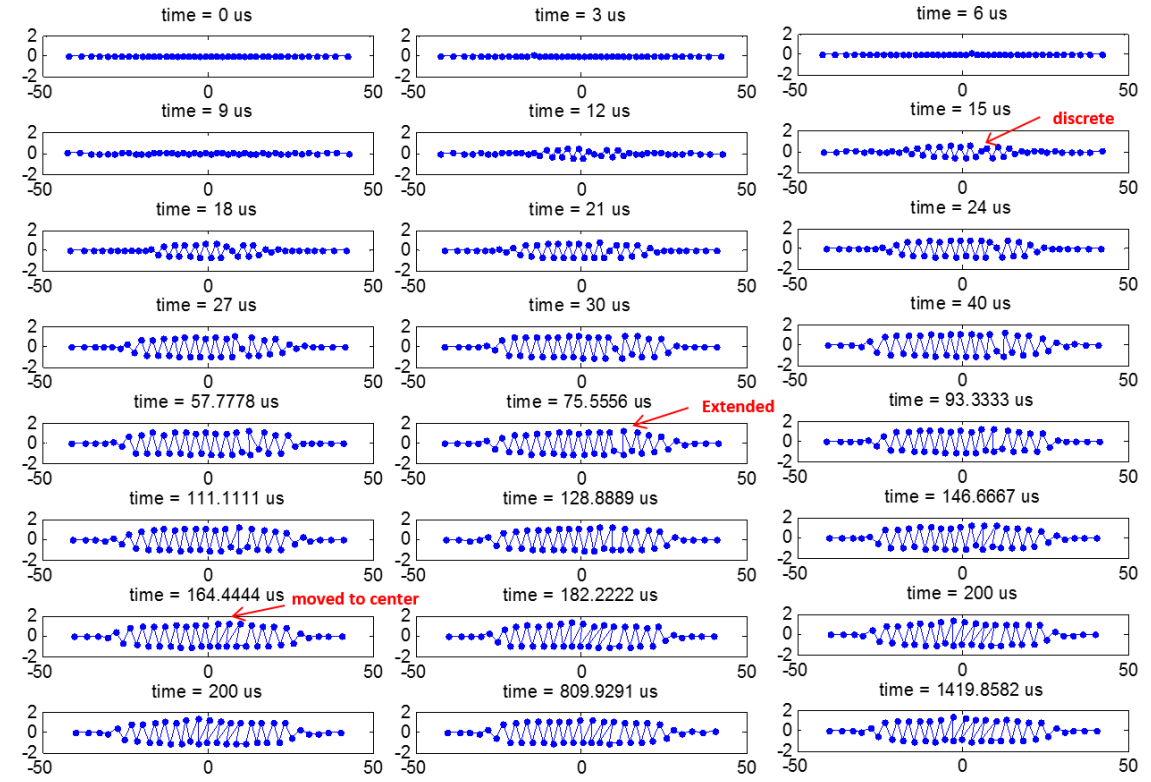


Figure 5.7: Simulation frames showing nucleation of a discrete kink, and the evolution after nucleation into an extended kink, and migration of the extended kink to the center. Simulation is at  $V_f = 5.8$  V ( $\omega_y/2\pi = 342$  kHz).

## 5.2 Probability of kink generation vs. quench rate

### 5.2.1 Experimental measurement of number of kinks vs. quench rate

With an eye towards subsequent dynamics studies, we work with discrete kinks and operate at  $V_f = 4.8$  V, where their maximum number is detected. The quench time varies over the range of  $2\tau_Q = 10 - 70 \mu\text{s}$ . Figure 5.8(a) shows a log-log plot of the average number of kinks detected per run (black triangles) as a function of the scaled rate,  $1/(\omega_z \cdot 2\tau_Q)$ . Data for 41-43 ions is combined and includes 1000-5000 runs. Error bars are calculated assuming a binomial distribution, which is approximately consistent with fluctuations.<sup>3</sup>

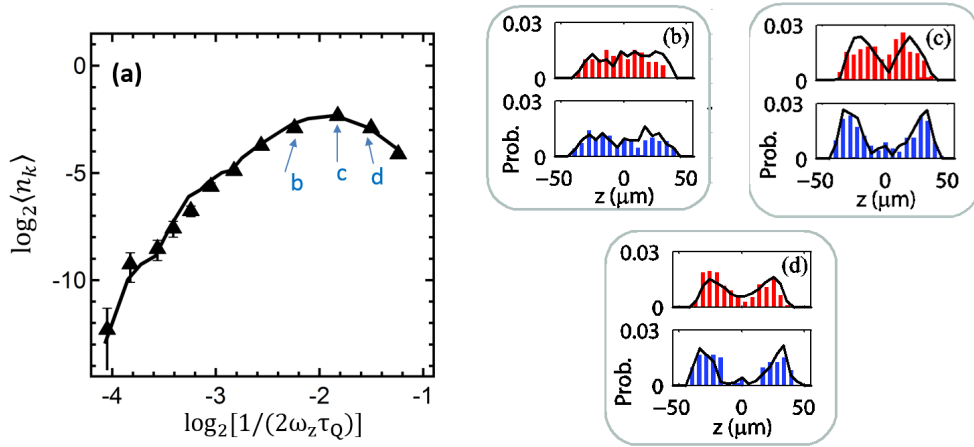


Figure 5.8: Experiment: (a): Average number of kinks observed per run vs. scaled quench rate for standard trap with  $\omega_z/2\pi = 37.6$  kHz (triangles). Data for 41-43 ions include 1000-5000 runs. Error bars are calculated binomial, approximately consistent with fluctuations. Solid line is a molecular dynamics simulation with parameters including  $\omega_z/2\pi = 38.2$  kHz (see text), and shown 2 ms after the quench. Statistical uncertainties of simulation less than or equal to the experiment. (b)-(d): Observed position distributions of kinks for 42 ions (red, upper) and 43 (blue, lower) in standard trap at quench time  $2\tau_Q$  of (b) 20, (c) 15, and (d) 12  $\mu\text{s}$  with simulations (lines) for comparison.

As the quench rate increases from  $1/(\omega_z \cdot 70\mu\text{s})$ , the number of kinks grows, peaks at  $1/(\omega_z \cdot 15\mu\text{s})$ , and begins to drop after that. Figure 5.8(a) also includes results of molecular dynamics simulation, performed as described above. The simulation (solid black line) shows the number of kinks 2 ms after the end of the ramp ( $2/3$  of the exposure time in the

<sup>3</sup>The use of errors estimated from a binomial distribution is entirely sufficient for the data presented. The only situation where multiple kinks are relevant is for the fast quench region, which are rare indeed. We have checked the fluctuations, and they match reasonably well to binomial statistics, within about a factor of 2 in the case of fast quench points. For the fast quenches, the error bars are already smaller than the data symbols. For the slow and medium quenches where the error bars are significant, single-kink nucleation dominates and binomial errors are suitable.



experiment), by which time the kink number has stabilized. The simulation matches the number of kinks observed in the experiment extremely well, and reproduces features in the observed kink distributions, related to rapid post-nucleation dynamics (Figs. 5.8(b)–(d)). The detected number of defects formed as a function of quench rate does not follow a power-law scaling over the quench range shown. This is mainly due to kink losses by the 3-ms detection time. To understand the effect of losses before detection in the experiment, we next use the simulation to assess the dynamics at early times, including during the ramp.

## 5.2.2 Determining the effect of losses from simulation

In this section we investigate the effect of losses using the simulation results. All the presented plots in this section are from simulations.

Finding the number of nucleated kinks at "early times" in the simulation requires extra caution, since at early times the amplitude of the symmetry-broken state is still small and approaching the amplitude of thermal and/or dynamical excitations. In principle, one should consider kinks when the symmetry-broken state is some factor larger in size than the fluctuations. The challenge is that the larger the factor, the longer one must wait for the zigzag amplitude to grow, and so the more time there is for the kinks to escape. This is an issue of the inhomogeneous system and particularly bad for slow ramps where the front grows very slowly outward after the kinks have been formed. We use a number of filtering processes on the simulation results to find the estimate of kink numbers before loss. To suppress the counting of thermal fluctuations, kinks are counted at early times only inside a region of sufficiently large zigzag amplitude ( $0.15a_y$ ). This value is determined in part from a consideration of the amplitude of thermal fluctuations in the initially linear string ( $0.03a_y$ ) and the amplitude of zigzag fluctuations following the ramp (maximum of  $0.2a_y$  at the edges of the zigzag region for the fastest ( $10 \mu\text{s}$ ) quenches). At the same time, to tidy up fluctuations on the edges of the crystal, a cut is also made based on the ion site, in which kink-counting is limited to an inner region of the crystal, and the 9 outer ion-sites on each side are excluded. Samples of the kink filtering process for a fast  $10\text{-}\mu\text{s}$  quench and a slow  $70\text{-}\mu\text{s}$  quench with an end-point of  $V_f=4.8 \text{ V}$  are shown in Figs. 5.9(a) and (b), in which the results of  $> 10$  simulation runs are overlaid in each plot. Following the filtering, the number of kinks as a function of time for different quench times are presented in Fig. 5.9(c). Typical behaviour shows a rise in the proto-kink number during the first part of the ramp, then a decay over  $\sim 20\text{--}1000 \mu\text{s}$ , followed by a very slow decay above 1 ms. Depending on the quench rate the behaviour is somewhat different as follows:

- 1 – Slow ramps produce fewer kinks as expected, and as seen in the experiment.
- 2 – Very fast ramps ( $2\tau_Q < 20 \mu\text{s}$ ) show anomalously high loss, presumably due to excitation of the axial breathing mode. The associated additional kinetic energy in the system is eventually removed by laser cooling. The kink decay rate over 100's of microseconds in Fig. 5.9(c) (e.g. for  $2\tau_Q = 10\mu\text{s}$ ) is presumably related to the cooling time constant

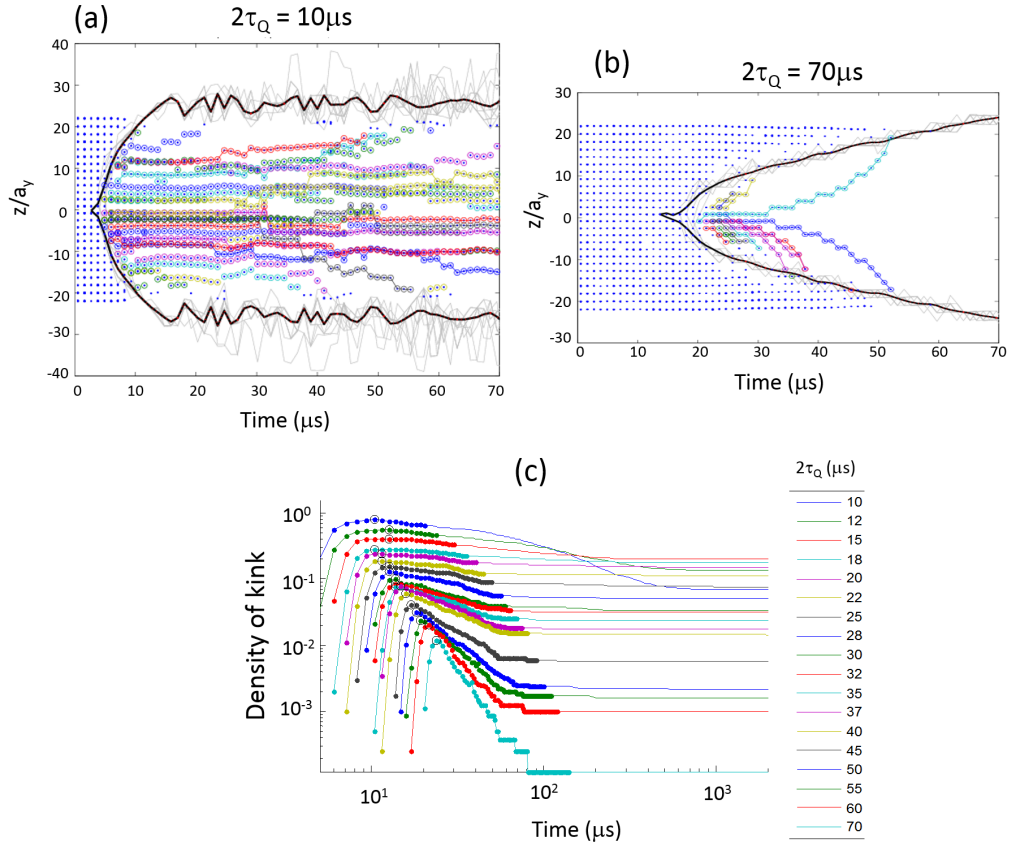


Figure 5.9: Simulation: The selected kinks at early times after (a) a fast quench ( $2\tau_Q = 10 \mu\text{s}$ ) and (b) a slow quench ( $2\tau_Q = 70 \mu\text{s}$ ). The quench begins at  $t = 0$ . Color-coded points show identified trajectories. The blue points are potential kinks rejected by the filtering process. The grey lines show the edges of the zigzag region for individual simulation runs. The black line indicates the averaged zigzag edge defined by  $0.15a_y$  used to window the valid kinks. The outer 9 ion-sites on each edge are also excluded. (c): The density of kinks as a function of time for different quench rates.

( $\eta^{-1} = 200 - 400 \mu\text{s}$ ).

3 – For the 20 – 70  $\mu\text{s}$  ramp times, short-term loss of kinks (over  $< 100 \mu\text{s}$ ) is observed with an increasing decay rate at slower ramps (see Fig. 5.9(c)). This is not due to the excitation of the axial breathing mode. The decay times are too short to be related to cooling, and at longer ramp times, excitation of the axial breathing mode becomes negligible. From the simulations, it appears that the short term loss is simply related to kinks leaving the zigzag region early in the ramp when the zigzag region is still small. At the same time, it is not even clear how "real" such kinks are given that the zigzag amplitude has not yet increased to a large size before they leave.

To reject suspect counts at very early times, we added another layer of filtering to the kink-counting in the simulation. There is a minimum time that does arise from the KZM:

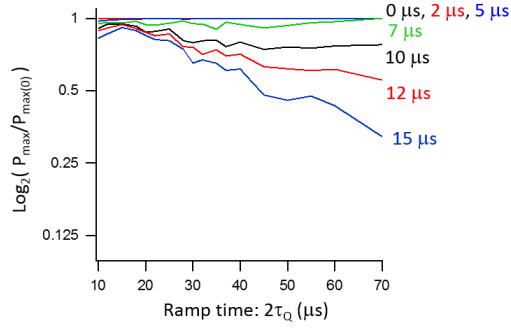


Figure 5.10: Simulation: The effect of a delay in counting on the maximum number of counted kinks as a function of quench time. We chose a  $7\mu\text{s}$  delay time. The plots are shown for a threshold on zigzag amplitude of  $0.15a_y$ .

one could argue that one should only count after the freeze-out time, which is  $1\mu\text{s}$  for fast quenches ( $10\mu\text{s}$ ), and  $2\mu\text{s}$  for slow quenches ( $70\mu\text{s}$ ). Although the threshold of  $0.15a_y$  ( $\sim 0.54\mu\text{m}$ ) already isolates longer lived defects, we restricted the counting of kinks to  $7\mu\text{s}$  after the first arrival of the front at the crystal center. Figure 5.10 shows that in the end, the  $7\mu\text{s}$  delay time has a very small effect on the maximum number of counts compared to no delay. The final results for the early counts in the simulation is shown as the black dashed line in Fig. 5.11.

### 5.2.3 Comparison to the IKZM predictions

In summary, we found that at fast quenches, there is enhanced loss due to the non-adiabatic excitation of vibration modes, and before the crystal is re-cooled. Kink-pair annihilation also plays a minor role. At slow quenches, we again see a loss of kinks, which worsens with decreasing quench rate. In this case, the zigzag region expands too slowly to trap the kinks, and they escape to the zigzag edges during the quench. Although kink losses in the experiment mask the intrinsic nucleation rate – see, however, [8, 118] – we comment briefly on the power-law scaling for the simulation and experiment.

Figure 5.11 covers about three octaves in quench rate separated by  $\log_2(1/2\omega_z\tau_Q) = -3.1$  and  $-2.1$  (yellow region). The KZ theory [8, 61] suggests that our data covers two regimes of nucleation: For the slow-quench range, we expect a DIKZM power law of  $8/3 = 2.67$ , which agrees with the fit value of  $2.5(2)$  for the early-counted simulation (with significant systematic error associated with rapid losses). For the fast-quench range, where the nucleation region is large enough that the nucleation of two or more kinks becomes significant in the simulation, one expects to cross over towards the IKZM power law of  $4/3 = 1.33$ . The early-counted simulation gives a fit value of  $1.7(1)$ . We note that all cases of two kinks observed in the experiment [Fig. 5.4(d)], albeit rare, occur in the fast-quench region.

Finally, in the middle octave of quench rate, where the kink losses are least, a fit to the *experimental* data gives a power law of 3.3(2), compared to the early-counted simulation value of 2.0(1). For comparison, we have also studied kink nucleation in a trap with all secular frequencies reduced by a factor of 2 (orange triangles in Fig. 5.11). Overall, the data match the results at higher trap frequency, which shows the weak sensitivity of nucleation and losses to effective cooling rate,  $\eta/\omega_z$ , over such variations, except perhaps for losses at the fastest quenches. The overall weak sensitivity shown also supports ignoring small (spatial) variations in cooling, corroborated by good agreement with simulations neglecting them. Note the cooling beam is also larger for this experiment.

Of several possibilities to reduce losses in our experiment, we note that an increase in ion number can help, particularly for slow quenches by reducing the crystal inhomogeneities that transport kinks outward. We performed a simulation of 84 ions with optimized Doppler cooling (detuning -11.3 MHz,  $s_0 = 2.0$ ) and with  $\omega_z/2\pi = 20.6$  kHz, chosen to match the transverse critical frequency for 42 ions at crystal center. As shown in Fig. 5.11, a doubling of the ion number (and using twice better cooling) already leads to a significant reduction in losses over the same quench range, albeit in a scaling regime closer to IKZM.

### 5.3 Kink dynamics

Finally, we investigate the dynamics of single discrete kinks, and measure their axial motion in the crystal and their lifetime. The experiments are performed at  $V_f = 4.8$  V and  $2\tau_Q = 20$   $\mu$ s, for which the initial distribution of the kinks is relatively uniform (Fig. 5.8(b)). Ten pictures, with a read-out limited frame rate of  $(40 \text{ ms})^{-1}$ , are taken using the CCD camera. Figures 5.12(a) and (b) show the trajectories of kinks in crystals of 42 and 43 ions for three initial axial positions: the center site and four sites away on either side. The kinks move between sites corresponding to local potential wells separated by the axial lattice spacing ( $5.6 \mu\text{m}$ ) [160]. The 40-ms frame separation of our camera does not permit us to resolve fast dynamics, including the motion between sites. Nevertheless, it can be seen that, for 42 ions, most of the kinks that begin at the center of the crystal either stay there or move by one site. In comparison, the central kinks in a string of 43 ions migrate to the edges faster. For both cases, kinks closer to the edges tend to move outwards, as expected. Samples of raw images showing the kink trajectories are shown in Figs. 5.13 and 5.14. To calculate the lifetime of the kinks as a function of their initial position, the survival time  $t_i$  of each kink is obtained by tracking it through the 10 CCD frames over 0.4 s. The lifetime is then obtained from a maximum likelihood estimate to the set of survival times. The method includes the effect of the camera readout time that limits the time between CCD frames to  $\Delta t = 40$  ms. We calculate the likelihood for measuring  $N$  kinks having survival time  $t_i$  with  $m$  in the final frame at  $t = T_f$ , and assuming that the decay rate of the kinks

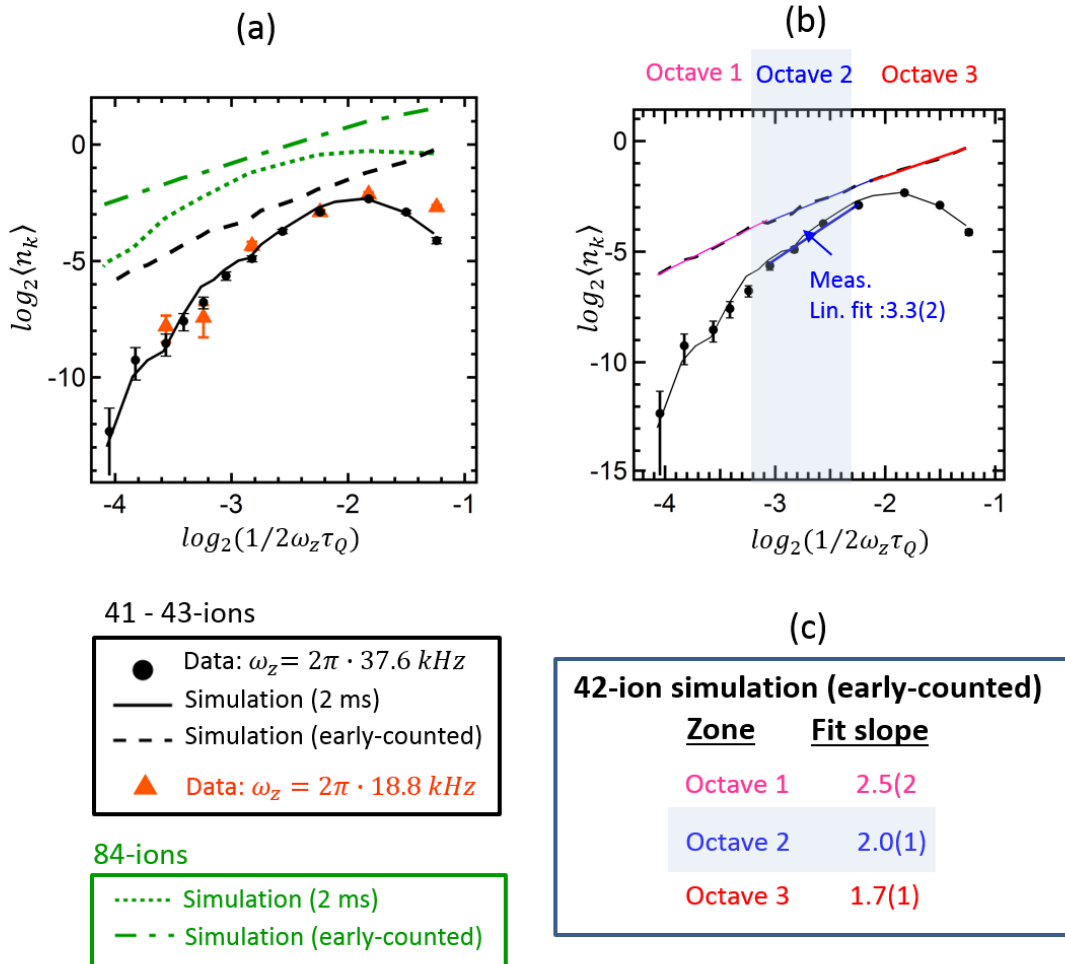


Figure 5.11: Experiment: (a): Average number of kinks observed per run vs. scaled quench rate for standard trap with  $\omega_z/2\pi = 37.6$  kHz (black circles), and for one with secular frequencies reduced by 2 (orange triangles) with quench changed accordingly. The solid black line is a molecular dynamics simulation with parameters including  $\omega_z/2\pi = 38.2$  kHz (see text), and shown 2 ms after the quench. The dashed black line is the same simulation with "early counted" kinks. Dotted and dash-dotted lines (green) show kink number 2 ms after quench and shortly after nucleation, respectively, for a simulation of 84 ions with optimized Doppler cooling (detuning -11.3 MHz,  $s_0 = 2.0$ ) and with  $\omega_z/2\pi = 20.6$  kHz, chosen to match the transverse critical frequency for 42 ions at crystal center. The simulation plot is scaled using  $\omega_z/2\pi = 38.2$  kHz for direct comparison to 42 ions. (b): The blue region,  $\log_2(1/2\omega_z\tau_Q) = [-3.1, -2.1]$ , divides the plot into three octaves of quench rate. Shown are linear fits in each of the three octaves for a string of 42 ions to extract power-law scaling. The linear fit to the experimental measurements at  $\omega_z/2\pi = 37.6$  kHz in the middle octave gives a power-law exponent of 3.3(2) (c): Table of slopes obtained from linear fits to early-counted simulations of 42-ion (shown in b) and 84-ion strings (not shown).

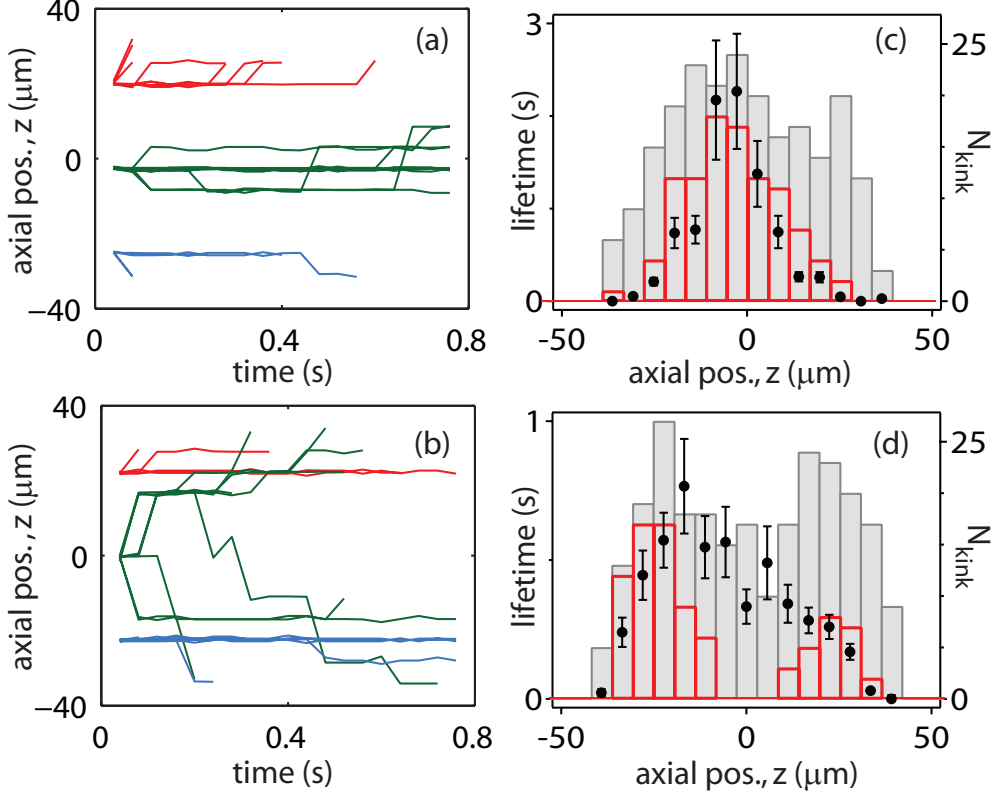


Figure 5.12: (a), (b): Axial trajectories of discrete kinks in zigzag crystals ( $V_f = 4.8$  V) with (a) 42 and (b) 43 ions for three different initial positions: center and four sites away on both sides. The number of trajectories for each case is 11 with fewer for  $z < 0$ . (c), (d): Exponential lifetime of kinks (filled circles) vs. initial position in crystals of (c) 42 and (d) 43 ions. Lifetimes and their uncertainties obtained from a maximum likelihood estimate including binning due to camera frame rate. Also shown are axial position distributions at  $t = 0$  ms (filled gray bars) and  $t = 400$  ms (open red bars).

are exponential, as follows:

$$\mathcal{L} = \prod_{i=1}^{N-m} e^{-t_i/\tau} (1 - e^{-\Delta t/\tau}) (e^{-T_f/\tau})^m. \quad (5.2)$$

The lifetime,  $\tau$ , is then found from the maximum likelihood estimation ( $d \ln \mathcal{L} / dt = 0$ ). In Figs. 5.12(c) and 4(d), we show the exponential lifetime of kinks as a function of their initial position as well as the distributions of kink positions at  $t = 0$  s (first frame) and  $t = 0.4$  s (last frame). In Fig. 5.12(c), we can see that the lifetime of kinks for 42 ions is highest near the middle of the crystal, and decreases roughly symmetrically towards the edges. Losses due to the position-dependent lifetime largely account for the observed time evolution of the position distribution. The maximum  $\sim 2$  s lifetime is likely limited by background-gas collisions, since crystal reordering events detected with a distinguishable dark ion occur

every 2–4 s on average. In Fig. 5.12, for 43 ions, the 0.3–0.5 s lifetime of central kinks contrasts with their complete absence in the position distribution after 0.4 s, and points to their migration away from the deeper zigzag region at the center of the crystal. Simulations show that this is associated with new dynamics in which the kink hops two sites [as observed in Fig. 5.12 center] via a transient deformation into an extended-like form. Asymmetries in the lifetime distributions are likely due to experimental imperfections. The difference between 42 and 43 ions is understandable, considering that the experiment is performed at  $V_f = 4.8$  V, near to the sharp onset of the bimodal distribution in Fig. 5.5(a). Since the zigzag phase begins 0.3 V lower for 43 ions, the onset of the bimodal distribution will also occur at a lower voltage. The longer lifetime of outer kinks for 43 vs. 42 ions and changes in dynamics with ion number and density are interesting and could be explored in a future work.

## 5.4 Comparison to other experiments and conclusion

Three other groups have observed kinks in an ion crystal [8, 118, 159], two of which tested the KZM scaling in ion-trap systems at about the same time as us. The experimental approaches of these groups are somewhat different than ours. Pyka *et al.* [8] also quenched across the transition by weakening the transverse confinement, but chose a farther endpoint that brought the crystal deeper into the zigzag. This helped with reducing the kink losses by forcing a change from discrete into extended kinks, which then transfer to the center of the crystal. Ulm *et al.* [118] quenched across the transition by increasing the axial confinement, and used a shaped ramp function to suppress the excitation of the axial breathing mode. Both of these experiments also have a faster damping rate (fast cooling rate), and so the losses in their systems would be expected to be smaller. The size of the systems used (see table below) along with the range of applied quench rates correspond to the Double KZM region for the other two experiments, whereas our early counted simulation appear to indicate that our experiment stands between DIKZM and IKZM regimes. Pyka *et al.* and Ulm *et al.* both obtained a good match with the DIKZM value of  $8/3$  over a limited quench range. Our experimental result, specified for the lowest loss regime, is  $\sim 1.6 \times$  higher than the pre-loss value obtained from simulations.

Paper	Num. of ions	Max. num. kinks	Fitted exponent
Pyka <i>et al.</i> [8]	$29 \pm 1$	1	$2.68 \pm 0.06$
Ulm <i>et al.</i> [118]	16	1	$2.7 \pm 0.3$
Ejtemaee <i>et al.</i> [145]	$42 \pm 1$	2	$3.3 \pm 0.2$

In regard to kink dynamics, our own experiment is unique in its detailed study of post-nucleation kink dynamics including both spatial and number sensitivities. We note that Mielenz *et al.*, a fourth group investigating kinks in ion traps, has explored in particular

the trapping potential created for extended kinks from both a theoretical and experimental perspective [159].

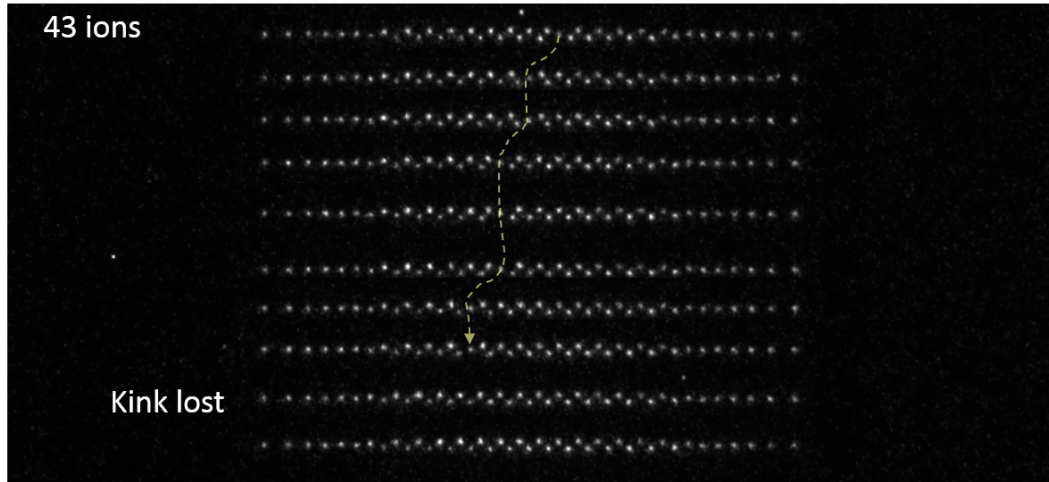
Both of these experiments are solely focused on nucleation measurements coupled with theoretical discussion, whereas our work goes beyond nucleation studies and explores post-nucleation dynamics of discrete kinks including transformation of shape, motion and lifetime in the crystal, and sensitivity of behaviour to unit change in ion number.

While the experimental results of [8, 118] seem to provide reasonable agreement with the KZM prediction, del Campo and Zurek [79] have expressed some concerns about the extent to which the limited data of these three experiments can be regarded as a verification of the KZM. Over and above the experimental issues - the restricted range of quench rates and kink losses - they question the applicability of IKZM theory to small sized ion chains for two reasons. First, the KZM derivation of the inhomogeneous power scaling depends on the size of the nucleation region set by the front propagation, but at the same time simulations indicate that the boundary of the region where kinks are formed is not so sharply defined. If the width of the boundary region were on the order of a domain size, this would have significant implications on the scaling for small systems that span one or few domains at freeze-out. Second, before the predictions of the KZM can be employed, the applicability of the thermodynamic approximation, used to derive the critical exponents that define the universality class of the system, needs to be justified.

To conclude, we have studied the spontaneous nucleation and post-nucleation dynamics of kinks formed as a result of fast quenches across the linear-zigzag transition in trapped-ion crystals. We measured the number of nucleated kinks as a function of quench rate, and have shown how losses mask the intrinsic nucleation rate. To address the issues brought up by del Campo and Zurek, the future direction of this type of experiment are towards many ions, with multiple domains and several kinks. We expect that a shallower quench preserving the discrete, localized character of kinks offers the best shot at reducing losses due to kink interaction and annihilation in larger ion crystals in a linear Paul trap. We have also pointed out how increasing the number of ions can help to expand the range of quenches where loss is reduced. We have also studied the post-nucleation dynamics of kinks, and have observed long lifetimes, which may allow future explorations of internal kink dynamics [59]. A natural future direction is the study of linear-zigzag dynamics in the quantum regime [57], which is the direction pursued in the remainder of this thesis.



**(a) Typical departure**



**(b) Unusual departure (back and forth motion)**

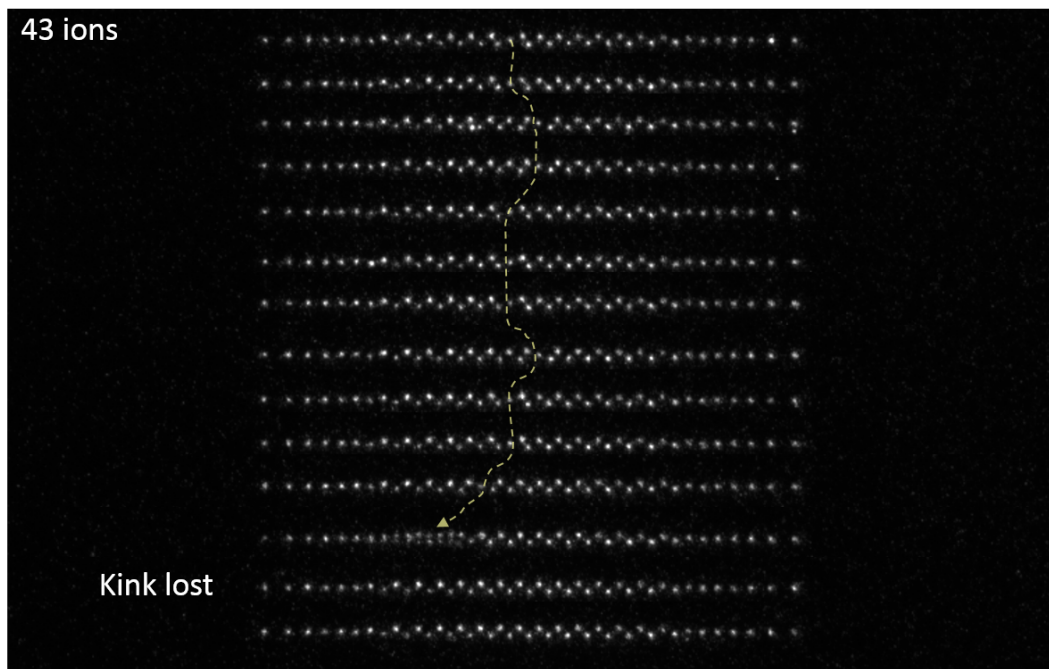
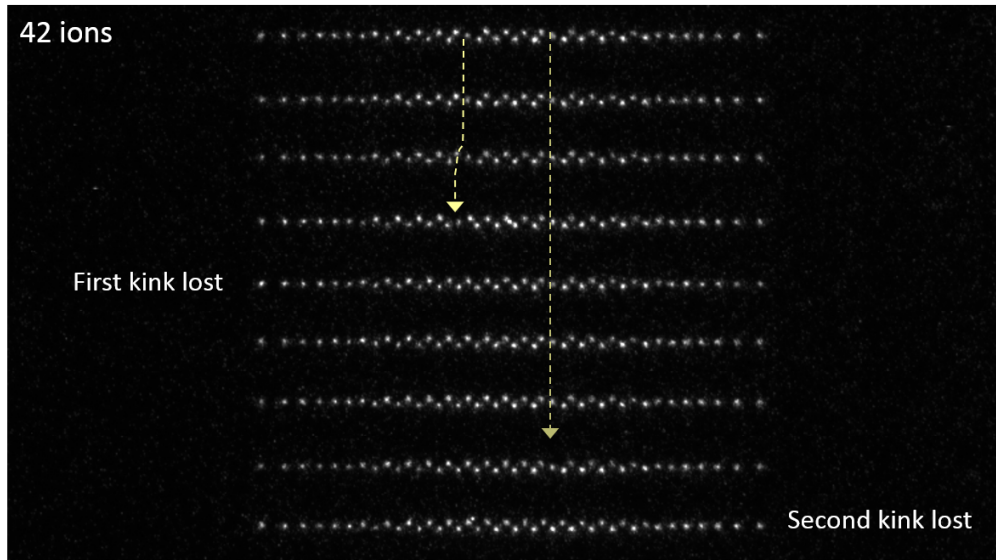


Figure 5.13: Images of a crystal of 43 ions. The separation between frames is 40 ms. (a) A typical departure of a kink through the edges of the ion crystal. (b) An unusual motion of a kink with back- and forth-motion before departure.

**(a) Two kinks' departure**



**(b) Extended-kink departure**

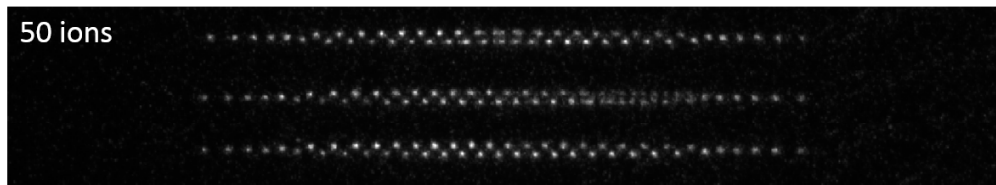


Figure 5.14: (a) A crystal of 42 ions with two discrete kinks. The one on the left, leaves the crystal within 5 frames (200 ms), while the kink on the right remains on the same site for 8 frames (320 ms) and is gone on the 9<sup>th</sup> frame. (b) Departure of an extended kink in a crystal of 50 ions (Extended like this one are not part of the presented data of post nucleation dynamics and lifetime).

## Chapter 6

# Dynamics Near the Linear-Zigzag Transition in the Quantum Regime

In the second part of this thesis, we continue with exploring the dynamics of the linear-zigzag transition, but now in the quantum regime. For a first goal of experiments in the quantum regime we seek to observe tunnelling oscillations between the two possible zigzag structures and, in doing so, to prepare superpositions of the two structures. In this chapter, we will go through the theoretical model of the coherent oscillation between zig and zag structures and investigate the requirements to make such tunneling measurements possible. We also propose an experiment sequence that suits best our setup and point out potential challenges of this experiment.

### 6.1 Introduction to the L-Z transition in the quantum regime

The interesting properties of the linear-zigzag (LZ) transition in trapped ion systems along with the high controllability available in these systems provide a useful platform for exploring many aspects of this transition, and hence motivated many intriguing proposals in recent years [54, 57, 59–61]. In the first part of this thesis, we followed one of these proposals [61], and studied the nucleation of topological defects. The dynamics involved are essentially classical with thermal fluctuations seeding the nucleation of kinks. In this part, we proceed to the proposals focused on the study of the LZ transition in the quantum regime.

As we described in previous chapters, the LZ transition is a second-order symmetry breaking transition. The resulting tunable double-well potential formed as the transition is crossed provides the opportunity to explore a variety of quantum effects. For instance, one can imagine creating a Schrödinger-cat state consisting of a superposition of the zig and zag configurations. Extending this idea, a proposal has been made to prepare a Schrödinger-cat state involving structural states entangled with spin [57]. Besides its application to preparing multiparticle quantum states of fundamental interest, the double well can also

be used as an interferometer to characterize the properties of environmental noise [161]. The immediate direction of our group is set to assess the technical feasibility of preparing superpositions of zig and zag, and observing/controlling quantum coherence of the system through the tunneling between the two configurations.

The first Schrödinger-cat state prepared in an ion-trap system involved the spin and motion of a single ion [162]. Since then, a Schrodinger cat state (in the form of a generalized GHZ state) consisting of the spins of up to six ion-qubits [163] and later 14 ion qubits [164] has also been demonstrated. A Schrödinger-cat state involving the zigzag structure involves different degrees of freedom and so will be sensitive to different decoherence mechanisms in the ion-trap environment. It has been pointed out elsewhere that zigzag superpositions may be less susceptible to environmental noise than might otherwise be expected due to the energy gap opened up by the double-well potential. The tunneling between two structural states in a rotor consisting of three trapped ions has recently been reported in [165]. Our system uses the zigzag mode instead of the rotational modes considered in [165] and in principle has the potential to compare the behaviour of various numbers of ions more easily.

The experimental studies of the zigzag dynamics in the quantum regime requires a high level of control and stability in the experiment, which can become technically challenging. In the remaining part of this thesis, we address some of these challenges and technical improvements made to make this experiment possible for the future.

## 6.2 Zigzag double-well potential and tunneling rate

In this section, we investigate the feasibility of our experimental setup for the manipulation of coherent double-well dynamics. Following Retzker *et al.*'s qualitative/semiquantitative calculation [57], we estimate the tunneling rate between the zig and zag configurations in a string of four  $^{171}\text{Yb}$  trapped ions.

In order to find the tunneling rate between the two structural states, the effective double-well potential needs to be found. Similar to our calculations in Chapter 3, Retzker *et al.* Taylor-expand the 2-D potential energy of a string of trapped ions to fourth order. Ignoring the coupling to axial modes, they show that the effective potential has the familiar quartic double-well structure:

$$V = \frac{1}{2}a\phi_{zz}^2 + \frac{1}{4}b\phi_{zz}^4, \quad (6.1)$$

where  $\phi_{zz}$  is the dimensionless transverse field amplitude associated with the zigzag mode and the coefficient  $a$  is positive (negative) on the linear (zigzag) side of the transition. Retzker *et al.* showed that for a barrier height that embeds two motional energy levels (see for example Fig. 6.1(f),(g)), a tunneling rate of 20–50 kHz can be expected in strings of 3–7 ions ions with an axial trap frequency of 1 MHz. A measurement of these tunneling rates was found to require placement of the transverse trap frequency within about 2-4 kHz of the critical point on the zigzag side.

Following the same procedure, we expand the potential energy to fourth order, but include the effect of the axial displacements on the double well (see Chapter 3, section 7 for details). Using the quadratic and quartic coefficients of the effective potential, other parameters such as well separation, tunneling rate, and local frequency of each well can be calculated as a function of trap anisotropy  $\alpha$ , or equivalently as a function of the deviation of the transverse trap frequency from the critical point  $\Delta\omega_y = \omega_y - \omega_{y,c}$ .

**Well separation:** This is the distance between the two minima of the double well, given by  $2\sqrt{-a/b}$ . This can be related to the actual displacement of the ions in the zigzag structure, which is in general smaller (by a factor of 0.67 for the central ions of a four-ion crystal).

**Energy levels and tunneling frequency:** The quantum energy levels provide access to the zigzag-mode transition frequency and the tunneling frequency for the double-well structure. The spacing between the two lowest energy levels,  $n = 0$  and  $n = 1$ , corresponds to the tunneling frequency for the case of the two levels lying below the barrier.

**Local frequency:** In the classical model of the transition, this is the soft-mode frequency that goes to zero at the critical point, and is proportional to  $\sqrt{-2a}$ . In the quantum double-well model, the local frequency is the spacing between  $n = 0$  and  $n = 2$  energy levels. In a deep double well (*i.e.* far from the critical point), the local frequencies of the classical and quantum models become the same. Note that on the linear side of the transition where we have only a single well, the local frequency is given by the splitting between the  $n = 0$  and  $n = 1$  states.

As we showed in Chapter 3 section 7, including the effect of axial-transverse coupling only affects the quartic term and not the quadratic term. This means that the dependence of the double-well structure on  $\omega_y$  is affected by the axial displacement, but the dependence of the classical frequency (local potential curvature about equilibrium) is not. For instance, at a point 2 kHz away from the critical point, ignoring the axial correction in a four-ion crystal results in a factor of 2 smaller displacement of a middle ion, as inferred from the well separation.

Figure 6.1 shows the effective potential and the first five motional energy levels of a string of four trapped ions as the linear-zigzag transition is crossed. The eigen-energies of the double-well potential are found by a numerical calculation in which the wave function is expressed in terms of a basis set of an infinite square well [166]. The calculations are performed for a string of four  $^{171}\text{Yb}$  ions at a fixed axial trap frequency of  $\omega_z/2\pi = 370$  kHz. The critical transverse frequency is  $\omega_{y,c}/2\pi = 754$  kHz. The effect of micro-motion, which leads to some shifts in the critical point [118], is not included. On the zigzag side, the size of the embedding square well is chosen to be four times the double well separation for each calculated point. On the linear side, the square well is 60 times the transverse harmonic oscillation size. On the linear side, the potential approaches a pure quadratic form away from the critical point, and the energy levels become equally spaced (Fig. 6.1(a),(b)). At

the critical point the potential becomes pure quartic (Fig. 6.1(c)), and on the zigzag side it becomes a quartic double well.

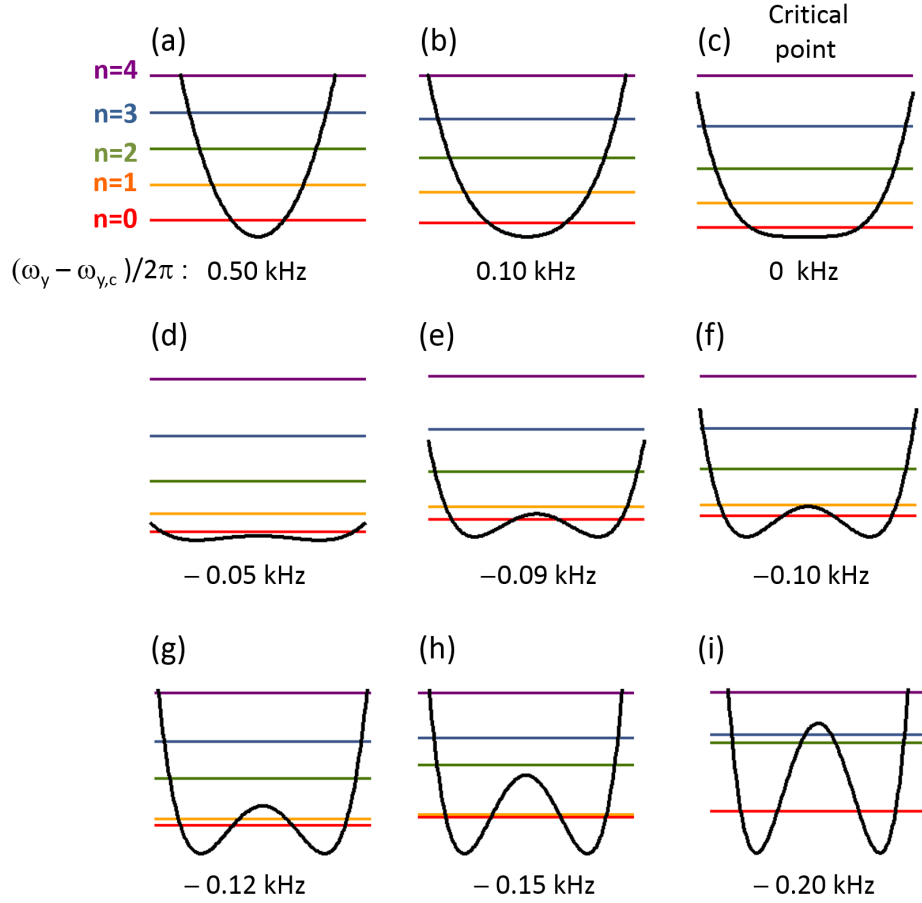


Figure 6.1: The scaled effective potential  $V(\phi_{zz})$  and the level structure of the first five motional energy levels of a string of four  $^{171}\text{Yb}$  ions for different deviations from the critical point. Each plot shows the scaled potential over the extent of the embedding square well used to solve for the energy levels (see text). For quantitative results, see Fig. 6.2. Plot (a) and (b) are on the linear side, where the effective potential is quadratic far from the critical point and has a single-well form. Plot (c) is right at the critical point (c.p.), where the effective potential is quartic. Plot (d) is slightly after the c.p., where the double well is starting to shape. Plot (e) is a double well that embeds only the first energy level ( $n = 0$ ). Plot (f) is when the second energy level ( $n = 1$ ) is just below the barrier (the point with the highest tunneling frequency). Plots (g) and (h) show how the two lowest energy levels approach degeneracy further past the critical point. Plot (e) is even deeper into zigzag, where the third and fourth energy levels are approaching degeneracy as well.

Figure 6.2 shows the calculated values of the well separation, classical local frequency (soft mode frequency), quantum local frequency (the energy separation between  $n = 2$  and

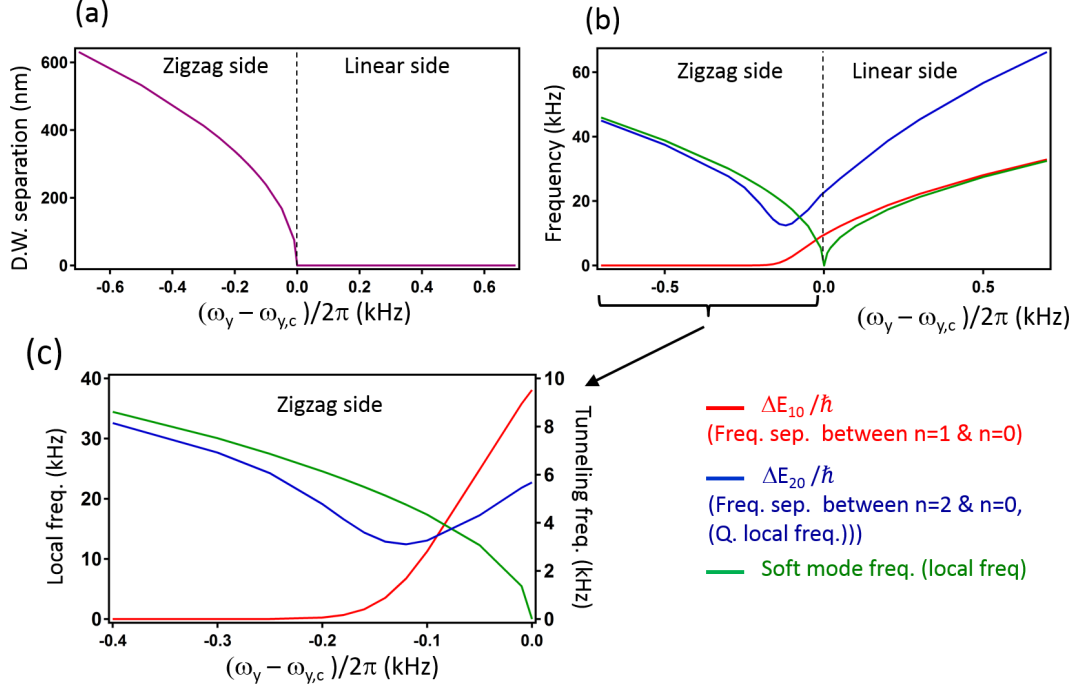


Figure 6.2: (a) The well separation and (b) classical local frequency (soft mode frequency)(green), quantum local frequency (proportional to energy separation between  $n = 2$  and  $n = 0$ )(blue) and the separation between the first two energy levels (corresponding to tunneling frequency) (red) in kHz, as a function of transverse frequency deviation from the critical point. (c) Same as plot (b) on the zigzag side, where the tunneling frequency is the right axis and the local frequencies are the left axis. The calculations are for a string of four  $^{171}\text{Yb}$  ions, at a fixed axial trap frequency  $\omega_z = 2\pi \cdot 370$  kHz.

$n = 0$  on the zigzag side,  $\Delta E_{20}/\hbar$ ), and the separation between the lowest two energy levels,  $\Delta E_{10}/\hbar$ , as a function of transverse frequency deviation from the critical point. The plots cover both linear and zigzag regimes for four  $^{171}\text{Yb}$  ions with the same trap frequency parameters as for Fig. 6.1.

Figure 6.2(b) shows that far from the transition on the linear side,  $\Delta E_{10}/\hbar$  approaches the classical zigzag frequency as obtained from small oscillation analysis, and  $\Delta E_{20} \simeq 2\Delta E_{10}$ , as is expected for a simple harmonic oscillator (SHO). On the zigzag side and far from the transition,  $\Delta E_{20}/\hbar$  matches the classical local frequency, which is equivalent to the zigzag mode frequency from small oscillation analysis. Near the transition, the quartic term in the potential opens a gap between (near degenerate) SHO levels, and where the first two energy levels lie below the barrier (Fig. 6.1(f)–(i)),  $\Delta E_{10}/\hbar$  is the tunneling frequency. The largest level splitting between  $n = 0$  and  $n = 1$  is  $\sim 10$  kHz. As we go deep into the zigzag the two levels become degenerate (Fig. 6.1(g),(h)) (*i.e.*  $\Delta E_{10}/\hbar$  approaches zero). Note that the energy gap does not go to zero at the transition. This means that in principle

it should be possible to prepare a ground state in the double well adiabatically from the linear side. The highest tunneling frequency occurs when the  $n = 1$  level is just below the barrier. This occurs near  $\omega_y - \omega_{y,c} = -0.1$  kHz (Fig. 6.1(f)), giving a tunneling frequency of 2.8 kHz, at a local frequency of 13.1 kHz.

In assessing the quantum model, as the critical point is approached, the zigzag local frequency gets lower and more sensitive to trap parameters, making the system more susceptible to technical noise. The tunneling frequency is also very sensitive to frequency shifts which means that a high stability (of  $\sim 10 - 20$  Hz) for  $\omega_y - \omega_{y,c}$  is required to preserve the coherence and obtain a tunnel oscillation with reasonable fidelity.

### 6.3 Outline of the proposed experiment

The following is a proposed procedure, consisting of four stages, to perform a zigzag tunneling measurement in a string of 4 ions. The summary of these four stages is shown in Fig. 6.3. Starting on the linear side, all the vibrational modes are cooled to a few quanta of vibration (using Sisyphus cooling, to be described in next chapter), and the transverse zigzag mode is Raman sideband cooled to the motional ground state. The second stage involves preparing the zig or zag configuration deterministically. While keeping the axial trap frequency fixed, the transverse trap frequency is reduced to ramp across the linear-zigzag transition as adiabatically as feasible. An optical dipole force from a far detuned, tightly focused laser (blue plug beam, see Chapter 7) can optionally be applied to bias the double well during the ramp to prepare the zig or zag state deterministically. To clean up energy acquired during the ramp, the zigzag mode is cooled to near the ground state again. (In principle, re-cooling is not required, but we have found it necessary to clean up after the ramp.) In the third stage, the crystal is ramped back closer to the critical point, where the tunneling frequency is measurably large, and a variable wait time allows for tunneling to occur. In the final readout stage, the crystal is ramped deep into the zigzag side and the structural state of the crystal is measured with a fluorescence image. As a function of wait time, the crystal structure should tunnel oscillate between zig and zag, in analogy with a Rabi oscillation in a driven two-level system. Tunneling oscillations as a Rabi-type experiment can provide information on system decoherence [167]; however more traditionally, a decoherence assessment is made with a Ramsey-type experiment. The analogy of a Ramsey experiment, if feasible, would involve a more complicated sequence of tunnel operations and voltage ramps. We note that there are other possibilities for manipulation and readout of the double-well external dynamics through coupling of the lowest energy levels via rf or laser interactions, or through adiabatic transfer between the single and double well with coherent ion-laser operations on the motion in the single well (see [57]).



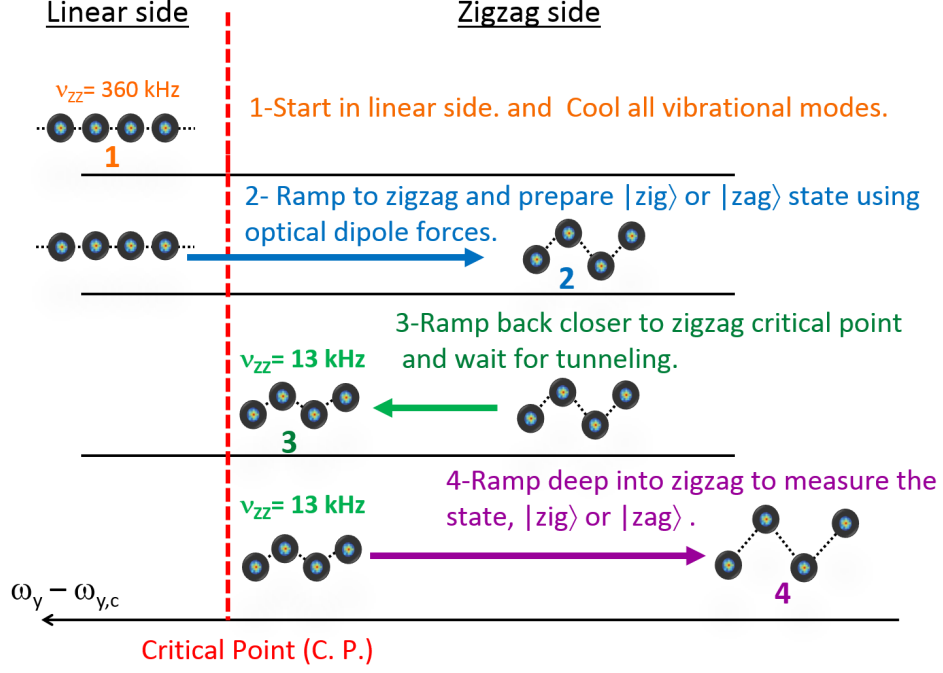


Figure 6.3: The four stages of the proposed experiment for measuring the tunneling oscillations between the zig and zag configurations near the critical point of the L-Z transition.

### 6.3.1 Preparing the setup for a zigzag tunneling measurement and outline of potential challenges

This experiment requires a high level of control and stability, and there are a number of techniques that need to be developed and technical issues to be explored in order to realize a successful tunneling measurement. Below is a list of technical improvements/challenges that are required to be addressed for our experimental setup.

1) One of the key requirements for investigating the L-Z transition in the quantum regime is the ability to cool the zigzag vibrational mode of the string to the ground-state of motion with a high probability. Given the relatively high Doppler average energy in our trap, we also expect it to be necessary to cool the other vibrational modes of the string with a sub-Doppler cooling technique to a few quanta of vibration. This is to suppress the potential effects of nonlinear coupling between modes near the zigzag transition, including the potential for heating, and to reduce the effect of spectator modes on Raman operations.

2) In order to achieve the required high  $\sim 10 - 20$  Hz stability in  $\omega_y - \omega_{y,c}$ , we estimate that 0.4 mV voltage stability in the  $\sim 1$  V dc voltages provided by the trap rods, 4 mV stability in the  $\sim 50 - 100$  V dc voltages provided by the axial endcaps, and finally 3–10 mV stability in the rf voltage in a range of a few 100 V are required. Achieving such high voltage stabilities, in particular for the rf, can be a challenge for our experimental setup.

3) By testing the asymmetry in the outcome of ramping across the transition, we found a bias in the resulting double-well potential of our trap setup. Such a bias which was not discernable in the KZM experiments at Doppler temperatures becomes significant for ground-state cooled crystals undergoing slow ramps. Most likely this bias is due to a hexapole term arising from the needles being displaced relative to the rods, which gives rise to a cubic term in the potential that breaks symmetry. To reduce the effect of this bias, we chose to perform the experiment with four ions rather than three.

4) A major challenge for this experiment will be the decoherence rates. First, there is the loss of motional coherence due to heating out of the two lowest energy levels, especially at low frequencies, where the tunneling measurement is performed. The size of this decoherence can be assessed by measuring the heating rate of the zigzag mode near the critical point of the LZ transition, on the zigzag side. Finally, there are the sources of fluctuations, in particular the cubic term mentioned above, leading to loss of coherence between the lowest energy levels and so loss of tunneling contrast.

In the next chapter, we address the first issue mentioned above and show a successful implementation of polarization-gradient cooling that provides sub-Doppler cooling of all the vibrational modes of a four-ion string simultaneously. We also demonstrate the resolved sideband cooling of the transverse zigzag mode on the linear side of the transition.

Although it will not be discussed in this thesis, we note here briefly that we have already demonstrated deterministic preparation of zig or zag states for a four-ion crystal, successfully sideband cooled the crystal on the zigzag side, and we have made some initial assessments of the zigzag bias and trap stability. We also have made preliminary heating assessments of the local zigzag mode on both sides of the transition near the critical point ( $\omega_{zz}/2\pi = 50 - 100$  kHz).

## Chapter 7

# Laser Cooling to Near Ground State of Motion

This chapter is focused on two laser cooling techniques, polarization-gradient (P-G) cooling and resolved sideband cooling, used together in our experiment to achieve ground-state cooling in a string of 1-4 trapped  $^{171}\text{Yb}$  ions. We start with approximate semiclassical and quantum analytical theoretical models of the P-G cooling, and discuss how numerical simulations, using these models as their bases, add various complications of the system for a better understanding of the experimental results. Then, we proceed to the theory of two-photon stimulated Raman transitions, and their application in thermometry. Next, we will provide an overview of the experimental setup and operation process, followed by the experimental results of P-G cooling, including the cooling rate and final average energy measurements for a single  $^{171}\text{Yb}$  ion. We then go through the theory of the resolved sideband cooling and discuss it for the case of multiple-ion strings. At the end, we present ground-state cooling results of a single ion and the normal modes of a four-ion string.

### 7.1 Introduction and motivation

The investigation of the linear-zigzag transition in the quantum regime requires the transverse zigzag mode of the ion crystal to be cooled to the ground-state of the motion with a high probability. Even though we are considering the transverse zigzag motion, motional energy in the orthogonal axial direction is also relevant, since near the linear-zigzag transition and increasingly into the zigzag region, the axial and transverse motions are coupled. Given the relatively high Doppler average energy in our trap we expect it be necessary to cool the other modes of the string with some amount of sub-Doppler cooling to a few quanta of vibration, or better. This should be sufficient to remove thermal spectator effects in Raman transitions (see Section 7.11) and so allow for a clean spectroscopy of the zigzag mode. Cooling the other modes is also intended to suppress the effect of nonlinear couplings

near the linear-zigzag transition, causing a thermal shift and fluctuations in the transition's critical point [60]. In practice, such nonlinear couplings can also lead to heating of the zigzag mode, as suggested in [57], but this is probably not a significant effect for few-ion strings considered in our case [57].

To achieve ground-state cooling, sub-Doppler cooling techniques, such as resolved sideband cooling [168, 169] or electromagnetically induced transparency (EIT) cooling [170] are commonly employed. In our experiment, we implement resolved sideband (Raman) cooling for the ground-state cooling of the transverse zigzag motion. In ion trap experiments, depending on the strength of the trap *i.e.* the size of the secular trap frequency, Doppler cooling commonly achieves average energies corresponding to average vibrational quantum numbers of  $\bar{n} \sim 5 - 30$ . In weaker ion traps, as in our case, the Doppler-achieved  $\bar{n}$  is on the higher side of the range. In these cases, the resolved sideband cooling of the modes starting from Doppler temperatures becomes challenging, since a large number of pulses in a complicated time sequence is required to walk the ion(s) down to the ground state. There is also an added technical challenge if all 3-N modes of an ion string with different frequencies need to be simultaneously cooled. Typically, resolved sideband cooling, and other ground-state cooling methods, are initiated at a low  $\bar{n}$ , in the so-called Lamb-Dicke (LD) regime, where higher order momentum diffusion contributions in the relaxation process are suppressed. In our experiment, to have a low initial  $\bar{n}$  suitable for resolved sideband cooling, we implement 3-D Sisyphus cooling in the form of polarization gradient cooling, well-known in neutral atom experiments, as an intermediate step between Doppler and resolved sideband cooling. Furthermore, the Sisyphus cooling acts to cool all 3-N vibrational modes of an ion string simultaneously.

Sisyphus cooling was first demonstrated definitively in a sodium gas within a 3-D optical molasses in 1988 [171]. The resulting sub-Doppler cooling came as a surprise and was unexplained at the time of the experiment. Within one year, two groups independently explained that the cooling was a result of optical pumping effects due to a spatial polarization variation in the optical molasses [172, 173]. The cooling technique was called polarization gradient cooling, the most common form of what is termed Sisyphus cooling (see below). Since then, this technique has become widely adopted in laboratory experiments to cool down neutral atomic gases of a variety of species to ultra-cold temperatures. In 1992, the idea of Sisyphus cooling was extended to the situation of bound atoms, where a proposal was made for achieving sub-Doppler temperatures for a trapped ion (atom) placed in an intensity gradient [174, 175]. Proposals to use a polarization gradient followed in 1993 [67, 176]. In 1994, the first demonstration of P-G cooling of trapped ions was shown for one and two Mg ions in a quadrupole ring trap [76]. However, the trap along the axis being cooled was so weak that ions were quasi-free, so that the essentials of the cooling process were the same as for free atoms. These experiments were later extended to study the transport of ions in a combined ion trap and optical lattice [177], and recent related experiments have

demonstrated lattice-assisted sideband cooling (but not Sisyphus cooling) for ions trapped in a combined ion trap and optical lattice [178].

Sisyphus cooling has seen more applications in the case of bound neutral atoms. P-G cooling has been used for cooling and localization of atoms in an optical lattice [69–71], where the light provides both the cooling and the confinement. P-G cooling has also been applied to the case where the trapping and cooling light are separate, including the case of atoms in far detuned optical lattices [72], single atoms trapped in an optical cavity [73], and single atoms in an optical tweezer as a precursor to sideband cooling [74]. As a related application, P-G cooling light has been used for the detection of single atoms in optical tweezers [179] and at sites in optical lattices [180]. A setup for counting atoms in optical tweezers with a blue detuned lattice included a Sisyphus cooling effect [181]. Finally, in 2005 work by Nuszmann *et al.* [75], 3-D laser cooling of single atoms into an optical dipole trap in the presence of an optical cavity was demonstrated in which several cavity cooling mechanisms worked in combination with a Sisyphus-type effect driven by a pump laser.

In this work, we demonstrate the first 3-D Sisyphus cooling of 1-4 trapped  $^{171}\text{Yb}$  ions in a linear Paul trap. We also present a detailed study of the polarization-gradient cooling of a single trapped ion, including measurements of the cooling rate and final average energy as a function of laser intensity, and compare the experimental results to both semiclassical and quantum simulations. Note that the 3-D cooling of trapped ions is achieved by using a 1-D standing wave, which is a significant technical simplification from the optical molasses setup for neutrals. We find Sisyphus cooling of trapped ions to be a simple, robust technique which can be of general use.

## 7.2 Theoretical models of Sisyphus cooling

Laser cooling is a wide ranging topic with a significant body of theoretical work. For reviews specific to trapped ions see for example [182, 183]. For Sisyphus cooling of trapped ions, the theoretical models take two approaches: semiclassical and quantum. In both of these approaches the laser-ion interaction (involving the ion’s internal state) is treated quantum mechanically, but the semiclassical approach treats the motion of the ion (the ion’s external state) classically. The theoretical models normally assume that the ion is strongly bound, so that its spatial spread in the trap is much smaller than the laser’s wavelength (known as the Lamb-Dicke limit (LDL)).

The first theoretical model extending the Sisyphus cooling idea to a trapped ion (atom) in the LDL involved 1-D semiclassical calculations for a three-level system in an intensity gradient standing wave with the trap assumed to be a harmonic well centered at the optimum point of maximum intensity gradient [174]. Even though the final energies are on the order of  $\bar{n} \approx 1$ , where one would expect a quantum description of the motion to become relevant, it was shown that in the LDL a semiclassical and quantum approach give the

same result for the cooling limit and cooling rate: a cooling limit of a few quanta, and a cooling rate proportional to the square of laser intensity, associated with the laser-ion saturation parameter  $s$ . This agreement was discussed as a peculiarity of the harmonic confining potential. Subsequent work [175], extending prior LDL calculations [158], developed a convenient quantum formalism to calculate laser cooling of a multi-level trapped ion in the LDL for general configurations, and used it to compare to the cooling rate and final energies in an intensity-gradient standing wave reported in [174]. Further models have explored the 1-D polarization-gradient cooling of a trapped ion with a  $J_g = 1/2 \rightarrow J_e = 3/2$  transition and in the Lin- $\perp$ -Lin polarization configuration using both full quantum calculations [67] and semiclassical calculations [176]. The upshot of these calculations is that the semiclassical and quantum results for P-G cooling in this situation agree as in the case of an intensity gradient, and they also predict a typical cooling limit of a few quanta and a cooling rate proportional to  $s^2$ . Polarization gradient cooling was, however, noted by the authors of [67] advantageous compared to the intensity gradient cooling technique, since it is less sensitive to optical phase *i.e.* less sensitive to misalignment of the polarization gradient with respect to the ion position. Finally, at about the same time as these works were published, semiclassical Monte Carlo simulations for the same  $J_g = 1/2 \rightarrow J_e = 3/2$  model were performed [184] and used to study the final cooling limit in the crossover from the case of a tightly bound particle in the LDL to the free-particle case. Good agreement with analytical theory was shown in both limits.

Semiclassical models can show discrepancies with quantum treatments of sub-Doppler cooling (see for example [184]), but the above theoretical studies of Sisyphus cooling for a trapped ion on a  $J_g = 1/2 \rightarrow J_e = 3/2$  transition clearly show that a semiclassical model can provide similar quantitative predictions in the LDL to the quantum calculations. The semiclassical model of Sisyphus cooling gives a particularly intuitive understanding of the cooling and so we have pursued this approach as a first model of P-G cooling of a  $^{171}\text{Yb}$  ion. For the range of parameters that were considered in our experiment, this will turn out to be a reasonable approximation. It worth noting that the particular polarization gradient configuration of the  $J_g = 1/2 \rightarrow J_e = 3/2$  model studied in [67, 176, 184] avoids the creation of any ground-state coherences, which allows for a very simple representation of the internal dynamics in terms of rate equations. This is not always the case, and other situations, such as our  $F_g = 1 \rightarrow F_e = 0$  system for  $^{171}\text{Yb}^+$ , can become more complicated due to coherent dark state formation in the ground state. For this reason, we have calculated a 1-D quantum analytical model for  $^{171}\text{Yb}^+$  following the approach of [67] to assess effects of the internal state of the ion on the cooling. These analytical models have potential limitations for ultimate comparison to experiment, in regard to the LD approximation, the effect of three axes of motion being cooled simultaneously, and technical effects in the implementation of the experiment. For comparison to experimental data, 3-D semiclassical simulations following the rate-equation approach of [184] have been performed with some

important differences related to our particular system. Finally, a limited set of quantum simulations has been performed to give a quantitative assessment of the sub-Doppler cooling mechanisms with minimal assumptions. A full quantum numerical simulation treats both the internal state of a trapped ion and its motion quantum mechanically and solves the master equation of the ion in interaction with the Sisyphus laser fields. Solving the master equation directly is difficult due to the large number of basis states, and a 3-D calculation rapidly becomes intractable as the number of states required increases. The Monte-Carlo wave function (MCWF) technique developed in 1990s enabled progress in laser cooling studies of free atoms [185, 186], and software packages now developed make this fairly convenient to implement. A full 3-D quantum numerical simulation still requires high computation power and can be time consuming, so we only consider 1-D simulations to compare to our experimental data.

### 7.3 Theoretical models of P-G cooling of a trapped $^{171}\text{Yb}^+$

Starting with a brief overview of the energy levels of the  $^{171}\text{Yb}$  ion used for the cooling studies, we first discuss the semiclassical theory of Sisyphus cooling for both a free and a trapped ion and provide a simplified model for the  $^{171}\text{Yb}$  ion, which forms the basis of the semiclassical simulations presented in this thesis. We then describe how semiclassical simulations account for the complications of the system and allow for a better understanding of the experimental results. At the end of this section, we briefly discuss the quantum approach to modeling Sisyphus cooling and point out the differences between the quantum and semiclassical models.

#### 7.3.1 Energy levels of $^{171}\text{Yb}$ ion

Our cooling studies are performed using trapped  $^{171}\text{Yb}$  ions. Unlike the  $^{174}\text{Yb}^+$  isotope used in our KZM studies,  $^{171}\text{Yb}^+$  has a non-zero nuclear spin of  $I = 1/2$ , which gives rise to hyperfine structure. The primary transition used for Doppler cooling, P-G cooling, and fluorescence detection is  $S_{1/2}(F = 1) \rightarrow P_{1/2}(F = 0)$ . (A detailed discussion of the  $S_{1/2}(F = 1) \rightarrow P_{1/2}(F = 0)$  transition of  $^{171}\text{Yb}$  ion with a comparison to the  $S_{1/2} \rightarrow P_{1/2}$  transition of  $^{174}\text{Yb}$  ion is provided in my Master's thesis [146]). The higher Zeeman multiplicity in the  $S_{1/2}(F = 1)$  ground state of this transition, compared to the  $P_{1/2}(F = 0)$  excited state, creates coherences between the ground-state Zeeman levels in the presence of an incident laser field, resulting in coherent dark-state population [146, 147, 187]. Applying an external magnetic field can suppress the effect of coherences by averaging them out in time. For this reason, a magnetic field of  $\sim 5.9$  G is applied in our experiment, which

results in Zeeman shifts of  $\delta_B = \pm 8.2$  MHz for the  $m_F = \pm 1$  ground-state levels<sup>1</sup>. The Zeeman-resolved hyperfine structure of the  $S_{1/2}(F = 1) \rightarrow P_{1/2}(F = 0)$  transition is shown in Fig. 7.1. Two of the hyperfine levels of the  $S_{1/2}$  state,  $|F = 0, m_F = 0\rangle \equiv |\uparrow\rangle$  and  $|F = 1, m_F = 0\rangle \equiv |\downarrow\rangle$ , separated by  $\omega_{HF}/2\pi = 12.6$  GHz form an effective spin-1/2 system that will be used for microwave and two-photon Raman transitions (see Section 7.5). These two states are preferred to other pairs of the Zeeman states, due to their reduced sensitivity to magnetic-field fluctuations at low field values.

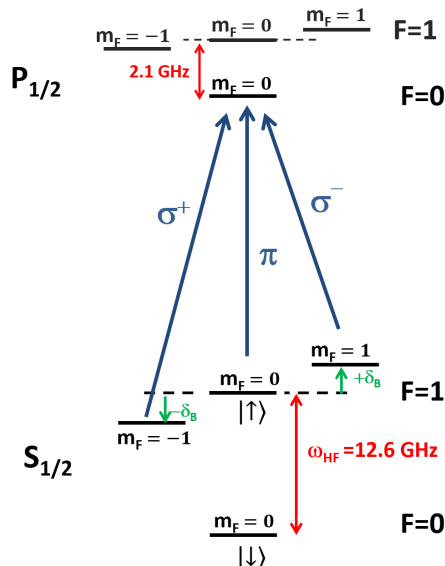


Figure 7.1: The Zeeman-resolved energy levels of the  $^2S_{1/2}$  and  $^2P_{1/2}$  states of  $^{171}\text{Yb}^+$  and the main  $S_{1/2}(F = 1) \rightarrow P_{1/2}(F = 0)$  transition used for Doppler cooling, P-G cooling, and fluorescence detection. The size of Zeeman shifts are exaggerated. The polarization resolved branching ratios for the three  $S_{1/2}(F = 1)$  sub-levels are all the same and equal to 1/3. Two of the hyperfine levels of the ground state,  $S_{1/2}|F = 0, m_F = 0\rangle \equiv |\uparrow\rangle$  and  $S_{1/2}|F = 1, m_F = 0\rangle \equiv |\downarrow\rangle$ , form an effective spin-1/2 system used for microwave and two-photon Raman transitions.

### 7.3.2 P-G cooling of a free atom— semiclassical approach

We start the theory of the semiclassical approach with the polarization-gradient cooling model of a free atom. The idea is then extended to the case of a bound atom in a similar way to [67, 176, 184].

A spatial dependent polarization gradient field can be created using two counter-propagating laser fields. The polarization gradient of the resulting standing wave depends on the po-

<sup>1</sup>Similar to the  $^{174}\text{Yb}^+$  isotope, in low magnetic fields, the Zeeman shift of a hyperfine level  $|F, m_F\rangle$  is  $\Delta E_B(F, m_F) = g_F \cdot m_F \cdot (\mu_B \cdot B) = g_F \cdot m_F \cdot (\hbar\delta_B)$ , where the Lande g-factor  $g_F = 1$  for  $^2S_{1/2}(F = 1)$ , and  $g_F = 1/3$  for  $^2P_{1/2}(F = 1)$  sub-levels



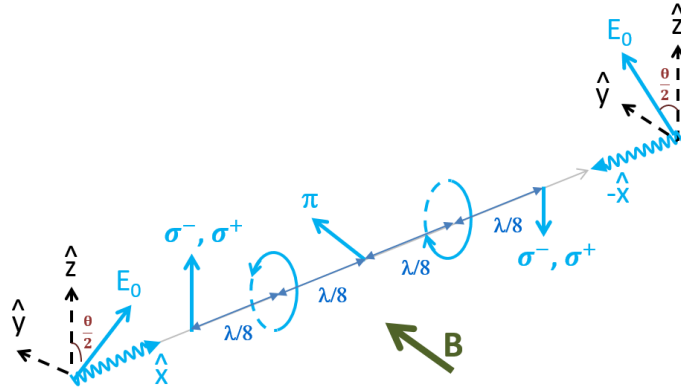


Figure 7.2: A polarization-gradient configuration formed by the superposition of two linearly polarized counter-propagating beams. The typical "Lin- $\perp$ -Lin" configuration corresponds to  $\theta = \pi/2$ .

larization of the original fields. We assume here that the laser's power and detuning are such that an atom interacting with the laser field can for the most part be considered in the ground state with only weak interactions with the laser field. In this case, the polarization gradient cooling works based on two main effects:

- 1 – State-dependent energy shifts: Due to the dipole interaction between the laser field and atom, energies of the ground-state sub-levels shift. This energy shift, known as ac Stark shift, depends on the dipole moment of the atom and the polarization of the field and leads to a state-dependent potential and dipole force.
- 2 – Optical pumping between more than one ground-state sub-level: Absorption and subsequent spontaneous emission from the excited state can transfer the atom between the ground-state sub-levels. Due to the spatial polarization variation, the optical pumping rates, and therefore the steady-state population of the sub-levels, become position dependent.

To understand how the combination of these two effects can lead to cooling, consider a free multi-level atom moving in a polarization-gradient standing wave. If the rate of optical pumping is slow compared to the rate of polarization variation experienced by the moving atom, the atom cannot adjust to the polarization variation adiabatically, and will therefore be able to move some distance along the state-dependent potential before it is optically pumped out of its Zeeman state. Since the ac Stark shifts of sub-levels are different, the atom can lose or gain energy when it is transferred between states. Cooling will happen when the optical pumping transfers the atom from a state with a higher potential to a state with a lower potential. In a proper polarization gradient setup, the probability of optical

pumping events that result in cooling is on average higher than the probability for events leading to heating, and the atom is cooled on average.

As a specific case of relevance to our experiment, we consider a polarization-gradient configuration formed by two counter-propagating laser beams with linear polarizations at the angles  $\pm\theta/2$  with  $\hat{z}$  (see Fig. 7.2). In the case of  $\theta = \pi/2$ , this is referred to a "Lin- $\perp$ -Lin" configuration. The magnitudes of the electric fields  $E_0$ , wavevectors  $k_l$ , and frequencies  $\omega_L$  are arranged to be the same for the two beams, so that we have

$$\vec{E}_1 = \frac{1}{2}E_0 [\cos(\theta/2)\hat{z} - \sin(\theta/2)\hat{y}] \left( e^{i(\omega_L t - \vec{k}_l \cdot \vec{r} - \phi)} + e^{-i(\omega_L t - \vec{k}_l \cdot \vec{r} - \phi)} \right), \quad (7.1)$$

$$\vec{E}_2 = \frac{1}{2}E_0 [\cos(\theta/2)\hat{z} + \sin(\theta/2)\hat{y}] \left( e^{i(\omega_L t + \vec{k}_l \cdot \vec{r} + \phi)} + e^{-i(\omega_L t + \vec{k}_l \cdot \vec{r} + \phi)} \right). \quad (7.2)$$

The electric field of the resulting standing wave in terms of the normalized polarization vector  $\vec{\epsilon}(\vec{r})$  is

$$\vec{E}(\vec{r}, t) = \frac{1}{2}E_0 \vec{\epsilon}(\vec{r}) e^{-i\omega_L t} + c.c., \quad (7.3)$$

$$\vec{\epsilon}(\vec{r}) = \frac{1}{\sqrt{2}} \cos(\theta/2) \cos(\vec{k}_l \cdot \vec{r} + \phi) \cdot (\hat{\epsilon}_+ - \hat{\epsilon}_-) + i \sin(\theta/2) \sin(\vec{k}_l \cdot \vec{r} + \phi) \cdot \hat{\epsilon}_0, \quad (7.4)$$

where we have chosen a polarization basis in terms of a quantization axis along  $\hat{y}$  ( $\vec{B} = B\hat{y}$ ). The spatial polarization gradient of the resulting standing wave is shown in Fig. 7.2. As can be seen, the polarization changes periodically between a pure  $\pi$ -polarization and a linear combination of circular left and right polarization ( $\sigma^-$ ,  $\sigma^+$ ) in  $\lambda/4$  intervals.

The interaction between the atom and the resulting laser field can be described by the dipole potential

$$V_{dip}(\vec{r}, t) = -\vec{d} \cdot \vec{E}(\vec{r}, t), \quad (7.5)$$

where  $\vec{d}$  is the electric dipole operator. In the following, we adopt the notation in [188]. The raising and lowering operators,  $\vec{d}^+$  and  $\vec{d}^-$ , are defined in terms of  $\vec{d}$  and excited/ground state projection operators,  $P_e$  and  $P_g$ . For a given pair of excited and ground states,  $e_j$  and  $g_k$ , we have

$$\vec{d}_{jk}^+ = P_{e_j} \vec{d} P_{g_k} = |e_j\rangle \langle e_j| \vec{d} |g_k\rangle \langle g_k| = D_{jk} \hat{d}_{jk}^+, \quad (7.6)$$

$$\vec{d}_{kj}^- = P_{g_k} \vec{d} P_{e_j} = |g_k\rangle \langle g_k| \vec{d} |e_j\rangle \langle e_j| = D_{kj}^\dagger \hat{d}_{kj}^-. \quad (7.7)$$

Here,  $D_{jk}$  is a reduced matrix element. Using the rotating wave approximation, the dipole potential can be written in terms of Rabi frequency  $\Omega$  as

$$V_{dip}(\vec{r}, t) = \frac{1}{2} \hbar \Omega \left( \vec{\epsilon}(\vec{r}) \cdot \hat{d}^+ \right) e^{-i\omega_L t} + h.c., \quad (7.8)$$

$$\Omega \equiv \frac{-DE_0}{\hbar}. \quad (7.9)$$

The matrix elements of the operator  $(\vec{\epsilon}(\vec{r}) \cdot \hat{d}^+)$  can easily be found knowing that the values of  $\hat{\epsilon}_q \cdot \hat{d}^+$ , with  $q = \{+, 0, -\}$  are just Clebsch-Gordan coefficients. In the limit of weak saturation for the atom-laser interaction, the excited state is only weakly populated. The excited state and optical coherences can be adiabatically eliminated in favor of a description solely in terms of the slowly evolving ground-state levels. Introducing a new dimensionless operator  $\Lambda(\vec{r})$  as

$$\Lambda(\vec{r}) = (\vec{\epsilon}(\vec{r}) \cdot \hat{d}^+)^\dagger (\vec{\epsilon}(\vec{r}) \cdot \hat{d}^+). \quad (7.10)$$

We can express the ac Stark shift of a given state  $|g_j\rangle$  as

$$U_{ac[j]}(\vec{r}) = \hbar\Delta \frac{(4s)}{2} \langle g_j | \Lambda(\vec{r}) | g_j \rangle. \quad (7.11)$$

Here,  $\Delta$  is the laser detuning, and  $4s$  is the saturation parameter of the two Sisyphus beams with  $s$  being the saturation parameter of each beam:

$$s = \frac{\Omega^2/2}{\Delta^2 + (\gamma/2)^2}. \quad (7.12)$$

The Rabi frequency associated with the  $S_{1/2} \rightarrow P_{1/2}$  transition of Yb can be written in terms of an on-resonant saturation parameter  $s_0$  associated with a single beam:

$$\Omega = \gamma \sqrt{\frac{s_0}{2}}. \quad (7.13)$$

In addition to the ac Stark shifts, the optical pumping rate out of the  $|g_k\rangle$  state also needs to be considered and can be written as

$$\Gamma_{j \rightarrow k}(\vec{r}) = \gamma \frac{(4s)}{2} \sum_{q=+,0,-} \left| \langle g_k | (\hat{\epsilon}_q^* \cdot \hat{d}^-) (\vec{\epsilon}(\vec{r}) \cdot \hat{d}^+) | g_j \rangle \right|^2, \quad (7.14)$$

where  $\gamma$  is the natural linewidth of the  $g \rightarrow e$  transition. To find the ac Stark shifts and optical pumping rates of the  $S_{1/2}(F=1)$  sub-levels for the  $^{171}\text{Yb}$  ion, we first assume that the magnetic field is sufficiently large and ignore the effect of ground-state coherences. Due to the symmetry of the polarization for the  $m_F = +1$  and  $m_F = -1$  states, and ignoring the small detuning shifts<sup>2</sup>, we can treat these two states as one effective  $m_F = \pm 1$  state. This reduces the problem to one of two effective states,  $|0\rangle$  and  $|\pm 1\rangle$ . Note that for the range of powers used in the experiment, one effect of the ground-state coherences is to give an accentuated imbalance in the population of the  $m_F = \pm 1$  states, but a quantum calculation shows that the sum of the two populations is not affected. We have considered the full Zeeman level structure in both of our semiclassical and quantum analytical models,

<sup>2</sup>Zeeman splitting breaks the symmetry between the  $m_F = \pm 1$  states and gives a different laser detuning for each, but we ignore these shifts in the following, since in the actual experiment the Zeeman splitting ( $\delta_B/2\pi = 8.2$  MHz) is small compared to the laser detuning ( $\Delta/2\pi = 310$  MHz).

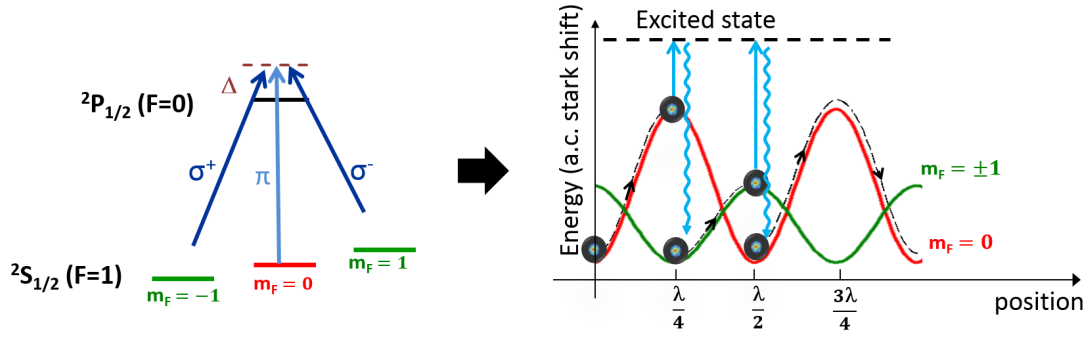


Figure 7.3: The sketch of the Sisyphus cooling process for a free  $^{171}\text{Yb}$  ion moving in a Lin- $\perp$ -Lin configuration. The ac Stark shifts (potentials) of the effective  $m_F = \pm 1$  state, shown in green, and of the  $m_F = 0$  state, shown in red, are plotted using Eq. 7.15 and 7.16, assuming  $\Delta > 0$ . The probability of the optical pumping is highest at the maximum point of a potential; the atom tends to end up in the state with a lower potential after pumping, and so loses an amount of kinetic energy lost to "climbing the hill". See also [9]

and in the simulations shown in later plots, but here we use the effective two-state model to simplify the presentation of the results. The ac Stark shifts of the two effective states,  $|0\rangle$  and  $|\pm 1\rangle$ , and the optical pumping rate out of each state in the polarization-gradient standing wave given by Eq. 7.4 are

$$U_{ac[0]}(\vec{r}) = \frac{1}{3}\hbar s\Delta \sin^2(\theta/2) \sin^2(\vec{k}_l \cdot \vec{r} + \phi), \quad (7.15)$$

$$U_{ac[\pm 1]}(\vec{r}) = \frac{1}{6}\hbar s\Delta \cos^2(\theta/2) \cos^2(\vec{k}_l \cdot \vec{r} + \phi), \quad (7.16)$$

$$\Gamma_{[0]}(\vec{r}) = \frac{2}{9}s\gamma \sin^2(\theta/2) \sin^2(\vec{k}_l \cdot \vec{r} + \phi), \quad (7.17)$$

$$\Gamma_{[\pm 1]}(\vec{r}) = \frac{2}{9}s\gamma \cos^2(\theta/2) \cos^2(\vec{k}_l \cdot \vec{r} + \phi). \quad (7.18)$$

For positive detunings, at the points of pure  $\pi$ -polarization, the ac Stark shift is at a maximum for  $|0\rangle$ , while it is at a minimum for the  $|\pm 1\rangle$  state (see Fig. 7.3). The opposite happens at points corresponding to a linear combination of  $\sigma^-$  and  $\sigma^+$  polarizations. Moreover, the rate of optical pumping out of a state is highest (lowest) when the atom is at the maximum (minimum) of the potential for that state. This means that for a moving atom the probability of an optical pumping event increases as the atom climbs the hill of the potential, and so it tends to end up in the state with lower potential energy after the pumping. Therefore on average, with each pumping cycle the atom will preferentially lose an amount of kinetic energy associated with "climbing the hill". As the atom moves across the polarization gradient, the loss of energy moving back and forth between potentials gives rise to a Sisyphus cooling force. Further discussion of the Sisyphus cooling force for free atoms in the specific case of an  $F=1 \rightarrow F=0$  transition can be found in [9].

### 7.3.3 P-G cooling of a bound ion – semiclassical approach

The concept of Sisyphus cooling of a free atom was first extended to a bound ion (atom) by Wineland *et al.* [174] for an intensity-gradient field and shortly after, the polarization-gradient version of Sisyphus cooling of a trapped ion was discussed by several authors [67, 176, 184]. A single ion confined in a 1-D harmonic trap and described by position  $x_i$  experiences a potential of  $U_{osc}(x_i) = \frac{1}{2}M\omega_i^2x_i^2$ , where  $\omega_i$  is the trap frequency along the  $i^{th}$  direction with  $i = \{1, 2, 3\}$ . As already noted above, an important concept in the interpretation of the cooling is the Lamb-Dicke limit. In the Lamb-Dicke limit, achieved for strongly bound ions, the spread of the ion's position is small compared to the wavelength of the cooling beam ( $\sqrt{k^2\langle x_i^2 \rangle} \ll 1$ ). It is convenient to define a Lamb-Dicke (LD) parameter in terms of the rms spread of the ion's wavefunction in the ground state  $x_{i0} = \sqrt{\frac{\hbar}{2M\omega_i}}$  as

$$\eta = kx_{i0} = \sqrt{\frac{\omega_R}{\omega_i}}. \quad (7.19)$$

Here,  $\omega_R$  is the recoil frequency. In the atom-laser interaction the appropriate LD parameter to consider will include the  $\vec{k}$ -projection onto the axis of interest ( $k \rightarrow k_i$ ). We will point this out in the text where necessary. It is important to keep the LD regime distinct from the condition on the LD parameter being small. In the LD limit, it is true that the LD parameter is very small, but  $\eta \ll 1$  is not sufficient to satisfy the LD limit. The LD limit is achieved when the ion is sufficiently cooled (low  $\bar{n}$ ) in a strong trap ( $\omega_i \gg \omega_R$ ). For a trapped ion with an average thermal energy of  $\hbar\omega_i(\bar{n} + 1/2)$ , the rms spread of the ion can be estimated as  $\langle x_i^2 \rangle = x_{0i}^2(2\bar{n} + 1)$ , and we are in the LD regime for  $\eta\sqrt{2\bar{n} + 1} \ll 1$ .

In our Sisyphus cooling setup for  $^{171}\text{Yb}^+$ , the trap frequencies are  $\{\omega_x, \omega_y, \omega_z\} = 2\pi\{0.790, 0.766, 0.525\}$  MHz. The LD parameter associated with each direction is  $\{\eta_x, \eta_y, \eta_z\} = \{0.052, 0.053, 0.09\}$ , which meets the condition  $\eta \ll 1$  well enough. However, at a typical Doppler temperature of  $\bar{n} \simeq 22$ , the values of  $\eta\sqrt{2\bar{n} + 1}$  associated with the  $\{\hat{x}, \hat{y}, \hat{z}\}$  directions are  $\{0.35, 0.36, 0.6\}$ , which indicates that we can likely expect deviations in behaviour from LDL predictions. (See [184] for a theoretical exploration of the crossover from the LD to free-ion limits for Sisyphus cooling). The cooling theories are particularly simple in the LDL and one can readily derive analytical expressions for the cooling rate and cooling limit. Even if the initial energies are such that the ion starts outside the LDL regime, one can still describe the final stages of cooling of the ion by the theoretical models in the LDL.

In addition to the LDL approximation, and following [174], we also assume

$$\Gamma_{[j]} \ll \omega_i \ll \gamma \ll |\Delta| \quad \text{and} \quad \omega_i \ll \delta_B. \quad (7.20)$$

Here,  $\Gamma_{[j]}$  is the rate of optical pumping out of the  $|j\rangle$  state where  $j \in \{0, \pm 1\}$ ;  $\omega_i/2\pi \approx 500 - 800$  kHz is the trap frequency along the  $i^{th}$  direction with  $i \in \{1, 2, 3\}$ ;  $\gamma/2\pi = 19.6$  MHz is the natural linewidth of the  $S_{1/2} \rightarrow P_{1/2}$  transition;  $\Delta/2\pi$  is the laser detuning,

which is set to 310 MHz in experiment; and  $\delta_B/2\pi$  is the Zeeman shift, which is set to 8.2 MHz. We discuss each of the four approximations as follows:

1 – The first approximation,  $\Gamma_{[j]} \ll \omega_i$ , implies that the trapped ion oscillates many times in between the optical pumping events. Therefore, it does not make sense to define a velocity dependent cooling force for the ion. Instead, the cooling effect will be calculated by averaging the processes over an oscillation cycle of the ion. As well, under this approximation the space-averaged steady-state Zeeman populations will be approximated by the populations at the average location of the ion  $\langle \rho \rangle_{avg} \simeq \rho(r_{avg})$ .

2 – The second approximation,  $\omega_i \ll \gamma$ , implies that the scattering event happens so fast compared to the ion's motion that the ion can be considered stationary during the scattering event. (This is the limit of un-resolved sidebands, and the resolved sideband limit is considered in Section 7.5).

3 – The third approximation,  $\gamma \ll \Delta$ , together with a low laser intensity leads to the limit of low saturation,  $s \ll 1$ , which allows the adiabatic elimination of the excited states in favor of a description in terms of Zeeman ground states.

4 – The fourth approximation,  $\omega_i \ll \delta_B$ , implies that two-photon Raman resonances between the Zeeman states can be ignored.

### The internal state of the trapped ion:

Ignoring the coherences between the  $S_{1/2}|1, m_F\rangle$  Zeeman ground states, and adiabatically eliminating the  $P_{1/2}|0, 0\rangle$  excited-state population, the evolution of the internal state of  $^{171}\text{Yb}^+$  is reduced to a set of rate equations for the ground-state Zeeman populations as follows:

$$\dot{\rho}_{[0]} = -\rho_{[0]}\Gamma_{[0]} + \rho_{[\pm 1]}\Gamma_{[\pm 1]}, \quad (7.21)$$

$$\dot{\rho}_{[\pm 1]} = -\rho_{[\pm 1]}\Gamma_{[\pm 1]} + \rho_{[0]}\Gamma_{[0]}. \quad (7.22)$$

The steady-state solution of the rate equations and the normalization condition  $\rho_{[0]}^{ss} + \rho_{[\pm 1]}^{ss} = 1$  give the steady-state populations of

$$\rho_{[0]}^{ss} = \frac{\Gamma_{[\pm 1]}}{\Gamma_{[0]} + \Gamma_{[\pm 1]}}, \quad (7.23)$$

$$\rho_{[\pm 1]}^{ss} = \frac{\Gamma_{[0]}}{\Gamma_{[0]} + \Gamma_{[\pm 1]}}. \quad (7.24)$$

Using the optical pumping rates of Eq. 7.17 and 7.18, the steady-state solutions can be written as

$$\rho_{[0]}^{ss}(x) = \frac{1}{4 \tan^2(\theta/2) \tan^2(\vec{k}_l \cdot \vec{x} + \phi) + 1}, \quad (7.25)$$

$$\rho_{[\pm 1]}^{ss}(x) = \frac{4 \tan^2(\theta/2) \tan^2(\vec{k}_l \cdot \vec{x} + \phi)}{4 \tan^2(\theta/2) \tan^2(\vec{k}_l \cdot \vec{x} + \phi) + 1}. \quad (7.26)$$

As noted above, the excited state adiabatically follows the ground states and so is given by

$$\rho_{ee}^{ss}(x) = \frac{\Gamma_{[0]}\rho_{[0]}^{ss} + \Gamma_{[\pm 1]}\rho_{[\pm 1]}^{ss}}{\gamma} = \frac{\left(\frac{10}{9}s\right) \sin^2(\theta/2) \sin^2(\vec{k}_l \cdot \vec{x} + \phi)}{4 \tan^2(\theta/2) \tan^2(\vec{k}_l \cdot \vec{x} + \phi) + 1}. \quad (7.27)$$

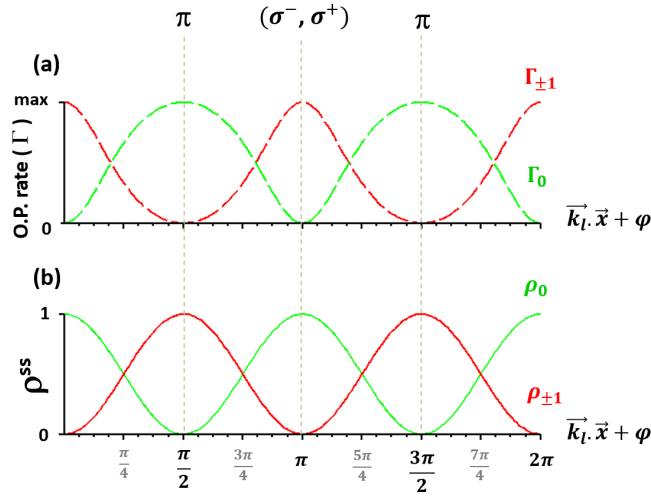


Figure 7.4: The comparison between (a) optical pumping rates and (b) steady-state populations for both  $|0\rangle$  and  $|\pm 1\rangle$  states as a function of position for the Lin. $\perp$ .Lin case.

In Fig. 7.4, the optical pumping rates (Eqs. 7.17 and 7.18) and steady-state populations of the two effective states (Eqs. 7.25 and 7.26) are compared for the case of  $\theta = \pi/2$ . As can be expected, when the optical pumping rate out of a state vanishes, that state is fully populated and the population of the other state is at a minimum, and vice versa.

### The external state of the trapped ion:

In the semiclassical approach of P-G cooling the external state of the trapped ion is treated classically. We reduce the cooling of a trapped ion in a 3-D trap to three independent 1-D equations for the energy along each principal trap axis, and distinguish the different directions by the label of  $i$ , where  $i = 1, 2, 3$ . This assumption will be tested later through simulation.

The total potential of a 1-D trapped ion in interaction with an off-resonant light field is  $U(x) = U_{osc}(x) + U_{ac}(x)$ . In this case, the ac Stark shift leads to a shift in the position of the minimum of the potential well. Since the ac Stark shift is state dependent, the shift in the potential will also be state dependent. The shift in the center of the potential well for the ion in the  $|j\rangle$  state can be found by solving for the minimum point of the energy  $U_{[j]}(x)$ . We can then rewrite the total potential as

$$U_{[j]}(x) = \frac{1}{2}M\omega_i^2 x_i^2 + U_{ac[j]}(x) = \frac{1}{2}M\omega_i^2 (x_i - x_{ic[j]})^2 + C_{[j]}, \quad (7.28)$$

where  $C_{[j]}$  represents a constant potential which is not of importance here since it is subtracted off when the change in energy is calculated for pumping events. In the LDL, the shift in the center of each potential well to lowest order in  $\eta$  is as follows:

$$x_{ic[0]} = -\frac{4}{3k_{li}} \left( \frac{\eta^2 s \Delta}{\omega_i} \right) \sin^2(\theta/2) \sin(2\phi) + \mathcal{O}(\eta^4), \quad (7.29)$$

$$x_{ic[\pm 1]} = \frac{2}{3k_{li}} \left( \frac{\eta^2 s \Delta}{\omega_i} \right) \cos^2(\theta/2) \sin(2\phi) + \mathcal{O}(\eta^4). \quad (7.30)$$

These equations indicate that the potential wells of the two states are shifted in opposite directions, and the direction of the shift depends on the sign of detuning  $\Delta$ .

To achieve optimum cooling, the center of the harmonic trap should be placed at the optimum point of maximum polarization gradient. In the LDL, the sizes of the ion's oscillations around the center of the potential well, and the shift of the center  $x_{ic}$ , are both very small compared to the laser's wavelength. The polarization varies on the same spatial scale as the wavelength, hence when the center of the trap is placed at the optimum point, it can be assumed that optimum cooling is achieved throughout the whole oscillation. For the Lin- $\perp$ -Lin polarization configuration presented here, the optimum point is located at  $\phi = \pi/4$ , which is in between the points of pure  $\pi^-$  polarization and the linear combination of  $(\sigma^+, \sigma^-)$ .

### A qualitative description of the P-G cooling of a trapped ion:

For both of the qualitative and quantitative descriptions to follow, it is assumed that the center of trap is located at the optimum cooling point, *i.e.*  $\phi = \pi/4$ , that the electric fields of the two counter-propagating Sisyphus beams are perpendicular, *i.e.*  $\theta = \pi/2$ , and that the beams are detuned above the resonance, *i.e.*  $\Delta > 0$ .

Figure 7.5 shows a simplified sketch of the Sisyphus cooling process of a single trapped  $^{171}\text{Yb}^+$ . The ion experiences the potential well  $U_{[\pm 1]}(x)$  when it is in the  $|\pm 1\rangle$  state, and  $U_{[0]}(x)$  when in the  $|0\rangle$  state. The centers of the two potential wells are separated by  $|x_{c[\pm 1]} - x_{c[0]}|$ . At each time, the ion's potential energy is defined based on the ion's



displacement from the center of the potential well it is experiencing. In the case shown in Fig. 7.5(a), an ion is oscillating in the  $U_{[\pm 1]}(x)$  potential well, and it goes through an optical pumping event when it gets to the point  $x_{o.p.}$ , displaced by  $\Delta x_{\pm 1}$  from  $x_{c[\pm 1]}$ , the center of  $U_{[\pm 1]}(x)$ . As a result of the optical pumping, the ion is transferred into the other state. Based on the approximation  $\omega_i \ll \gamma$  described above, the scattering event happens so fast that the ion will still be at the same position  $x_{o.p.}$  after the pumping. This means that the ion is now displaced by  $\Delta x_0$  from  $x_{c[0]}$ , the center of the new potential well  $U_{[0]}(x)$ . In this case, the optical pumping has brought the ion closer to the minimum point of its potential energy,  $|\Delta x_0| < |\Delta x_{\pm 1}|$ , which means that the ion has lost energy through the optical pumping event. Another optical pumping event can transfer the ion back to its original state. Depending on where the optical pumping occurs, the ion may gain or lose energy after the pumping event. Figures 7.5(b) and (c) depict possible heating and cooling

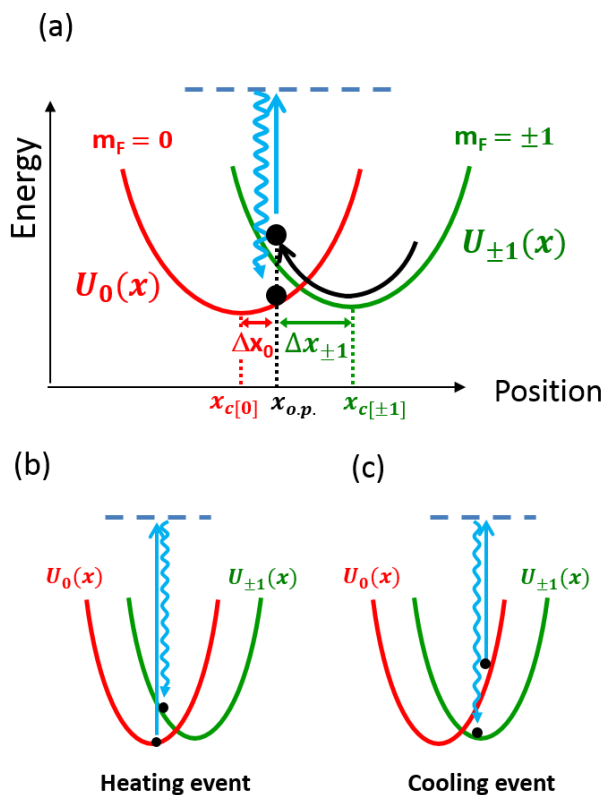


Figure 7.5: The Sisyphus cooling process of a single trapped  $^{171}\text{Yb}$  ion. (a) An ion in the  $|\pm 1\rangle$  state is oscillating in the  $U_{[\pm 1]}$  potential. At the point  $x_{o.p.}$ , displaced by  $\Delta x_{\pm 1}$  from the ion's potential center, an optical pumping event transfers the ion into the other state. As a result of optical pumping, the ion is brought closer to the center of its new potential  $U_{[0]}$  and loses energy. Samples of a (b) heating event and (c) a cooling event through optical pumping from the  $|\pm 0\rangle$  to the  $|\pm 1\rangle$  state.

events that can bring the ion back to its original state. After many of these optical pumping events, an overall cooling is obtained if the average number of cooling events is larger than the number of heating ones. This is achieved when the rate of optical pumping is higher at positions where it results in cooling compare to the positions where it results in heating. This condition is fulfilled when the center of the trap is placed at the optimum cooling point and the detuning is positive  $\Delta > 0$ .

### The quantitative description of the Sisyphus cooling mechanism:

After a long time compared to the optical pumping time ( $t > \Gamma^{-1}$ ), the variation of the external energy (kinetic and potential) can be expressed by:

$$\begin{aligned} \dot{E}(x) = & \rho_0^{ss} \langle \Gamma_{[0]} [U_{[\pm 1]} - U_{[0]}] \rangle_{[0]} + \rho_{[\pm 1]}^{ss} \langle \Gamma_{[\pm 1]} [U_{[0]} - U_{[\pm 1]}] \rangle_{[\pm 1]} \\ & + R_{dip} + R_{SE}, \end{aligned} \quad (7.31)$$

in which  $\langle \rangle_{[j]}$  represents the average over one period of oscillation in  $U_{[j]}$  potential. Similar to [67, 174], and based on the first approximation described above,  $\Gamma_j \ll \omega_i$ , the average population of each state is approximated by the population at the center of the trap, *i.e.* the averaged point. The first and second terms of Eq. 7.31 describe the average rates at which the potential changes due to  $|0\rangle \rightarrow |\pm 1\rangle$  and  $|\pm 1\rangle \rightarrow |0\rangle$  transitions, which include both cooling and heating events, and the last two terms describe heating terms. (Note that the small Doppler heating effect of the blue-detuned Sisyphus beams are neglected. This is acceptable as long as the Sisyphus beams are sufficiently far detuned, see [174]). The first one of two heating terms,  $R_{dip}$ , is the diffusive heating due to the fluctuations in the dipole force, and is calculated according to [189, 190] and ignoring Zeeman coherences. For a single running wave, this term would correspond to recoil heating on photon absorption as used in the Doppler cooling section (Chapter 4, Section 3). For the polarization-gradient standing wave,  $R_{dip}$  can be written as

$$R_{dip} = \frac{2}{3} \gamma s f_{li} E_r \left[ \frac{1}{2} \cos^2(\theta/2) \sin^2(\phi) (\rho_{-1} + \rho_1) + \sin^2(\theta/2) \cos^2(\phi) \rho_0 \right]. \quad (7.32)$$

The second of the two heating terms,  $R_{SE}$ , is the diffusive heating due to the random direction of spontaneously emitted photons (or equivalently recoil heating on emission), which can be written as

$$R_{SE} = \gamma \rho_{ee} f_{si} E_r = \frac{2}{3} \gamma s f_{si} E_r \left[ \frac{1}{2} \cos^2(\theta/2) \cos^2(\phi) (\rho_{-1} + \rho_1) + \sin^2(\theta/2) \sin^2(\phi) \rho_0 \right]. \quad (7.33)$$

At the optimum cooling point  $\phi = \pi/4$ , and assuming  $\theta = \pi/2$ , the summation of the two heating terms simplifies to

$$R_{dip} + R_{SE} = \gamma \rho_{ee} E_r (f_{li} + f_{si}). \quad (7.34)$$

Here,  $E_R$  is the recoil energy. Also,  $f_{li}$  and  $f_{si}$  are the same as Chapter 4 and reflect the average components of the absorption and emission recoil kicks along the  $i^{th}$  direction, where  $f_{si} = 1/3$  for isotropic emissions.

In the LDL, Eq. 7.31 can be Taylor expanded in  $k_{li}x_i$  up to second order. Ignoring the third and higher orders of the Lamb-Dicke parameter, the averages over first- and second-order terms can be simplified as

$$\langle k_{li}x_i \rangle_{[j]} = k_{li}x_{ci[j]}, \quad (7.35)$$

$$\langle (k_{li}x_i)^2 \rangle_{[j]} = \frac{2\eta_i^2 E}{\hbar\omega_i} + \mathcal{O}(\eta^4), \quad (7.36)$$

where  $x_{ci[j]}$  is the center of  $U_{[j]}$  potential well, and  $\eta_i$  represents the Lamb-Dicke parameter along the motion of interest, for which  $k_l \rightarrow k_{li}$  in the definition of LD parameter (Eq. 7.19). Substituting the averaged expressions of Eqs. 7.35 and 7.36 into the Taylor expanded Eq. 7.31, and ignoring terms of order  $\mathcal{O}(\eta^3)$  and higher, the rate equation of external energy simplifies to a linear function of energy, from which the cooling rate  $\Gamma_c$  and steady-state energy  $E_{ss}$  can be derived:

$$\dot{E} = -\Gamma_c E + R_{heat} = -\Gamma_c (E - E_{ss}), \quad (7.37)$$

$$E_{ss} = \frac{R_{heat}}{\Gamma_c} = \hbar\omega_i \left( \bar{n} + \frac{1}{2} \right). \quad (7.38)$$

Here,  $R_{heat}$  is the total heating term. At the optimum cooling point  $\phi = \pi/4$  and assuming  $\theta = \pi/2$ , we obtain the cooling rate, heating term and steady-state energy expressed in standard format as follows:

$$\Gamma_c = \frac{32}{45} (\eta_i^2 s\gamma) \xi_i, \quad (7.39)$$

$$R_{heat} = \frac{32}{45} \hbar\omega_i (\eta_i^2 s\gamma) \xi_i^2 + \frac{1}{10} (s\gamma) \left( f_{li} + \frac{1}{3} \right) E_R, \quad (7.40)$$

$$E_{ss} = \hbar\omega_i \left[ \xi_i + \frac{9}{64} \left( 1 + \frac{1}{3f_{li}} \right) \frac{1}{\xi_i} \right], \quad (7.41)$$

with

$$\xi_i = \frac{s\Delta}{8\omega_i}. \quad (7.42)$$

It can be seen that a positive cooling rate is only obtained when the laser is blue-detuned ( $\Delta > 0$ ). The cooling rate is proportional to  $s^2$  as predicted in earlier works [67, 174]. The first part of the total heating term in Eq. 7.40 is coming from heating events associated

with switching potentials, and is proportional to  $s^3$ . The second part is related to diffusion terms noted above and changes linearly with  $s$ . At low laser intensities, the heating linear in  $s$  dominates and  $E_{ss}$  diverges. At higher laser intensities, the first part of the heating term, proportional to  $s^3$ , overcomes the cooling and  $E_{ss}$  increases. There is an optimum laser intensity at which the cooling and heating rates are optimized, and the minimum steady-state energy is obtained. At the optimum power corresponding to  $\xi_i = \frac{3}{8} \left(1 + \frac{1}{3f_{ii}}\right)$ , the ion can be cooled to a minimum value of  $\bar{n} \simeq 0.5 - 1$  for  $f_{ii}$  between 1 and 1/2.

In summary, the analytical semiclassical model that we have presented above is a 1-D model of P-G cooling in the LDL, which provides a basic understanding of how the Sisyphus cooling works in our setup. However, the treatment of the internal energy-level structure involved in the  $S_{1/2} \rightarrow P_{1/2}$  cooling transition, was overly simplified by ignoring the ground-state coherences, and reducing the system into an effective two-state model. Additionally, only the  $P_{1/2}(F = 0)$  excited state was considered; that is, the  $P_{1/2}(F = 1)$  state which is 2.1 GHz away was ignored (see Fig. 7.1). In our experiment, the Sisyphus beams are detuned by  $\Delta = 2\pi(310 \text{ MHz}) \sim 16\gamma$  above the  $P_{1/2}(F = 0)$  state, which corresponds to a detuning of  $\Delta' = 2\pi(-1800 \text{ MHz}) \sim 92\gamma$  below the  $P_{1/2}(F = 1)$  state. This means that the saturation parameter for the  $P_{1/2}(F = 1)$  state is  $\sim 30$  times smaller than for the  $P_{1/2}(F = 0)$  state, and therefore the rate of optical pumping ( $\propto s$ ) due to the  $P_{1/2}(F = 1)$  state is a factor of  $\sim 30$  smaller as well. Note that the scattering from the  $P_{1/2}(F = 1)$  state also leads to loss of the ion from the cooling cycle into the  $S_{1/2}(F = 0)$  state. Compared to the  $P_{1/2}(F = 0)$  state the ac Stark shift ( $\propto s\Delta$ ) due to the  $P_{1/2}(F = 1)$  state is only a factor of  $\sim 5$  smaller, and can not be easily ignored.

Another major distinction between the above analytical model and the actual experiment is the lattice modulation. Parking the center of the trap at the optimum point and remaining there is very difficult experimentally, since it requires interferometric stability between the Sisyphus beams. To go around this problem we modulate one of the beams with respect to the other by a frequency of  $\omega_m$ . This will provide a moving standing wave that runs over the center of the trap, and the constant phase will change to  $\phi = (1/2)\omega_m t$ . The price of modulation is a lower cooling rate and a higher  $\bar{n}$  at the end, by roughly a factor of 2. The results of the analytical semiclassical model that we present later for comparison to analytical quantum and semiclassical simulations, consider the effect of the  $P_{1/2}(F = 1)$  state and treat the three Zeeman sub-levels of the ground state separately.

To extend the analytical calculations and obtain a more accurate model of the experimental situation, simulations were used. Although the development of the simulations are not part of this thesis work, we include a brief description of both semiclassical and quantum simulation features at the end of both approaches.

### 7.3.4 Semiclassical simulations of P-G cooling

The semiclassical simulation is similar to the one that we used for the KZM studies, and similar to the previous simulations done for the  $J = 1/2 \rightarrow J = 3/2$  transition [184]. We perform a Monte-Carlo simulation to solve for the classical motion of a single ion trapped in an ideal harmonic potential (*i.e.* under the pseudo-potential approximation) and in the presence of a Doppler beam and Sisyphus beams. For the semiclassical simulations used for the comparison to the experimental results, the lattice modulation of  $\omega_{mod}/2\pi = 0.080$  MHz is also added. In the simulation, a large number of independent particles are tracked simultaneously (typically 1000) and their positions and velocities are recorded vs. time. At the end of the simulation, energy is calculated by averaging over the ions. The basic sequence of the simulation is similar to the actual experiment. It starts with a period of equilibration to the Doppler temperature. The effect of Doppler cooling is included by calculating the number of photons scattered at each time step from a Poissonian distribution, which allows for a longer time step to be used. Each scattering event includes an absorption and a spontaneous emission. For the absorption, a full  $^{171}\text{Yb}^+$  resonance response expression (including magnetic field, polarization and the Doppler shift) is considered. For the spontaneous emission, the recoil distribution is determined from the magnetic field direction, and a random recoil is added to the ion's velocity for each emission event. At the end of the Doppler cooling time in the simulation, the Doppler beam is then removed and the Sisyphus beams become active. The effect of the Sisyphus beams is integrated into the motion by adding the force due to the ac Stark shift of both  $P_{1/2}(F = 0)$  and  $P_{1/2}(F = 1)$  states to the harmonic force of the trap. At each time step, the small probability of a pumping event between the three Zeeman states of  $S_{1/2}(F = 1)$  is calculated where only scattering from the  $P_{1/2}(F = 0)$  state is included. For each initial Zeeman state, there is a probability of a pumping event back to itself or into the other states. For each pumping event, a random recoil is included to account for the momentum diffusion due to spontaneous emission. The effect of recoil on absorption in [184] is replaced with a more general expression for the dipole force fluctuations suitable for all values of  $\phi$  (Eq. 7.32). The small Doppler heating effect of Sisyphus beams is ignored.

In the simulations, a lowest order correction due to the ground-state Zeeman coherences was implemented with the effect of modifying the pumping rates and ac Stark shifts of the outer  $m_F = 1$  and  $m_F = -1$  states. This improves the modeling of the Zeeman populations in the simulation at higher laser intensities, but ultimately has negligible effect on the cooling rate or steady-state energy, so it is not included in the results. Even though the scattering rate from the  $P_{1/2}(F = 1)$  state is small, it gives a noticeable contribution to the cooling limit, and so we have applied a correction factor where appropriate.

A final comment, the semiclassical simulation allows for the calculations to be done in 3-D, outside the Lamb-Dicke regime, and for a modulating lattice.

### 7.3.5 P-G cooling of a bound ion– quantum approach

In the quantum approach to modeling Sisyphus cooling, the motion of the trapped ion is treated quantum mechanically. This method also naturally allows the atom-laser interaction to be treated quantum mechanically including the effect of coherences in the ground and excited state manifolds. A fully quantum treatment of laser cooling can be obtained by deriving and solving the master equation for a trapped ion interacting with the cooling laser beams. In [158, 191, 192], the master equations for a two-level and three-level atom trapped in a harmonic potential and interacting with a running wave were derived and solved in the LDL. Cirac *et al.* [175] extended this work to a multi-level atom, general trap potential, and both running- and standing-wave configurations.

The master equation of a trapped ion interacting with a laser field can be written in terms of the density operator  $\rho$  as follows:

$$\frac{d\rho}{dt} = -\frac{i}{\hbar}[H, \rho] + \mathcal{L}\rho. \quad (7.43)$$

Here,  $H$  is the total Hamiltonian, and  $\mathcal{L}$  accounts for the damping caused by spontaneous emission and includes the recoil momentum transfer as a result of spontaneously emitted photons. The total Hamiltonian of the system includes three terms and is given by

$$H = H_{osc} + H_{int} + V_{dip}. \quad (7.44)$$

The terms are as follows:

1 –  $H_{osc}$  describes the harmonic trap potential,  $H_{osc} = \hbar\omega_i(a_i^\dagger a_i + \frac{1}{2})$ , where  $a_i$ , and  $a_i^\dagger$  are the annihilation and creation operators of a quantum of vibrational energy  $\hbar\omega_i$  along the  $i^{th}$  direction, where  $i = \{1, 2, 3\}$ . The eigenstates of  $H_{osc}$  are the Fock states  $|n\rangle$  and the eigenvalues are  $E_n = \hbar\omega_i(n + \frac{1}{2})$ .

2 –  $H_{int}$  describes the internal energy levels of the ion in the absence of the laser, and includes the Zeeman effect due to the external magnetic field.

3 –  $V_{dip}$  describes the ion-laser dipole interaction and is the same as Eq. 7.8, with  $x_i$  considered as an operator.

In the LD regime, the master equation of the trapped ion interacting with a laser field will have the same familiar form as the master equation of a damped harmonic oscillator interacting with a finite-temperature heat bath [158, 175]. In this case, the diagonal elements of the density matrix in the basis of Fock states, *i.e.* populations,  $\langle n|\rho|n\rangle = p_n$ , evolve as

$$\frac{dp_n}{dt} = (n+1)A_-p_{n+1} - [(n+1)A_+ + nA_-]p_n + nA_+p_{n-1}, \quad (7.45)$$

where the  $A_+$  and  $A_-$  coefficients determine transition rates between the Fock states.  $A_+$  is related to a heating event  $n \rightarrow n+1$ , and  $A_-$  is related to a cooling event  $n \rightarrow n-1$ .

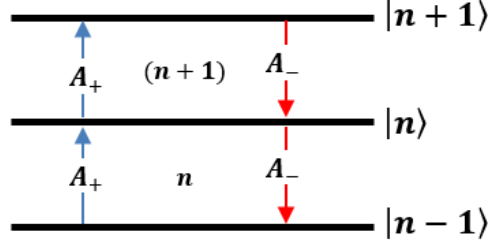


Figure 7.6: Illustration of the transition rates between the three Fock states using the rate coefficients  $A_+$  and  $A_-$ .

The first and last terms of Eq. 7.45 account for the transitions from the higher and lower Fock states into the  $|n\rangle$  state. The middle term describes the case of depopulation of the  $|n\rangle$  state into the higher and lower Fock states. The rate coefficients  $A_{\pm}$  are described as

$$A_{\pm} = 2Re[S(\mp\omega_i) + D], \quad (7.46)$$

where  $D$  is the diffusion coefficient due to spontaneous emission, and  $S(\omega_i)$  is the power spectrum of the dipole force fluctuations. The scaled dipole force operator is given by

$$F_i = -\frac{1}{k_{li}} \left. \frac{dV_{dip}}{dx_i} \right|_{x_i=0}. \quad (7.47)$$

The power spectrum  $S(\omega_i)$  can be calculated from a Fourier transform of the correlation function of the force

$$S(\omega_i) = \eta^2 \int_0^{\infty} dt e^{i\omega_i t} \langle F(t)F(0) \rangle_{ss}, \quad (7.48)$$

where  $\langle \rangle_{ss}$  refers to an expectation value calculated from the steady state of the internal ion dynamics. The dynamics of the average vibrational number  $\bar{n} = \sum_{n=0}^{\infty} np_n$  obeys the following equation:

$$\frac{d\bar{n}}{dt} = -(A_- - A_+)\bar{n} + A_+. \quad (7.49)$$

This equation has the same form as the energy-rate equation of the semiclassical approach (Eq. 7.37). The cooling rate  $\Gamma_c$ , and the steady-state  $\bar{n}$  are

$$\Gamma_c = A_- - A_+, \quad (7.50)$$

$$\bar{n}_{ss} = \frac{A_+}{A_- - A_+}. \quad (7.51)$$

For completeness, the equivalent of the heating term in the semiclassical equations is given by

$$R_{heat} = \hbar\omega_i \left( \frac{A_+ + A_-}{2} \right). \quad (7.52)$$

The 1-D analytical quantum calculations for the Sisyphus cooling of a single trapped  $^{171}\text{Yb}$  ion are performed using MAPLE software (with the added RACAH package for calculating Clebsch-Gordan coefficients). For the  $S_{1/2} - P_{1/2}$  transition involved in cooling, we include the full hyperfine structure for ground and excited states<sup>3</sup>. To find the cooling rate and final temperature, we start by deriving the dipole interaction operator and then calculate the dipole force operator. To calculate the fluctuation spectrum of the force,  $S(\omega_i)$ , we follow closely the procedure laid out in [175]. The diffusion term is also defined as  $D = (\gamma/2)\eta^2 f_{si} \sum_j \rho_{ee[j]}$ , where the summation is over both  $P_{1/2}(F=1)$  and  $P_{1/2}(F=0)$  excited state sub-levels, and for our case of isotropic scattering, we have  $f_{si} = 1/3$ . From the obtained values of  $D$  and  $S(\omega_i)$ , the transition rate coefficients  $A_{\pm}$ , and finally the cooling rate and steady-state  $\bar{n}$  are calculated. The results of these calculations are shown in the next section, where we compare the semiclassical and quantum analytical calculations with the semiclassical simulation.

In summary, compared to the 1-D analytical semiclassical model of the P-G cooling, the 1-D analytical quantum model treats the motion of the ion quantum mechanically and directly accounts for the effect of ground-state coherences, hyperfine states, and Doppler heating. However, this model is only suitable for a stationary lattice and the LD regime. To include the effect of phase modulation and to allow for the ability to investigate the cooling behaviour outside the LDL, we perform a quantum simulation.

### 7.3.6 Quantum simulation of P-G cooling

The quantum simulation is performed using the quTip Python package. This is a 1-D model and it includes the hyperfine structure with some limited approximations: The relaxation due to spontaneous emission includes the decay of Zeeman coherences into ground-state coherences, but ignores the effect of coherences between the well separated hyperfine manifolds. The lower  $S_{1/2}(F=0)$  hyperfine state is eliminated by assuming that any population of that state is immediately repumped back to the  $S_{1/2}(F=1)$  state. Similar to the semiclassical simulation, the trap is treated in the pseudo-potential approximation, and a lattice modulation of  $\omega_{mod}/2\pi = 0.080$  MHz is added in relevant cases. Each point is an average over a minimum of 40 monte carlo wavefunction trajectories. The majority of simulations are limited to a Hilbert space of 20 motional levels and use an initial Fock state of  $n_i = 8$  rather than a thermal state at Doppler temperature. For simulations starting in an initial thermal state of  $\bar{n} = 22$ , which is similar to the experiment, the simulations are expanded

---

<sup>3</sup> A continuous (recoilless) depopulation of the  $S_{1/2}(F=0)$  state is assumed for the calculations, whereas in the experiment a pulsed re-pump sequence is used (see later).



to a Hilbert space of 200 motional levels to avoid truncating the distribution. Increasing the size of the Hilbert space by a factor of 10 increases the calculation time considerably. For example at low laser intensities, where calculations take the longest, 80 processors with 7 days/processor would be required to find the cooling rate and  $\bar{n}_{ss}$  (compared to 40 processors with 3.5 days/processor for the smaller Hilbert space). A 3-D quantum simulation can take months to find the cooling rate and  $\bar{n}_{ss}$  for one laser intensity value. As a result, we only use a 1-D quantum simulation and use a 3-D semiclassical simulation to investigate the effect of motion in the other axes.

## 7.4 Comparison between analytical theoretical models and simulations

In this section, we compare the outcomes of the analytical theoretical models and semiclassical simulations under different conditions. Similar to our experimental measurements, we first investigate the cooling rate and cooling limit as a function of the cooling laser intensity and compare the predictions of the analytical models and semiclassical simulations in a situation that fits into the assumptions of all the models. Then we continue with tuning the parameters to investigate the effect of discrepancies between the models. The effect of the proximity to the Lamb-Dicke regime is studied by varying the trap frequency. The effect of ground-state coherences is studied by varying the magnetic field, and laser intensity. Finally, the effect of phase modulation is studied by varying the phase  $\phi$ .

### 7.4.1 Perfect assumptions, excellent match

Starting with a situation that fits into the assumptions of all the models, we investigate the laser intensity dependence of the cooling rate and steady-state energy, and compare the predictions of 3-D and 1-D semiclassical simulations to both 1-D semiclassical and 1-D quantum analytical models. Here, we consider the case of a static polarization gradient with the center of the trap located at the optimum cooling point of  $\phi = \pi/4$ . To assure that the system is in the Lamb-Dicke regime (which is an assumption for both semiclassical and quantum analytical models), we use trap frequencies of  $\{\omega_x, \omega_y, \omega_z\} = 2\pi\{2.258, 2.298, 1.575\}$  MHz, which are a factor of three higher than the experiment values. The projection of the laser beams' wave-vectors along the  $\{x, y, z\}$  directions are assumed to be the same as the experiment, namely  $\{k_x, k_y, k_z\} = \frac{2\pi}{\lambda}\{\frac{1}{2}, \frac{-1}{2}, \frac{1}{\sqrt{2}}\}$ . For the given trap frequencies, the Lamb-Dicke parameters associated with each direction are  $\{\eta_x, \eta_y, \eta_z\} = \{0.030, 0.031, 0.052\}$ , for which the system can be considered within the LD regime for the Doppler-cooled condition. Since the effect of ground-state coherences is ignored in the semiclassical models, a large magnetic field resulting in a Zeeman shift of  $\delta_B/2\pi = 18.2$  MHz is considered to reduce the effect of

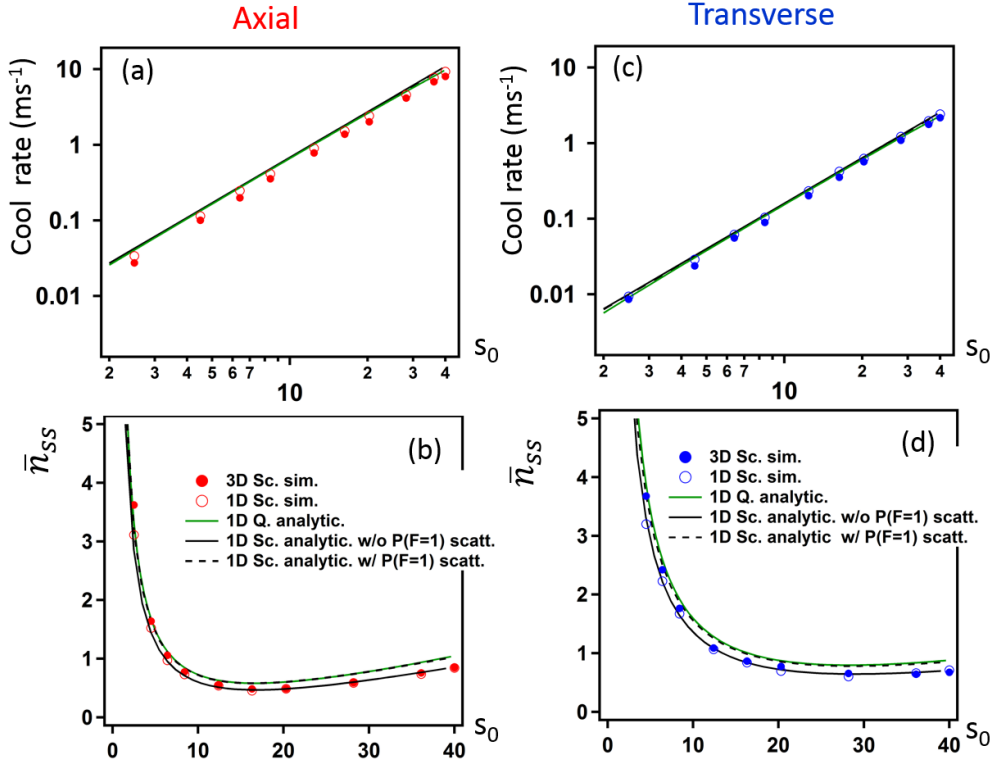


Figure 7.7: The calculation results of laser intensity dependence of the cooling rate (a and c) and cooling limit (b and d) in the axial (a and b) and transverse (c and d) directions. Calculations shown are the 3-D semiclassical simulation (filled circles), 1-D semiclassical simulation (open circles), analytical semiclassical model (black lines), and analytical quantum model (green line). The semiclassical analytical plots show a model with both ac Stark shift and scattering due to the  $P_{1/2}(F=1)$  state (black dashed line) and with the scattering effect omitted (black solid line). The related parameters are  $\{\eta_y, \eta_z\} = \{0.031, 0.052\}$ ,  $\delta_B/2\pi = 18.2$  MHz,  $\Delta/2\pi = 310$  MHz,  $\theta = \pi/2$ , and  $\phi = \pi/4$ .

coherences in the quantum models as well. (The experiment value of the Zeeman shift is  $\delta_B/2\pi = 8.2$ .) All the other related terms are similar to the experiment values.

In Fig. 7.7, we plot the cooling rate  $\Gamma_c$  and the steady-state  $\bar{n}$  as a function of the single beam saturation parameter  $s_0$  (*i.e.* laser intensity), in the axial ( $\hat{z}$ ) and transverse ( $\hat{y}$ ) directions. It can be seen that the results of all the models agree pretty well. For these conditions, the 1-D and 3-D semiclassical simulations match well, indicating that the effect of motion of other axes can be ignored and the problem can be treated as three 1-D cooling situations. The figure also includes the semiclassical analytical model both with and without scattering from the  $P_{1/2}(F=1)$  state included. The difference is small for these parameters. The model without scattering matches the simulation as expected.

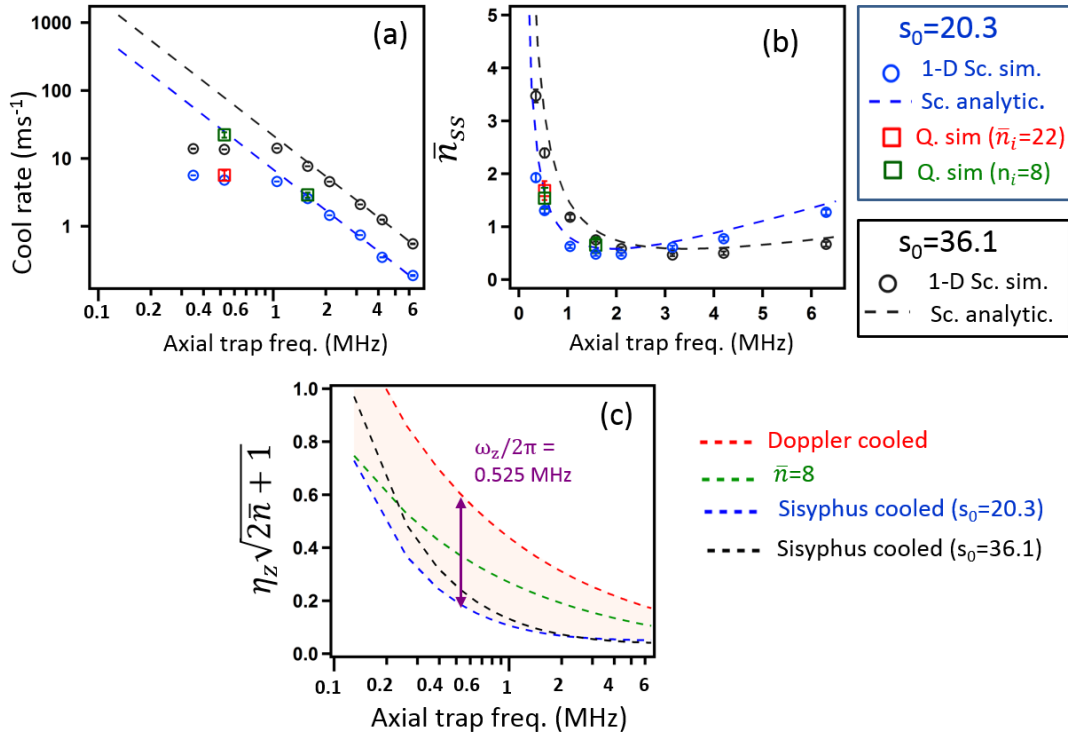


Figure 7.8: The results of the (a) cooling rate and (b) steady-state  $\bar{n}$  as a function of the axial trap frequency for two laser saturation parameters of  $s_0 = 20.3$  and  $s_0 = 36.1$ . The open circles are the results of 1-D semiclassical simulations and the dashed lines are the 1-D semiclassical analytical model (derived for the LD regime). Also, the squares represent the results of 1-D quantum simulations for  $s_0 = 20.3$ , and starting with an initial state of  $n_i = 8$  (green) and an initial Doppler thermal distribution (red). (c): The condition for the LDL is investigated in a plot of  $\eta_z \sqrt{2\bar{n} + 1}$  vs. axial frequency for the range of Doppler-cooled to Sisyphus-cooled average energies. The operation point of our experiment at  $\omega_z/2\pi = 0.525$  MHz is indicated. Other parameters are;  $\delta_B/2\pi = 18.2$  MHz,  $\Delta/2\pi = 310$  MHz,  $\theta = \pi/2$ , and  $\phi = \pi/4$ .

#### 7.4.2 The effect of the Lamb-Dicke regime:

To study the effect of the LD regime, the predictions of the 1-D semiclassical simulation are compared to the semiclassical analytical model over a wide range of axial trap frequencies. For this comparison, the cooling rate and  $\bar{n}_{ss}$  are calculated as a function of the axial trap frequency for two laser saturation parameters of  $s_0 = 20.3$  and  $s_0 = 36.1$ , which are chosen since they give simulations that are fast to run on computer due to the high cooling rates. We continue to use a static polarization gradient with  $\phi = \pi/4$  and the same Zeeman shift of  $\delta_B/2\pi = 18.2$  MHz. The semiclassical simulation is still performed in the same way as described before, where Doppler cooling is followed by Sisyphus cooling.

Before presenting the results, we note that as the trap gets weaker, the initial Doppler energy is the same, but the value of the corresponding  $\bar{n}$  increases. As a result, the size of the ion position fluctuations,  $\sqrt{\langle z^2 \rangle}$ , grows, and eventually the condition for the LDL ( $\sqrt{k_z^2 \langle z^2 \rangle} \simeq \eta_z \sqrt{2\bar{n} + 1} \ll 1$ ), will not be fulfilled. Figures 7.8(a) and (b) show the cooling rate and steady-state  $\bar{n}$  as a function of the axial trap frequency for the range of  $\omega_z/2\pi = 0.13 - 6.5$  MHz. Comparing the results of the semiclassical simulation and semiclassical analytical model, a deviation in the cooling rate from the LD theory at lower frequencies can be observed. The transition in behaviour is remarkably sharp. The conclusion one can infer is that as  $\bar{n}$  gets high and the size of ion wave-packet size grows to be comparable to the extent of the polarization gradient, the cooling rate gets weaker. Note that the  $\bar{n}_{ss}$  predictions of the LD theory and simulation match pretty well, which indicates that eventually as the ion's thermal energy is brought close to the ground state, the ion lies within the LDL.

In Fig. 7.8(c), the condition for the LD regime is investigated for the range of Doppler-cooled to Sisyphus-cooled energies. Our experiment is performed at an axial frequency of  $\omega_z/2\pi = 0.525$  MHz. At this frequency, the LD limit is reasonably well satisfied for low  $\bar{n}$ , so in the final stages of the cooling the LD theory should hold, and the steady-state  $\bar{n}$  should be correctly predicted by the LD theory. For the initial Doppler temperature, however, the size of the ion's position fluctuations grows by a factor of  $\sim 3$  such that the value of  $\sqrt{k_z^2 \langle z^2 \rangle} \approx 0.6$  is approaching unity. As a result, it is reasonable to expect to see an effect on the cooling rate. We also see similar effects in the quantum simulations. For our axial quantum simulations, most are done with a limited Hilbert space of 20 and for an initial state of  $|n_i = 8\rangle$ , but selected points have also been done with an initial Doppler thermal state with  $\bar{n}_i = 22$  to illustrate the difference (see Fig. 7.8 (a) and (b)). (The simulations with  $\bar{n}_i = 22$  require a 10 times larger Hilbert space and take a considerable time). We have emphasized the axial direction here, since as will be seen, the transverse direction in our setup does not show a strong deviation in cooling rate from the LD prediction. The trap frequency is higher ( $\omega_y/2\pi = 0.790$  MHz) and the polarization gradient is softer due to smaller  $\vec{k}$ -projection.

### 7.4.3 The effect of ground state coherences:

To investigate the effect of ground-state coherences, we use the 1-D quantum analytical model which inherently includes the effect of ground-state coherences, and we study the cooling rate and the steady-state  $\bar{n}$  as a function of the external magnetic field  $B$ . We choose a laser intensity corresponding to  $s_0 = 15$ , which is close to the optimum laser intensity for our experimental setup. In the limit of large magnetic fields, we expect the effect of coherences to become negligible and the system should reach a relatively steady behaviour in  $B$ . Figures 7.9 (a) and (b) indeed show that the cooling rate and steady-state  $\bar{n}$  start to stabilize at  $\delta_B/2\pi \simeq 4$  MHz and eventually approach the semiclassical prediction. Below

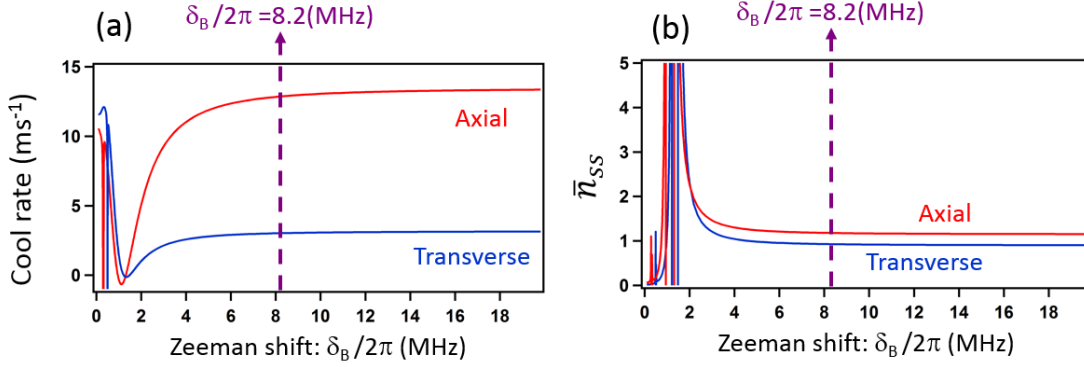


Figure 7.9: (a) Cooling rate and (b) steady-state  $\bar{n}$  as a function of the Zeeman shift, calculated using the 1-D quantum analytical model. Parameters used for the plots are an axial trap frequency  $\omega_z/2\pi = 0.525$  MHz, transverse trap frequency  $\omega_y/2\pi = 0.766$  MHz,  $s_0 = 15$ ,  $\theta = \pi/2$ , and  $\phi = \pi/4$ .

this value, ground-state coherences grow in strength and Raman resonances are encountered when the combined Zeeman and ac Stark shifts coincide with the trap frequencies. The decrease in cooling rate below  $\delta_B/2\pi = 4$  MHz is not surprising since dark-state formation will suppress the photon scattering. The complicated behaviour of the cooling rate near zero magnetic field is associated with EIT cooling and heating effects [183,193]. Our experiment is operated at  $\delta_B/2\pi = 8.2$  MHz, which lies in the safe region for the laser intensity shown in Fig. 7.9. Note that the magnetic field dependence varies with the laser intensity and at higher intensities we expect the system to stabilize at larger Zeeman shifts. For  $\delta_B/2\pi = 8.2$  MHz, the onset of coherence effects occurs for  $s_0 > 40$ , where an EIT heating effect appears for values of  $\phi$  near  $\pi/2$ .

#### 7.4.4 The effect of phase modulation:

Modulation of the lattice phase  $\phi$  causes the ion to experience a varying polarization-gradient. To understand the effect of the phase  $\phi$  on the P-G cooling, we first show in Fig. 7.10 (a), (b) and (c) the transverse heating rate, cooling rate and steady-state  $\bar{n}$  as a function of  $\phi$ . The Zeeman shift and the trap frequencies used for these calculations are similar to the ones used in our experiment:  $\delta_B/2\pi = 8.2$  MHz and  $\omega_y/2\pi = 0.766$  MHz. The time scale of the modulation plays an important role. For a slow average ( $\Gamma_c \ll \omega_m \ll \Gamma$ ), the steady-state  $\bar{n}$  can be determined from the cooling and heating rates averaged over  $\phi$ , *i.e.* averaging over the values shown in Fig 7.10 (a), and (b). For a fast average ( $\Gamma_c \ll \Gamma \ll \omega_m \ll \omega_i$ ), the ion's internal state cannot follow the changing laser polarization adiabatically. In this case, the Zeeman populations in the semiclassical model are replaced with ones determined from the phase-averaged pumping rates. Of course, for very fast modulation exceeding the trap frequency, the cooling will be suppressed. For

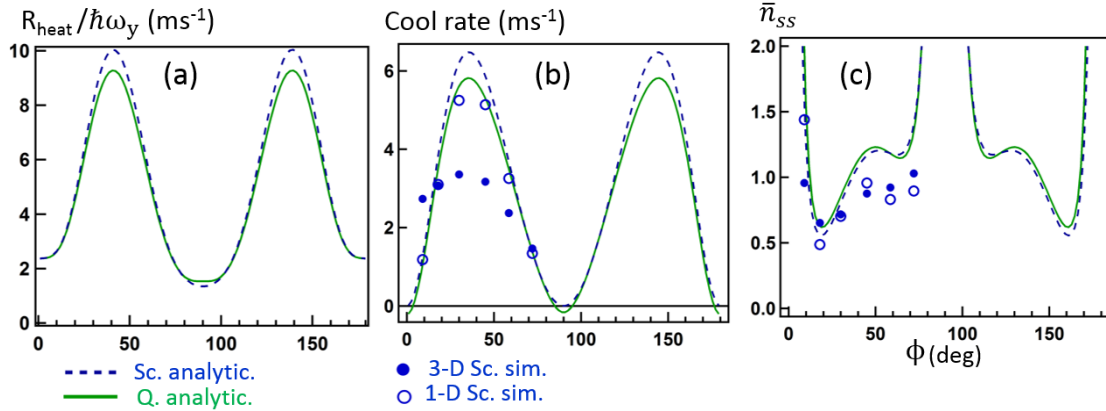


Figure 7.10: (a) Cooling rate, (b) heating rate, and (c) steady-state  $\bar{n}$  as a function of phase  $\phi$ . The calculations are for the transverse direction with  $\omega_y/2\pi = 0.766$  MHz and at a saturation parameter of  $s_0 = 20.3$ . The other parameters are similar to the ones used in the experiment:  $\delta_B/2\pi = 8.2$  MHz,  $\Delta/2\pi = 310$  MHz, and  $\theta = \pi/2$ . The blue circles show the 3-D (filled circle) and 1-D (open circle) semiclassical simulations. The lines represent the analytical models, where the black dashed line is a semiclassical model and the green line is a quantum model. The discrepancy in  $\bar{n}_{ss}$  between simulation and analytical models in (c) is due to the omission of the  $P_{1/2}(F = 1)$  state's pumping effect in the simulations.

our experiment with  $\omega_m/2\pi = 0.08$  MHz, we are in between the slow and fast limits. In Fig. 7.11 we show the effect of slow and fast modulation compared to the optimum static case at  $\phi = \pi/4$  and compared to simulations at  $\omega_m/2\pi = 0.08$  MHz. As a result of the phase modulation, the cooling rate is reduced by a factor of  $\sim 2$ , and the cooling limit (minimum steady-state  $\bar{n}$ ) is higher by about the same amount. The difference between slow and fast averages is not very large, and either case matches the simulations reluctantly well.

The residual discrepancy in  $\bar{n}_{ss}$  between the semiclassical and quantum simulations in Fig. 7.11(b) is primarily due to the omission of scattering from the  $P_{1/2}(F = 1)$  states. For the modulated case, we find that a simple correction vs.  $s_0$  can be applied to account for this effect. The correction is determined from a comparison of the semiclassical and analytical models with and without the effect of the  $P_{1/2}(F = 1)$  scattering. The corrections for the slow and fast averaging limits of the theory match closely. The effect of applying the correction to the semiclassical simulation is shown in Fig. 7.12. The agreement with the quantum simulation is improved. The correction factor is included in our comparison to the experiment. Note that the  $P_{1/2}(F = 1)$  pumping effect has little effect on the cooling rate and so no correction is performed. The phase modulated and corrected semiclassical simulation and the phase modulated quantum simulation will be used in Section 7.8 for the comparison to the experimental results, but first we discuss the two-photon stimu-

lated Raman transition technique, which is used for the thermometry in Sisyphus cooling measurements.

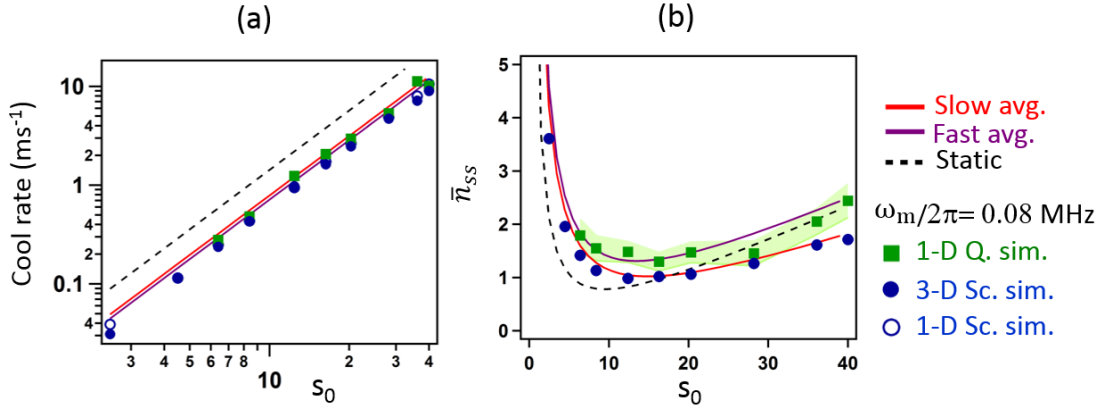


Figure 7.11: Phase averaged (a) cooling rate and (b) steady-state  $\bar{n}$  as a function of  $s_0$ . The effect of slow (red line) and fast (purple line) modulation is compared to the static case at the optimum point (black dashed line). Also, the 3-D/1-D semiclassical simulation (blue circles) and 1-D quantum simulation (green square) for a lattice modulation of  $\omega_m/2\pi = 0.08$  MHz, are shown for comparison. The shaded region indicates the standard deviation of the  $\bar{n}$  fluctuations in steady state for the quantum simulation. The uncertainty in  $\bar{n}_{ss}$  value is similar. These plots are calculated for the transverse direction with  $\omega_y/2\pi = 0.766$  and  $\delta_B/2\pi = 8.2$  MHz,  $\Delta/2\pi = 310$  MHz, and  $\theta = \pi/2$ .

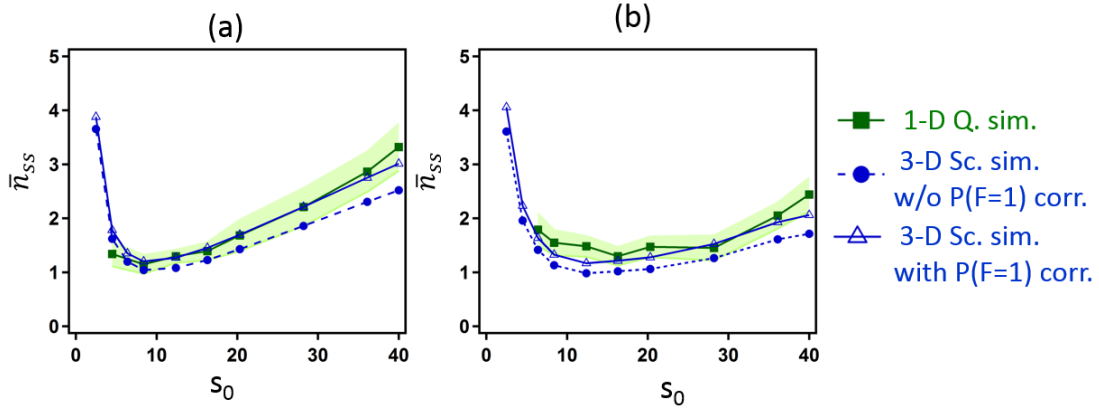


Figure 7.12: The  $P_{1/2}(F = 1)$  state pumping correction to 3-D semiclassical simulations of  $\bar{n}_{s,s}$  vs.  $s_0$  for the (a) axial and (b) transverse directions. The green squares are 1-D quantum simulation and blue filled circles are 3-D semiclassical simulation without any correction (same as Fig. 7.11(b)). The open blue triangles are 3-D semiclassical simulations considering the effect of the  $P_{1/2}(F = 1)$  scattering.

## 7.5 Motion-sensitive stimulated Raman transitions

Following the treatment of [20, 183], we briefly summarize the theory behind stimulated two-photon Raman transitions and the application of motion-sensitive transitions for thermometry of a trapped ion. The thermometry will be used to evaluate the Sisyphus cooling performance. In a later section we will also return to discuss the same Raman technology for use in sideband cooling of ions to their ground state of motion.

Before discussing the case of two-photon transitions in the presence of two laser beams for coupling hyperfine spin states, we first start with the simpler case of a single ion interacting with a single laser beam. The laser beam drives transitions between both internal and motional states of the trapped ion and is assumed to be coupled to only two internal states. The two internal states can be represented as an effective spin-1/2 system. In this case, the unperturbed Hamiltonian of the trapped ion describing its motion and internal levels can be written as

$$\begin{aligned} H_0 &= H_{osc} + H_{int} \\ &= \hbar\omega_i(a_i^\dagger a_i + \frac{1}{2}) + \frac{\hbar\omega_0}{2}(1 + \sigma_z), \end{aligned} \quad (7.53)$$

where  $\sigma$  is the Pauli spin operator and  $\omega_0$  is the frequency of the optical transition driven by the laser. Assuming that the levels have long lifetimes, ( $\omega_i \gg \gamma$ ), which brings us to the resolved-sideband limit, the interaction Hamiltonian for a dipole transition can be written as<sup>4</sup>

$$\begin{aligned} V_{dip} &= -\vec{d} \cdot \vec{E}(t) \\ &= \frac{\hbar\Omega}{2} \cdot (\sigma_+ + \sigma_-) \left( e^{i(k_i x_i - \omega_L t + \phi)} + e^{-i(k_i x_i - \omega_L t + \phi)} \right) \\ &= \frac{\hbar\Omega}{2} \cdot (\sigma_+ + \sigma_-) \left( e^{i(\eta_i(a_i^\dagger + a_i) - \omega_L t + \phi)} + c.c. \right), \end{aligned} \quad (7.54)$$

where  $\omega_L$  is the laser frequency and  $\eta_i$  is the Lamb-Dicke parameter along our axis of interest. The dipole interaction Hamiltonian can be transformed into the interaction picture using the time evolution operator  $U_0 \equiv e^{-iH_0 t/\hbar}$ , giving

$$V_I = U_0^\dagger V_{dip} U_0. \quad (7.55)$$

Now using the rotating wave approximation (RWA) to neglect fast oscillating terms at frequency  $\omega_L + \omega_0$ , and setting  $\delta = \omega_L - \omega_0$ , we will have

$$V_I = \frac{\hbar\Omega}{2} \sigma_+ \exp \left[ i\eta_i(a_i e^{-i\omega_i t} + a_i^\dagger e^{i\omega_i t}) - i(\delta t - \phi) \right] + h.c.. \quad (7.56)$$

---

<sup>4</sup>The calculations for quadrupole transitions can also be done with a similar approach. In fact, given that the typical trap frequencies are on the order of MHz, the resolved sideband limit cannot be achieved with a dipole transition, and quadrupole transitions are more practical. A practical example is the  $S \rightarrow D$  transition of  $^{40}\text{Ca}^+$ .



The wave function of the ion can be written as

$$\psi = \sum_{M_z=\uparrow,\downarrow} \sum_{n=0}^{n=\infty} C_{M_z,n}(t) |M_z\rangle |n\rangle, \quad (7.57)$$

where  $|M_z\rangle$  and  $|n\rangle$  are time-independent internal (spin) and motional states respectively, which in general become entangled during the laser-ion interaction. The coefficients  $C_{M_z,n}(t)$  are time-dependent and can be found using Schrödinger's equation. For the transitions between  $|\uparrow, n'\rangle$  and  $|\downarrow, n\rangle$ , driven by a near resonant field ( $\Delta = \delta - (n' - n)\omega_z \ll \omega_i$ ), these coefficients evolve as [20]

$$\dot{C}_{\uparrow,n'} = -i^{(1+|n'-n|)} e^{-i(\Delta t - \phi)} \Omega_{n',n} C_{\downarrow,n} \quad (7.58)$$

$$\dot{C}_{\downarrow,n} = -i^{(1-|n'-n|)} e^{-i(\Delta t - \phi)} \Omega_{n',n} C_{\uparrow,n'}, \quad (7.59)$$

where the generalized Rabi frequency  $\Omega_{n',n}$  is given by [20]

$$\begin{aligned} \Omega_{n',n} &\equiv \Omega |\langle n' | e^{i m_i (a_i + a_i^\dagger)} | n \rangle| \\ &= e^{-\eta_i^2/2} \sqrt{\frac{n_{<}}{n_{>}}} \eta_i^{|n'-n|} L_{n_{<}}^{|n'-n|}(\eta_i^2). \end{aligned} \quad (7.60)$$

Here,  $n_{<}$  and  $n_{>}$  are, respectively, the smaller and larger of  $n$  and  $n'$ , and  $L_n^\alpha$  is the generalized Laguerre polynomial defined as

$$L_n^\alpha(X) = \sum_{m=0}^n (-1)^m \binom{n+\alpha}{n-m} \frac{X^m}{m!}. \quad (7.61)$$

The solution of Eqs. 7.58 and 7.59 shows a sinusoidal Rabi oscillation between  $|\uparrow, n'\rangle$  and  $|\downarrow, n\rangle$  states. For the resonance case, corresponding to  $\Delta = 0$  or  $\omega_L = \omega_0 + (n' - n)\omega_i$ , the time evolution of the wave-function becomes

$$\psi(t) = \begin{pmatrix} \cos\left(\frac{\Omega_{n',n}t}{2}\right) & -ie^{i[\phi+\frac{\pi}{2}|n'-n|]} \sin\left(\frac{\Omega_{n',n}t}{2}\right) \\ -ie^{-i[\phi+\frac{\pi}{2}|n'-n|]} \sin\left(\frac{\Omega_{n',n}t}{2}\right) & \cos\left(\frac{\Omega_{n',n}t}{2}\right) \end{pmatrix} \cdot \psi(0). \quad (7.62)$$

For instance, suppose  $\psi_0 = |\downarrow, 0\rangle$ ; then for the  $n \rightarrow n$  carrier transition, the  $n \rightarrow n-1$  first red-sideband transition (Fig. 7.13 (a)), and the  $n+1 \rightarrow n$  first blue-sideband transition (Fig. 7.13 (b)), which are normally used in cooling processes and thermometry, the wave-

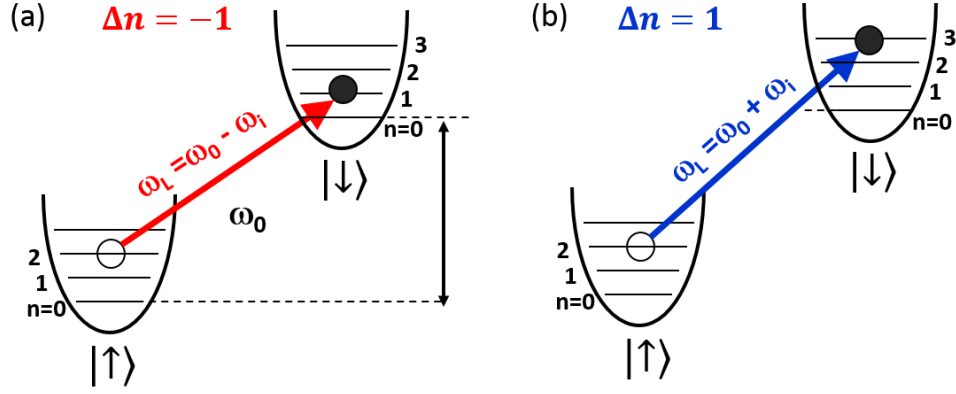


Figure 7.13: (a) The first red-sideband transition and (b) blue-sideband transition driven by a single laser beam.

functions and the associated Rabi frequencies are as follows:

$$\psi(t) = \cos \Omega_c t |\downarrow, n\rangle - e^{i\phi} \sin \Omega_c t |\uparrow, n\rangle, \quad \Omega_c = \Omega e^{-\eta_i^2/2} L_n^0(\eta_i^2), \quad (7.63)$$

$$\psi(t) = \cos \Omega_{rsb} t |\downarrow, n\rangle + e^{i\phi} \sin \Omega_{rsb} t |\uparrow, n\rangle, \quad \Omega_{rsb} = \Omega e^{-\eta_i^2/2} \frac{\eta_i}{\sqrt{n}} \cdot L_{n-1}^1(\eta_i^2), \quad (7.64)$$

$$\psi(t) = \cos \Omega_{bsb} t |\downarrow, n\rangle + e^{i\phi} \sin \Omega_{bsb} t |\uparrow, n\rangle, \quad \Omega_{bsb} = \Omega e^{-\eta_i^2/2} \frac{\eta_i}{\sqrt{n+1}} \cdot L_n^1(\eta_i^2). \quad (7.65)$$

Figures 7.14, show the scaled Rabi frequencies of the carrier and blue-sideband transitions as a function of  $n$  for two Lamb-Dicke parameters of  $\eta = 0.2$  (Fig. 7.14(a)) and  $\eta = 0.02$  (Fig. 7.14(b)). Note that a laser beam of  $\omega_L = \omega_0 + \omega_i$  can drive the blue-sideband transition of any given initial vibrational level  $n$ . Since the Rabi frequency is  $n$ -dependent, the population of each pair of coupled  $n$  and  $n + 1$  levels oscillates with a different Rabi frequency. This can cause a loss of contrast in the Rabi oscillation when the initial state is not in a single vibrational level. In general, the dependence of the Rabi frequency on initial  $n$  provides the capability for thermometry, which will be discussed in Section 7.6. For now we note a few basic features of the  $n$  dependence. The sensitivity of the Rabi frequency to  $n$  becomes stronger when the LD parameter is higher, as can be seen in Fig. 7.14. In the LDL, the dipole interaction Hamiltonian in the RWA (Eq. 7.56) can be expanded in terms of  $\eta$  to give

$$\begin{aligned} V_I &\simeq \frac{1}{2} \hbar \Omega \sigma_+ \left[ 1 + i\eta_i (a_i e^{-i\omega_i t} + a_i^\dagger e^{i\omega_i t}) \right] e^{i(-\delta t + \phi)} + h.c. \\ &= \frac{\hbar}{2} \Omega \sigma_+ e^{-i(\delta t + \phi)} + \frac{i\hbar}{2} \Omega (\eta_i a_i \sigma_+) e^{-i(\omega_i t + \delta t - \phi)} + \frac{i\hbar}{2} \Omega (\eta_i a_i^\dagger \sigma_+) e^{i(\omega_i t - \delta t + \phi)} + h.c., \end{aligned} \quad (7.66)$$

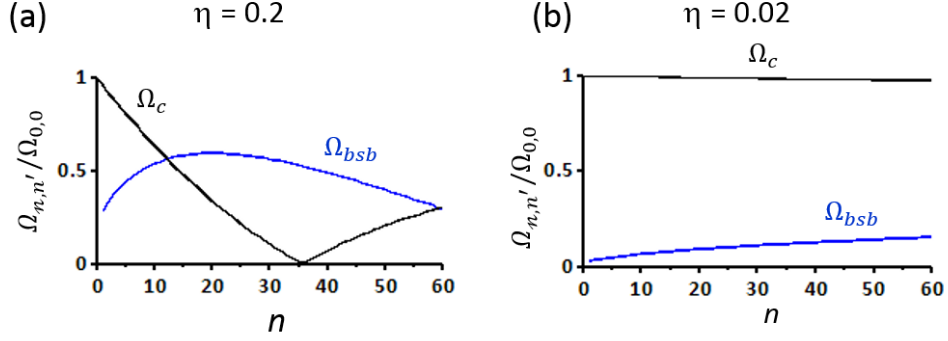


Figure 7.14: The scaled Rabi frequencies of carrier and blue-sideband transitions for the Lamb-Dicke parameters of (a)  $\eta = 0.2$  and (b)  $\eta = 0.02$ .

where the first term is associated with the carrier, the middle term is associated with the red-sideband transition and the last term is associated with the blue-sideband transition. Under a second rotating wave approximation, the Hamiltonian term for each of these transitions simplifies to:

$$H_c = \frac{\hbar}{2} \Omega \sigma_+ e^{-i(\Delta t + \phi)} + h.c., \quad (7.67)$$

$$H_{rsb} = \frac{i\hbar}{2} \Omega (\eta_i a_i \sigma_+) e^{-i(\Delta t + \phi)} + h.c., \quad (7.68)$$

$$H_{bsb} = \frac{i\hbar}{2} \Omega (\eta_i a_i^\dagger \sigma_+) e^{-i(\Delta t + \phi)} + h.c.. \quad (7.69)$$

The Rabi frequencies of these transitions in the LDL can therefore be written as

$$\Omega_c = \Omega, \quad (7.70)$$

$$\Omega_{rsb} = \eta_i \sqrt{n} \Omega, \quad (7.71)$$

$$\Omega_{bsb} = \eta_i \sqrt{n+1} \Omega. \quad (7.72)$$

We can see that in the LDL the carrier transition becomes motion-insensitive, whereas the sideband Rabi oscillations get slower at lower  $n$  (and so also at lower  $\bar{n}$  for the case of a thermal state). The Rabi frequency for the red sideband vanishes for an ion in the motional ground state.

### Two-photon stimulated Raman transitions:

For several ion species in use, the two internal states involved in coherent operations are hyperfine ground-state levels separated by a microwave frequency [194]. For instance, in  $^{171}\text{Yb}^+$  the two states are 12.6 GHz apart. In these cases, instead of an optical field, a

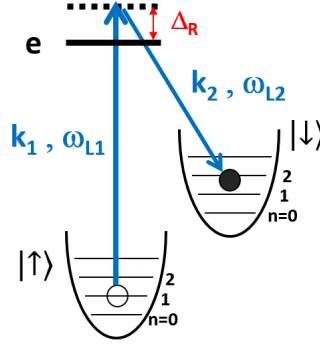


Figure 7.15: The first blue-sideband transition driven by a pair of laser beams in a stimulated two-photon Raman process.

microwave field is required to drive the single-photon transitions. The strength of the first sideband coupling between the motion and internal states of an ion depends on the gradient of the applied electromagnetic field. The field gradient  $\propto \lambda^{-1}$  for a microwave plane wave across the extent of a trapped ion's wavepacket is so small that the coupling becomes negligibly small. There are different ways to go around this problem. For example, it has been shown in recent experiments that gradients in the near field of microwave radiation [195], or a gradient in an applied dc magnetic field together with uniform microwaves [196,197], can be used to obtain spin-motion coupling. The more traditional approach, and the one discussed here, is a two-photon stimulated transition through a third optical level (see Fig. 7.15). In a two-photon stimulated Raman transition, two laser beams,  $\vec{E}_\alpha = E_{0\alpha} \cos(k_{l\alpha}x - \omega_{l\alpha}t - \phi_\alpha)\hat{e}_\alpha$  with  $\alpha = 1, 2$ , are used to couple the two ground-state hyperfine levels through an excited state  $|e\rangle$ . To a good approximation each laser beam couples the excited state to only one of the ground states. The dipole coupling strength between the ground state  $|M_z\rangle$  and excited state  $|e\rangle$  from laser field  $E_\alpha$  is given by  $\Omega_{M_z,\alpha} = -\frac{1}{2\hbar}\vec{d}_{M_z} \cdot \hat{e}_\alpha E_{0\alpha}$ . Both beams are detuned from the excited state by  $\Delta_R$ . When the detuning is much larger than the linewidth of the optical transition  $\gamma$  and the coupling strength  $|\Omega_{M_z,\alpha}|^2$ , the rate of spontaneous emission from the excited state becomes small compared to the stimulated two-photon transition rate. In the limit of large detuning, the excited state can be eliminated adiabatically and the problem is reduced to a two-level problem again. The interaction Hamiltonian of the two far-detuned laser beams and the ion is:

$$V_I = \frac{1}{2}\hbar\Omega(\sigma_+ + \sigma_-)(e^{i(\Delta k_i x_i - \Delta\omega_L t + \Delta\phi)} + e^{-i(\Delta k_i x_i - \Delta\omega_L t + \Delta\phi)}) + \frac{\hbar(\chi_\uparrow - \chi_\downarrow)}{4}\sigma_z. \quad (7.73)$$

This equation is very similar to the atom-laser interaction for a single beam (Eq. 7.54) with  $k_i \rightarrow \Delta k_i$  and  $\omega \rightarrow \Delta\omega$ . The last term of this equation is related to the ac Stark shift of the

ground-state levels  $\chi_{M_z} = (|\Omega_{M_z,1}|^2 + |\Omega_{M_z,2}|^2)/2\Delta_R$ . Although the control and stability of these ac Stark shifts may be of practical significance, they can be absorbed into an effective transition frequency for the two-level system. In this case, Eq. 7.73 will become exactly the same as Eq. 7.54:

$$V_I = \frac{1}{2}\hbar\Omega(\sigma_+ + \sigma_-)(e^{i(\Delta k_i x_i - \Delta\omega_L t + \Delta\phi)} + e^{-i(\Delta k_i x_i - \Delta\omega_L t + \Delta\phi)}), \quad (7.74)$$

$$\Omega = \Omega_{\uparrow,1}\Omega_{\downarrow,2}^*/2\Delta_R. \quad (7.75)$$

The base Rabi frequency  $\Omega$  directly couples the two ground states. The generalized Rabi frequency  $\Omega_{n',n}$  between  $|\uparrow, n'\rangle$  and  $|\downarrow, n\rangle$  is the same as Eq. 7.60. For the two-photon Raman transition, the Lamb-Dicke parameter is defined as  $\eta_i = \Delta k_i x_{i0}$ . Note that for co-propagating laser beams we will have  $\eta_i = 0$ , which means that the two-photon transition can change the spin but not the internal states of the ion. This configuration can be used for motion-independent operation on the ion spin. The highest value of the first-sideband coupling  $\eta\Omega$  is achieved for a counter-propagating configuration, in which case  $\Delta k = 2k$ .

## 7.6 Thermometry using stimulated Raman transitions:

Atom-laser interactions in the resolved sideband limit, including the technology of two-photon stimulated Raman transitions, have different applications including resolved sideband cooling, and different types of thermometry. One of the common forms of thermometry is known as sideband thermometry. In this technique, the average motional population  $\bar{n}$  can be found from the asymmetry between the red- and blue-sideband transitions. For most laser cooling techniques, including Doppler cooling and Sisyphus cooling discussed here, it can be assumed that the outcome of cooling has a thermal distribution, for which the occupation probability of the  $n^{\text{th}}$  motional state is

$$P_n = \frac{\bar{n}^n}{(1 + \bar{n})^{n+1}}. \quad (7.76)$$

To find  $\bar{n}$ , a single ion is first prepared in the  $|\downarrow\rangle$  state. Then the first blue-sideband transition is driven for a varying time  $t$ , which results in a transfer between the  $|\downarrow, n\rangle$  and  $|\uparrow, n+1\rangle$  state with a Rabi frequency of  $\Omega_{n,n+1}$ . Finally, the probability of observing the  $|\uparrow\rangle$  state is measured over several iterations, yielding the averaged Rabi oscillation signal:

$$P_{\uparrow}^{bsb}(t) = \sum_{n=0}^{\infty} P_n \cdot \sin^2\left(\frac{\Omega_{n+1,n}t}{2}\right). \quad (7.77)$$

The same process is repeated for the first red-sideband transition, and so using the symmetry of the Rabi transition  $\Omega_{m,m+1} = \Omega_{m+1,m}$ , we will have:

$$\begin{aligned} P_{\uparrow}^{rsb}(t) &= \sum_{n=1}^{\infty} P_n \cdot \sin^2\left(\frac{\Omega_{n-1,n}t}{2}\right) \\ &= \sum_{m=0}^{\infty} P_{m+1} \cdot \sin^2\left(\frac{\Omega_{m+1,m}t}{2}\right), \end{aligned} \quad (7.78)$$

which has the same Rabi frequency dependence as  $P_{\uparrow}^{bsb}(t)$ . As a result, the ratio of the two populations only depends on  $\bar{n}$ , and is independent of Rabi frequency, signal time or the LD parameter:

$$\frac{P_{\uparrow}^{rsb}}{P_{\uparrow}^{bsb}} = \frac{\bar{n}}{\bar{n} + 1}. \quad (7.79)$$

This method is most effective at low mean energies corresponding to  $\bar{n} \leq 5$ , where there is a distinct difference between the red and blue sidebands. Due to this limitation, sideband thermometry cannot be used for our Sisyphus studies, in which  $\bar{n}$  varies from Doppler temperatures to a few quanta. We use an alternative thermometry technique based on the motion-sensitive carrier transition, which reveals  $\bar{n}$  through a loss in contrast (and change in Rabi frequency). Similar to sideband thermometry, we start in the  $|\downarrow\rangle$  state, drive the carrier transition for a varying time  $t$ , and measure the probability of transfer to the  $|\uparrow\rangle$  state. Assuming a thermal distribution, the  $\bar{n}$  value can be found by fitting the measured Rabi oscillation to

$$P_{\uparrow}^c(t) = \sum_{n=0}^{\infty} P_n \sin^2\left(\frac{\Omega_{n,n}t}{2}\right). \quad (7.80)$$

This expression applies straightforwardly to the motion-sensitive carrier oscillations in the axial direction, but our carrier oscillation data in the transverse direction requires some additional interpretation. In the transverse direction, our Raman setup couples to both  $x$  and  $y$  transverse motions with equal Raman wave-vector projection onto each axis. We have found that an approximate model for the transverse carrier is adequate and simplifies the fitting for  $\bar{n}$ . The transverse trap frequencies are very close (23 kHz in 800 kHz), and so we can make the useful simplification that the temperatures are the same in the two axes. At the same time, since the trap frequencies are close, there are Raman transitions related to cross-mode coupling between the axes with resonances near to the carrier [20]. Our carrier Rabi frequency is strong enough that we do not resolve the closest transitions. One simplified model is to ignore the cross coupling resonances, which are suppressed in the LDL, and consider a 2-D fit model with independent  $x$  and  $y$  axes. Another approach, which we adopt here for our fits, is to assume an effective 1-D model with motional Raman coupling along the direction of the transverse Raman wave-vector. We have compared the approximate models to simulated data, and the systematic effect on the obtained  $\bar{n}$  values ( $\leq 10\%$ ) will be described as part of a future paper [198].

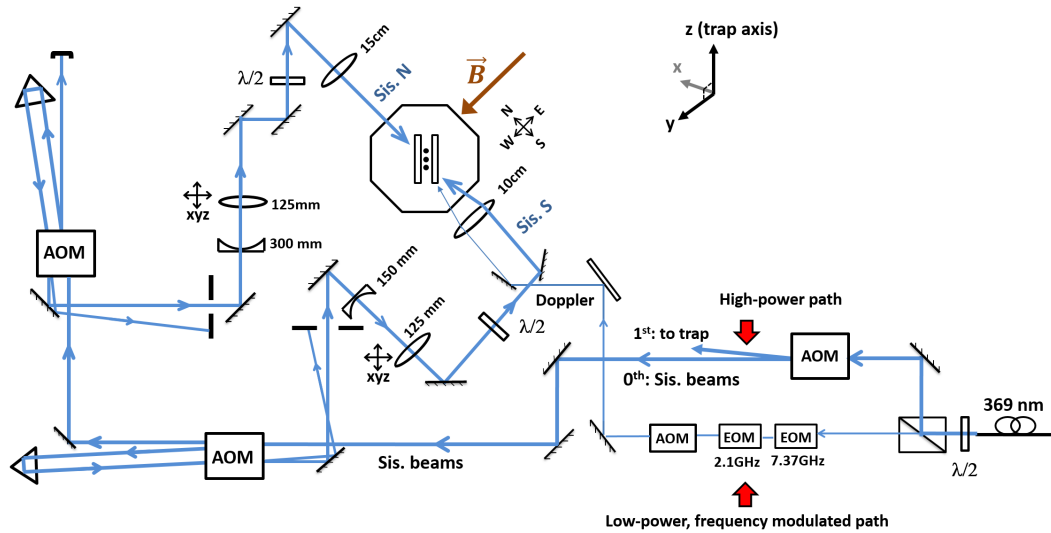


Figure 7.16: The optical path of the north and south Sisyphus beams along with the Doppler cooling/detection beam.

Several examples of carrier Rabi oscillation measurements and fits are shown in Fig. 7.24. In this technique, near the ground state (*i.e.* well below  $\bar{n} \simeq 1$ ) where the carrier is only weakly sensitive to the initial motional state, the lowest measurable  $\bar{n}$  can be limited by other damping mechanisms. This is not relevant to the case of Sisyphus cooling, but is likely to become so for ground-state cooling measurements, for which we use sideband thermometry as is common practice.

## 7.7 Experimental setup for Sisyphus cooling

Before discussing the experimental results for Sisyphus cooling, we briefly describe the details of the experimental setup used for these measurements. This includes the Sisyphus beams, Raman beams and the details of the setup for the cooling measurements.

### 7.7.1 Sisyphus beams

#### The formation of two Sisyphus beams:

The two counter-propagating Sisyphus beams, which enter the vacuum chamber from the north and south sides, are derived from the 369.5-nm detection and Doppler cooling laser. It was shown in Chapter 4 that the 369.5-nm laser beam is brought closer to the trap through an optical fiber. The output of the optical fiber goes through a polarized beam-splitter (PBS) that divides the beam into two paths (see Fig. 7.16). The beam that passes through

the PBS, has a lower power of  $\sim 200 \mu\text{W}$  and is directed to a frequency modulated path. This beam is used for Doppler cooling and detection. The other part that reflects from the PBS has a higher power of  $\sim 700 \mu\text{W}$  which goes through an acousto-optic modulator (AOM). The first order output of the AOM is sent to the trap to be used for both loading and far detuned Doppler cooling of the ions, while the zeroth order is used for the Sisyphus beam path. This path has a power of  $600 \mu\text{W}$  and is sent to a first double-pass AOM. The double-pass output beam forms the south Sisyphus beam. The AOM also acts as a beam splitter with the zeroth order on first pass being directed to a second double-pass AOM for the north Sisyphus beam. Having two independent AOMs allow us to tune power and frequency of each Sisyphus beam separately. The double-pass setup allows for changing the AOM frequency without misalignment. The double pass configuration results in a 400-MHz frequency shift with respect to the original high power beam. The 369.5-nm laser is locked 90 MHz below the resonance frequency. As a result, both Sisyphus beams are detuned 310 MHz above the  $^2S_{1/2}(F=1) - ^2P_{1/2}(F=0)$  resonance. The north Sisyphus beam is typically modulated by  $\omega_m/2\pi = 2 \times 0.040 = 0.080$  MHz with respect to the south Sisyphus beam. The setup of the Sisyphus beams was one of the technical contributions as part of this thesis work.

### Adjustments of the Sisyphus beams:

**Alignment/focus adjustment:** Each of the Sisyphus beams is focused into the trap using a pair of concave/convex lenses, which result in an estimated beam waist of  $\sim 80 \mu\text{m}$  on the ions. One of the lenses in each path is mounted on an XYZ transition stage which allows fine adjustments of the beam on the ion. The beams' alignment on the ion is adjusted on a daily basis.

**Polarization adjustment:** The polarization configuration of the Sisyphus beams needs to be Lin- $\perp$ -Lin *i.e.* with  $\theta = \pi/2$  in Fig. 7.2. For this situation, the Sisyphus beams are linearly polarized and the angle between their electric field  $\vec{E}$  and the applied magnetic field  $\vec{B}$  should be  $|\theta_{BE}| = 45^\circ$ . Two half-wave plates are used to adjust the polarization of each beam independently. The polarization calibration is done by measuring the differential ac Stark shift,  $\Delta U_{ac} = U_{ac}(\uparrow) - U_{ac}(\downarrow)$ , due to each beam as a function of polarization angle. The two hyperfine states  $|\uparrow\rangle$  and  $|\downarrow\rangle$  are separated by  $\Delta_s/2\pi = 12,644$  MHz. Including the full hyperfine structure of the  $^2P_{1/2}$  excited state, consisting of  $P_{1/2}(F=1)$  and  $P_{1/2}(F=0)$  states, separated by  $\Delta_p/2\pi = 2105$  MHz, the differential ac Stark shift due to each linearly polarized Sisyphus beam at a polarization angle of  $\theta_{BE}$  is

$$\Delta U_{ac}(\theta_{BE}) = \frac{s_0 \gamma^2}{24 \Delta} \left( \left[ 1 + \frac{\Delta}{\Delta_p - \Delta} \right] \cos^2 \theta_{BE} - \frac{\Delta}{\Delta_p - \Delta} + \frac{\Delta}{\Delta_s + \Delta_p - \Delta} \right), \quad (7.81)$$



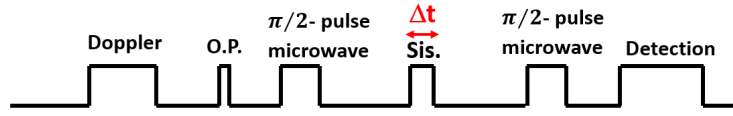


Figure 7.17: The pulse sequence of the microwave Ramsey experiment to measure the differential ac Stark shift of a single Sisyphus beam. Ramsey oscillations are obtained by varying the exposure time  $\Delta t$  of the Sisyphus beam.

which depends on the laser intensity ( $\propto s_0$ ), polarization ( $\theta_{BE}$ ) and detuning of the beams measured relative to the  $P_{1/2}(F=0)$  excited state ( $\Delta$ ). Experimentally, the differential ac Stark shift can be measured using a microwave Ramsey experiment. The pulse sequence of the Ramsey experiment is shown in Fig. 7.17. The sequence starts with a 3-ms Doppler cooling pulse followed by a short 50- $\mu$ s optical pumping pulse used to initialize the ion into the  $|\downarrow\rangle$  state. Then a single pulse of one Sisyphus beam, sandwiched in time between two microwave  $\pi/2$ -pulses, is applied to the ion for a variable time. The sequence ends with a 0.4-ms detection pulse to read out the ion spin state. The differential ac Stark shift is obtained from the resulting Ramsey oscillations. To calibrate the polarization, the differential ac Stark shift of each beam is measured as a function of the polarization angle at a fixed laser intensity. The polarization angle is varied by a half-wave plate (HWP) for which  $\theta_{BE} = 2(\theta_{\lambda/2} - \theta_0)$ , where  $\theta_0$  is an offset angle for each wave plate. The results of  $\Delta U_{ac}$  measurements as a function of the HWP angle  $\theta_{\lambda/2}$  are shown in Fig. 7.18. The lines show the fit to Eq. 7.82. The difference between the half-wave plates' offset angles lead to a shift in the plots for the two beams. The larger maximum is achieved when the laser's linear polarization is parallel to the magnetic field ( $\vec{E} \parallel \vec{B}$ ) corresponding to pure  $\pi$ -polarization, and the smaller maximum is related to the perpendicular case corresponding to an equal superposition of left and right circular polarizations. Based on the calibration results, the HWP angles of the north and south beams were set to  $\theta_{\lambda/2} = 18^\circ$  and  $29^\circ$ , respectively, to obtain a Lin- $\perp$ -Lin configuration. These values are kept constant for all the experiments.

**Power adjustment:** The powers of the Sisyphus beams are adjusted on a daily basis to balance the intensities incident on the ion(s). The powers of the beams are changed by varying the rf powers driving the two AOMs. To balance the intensities of the beams, the differential ac Stark shifts of the two beams are matched to 5–10 %. The differential ac Stark shift of each beam, for which the polarization is permanently set to  $\theta_{BE} = 45^\circ$ , is given by

$$\Delta U_{ac}(\pi/4) = \frac{s_0}{48} \frac{\gamma^2}{\Delta} \left( 1 - \frac{\Delta}{\Delta_p - \Delta} + \frac{2\Delta}{\Delta_s + \Delta_p - \Delta} \right) = \frac{s_0}{44.51}, \quad (7.82)$$

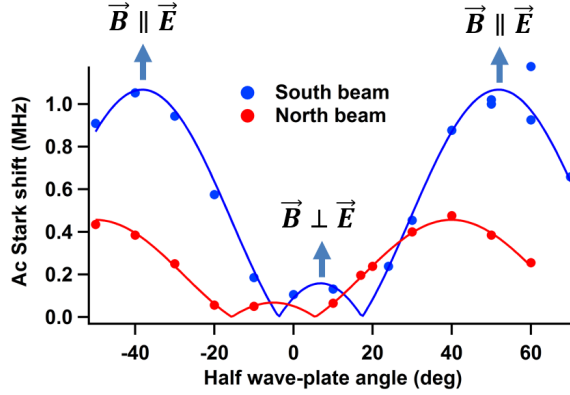


Figure 7.18: Polarization calibration of south (blue) and north (red) Sisyphus beams. The points show the measure values and the lines show the fit results.

for which the detunings are  $\Delta_s/2\pi = 126443$  MHz,  $\Delta_p/2\pi = 2105$  MHz, and  $\Delta/2\pi = 310$  MHz. The waist sizes of the two beams are not perfectly matched, and so the beam powers entering the trap are different by a factor of 2 or less when the ac Stark shifts are balanced. Finally, we note that Eq. 7.82 is inverted to obtain an in situ calibration of  $s_0$  for our cooling results.

## 7.7.2 Raman beams

**Producing Raman beams:** The Raman beams for the two-photon Raman transition, used for both thermometry and sideband cooling of  $^{171}\text{Yb}^+$ , are produced by a frequency doubled Titanium:Sapphire laser system. The fundamental wave at 739 nm is produced by a Spectra-Physics/Sirah Mattise TX Lite, and is frequency doubled to 369.5 nm in a Tehknoscan resonant doubler unit. The fundamental wave is tuned to 738.950 nm (369.475 nm doubled), which is 100 GHz above the  $S_{1/2} - P_{1/2}$  resonance frequency. An external reference cavity stabilizes the laser frequency. The power of the fundamental wave is  $\sim 600$  mW, and the power of the UV output of the doubler is  $\sim 40 - 50$  mW. The optical setup of the Raman beams is similar to one developed by a group at Michigan [199]. An electro-optic modulator (EOM) is used to bridge the 12.6-GHz hyperfine splitting. However, due to the high UV laser power and the large hyperfine splitting, the production of two Raman beams with a frequency difference of 12.6 GHz, and with relative phase stability, requires a more complicated setup in which the EOM is placed before the doubler.

Since a 12.6-GHz EOM is not commercially available, the fundamental wave is frequency modulated by an EOM at  $\omega_{HF}/2$ . The output of the EOM can be written as

$$E_{IR} = \frac{1}{2} E_0 e^{ikx - \omega t} \sum_{n=-\infty}^{\infty} J_n(\phi) e^{in(\delta kx - \omega_{HF}t/2)} + c.c., \quad (7.83)$$

where  $E_0$  is the field amplitude of the input beam,  $J_n(\phi)$  is the  $n^{\text{th}}$  order Bessel function with modulation index  $\phi$ , and  $\delta k = \omega_{HF}/2c$ . To produce the UV sidebands spaced by  $\omega_{HF}$ , the output of the EOM is frequency-summed in the doubler cavity. The free spectral range of the doubler cavity is tuned to a subharmonic of the modulation frequency ( $\omega_{FSR} = \omega_{HF}/24$ ), so that all the comb lines resonate simultaneously. The UV comb spectrum is effectively the same as for the IR, but with a doubled carrier frequency and doubled phase modulation  $2\phi$ . In the presence of all the frequency comb lines, any pair with a frequency difference of  $\omega_{HF}$  can drive the Raman transition. This leads to a destructive interference and the net Rabi frequency reduces to zero:

$$\Omega = 2\Omega_0 \sum_{n=-\infty}^{\infty} J_n(2\phi)J_{n+2}(2\phi)e^{i(2\delta kx)} = 0. \quad (7.84)$$

In order to solve this issue, a Mach-Zehnder (MZ) interferometer can be employed to create a phase shift in the sidebands. The non-copropagating Raman beam geometry is essentially a form of a MZ interferometer, where the modulated beams are split and recombined at the ion position. For a relative path length  $\Delta x$  between the two beams, the phase of the  $n^{\text{th}}$  sideband is shifted by an  $n$ -dependent value of  $n\delta k\Delta x$ . As a result, the net Rabi frequency of Eq. 7.84 changes to

$$\Omega = \Omega_0 e^{i\delta k(2x+\Delta x)} \sum_{n=-\infty}^{\infty} J_n(2\phi)J_{n-2}(2\phi) \cos[2k\Delta x + (n-1)\delta k\Delta x]. \quad (7.85)$$

The optimum Rabi frequency can be obtained when  $\Delta x$  is adjusted properly so that  $\delta k\Delta x = (2j+1)\pi$ , with  $j$  being an integer (and with  $2k\Delta x = n\pi$ ). Unfortunately, the  $k\Delta x$  factor in the cosine term of Eq. 7.85 requires a high optical stability in the setup, which is difficult to achieve considering that the path lengths of the two beams are of the order of a meter. To go around this problem, a relative frequency shift of  $\Delta\omega \gg \Omega$  is introduced between the two beams, which is compensated for by changing the modulation frequency of the EOM by  $\pm\Delta\omega/2$ . The resulting net Rabi frequency is :

$$\Omega = \Omega_0 e^{-ik\Delta x} e^{-2i\delta k\Delta x} \sum_{n=-\infty}^{\infty} J_n(2\phi)J_{n-2}(2\phi) e^{in\delta k\Delta x} = \Omega_0 e^{-ik\Delta x} e^{-2i\delta k\Delta x} J_2(4\phi \sin(\delta k\Delta x/2)), \quad (7.86)$$

where the  $\cos(k\Delta x)$  dependence giving an amplitude sensitivity is changed to a phase factor  $e^{-ik\Delta x}$ .

In our setup, for an optimized path length the phase modulation index of the EOM is  $\phi = 0.77$ , which results in  $\Omega = 0.25\Omega_0$ . In order to perform cooling and thermometry for both axial and transverse trap directions, two pairs of Raman beams are needed, where the wave-vector difference of each pair is along one of the trap directions. Three Raman beams is enough to produce the two pairs. The simplified optical setup for the three perpendicular

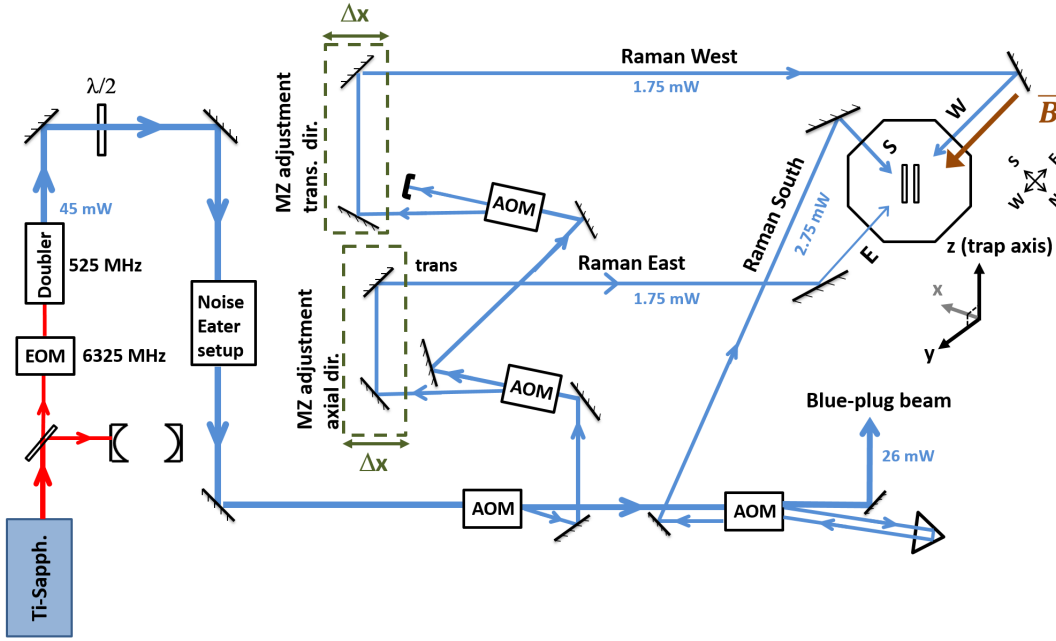


Figure 7.19: The simplified optical path of the three perpendicular Raman beams entering the trap from south, west, and east sides. The south and east beams are used for the axial thermometry and sideband cooling, while the south and west beams are used for the transverse direction.

Raman beams entering the trap from the south, west and east sides is shown in Fig. 7.19. The south/east combination of beams is used for thermometry and sideband cooling in the axial direction, while the south/west combination is used for the transverse direction.

The first AOM after the doubler and noise eater acts as a beam splitter which produces the two beam paths of the MZ interferometer. The first-order beam is used to form the Raman west and Raman east beams with another pair of AOMs. Mirrors, lenses and a half-wave plate for each beam allows the adjustment of beam focus, alignments and polarization. The Raman south beam (which is the common beam for both trap directions) is derived from the zeroth order beam of the beam-splitter AOM. This path is also used to generate a dipole force beam ("blue plug beam") for the deterministic zig/zag state preparation, as described in Chapter 6. For a carrier transition the Raman south beam is modulated by  $\Delta\omega = 2 \cdot (3.5) \text{ MHz}$ , relative to the east/west beams, which is compensated for by setting the EOM frequency to 6325 MHz. The AOM in each path allows for independent power adjustment for each Raman beam. We use the common south Raman beam for frequency tuning of Raman transitions since the double-pass configuration of its AOM allows for frequency tuning with minimal misalignment at the ion.

**Power stability of the Raman beams:**

The power stabilization of the Raman beams is done with a home-made noise-eater feedback setup. The UV beam from the doubler goes through a noise-eater AOM, in which  $\sim 10\%$  of the zeroth order power is monitored by a photo-diode and stabilized around a setpoint with a servo circuit. The output of the circuit is an error signal which gets mixed with the rf signal that is fed to the AOM. Depending on the voltage of the error signal, the modulation strength of the AOM and correspondingly the power of the zeroth order is corrected. The circuit diagram of the noise-eater is shown in Fig. 7.20. The design of the circuit is similar to the one found in [199] with some minor modifications (shown in red) to eliminate slow drifts and improve the performance. The performance of the noise-eater is also shown in Fig. 7.20. Adding the noise-eater reduces the standard deviation of the power noise from 0.08 to 0.009. Given the long duration of typical experiments and the emphasis on Raman Rabi fits in the measurements, the noise-eater has been crucial to obtaining the results in this thesis work.

**Raman beam adjustments:**

The power of each pair of Raman beams is adjusted on a daily basis to balance their intensities in the same way as was done for the Sisyphus beams by measuring the differential ac Stark shifts of the two beams separately. Note that depending on the direction in use, the power of the south beam is adjusted to balance the other beam.

As noted above, the perpendicular Raman beams entering from the south and west sides of the trap are used for the axial direction, and the perpendicular south and east Raman beams are used for the transverse direction. Figure 7.21 shows the wavelength difference  $\Delta\vec{k}$  of each pair of beams with respect to the trap axis. The transverse Raman setup allows us to couple to both  $\hat{x}$  and  $\hat{y}$  motions in the trap. The transverse trap frequencies  $\omega_x$  and  $\omega_y$  are very close (23 kHz different in 800 kHz), and the temperatures are expected to be about the same, so for the single ion's transverse thermometry based on motion-sensitive carrier oscillations, we find it convenient to assume a coupling along  $\Delta\vec{k}_T$  to simplify the theory.

**7.7.3 The cooling experiment setup**

The detailed studies of Sisyphus cooling are performed for a single  $^{171}\text{Yb}$  ion in the same linear Paul trap as the KZM studies but with a slightly higher rf frequency of  $\Omega_T/2\pi = 17.4$  MHz. The transverse secular trap frequencies are  $\{\omega_x, \omega_y\} = 2\pi\{0.790, 0.766\}$  MHz, while the axial secular trap frequency is at a frequency of  $\omega_z/2\pi = 0.525$  MHz. These frequencies are determined from Raman spectroscopy. A magnetic field is applied to suppress the effect of coherent population trapping, and results in a Zeeman shift of  $\pm\delta_B/2\pi = 8.2$  MHz for the  $S_{1/2}|F = 1, m_F = \pm 1\rangle$  sub-levels of the ground state.

At the start of each experiment day, the output power of the 369.5-nm laser used for Doppler cooling, fluorescence detection and Sisyphus cooling, and the power of the Ti-

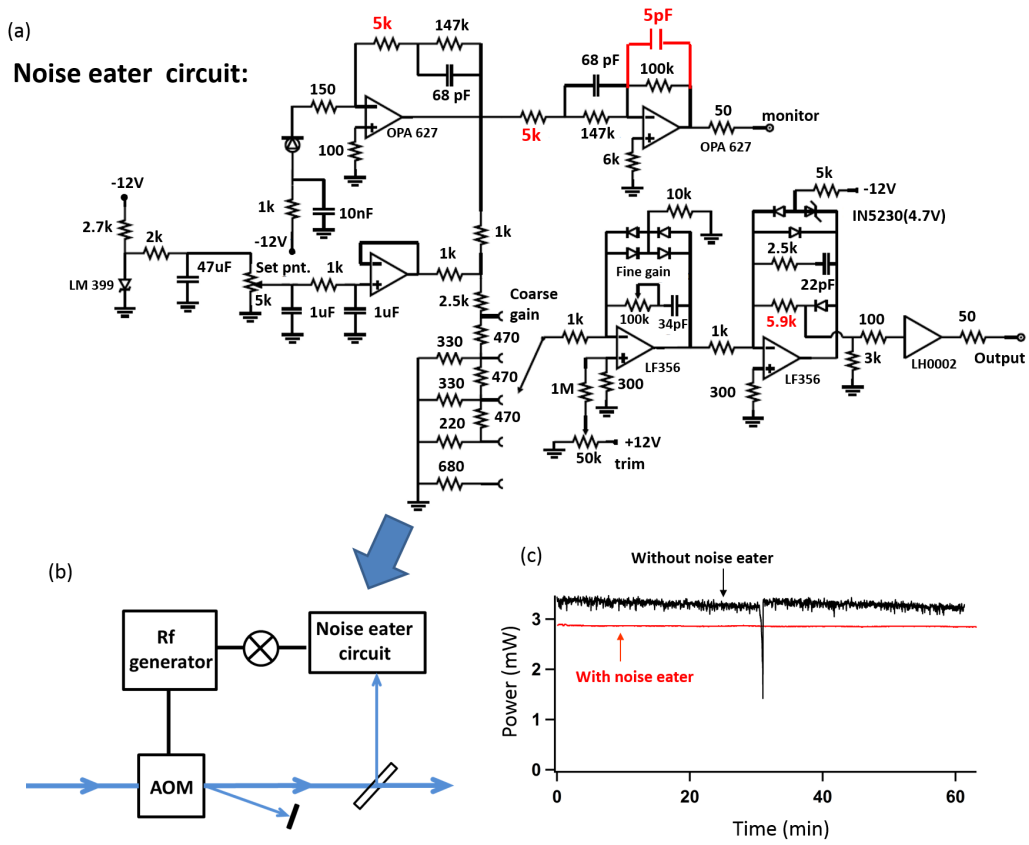


Figure 7.20: (a) The circuit diagram of the noise-eater. (b) The noise-eater setup used to stabilize the laser power of the Raman beams. (c) The performance of the noise-eater showing the laser power with and without the servo active.

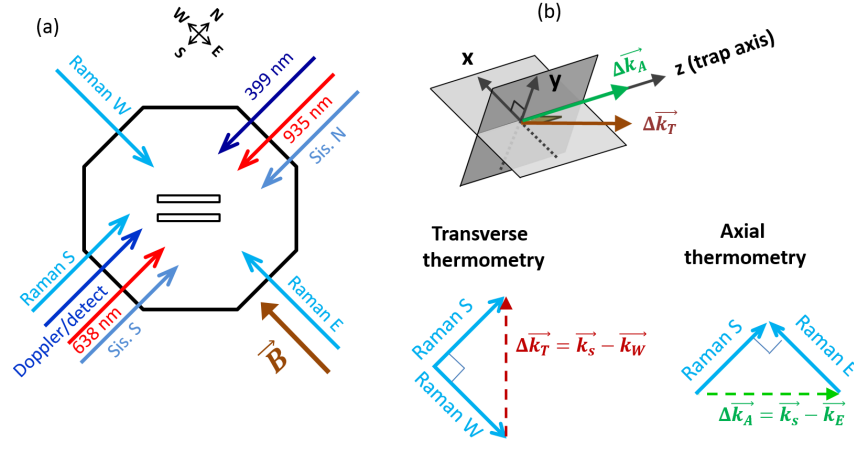


Figure 7.21: (a) All the laser beams used in our experiment and their entry directions into the trap. (b) The  $\Delta\vec{k}$  (compared to the trap axis) of south/west and south/east Raman beams applied for the transverse and axial thermometry (or sideband cooling).

Sapph. laser used for the Raman beams are optimized. The output power of the 369.5-nm laser is  $\sim 3$  mW, and about half of that is fiber coupled to the experiment. The output power of the frequency-doubled Ti-Sapph. laser is  $\sim 45$  mW, and 15% of that is used for the Raman beams. Once the ion is loaded, first micro-motion is nulled, and then the alignments of all the related laser beams are optimized on the ion. These beams include the Doppler/detection beam, the 935-nm re-pump beam (for D-state depopulation), the north/south Sisyphus beams, and the south/west/east Raman beams. In the case of the Sisyphus and Raman beams, the intensities of each pair of the beams are also balanced. The general sequence of Sisyphus cooling measurements is similar for the cooling rate and steady-state  $\bar{n}$  measurements (see Fig. 7.22). The main components of these measurements are: Doppler cooling, state preparation, Sisyphus cooling, Raman pulse, state detection, and finally data collection.

**Doppler cooling:** The  $S_{1/2}(F=1) \rightarrow P_{1/2}(F=0)$  Doppler cooling transition of  $^{171}\text{Yb}^+$  is driven by a 369.5-nm beam that is tuned 10 MHz below resonance. In order to have efficient Doppler cooling, a hyperfine repump of the  $S_{1/2}(F=0)$  state is also active during the Doppler cooling process. The hyperfine repump is obtained by modulating the Doppler beam with a 7.37-GHz EOM, and the second modulation sideband drives the  $S_{1/2}(F=0) \rightarrow P_{1/2}(F=1)$  transition. The power of the Doppler cooling beam at the ion's location is  $\sim 4 \mu\text{W}$  and it brings down the average energy of the ion to  $\bar{n} \simeq 22$  in the axial direction and  $\bar{n} \simeq 20$  in the transverse direction.

**State preparation:** The ion can be initialized in either of the spin levels,  $S_{1/2}|F=0, m_F=0\rangle \equiv |\downarrow\rangle$  or  $S_{1/2}|F=1, m_F=0\rangle \equiv |\uparrow\rangle$ , via optical pumping and microwave spin flips. The optical pumping is obtained by frequency modulating the Doppler beam at 2.1 GHz using an EOM. The optical pumping drives the  $S_{1/2}(F=1) \rightarrow P_{1/2}(F=1)$  transition, and so

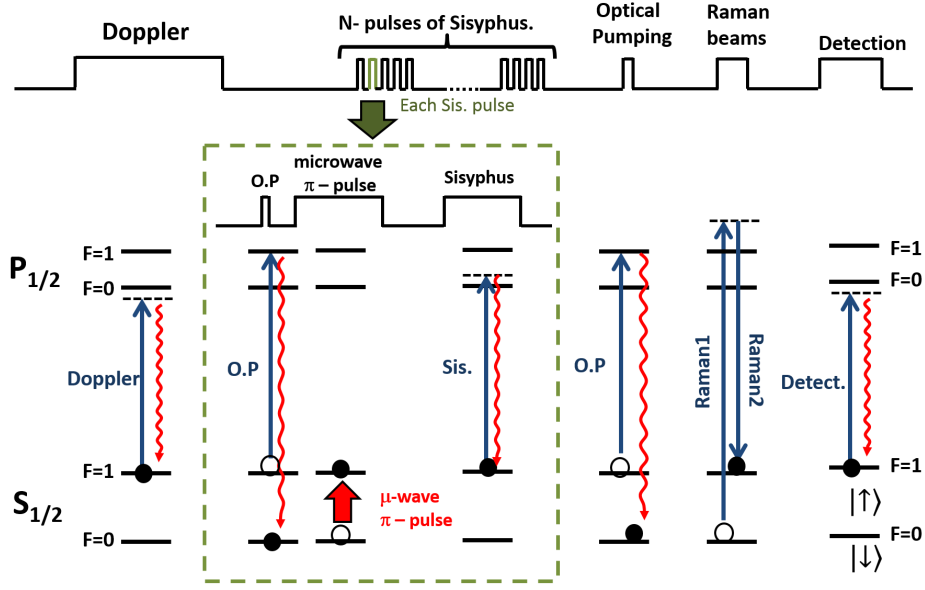


Figure 7.22: The sequence of pulses used for the Sisyphus cooling experiments. The optical transitions that are driven with each pulse are also depicted with Zeeman structures suppressed for clarity. The sequence starts with a long Doppler cooling period, followed by a variable number  $N$  of Sisyphus pulses. Each Sisyphus pulse includes a short ( $10 \mu\text{s}$ ) optical pumping pulse, followed by a microwave  $\pi$ -pulse. These two pulses initialize the ion into the  $S_{1/2}|F = 1, m_F = 0\rangle$  state, ready for the Sisyphus beams. The Sisyphus cooling sequence is followed by a  $50\text{-}\mu\text{s}$  optical pumping pulse that prepares the ion in the  $S_{1/2}|F = 0, m_F = 0\rangle$  state for a two-photon Raman carrier transition for thermometry. The sequence ends with a detection pulse. During spin-sensitive fluorescence detection, the fluorescence cycle is active for the  $S_{1/2}(F = 1)$  state but is closed to the  $S_{1/2}(F = 0)$  state.

initialize the ion into the  $|\downarrow\rangle$  state. The ion can be transferred to the  $|\uparrow\rangle$  state by applying a microwave  $\pi$ -pulse after the optical pumping.

**Sisyphus cooling:** The details of the Sisyphus beams are provided in the previous section. The detuning of these beams are  $\Delta/2\pi = 310 \text{ MHz}$  above the  $S_{1/2}(F = 1) \rightarrow P_{1/2}(F = 0)$  resonance. One of the beams is modulated with respect to the other by a frequency of  $\omega_m/2\pi = 0.080 \text{ MHz}$ . The projections of the north Sisyphus beam's wavevector along the  $\{\hat{x}, \hat{y}, \hat{z}\}$  directions are  $\frac{2\pi}{\lambda} \{\frac{1}{2}, \frac{-1}{2}, \frac{1}{\sqrt{2}}\}$ . For the given trap frequencies, the Lamb-Dicke parameters for the transverse direction are  $\{\eta_x, \eta_y\} = \{0.052, 0.053\}$ , and for the axial direction the value is  $\eta_z = 0.090$ . Our primary data consists of both cooling-rate and steady-state  $\bar{n}$  measurements performed at different laser intensities. As mentioned above, the intensities of the Sisyphus beams on the ion are determined in situ from their differential ac Stark shifts ( $s_0 = 44.51\Delta U_{ac}$ ), which are balanced to better than 10% uncertainty for each intensity value.

The Sisyphus beams primarily drive the  $S_{1/2}(F = 1) \rightarrow P_{1/2}(F = 0)$  transition; however the



ion can also be weakly optically pumped via the  $P_{1/2}(F = 1)$  state into the dark  $S_{1/2}(F = 0)$  state, which is closed to the cooling cycle. In order to have effective cooling, a repump back into the cooling cycle is required. To this end, the Sisyphus cooling is implemented through a pulse method. Each of the  $N$  Sisyphus cooling pulses includes two parts: 1 – Initialization into the  $|\uparrow\rangle$  state to prepare the ion for the next cooling pulse. This is done by applying a 10- $\mu\text{s}$  optical pumping pulse followed by a microwave  $\pi$ -pulse. 2 – Exposure of the Sisyphus beams for a time duration of  $\tau_{sis}$ . The total Sisyphus cooling time,  $N\tau_{sis}$ , can be varied by changing the number of cooling pulses  $N$  or the single-pulse cooling time  $\tau_{sis}$ . Depending on the laser intensity, the value of  $\tau_{sis}$  is chosen to keep the probability of pumping dark at a small level.

**Raman pulse:** The thermometry is performed by driving the motion-sensitive two-photon carrier transition  $|\downarrow, n\rangle \rightarrow |\uparrow, n\rangle$ . The Raman pulse is preceded by a 50- $\mu\text{s}$  optical pumping pulse that prepares the ion in the  $|\downarrow\rangle$  state. To measure  $\bar{n}$  in the transverse direction, the west and south Raman beams are activated, while for the axial direction, the east beam and a matched lower intensity south Raman beam are activated. A lower Raman intensity is used for the axial direction to account for the smaller separation of the 1<sup>st</sup> sideband from the carrier due to the lower secular frequency.

**State detection:** The spin state read out is achieved by using the fluorescence detection beam, which is the same as the Doppler cooling beam with a detuning of 10 MHz below the  $S_{1/2}(F = 1) \rightarrow P_{1/2}(F = 0)$  resonance. Since the  $S_{1/2}(F = 1) \rightarrow P_{1/2}(F = 0)$  transition is closed to the  $S_{1/2}(F = 0)$  state, an ion in the  $|\uparrow\rangle$  state will continue to scatter photons and is detected as bright, while the  $|\downarrow\rangle$  state will stay dark due to the large hyperfine splitting. To measure the ion's state, the detection beam is activated for 0.4 ms and the fluorescence photons during that time are collected and counted by a photo-multiplier tube (PMT). A discriminator threshold of 4 photon counts is used to distinguish the  $|\uparrow\rangle$  (bright) state and  $|\downarrow\rangle$  (dark) state. For each experiment, a photon count above threshold is recorded as a count of 1. Typically we achieve single-shot detection efficiencies of  $> 90\%$  for both states with  $\sim 12$  photons collected from the bright state in 0.4 ms.

**Data collection:** As mentioned before, the experiment is controlled by LabView software which creates the timing sequence through a spincore pulser card, and collects photon counts from the PMT using a National Instruments counter card. For the Sisyphus cooling measurements the length of the Raman time scan, the scan time step, and the number of experiments that are repeated per step can all be set by the user to acquire a carrier Rabi flopping curve. Our displayed data shows the probability  $P_{\uparrow}(t)$  following the Raman pulse, averaged over the experiments per point without any applied correction.

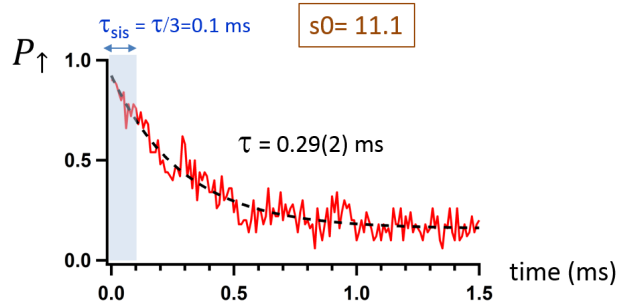


Figure 7.23: The measurement for the rate of pumping to the dark  $S_{1/2}(F=0)$  state in the presence of two Sisyphus beams at  $s_0 = 11$ . A pumping time of  $\tau = 0.3$  ms is found from an exponential fit, and the single-pulse cooling time is set to  $1/3$  of that value (0.1 ms) for all the measurements at that power.

## 7.8 Experimental results of the Sisyphus cooling of a single ion

We measure the cooling rate and steady-state  $\bar{n}$  of the Sisyphus cooling for a single  $^{171}\text{Yb}^+$ , in both axial and transverse directions. The experimental results are then compared to 3-D semiclassical, 1-D semiclassical, and 1-D quantum simulations.

### 7.8.1 Sisyphus cooling rate measurement:

We first present the results of the cooling rate measurement, performed as a function of the laser intensity. The cooling rate at each intensity value is extracted from a set of measurements of  $\bar{n}$  vs. Sisyphus cooling time, where the value of  $\bar{n}$  at each time is obtained from a Rabi-oscillation on the motion-sensitive carrier transition. This is done in both axial and transverse directions.

At each laser intensity, the decay rate into the dark  $S_{1/2}(F=0)$  state in the presence of the two Sisyphus beams is first measured (see Fig. 7.23), and fit to an exponential decay to find the pumping rate. The single-pulse Sisyphus cooling time  $\tau_{sis}$  is then set to  $1/3$  of the decay time. In this way, during the time  $\tau_{sis}$ , the ion will remain in the bright state (*i.e.* in the cooling cycle) with an average probability of 85%. The cooling time  $N\tau_{sis}$  is then varied by varying the number of Sisyphus cooling pulses  $N$ . The pulse sequence of each experiment run is the same as that shown in Fig. 7.22, with a 6.6-ms Doppler cooling time followed by the  $N$  Sisyphus cooling pulses, the Raman carrier transition, and finally the 0.4-ms readout. Thermometry for either the axial or transverse direction is enabled by the appropriate pair of Raman beams as discussed above. The measurement at each cooling time consists of a carrier time scan with a duration of 0.2(0.1) ms for the axial (transverse) direction. The number of time steps for each scan is 0.1(0.05)  $\mu\text{s}$  with 50 experiment runs

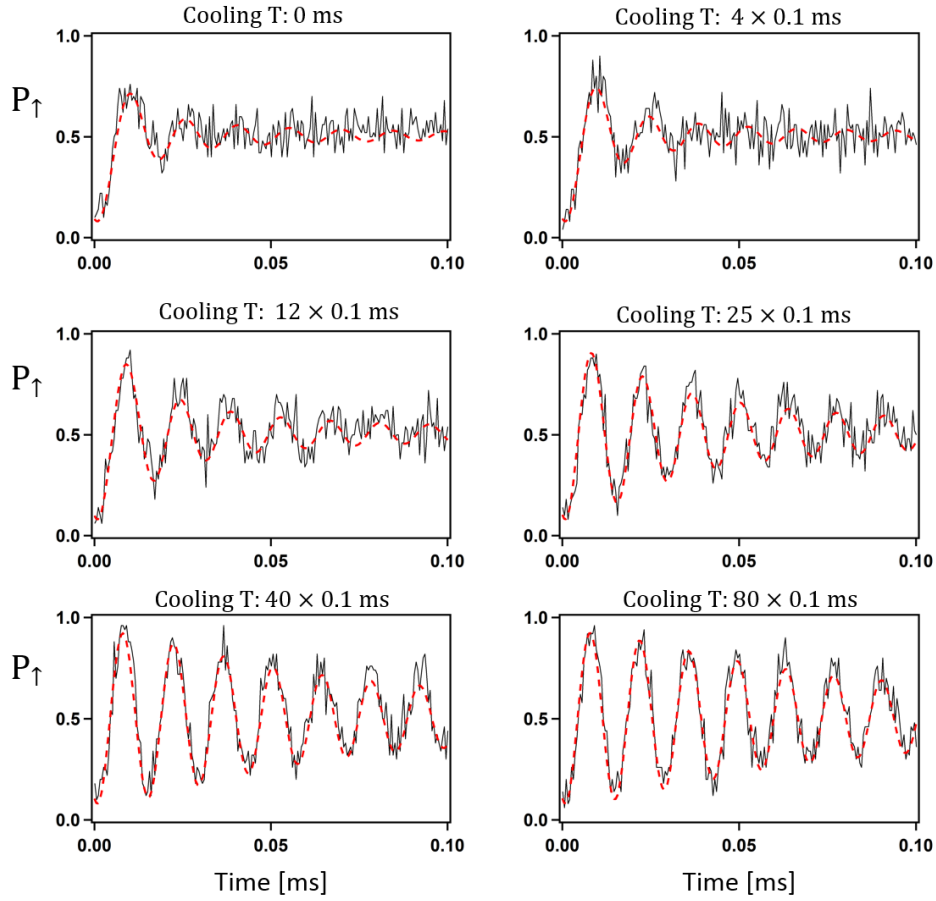


Figure 7.24: A selection of carrier scans vs. cooling time for the transverse direction and at a saturation parameter of  $s_0 = 11$ . The scans are fit to a thermally averaged Rabi oscillation (red line) to derive  $\bar{n}$  for each cooling time.

used for averaging at each point. A set of typically 15-20 measurements are performed to define the dependence of the ion's average energy on the cooling time. A selection of carrier scans vs. cooling time at  $s_0 = 11$  is shown in Fig. 7.24.

Each time scan represents the probability of being in the bright  $|\uparrow\rangle$  state, *i.e.* in the  $S_{1/2} |F = 1, m_F = 0\rangle$  state, following the carrier transition, and so is expected to exhibit Rabi oscillations (see Eq. 7.80). It can be seen in Fig. 7.24 that for the longer cooling times, the coherence contrast clearly increases, as does the Rabi frequency, which is a sign of a lower  $\bar{n}$ . Above a certain cooling time, the carrier oscillation is observed to remain unchanged as the cooling time becomes longer. This indicates that a final steady-state  $\bar{n}$  has been achieved. To find the  $\bar{n}$  for each cooling time, each plot is fit to Eq. 7.80 with an initial thermal distribution, and with some added modifications to account for experimental

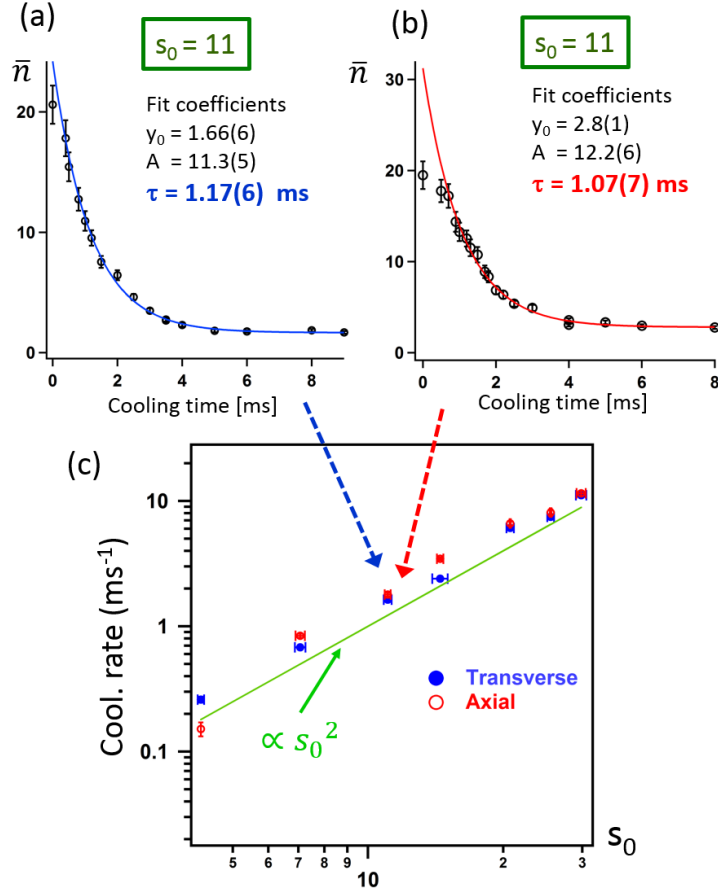


Figure 7.25: (a) Transverse  $\bar{n}$  and (b) axial  $\bar{n}$  as a function of Sisyphus cooling time at a single beam laser intensity corresponding to saturation parameter  $s_0 = 11$ . The plots are fit to an exponential decay to find the cooling rates at that laser intensity. (c) The complete data set of cooling rate over a range of laser intensities for both the axial and transverse directions. Note that the error bars for the  $\bar{n}$  values are from the carrier fits and the error bars for the cooling rates are from the exponential fits. The green line shows  $s_0^2$  scaling as a guide to the eye.

imperfections as follows:

$$\begin{aligned}
 P_{\uparrow}^c(t) &= (\xi_{\uparrow} - \xi_{\downarrow}) \sum_{n=0}^{N_f} P_n \sin^2 \left( \frac{2\pi\Omega_{n,n}(t-t_0)}{2\Omega_{00}} \right) + \xi_{\downarrow} \\
 &= (\xi_{\uparrow} - \xi_{\downarrow}) \sum_{n=0}^{N_f} \frac{\bar{n}^n}{(\bar{n} + 1)^{n+1}} \sin^2 \left( \frac{2\pi\eta^2 L_n^0(\eta^2)(t-t_0)}{2} \right) + \xi_{\downarrow},
 \end{aligned} \tag{7.87}$$

where  $\xi_{\uparrow}$  and  $\xi_{\downarrow}$  are bright-state and dark-state detection efficiency parameters, coming from the calibration measurements at the start of the day, and are held fixed in the fit. Typical values are  $\xi_{\uparrow} = 0.92$  and  $\xi_{\downarrow} = 0.06$ . The time offset  $t_0 \sim 1\mu\text{s}$  accounts for propagation

delays in the turn-on of the Raman AOM's. The time offset is also held constant in the fits over all data sets for each direction, but is different for the axial and transverse directions. The higher limit of the summation is  $N_f = 500$ . The only free fit parameters in the function are the carrier  $2\pi$ -time  $t_c$  and  $\bar{n}$ . The extracted  $\bar{n}$  values are then plotted vs. the Sisyphus cooling time, and fit to an exponential decay of the form  $\bar{n}_0 + A \exp(-(t - t_0)/\tau)$ , to extract the cooling rate  $\tau^{-1}$  at the given laser intensity. To omit the initial cooling dynamics, only the measured points with  $\bar{n} \leq 15$  are considered. Figures 7.25(a) and (b) show the transverse and axial  $\bar{n}$  vs. cooling time along with the resulting exponential decay fits for a single laser intensity corresponding to  $s_0 = 11$ . The error bars for the  $\bar{n}$  values are obtained from the carrier fits. Since on average the ion is cooled 85% of the time, due to the effect of pumping dark, the actual cooling rate is higher than the extracted value and is calculated as  $\Gamma_c = (\tau/0.85)^{-1}$ . Figure 7.25(c) shows the complete data set of axial and transverse cooling rates over a range of  $s_0$  (*i.e.* laser intensity), where the error bars of the cooling rates are from the exponential fits, and the error bars for the saturation parameter include calibration and drift uncertainties. It can be seen that the cooling rate values in the axial and transverse directions are very close, and they are roughly proportional to  $s_0^2$  as expected.

### 7.8.2 Sisyphus cooling limit:

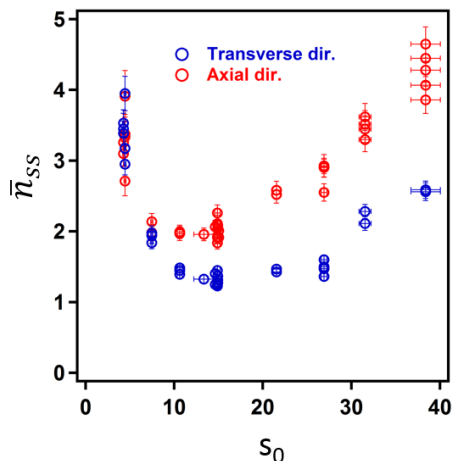


Figure 7.26: Measured steady-state  $\bar{n}$  vs. laser intensity, in terms of the single-beam on-resonant saturation parameter  $s_0$ , for the axial (red) and transverse (blue) directions. A minimum of  $\bar{n}_{ss} \simeq 1 - 2$  is observed at an optimum value of  $s_0 = 10 - 20$ , depending on the axis.

Next, we present measurements of the steady-state  $\bar{n}$  as a function of the laser intensity. These measurements are very similar to the cooling rate measurements. Potential heating sources such as micro-motion and Sisyphus laser noise are checked and minimized (if

necessary) on a regular basis. At each intensity, the steady-state  $\bar{n}$  is found by measuring the  $\bar{n}$  after a sufficiently long cooling time. To assure that the steady-state is reached, the total cooling time  $N\tau_{sis}$  at each intensity is adjusted to cover several cooling time constants ( $1/\Gamma_c$ ), which are obtained from the prior measurements. The single-pulse cooling time  $\tau_{sis}$  is adjusted to keep the probability of pumping out of the cooling cycle into the dark  $S_{1/2}(F=0)$  state at a fixed value of 0.8, and the number of pulses is chosen accordingly to get the required cooling time.

Similar to the measurements described in previous section, a carrier time scan is performed and the value of  $\bar{n}_{ss}$  is derived from a fit to Eq. 7.87. As expected, there is a minimum thermal energy - the Sisyphus cooling limit - that is obtained at an optimum laser intensity. The minimum energy in the transverse direction corresponds to  $\bar{n}_{ss} \simeq 1$ , while in the axial direction it is a higher value of  $\bar{n}_{ss} \simeq 2$  with the lower optimum intensity being due to the weaker confinement.

Next, we compare the experimental results of the  $\bar{n}_{ss}$  and cooling limit vs. laser intensity to the 1-D quantum and 3-D semiclassical simulations.

### 7.8.3 Comparison between experimental results and simulations

The comparison of the measured cooling rates and steady-state  $\bar{n}$  to the 3-D and 1-D semiclassical simulations, and the 1-D quantum simulations, are shown in Fig. 7.27. For the transverse cooling rate, all the simulation models match the experimental results reasonably well, while in the weaker axial direction, the 3-D semiclassical simulation matches the data slightly better overall than the 1-D semiclassical and noticeably better than the quantum simulations. The discrepancy between the 1-D and 3-D semiclassical simulations indicates that the transverse motion has some effect on the axial cooling behaviour, perhaps the additional effect of the transverse delocalization of the ion or correlations between the motions. Simulations in a factor of three tighter trap (that is deeper in the LDL) do not show this difference. The higher axial cooling rate predicted by the 1-D quantum simulation, by about an overall factor of 3-4, is related to the lower initial state ( $n_i = 8$ ) used in the calculation. A thermal initial state with  $\bar{n}_i = 22$ , (see Fig. 7.27(a)) as used in the semiclassical simulation, brings the quantum simulation result closer to the experiment, indicating the effect of deviations from the LDL.

For the transverse steady-state energy (*i.e.* the steady-state  $\bar{n}$  values), the 1-D quantum simulation matches the experiment reasonably well over the range considered. The transverse semiclassical simulations show similar good agreement, with perhaps the start of some deviations at larger intensity, which could be due to the effect of ground-state coherences. In the axial direction, there is a discrepancy between the experiment and theory by up to a factor of 2, although the general behaviours agree. Comparing the simulations first, we note that the quantum and semiclassical simulations agree well, and the quantum calculations show that the final energy is independent of initial motional state as expected. (Compare

$n_i = 8$  and  $\bar{n}_i = 22$  simulations in Fig. 7.27). The 3-D and 1-D semiclassical simulations also match, which suggests that the influence of other trap axes can be ignored at low energies. The origin of the discrepancy between the simulations and experiment in the axial direction is not clear. A test of the carrier thermometry for a ground-state cooled ion shows that the measurement is not baseline limited, and systematics in the fitting do not seem likely. The higher  $\bar{n}_{ss}$  values may be due to technical aspects not included in the modelling process, including the rf potential and the pulsed method of cooling and hyperfine repump. The measured heating rate in the axial trap direction of 0.015 phonons/ms is too small to explain the effect.

Finally, we comment briefly on possible systematic effects associated with the carrier fit model for the transverse direction. The reasonable agreement between the experimental and theoretical predictions in the transverse direction is obtained from fits to an effective 1-D model of carrier Rabi oscillations involving the two transverse directions (see discussion in Section 7.6). Using fits that consider a 2-D carrier model but ignore the effect of cross-mode Raman couplings does not affect the cooling rates obtained, but shifts the steady-state  $\bar{n}$  values up by  $\sim 10\%$  and reduces the match between experiment and theory. The effect of cross-mode coupling on the carrier Rabi oscillations and the comparison between the two fit models will be presented in a

In conclusion, we have demonstrated 3-D Sisyphus cooling of a single  $^{171}\text{Yb}$  ion and investigated the cooling rate and steady-state  $\bar{n}$  as a function of laser intensity. Our measurement results reasonably agree with the predictions of simulations based on the quantum and semiclassical theoretical models.

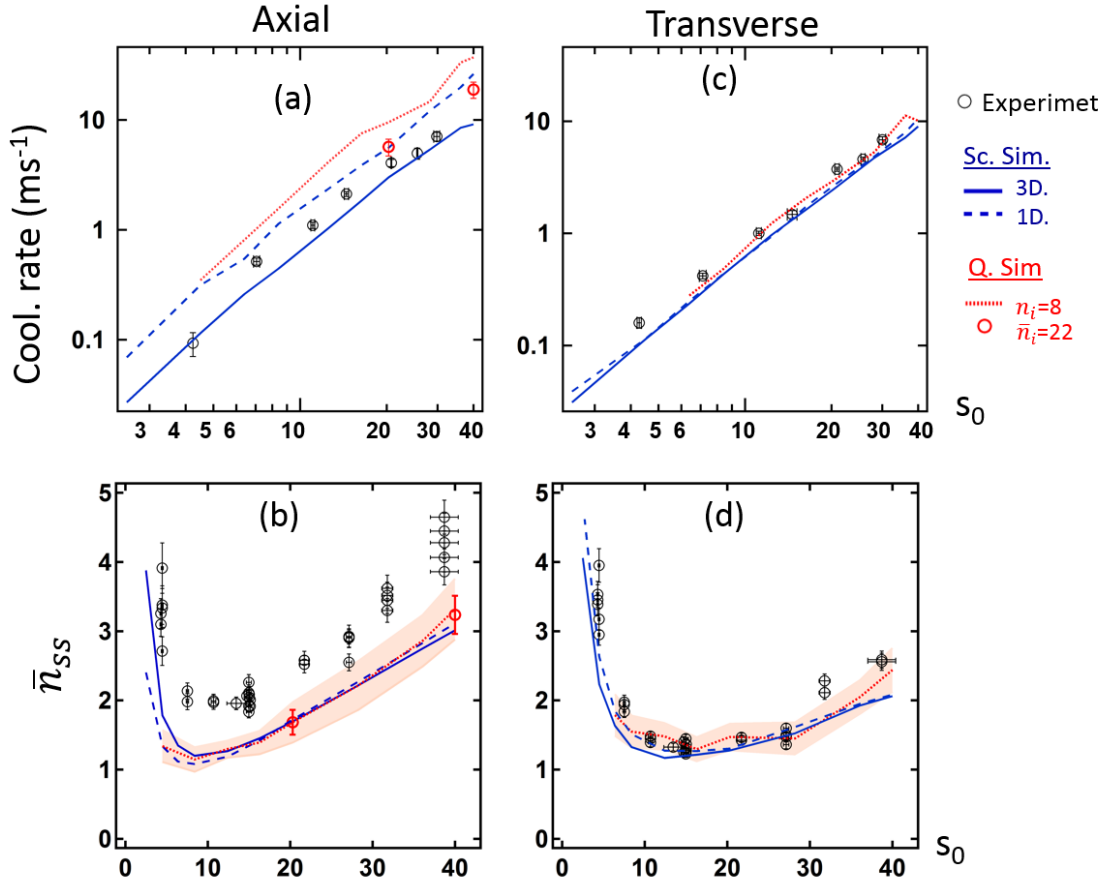


Figure 7.27: The cooling rate ((a) and (c)) and steady-state quantum number  $\bar{n}$  ((b) and (d)) as a function of laser intensity for the axial ((a) and (b)) and transverse ((c) and (d)) directions. The experimental measurements (black open circles) are compared to 3-D semiclassical simulations (solid blue line), 1-D semiclassical simulations (dashed blue line), and 1-D quantum simulations (red). The quantum simulations include those with an initial thermal state with  $\bar{n}_i = 22$  (red open circles), and an initial state of  $n_i = 8$  (red dotted line). The shaded region indicate the standard deviation of the  $\bar{n}$  fluctuations in steady state for the quantum simulation. The uncertainty in the  $\bar{n}_{ss}$  values obtained from the simulation is smaller.



## 7.9 Resolved sideband cooling using two-photon stimulated Raman transitions

With Sisyphus cooling in hand, we now proceed to the final goal of ground-state cooling. We first briefly review the technique of Raman sideband cooling for a single ion. We then go on to consider the case of Raman transitions for multiple trapped ions, and finally present both Sisyphus and sideband cooling results for a string of 4 ions.

In our experiment, ground-state cooling of trapped  $^{171}\text{Yb}$  ions is obtained by resolved sideband cooling based on the two-photon stimulated transition technique. We use the  $S_{1/2}|F=0, m_F=0\rangle$  state, labeled  $|\downarrow\rangle$ , and the  $S_{1/2}|F=1, m_F=0\rangle$  state, labeled  $|\uparrow\rangle$ , separated by a frequency of  $\omega_{HF}/2\pi = 12.6$  GHz. The Raman beams are far detuned from the excited state  $P_{1/2}$  ( $\Delta_R/2\pi = 100$  GHz). For ground-state cooling of a single ion's center-of-mass motion in the  $i^{\text{th}}$  direction, the frequency difference between the two Raman beams (ideally) needs to be set to  $\omega_{L2} - \omega_{L1} = \omega_{HF} - \omega_i$  to drive a red-sideband transition.

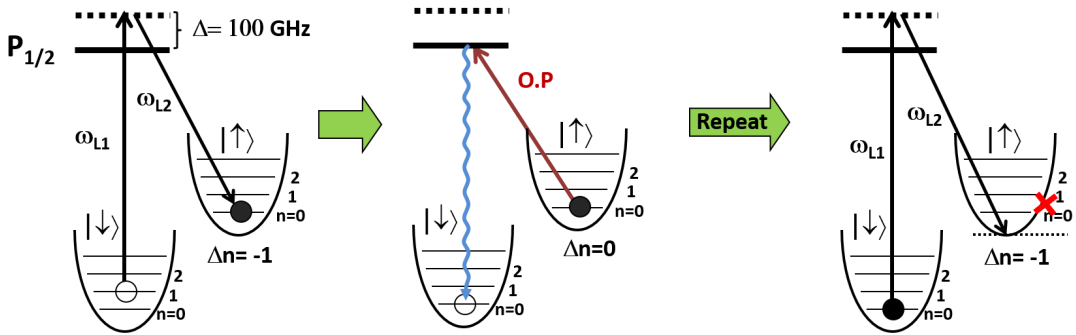


Figure 7.28: The ground-state cooling process is performed in two steps: first, a red-sideband transition driven by two Raman beams transfers the ion into a lower motional state:  $|\downarrow, n\rangle \rightarrow |\uparrow, n-1\rangle$ . Second, an optical pumping step resets the spin state:  $|\uparrow, n-1\rangle \rightarrow |\downarrow, n-1\rangle$ . The two steps are repeated until the ion reaches the ground state, which is decoupled from the red-sideband transition.

The basic concept behind sideband cooling is shown in Fig. 7.28. Starting with the ion in the  $|\downarrow, n\rangle$  state, a stimulated Raman transition tuned to the first red-sideband transition, and of suitable duration, transfers the ion into the  $|\uparrow, n-1\rangle$  state. The ion is then reset to the original spin state via optical pumping ( $|\uparrow, n-1\rangle \rightarrow |\downarrow, n-1\rangle$ ), and the process is repeated until the ion reaches the ground state. An efficient reset with optical pumping, in which the motional state  $n$  remains unchanged with a high probability, is only achieved in the LDL. When the initial energy of the ion ( $n_i$ ) is high, the probability of diffusion to a different motional state on recoil becomes higher, and there will be an increasing likelihood of being transferred into a higher motional state. In each scattering event, the ion gains an energy of  $\hbar(\omega_0 - \omega_i)$  through the photon absorption, and loses an energy on average of

$\hbar(\omega_0 - \omega_R)$  through the spontaneous emission. In the limit of  $\omega_R \ll \omega_i$  corresponding to tight traps and a small LD parameter, and assuming low initial energies, the ion loses a net energy of  $\hbar\omega_i$  over each scattering event.

Note that in the above discussion, it was assumed that the ion initially occupies a single vibrational state  $n$ . In practice, the initial vibrational level of the ion has an  $n$  value that is thermally distributed with mean set by for example the Doppler cooling limit. However, since the red-sideband Rabi frequency is  $n$ -dependent, a fixed pulse time can only be chosen to satisfy the  $|\uparrow, n-1\rangle \rightarrow |\downarrow, n-1\rangle$  transition with 100% efficiency for a single  $n$  value. Another problem with a fixed pulse time is that the ion can get trapped in a motional state when  $\Omega_{n,n-1}t = m\pi$ , ( $m$  being an integer). These problems can be remedied by using a pulse sequence that sweeps in from high to low  $n$ . For example in a 60-pulse sequence, for each step based on the  $n$  dependent Rabi frequency given by Eq. 7.60, a  $\pi$ -time for  $60 \rightarrow 59$ , then  $59 \rightarrow 58$  etc is chosen. To avoid the complications due to the added momentum diffusion discussed above, and to avoid a large number of pulses, sideband cooling is normally aimed to start in the LD regime. To understand ground-state cooling of an ion string, we next describe Raman transitions in the case of multiple ions.

## 7.10 Raman transition and thermometry of multiple ions

The idea of the single-ion interaction with a laser field can be extended to the case of an array of multiple ions as follows. We first assume that the laser field is applied to only one ion in the string, and in the end we will consider the case of all ions being illuminated uniformly by the Raman beams, which is the case in our experiment.

Even assuming that the laser field is applied to only one ion ( $j^{\text{th}}$  ion) in the string of  $N$  ions, we will have the new feature that the ion has components of motion from all  $3N$  collective vibrational modes. The dipole interaction Hamiltonian of Eq. 7.54 for the  $j^{\text{th}}$  ion can be written as

$$V_{dip-j} = \frac{\hbar\Omega}{2}(\sigma_{j+} + \sigma_{j-}) \left( e^{i(k \cdot x_j - \omega_L t + \phi_j)} + e^{-i(k \cdot x_j - \omega_L t + \phi_j)} \right) \quad (7.88)$$

For the case of a linear string, the motions in  $\hat{x}$ ,  $\hat{y}$  and  $\hat{z}$  directions are decoupled and the position operator can be expressed in terms of the normal-mode coordinates  $\phi_k$  with  $k \in \{1, 2, \dots, 3N\}$ , and the associable eigenvectors  $\psi_{jk}$  as follows:

$$x_j = \sum_{k=1}^{3N} \psi_{jk} \phi_k, \quad \phi_k = \phi_{k0}(a_k + a_k^\dagger). \quad (7.89)$$

The dipole Hamiltonian in the interaction picture with the RWA can then be written in terms of normal mode coordinates as

$$V_{Ij} = \frac{\hbar\Omega}{2} \sigma_{j+} \exp \left[ i \sum_{k=1}^{3N} \eta_{jk} (a_k e^{-i\omega_k t} + a_k^\dagger e^{i\omega_k t}) - i(\delta t - \phi_j) \right] + h.c., \quad (7.90)$$

where the Lamb-Dicke parameter associated with the  $k^{\text{th}}$  mode is  $\eta_{jk} \equiv k\psi_{ik}\phi_{k0}$ . In this case, the Rabi frequency of the  $k^{\text{th}}$  mode will become

$$\Omega_{j\{n'_k, n_k\}} \equiv \Omega \left| \langle \{n_{p \neq k}\}, n'_k | \prod_{l=1}^{3N} e^{i\eta_{jl}(a_l + a_l^\dagger)} | \{n_{p \neq k}\}, n_k \rangle \right|. \quad (7.91)$$

If we define  $\Omega_{j\{n'_k, n_k\}}^{(0)}$  to be the Rabi frequency of the  $k^{\text{th}}$  mode and for the  $j^{\text{th}}$  ion in the absence of all the other modes  $\{p \neq k\}$ ,

$$\Omega_{j\{n'_k, n_k\}}^{(0)} \equiv \Omega \left| \langle n'_k | e^{i\eta_{jk}(a_k + a_k^\dagger)} | n_k \rangle \right|, \quad (7.92)$$

the general Rabi frequency can be written in terms of  $\Omega_{j\{n'_k, n_k\}}^{(0)}$  and all the other  $3N - 1$  modes (spectator modes) labeled by  $p$  as follows:

$$\begin{aligned} \Omega_{j\{n'_k, n_k\}} &= \Omega_{j\{n'_k, n_k\}}^{(0)} \left| \langle \{n_{p \neq k}\} | \prod_{p \neq k} e^{i\eta_{jp}(a_p + a_p^\dagger)} | \{n_{p \neq k}\} \rangle \right| \\ &= \Omega_{j\{n'_k, n_k\}}^{(0)} \prod_{p \neq k} e^{-\eta_{jp}^2/2} L_{n_p}(\eta_{jp}^2). \end{aligned} \quad (7.93)$$

The states of the spectator modes are normally assumed to be thermally distributed with a mean vibrational number  $\bar{n}_p$ . If we average over the thermal distribution, the mean-squared Rabi frequency simplifies to

$$\bar{\Omega}_{j\{n'_k, n_k\}} = \Omega_{j\{n'_k, n_k\}}^{(0)} \prod_{p \neq k} e^{-\eta_{jp}^2(\bar{n}_p + 1/2)}. \quad (7.94)$$

In the Lamb-Dicke limit ( $\eta_{jp}^2(\bar{n}_p + 1/2) \ll 1$ ), it can be seen that the effect of the spectator modes can be ignored. More importantly, we do not show it here but the fluctuations in the Rabi frequency are also suppressed [20].

In the LDL limit, when the laser light shines *uniformly* on the whole string, as is the case in our experiment, all the ions couple to the field simultaneously and the Hamiltonian of the system can be written as

$$V_I = \frac{\hbar\Omega}{2} \sum_{j=1}^N \sigma_{+j} \exp \left[ i \sum_{k=1}^{3N} \eta_{jk} (a_k e^{-i\omega_k t} + a_k^\dagger e^{i\omega_k t}) - i(\delta t - \phi_j) \right] + h.c. \quad (7.95)$$

Due to the entanglement between the spin state of the system and the collective motion, the system cannot be treated as  $N$ -independent spin-1/2 systems, and the time-dependent wave-function of the system becomes quite complicated during a Rabi oscillation. For instance, in a string of  $N = 4$  ions, when the blue-sideband of the  $k^{\text{th}}$  mode is driven, the time dependent wave-function of the system involves a ladder of states from  $|\downarrow\downarrow\downarrow\downarrow, n_k\rangle$  all the way up to  $|\uparrow\uparrow\uparrow\uparrow, n_k + 4\rangle$ .

Nevertheless, the resolved sideband cooling of a string of ions in principle is the same as for a single ion. As long as the vibrational modes are resolved, any particular mode with frequency  $\omega_k$  can be cooled to the ground-state by tuning the Raman beams to  $\omega_{L2} - \omega_{L1} = \omega_{HF} - \omega_k$  to drive the first red sideband of that given mode. However, the recoil energy on reset is spread over all the modes and so heats all of them. In order to ground-state cool a string, all the modes need to be cooled simultaneously.

### 7.10.1 Thermometry:

For multiple trapped ions in our setup, the thermometry techniques using two-photon Raman transitions are not as simple as the case of a single ion, since all the ions are driven simultaneously in the transition and the connection between sideband Rabi oscillation and  $\bar{n}$  is more complicated<sup>5</sup>. For instance, in the case of sideband thermometry, where red and blue sideband transitions are driven, the value of  $\bar{n}$  cannot be directly derived from the sideband asymmetry. Nevertheless, the average  $\bar{n}_k$  of a vibrational mode in a multi-ion string can be obtained by fitting to the Rabi oscillation for the sidebands. In this case, the probability of observing the  $|\uparrow\rangle$  state for  $N$  ions, following a transition for the  $k^{\text{th}}$  mode, is

$$P_{\uparrow}(t) = \sum_{n_k=0} P_{n_k} P_{\uparrow, n_k}(t), \quad (7.96)$$

where  $P_{n_k}$  is given by a thermal distribution, and  $P_{\uparrow, n_k}(t)$  is found numerically by solving the Schrödinger equation (using Eq. 7.95) for each  $n_k$  in Python. Since we start from a Sisyphus cooled energy, the LD condition is satisfied and the spectator modes can be ignored in the calculation of  $P_{\uparrow, n_k}$ . In our experiment, the thermometry of four ions is performed by driving the red sideband starting from the  $|\downarrow\downarrow\downarrow\downarrow\rangle$  state and the  $|\uparrow\uparrow\uparrow\uparrow\rangle$  state. The value of  $\bar{n}$  is then found by simultaneously fitting the two Rabi oscillations to functions of the form of Eq 7.96. The red sideband applied to the  $|\uparrow\uparrow\uparrow\uparrow\rangle$  state, which gives equivalent information to the blue sideband applied to the  $|\downarrow\downarrow\downarrow\downarrow\rangle$  state, is obtained by first flipping the spins with a microwave  $\pi$ -pulse ( $|\downarrow\downarrow\downarrow\downarrow\rangle \rightarrow |\uparrow\uparrow\uparrow\uparrow\rangle$ ), and then applying the red sideband. Thus, we refer to this as " $\pi$ +red" sideband for convenience. Numerical simulation results for two samples of red and " $\pi$ +red" sideband Rabi oscillations for the transverse center-of-mass mode of a four-ion string are shown in Figs 7.29 (a) and (b).

---

<sup>5</sup>Individual addressing of ions is possible but more technically challenging than uniform illumination.

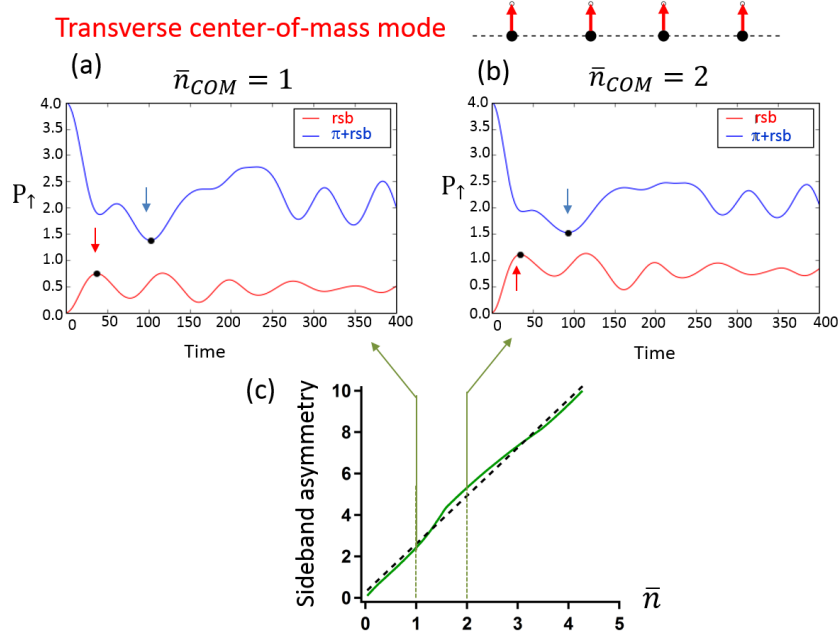


Figure 7.29: (a), (b) Simulation results of red-sideband Rabi oscillations for the transverse center-of-mass mode, starting from the  $|\downarrow\downarrow\downarrow\downarrow\rangle$  state (red line) or the  $|\uparrow\uparrow\uparrow\uparrow\rangle$  state (blue line) in a four-ion string with (a)  $\bar{n} = 1$  or (b)  $\bar{n} = 2$ . The sideband asymmetry for each pair of sideband oscillations is found by locating the maximum and minimum points of oscillations (shown by black points in (a), (b)). (c) The sideband asymmetry vs.  $\bar{n}$  (green line). This plot can be fit to a linear function (black dashed line) to obtain the approximate correction factor of 2.32(2) relating the sideband asymmetry to  $\bar{n}$  for the transverse COM mode of a four-ion string.

Alternatively, an approximate evaluation of  $\bar{n}_k$  can be obtained from the sideband asymmetry together with a mode-dependent correction factor. These correction factors are found from a linear fit to the numerical simulations of  $\bar{n}$  vs. sideband asymmetry (Fig. 7.29 (c)), ignoring spectator modes. For the case of four ions, these correction factors vary between 1–3 and are listed in Fig. 7.31. The approximate evaluation of  $\bar{n}$  is useful for quick estimates during the experiment, but for the analysis of our experimental results, we use fits.

## 7.11 Experimental results of sideband cooling

### 7.11.1 Sideband cooling of a single ion:

For sideband cooling of a given center-of-mass mode of a single ion, the experiment setup is mostly the same as for the Sisyphus cooling experiments described above. Separate rf synthesizers are used to drive the Raman south AOM for sideband cooling or thermometry operations. The thermometry uses a lower laser power to reduce off-resonant transitions from the carrier and other sidebands. We drive the sideband cooling transitions with higher

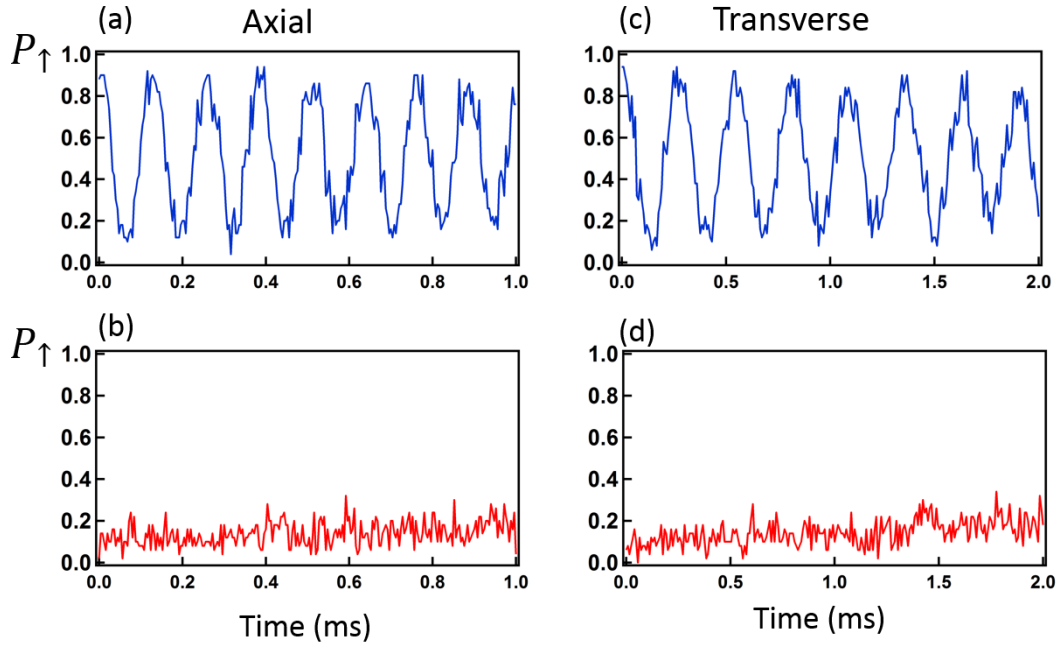


Figure 7.30: Rabi time scans used for the thermometry of a single sideband-cooled  $^{171}\text{Yb}$  ion. Both axial (a, b) and transverse  $y$  directions (c, d) are shown. The top panels (a, c) show the red sideband starting in the  $|\uparrow\rangle$  state and the bottom panels (b, d) show the red sideband starting in the  $|\downarrow\rangle$  state. The suppression of the red sideband oscillations in the later case indicates cooling to near the ground state of motion.

laser power, which is useful in the transverse direction where power broadening of the Raman sideband transition ( $\pi$ -time of 20–30  $\mu\text{s}$ ) allows us to simultaneously cool both transverse COM modes (typically spaced by 30 kHz). The experiment procedure follows that of the Sisyphus cooling. After the ion has been first Doppler cooled for 6.6 ms and then Sisyphus cooled for  $30 \times 0.2\text{ms} = 6$  ms, we tune the frequency of the sideband cooling synthesizer to the first sideband of the mode of interest and determine the time for a Rabi  $\pi$ -pulse. We then activate the sideband cooling sequence, programmed as described above typically with 30 pulses, and finally we use a thermometry sequence to assess the cooling outcome. In this situation the thermometry is performed with the sideband asymmetry technique (see Sec 7.7), for which the blue sideband is replaced by the " $\pi$ +red" sideband, *i.e.* the red sideband transition starting from the  $|\uparrow\rangle$  state.

Figure 7.30 shows a typical sideband cooling result for both the axial and transverse-  $y$  center-of-mass mode of a single ion. The suppression of the red sideband transition starting from the  $|\downarrow\rangle$  states indicates a final energy near to ground state with high probability. We find  $\bar{n} \leq 0.1$  for both the transverse motion with trap frequency of  $\omega_y/2\pi = 0.804$  MHz, and the axial motion with the trap frequency of  $\omega_z/2\pi = 0.324$  MHz.

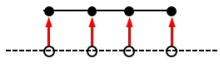
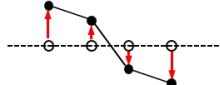
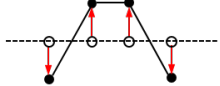

Mode	Transverse configuration	Frequency (kHz)			Sideband asymm. correction fac.
		x-axis	y-axis	z-axis	
Center-of-mass		836	814	328	2.32
Symm. Stretch or Rocking		768	745	568	1.75
Asymm. Stretch or Bending		662	635	789	2.44
Zigzag		499	463	999	1.8

Figure 7.31: The measured frequencies of the normal modes of a four-ion string along the three axes of motion, and the estimated sideband asymmetry correction factor for each mode.

### 7.11.2 Sisyphus and sideband cooling of a four-ion string

We now consider the case of a four-ion string. Following a period of Sisyphus cooling, we use sideband spectroscopy to measure the frequencies of the normal modes in all three axes. The measured frequencies of all 12 normal modes of a linear four-ion string in a typical trap setup are shown in the table of Fig. 7.31. The frequency difference between the two transverse modes varies between 21 kHz for the zigzag and 36 kHz for the COM mode. Similar to the single-ion case, for any given mode, both of the transverse axes are sideband cooled simultaneously. The simultaneous cooling is implemented by interleaved cooling pulse sequence for the resolved  $x$  and  $y$  modes.

For the four-ion string, the thermometry is performed by driving the red sideband and the " $\pi$ +red" sideband, and fitting both results simultaneously to find  $\bar{n}$  with a better accuracy (see Section 7.11). Figure 7.32 shows samples of  $\bar{n}$  measurements for the transverse bending mode, transverse zigzag, and axial zigzag mode. For each mode the Sisyphus-cooled and sideband-cooled results are shown. In a similar fashion to the carrier transition fits used for the Sisyphus cooling results of a single ion, we modify the fit function of Eq. 7.96 to account for experimental modifications and imperfections. These include detection efficiencies, in this case without the use of a discriminator (efficiencies held fixed in the fit); AOM delay (held fixed); and carrier Rabi frequency (a free fit parameter). In addition, we account approximately for the effect of spontaneous emission during the Raman Rabi time scans by including a linear baseline to the red sideband scan. Finally, we account approximately for the effect of residual Raman intensity differences across the four ions (primarily giving detuning variations) by adding an envelope function of variable timescale and final offset to the " $\pi$  + red" sideband scan. We have used either an exponential decay or cosine beat

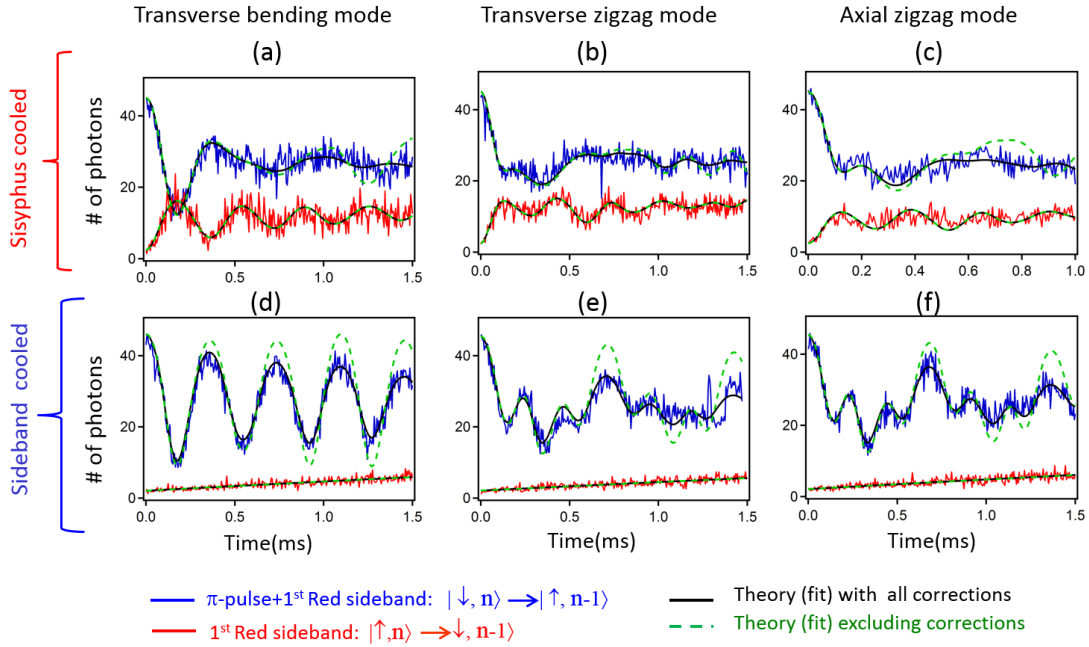


Figure 7.32: Sideband Rabi oscillations for three vibrational modes of a four-ion string following (a, b and c) Sisyphus cooling and (d, e and f) Raman sideband cooling for: (a and d) The transverse bending mode, (b and e) the transverse zigzag mode, and (c and f) the axial zigzag mode. Note that no discrimination between photon count levels is used in our four-ion detection, and so the vertical axes show the total number of counted photons in 0.4 ms. Black lines show fits including corrections for experimental imperfections (see text). Dotted lines show the ideal model with contrast envelope removed. Average vibrational number  $\bar{n}$  from the Sisyphus fits are (a) 1.60(4) for the transverse bending mode, (b) 1.95(4) for the transverse zigzag mode, and (c) 1.11(4) for the axial zigzag mode. The fits to the sideband cooled data constrain  $\bar{n} \leq 0.05$ .

for the envelope function. For the sideband-cooled scans, the three parameters describing spontaneous emission and intensity-balance effects are allowed to vary in the fits. The spontaneous emission correction is typically held fixed in the Sisyphus fits. Figure 7.32 shows example fits to the modified theory (black), for both Sisyphus and sideband cooled modes. The fit expression with the contrast envelope omitted (green) is also included to show the effect at long times.

The Sisyphus cooling reduces the average energy of the transverse zigzag mode to  $\bar{n} \simeq 2$ . Performing sideband cooling on the Sisyphus-cooled zigzag mode brings the averaged motional state down to  $\bar{n} \leq 0.05$ . We have successfully performed sideband cooling of all four modes of a four-ion string in the both axial and transverse directions. We have also performed simultaneous ground-state cooling of multiple transverse or axial vibrational modes, which are not shown in this thesis.



## 7.12 Conclusion

In conclusion, we have demonstrated that we can cool all modes of motion in an ion crystal of up to four ions to near  $\bar{n} \sim 1 - 2$  using Sisyphus cooling. This represents a lowering of the center-of-mass energy of  $> 20$  from Doppler values for the trap considered. Combining Sisyphus and Raman sideband cooling, we have achieved ground-state cooling for each of the modes of a four-ion crystal. For three ions we have also demonstrated simultaneous sideband cooling of all axial and all transverse modes following Sisyphus cooling. Overall, Sisyphus together with Raman cooling has enabled us to achieve the low temperatures towards the study of quantum regime of the linear-zigzag transition.

One obvious question is how much extra time Sisyphus cooling adds on top of the Doppler pre-cooling to an experimental sequence. It is interesting to compare the Sisyphus technique to other cooling methods for ions. The Sisyphus cooling rate of  $\sim 1 \text{ ms}^{-1}$  is certainly slower compared to Doppler cooling with a cooling rate of  $\sim 100 \mu\text{s}^{-1}$ , but in practice the Sisyphus sequence of 6 ms is only a factor of  $\sim 2$  longer than the typical Doppler cooling time used in this (and other) ion trapping experiments. Compared to the techniques of sideband cooling [22] and EIT cooling [170] used to achieve ground-state cooling, the Sisyphus technique cannot reach as low temperatures, but it benefits from a simplicity and robustness in part because it is not a resonant process. This permits the cooling of multiple modes of motion for an ion string without fine tuning of multiple cooling parameters. We should note, however, that Raman sideband cooling can cool all transverse modes simultaneously if the transverse confinement is strong enough to bring all modes close to degeneracy, but such a simplification does not arise in the axial direction. EIT cooling does have sufficient bandwidth to cool several modes simultaneously and has been demonstrated, for example, to cool three axial modes of a mixed species  $\text{Be}^+ - \text{Mg}^+$  crystal to below  $\bar{n} \sim 0.1 - 0.2$  in 40  $\mu\text{s}$  [200], but doing the same for more ions or all axes will become more challenging. Like EIT cooling, the Sisyphus technique requires much less optical power than for Raman cooling. We use typically 10 – 20  $\mu\text{W}$  per beam compared to 1 mW per beam for the Raman transitions. It is also a technical advantage that the Sisyphus beams can be derived directly from the Doppler cooling and detection laser and require the same single direction of optical access to enable 3-D cooling. Of course Sisyphus cooling works also outside the LD regime, which has allowed us to bridge Doppler and sideband cooling in our setup. One down side to Sisyphus cooling is that it does not tolerate large micro-motion. For Raman cooling, the micromotion will only reduce the sideband strength, but in the case of Sisyphus cooling the polarization-gradient effect is simply washed out. Our Sisyphus technique should easily extend to more than four ions although there might be some compromise in optimum cooling limit when the axial frequency is reduced to accommodate a large string. This would for example be of interest in recent proposals to study heat transport in ion strings [201–205]. It also may be useful

in quantum information applications where deep ground-state cooling is not required, for example in microwave-based logic [206, 207].

## Chapter 8

# Conclusion

In conclusion, we have studied the dynamics of a string of trapped ions near the critical point of the linear-zigzag (L-Z) structural transition. We measured the rate of spontaneous nucleation of topological kink-defects as a function of the quench rate across the LZ transition in a string of 42–43 Doppler-cooled and trapped  $^{174}\text{Yb}$  ions, and found good agreement with molecular dynamics simulations. Using the molecular dynamics simulations, we assessed the effect of kink losses and showed how they can mask the intrinsic nucleation rate, and result in a reshaping of the simple power-law dependence over the full range of quench rates used. We went beyond testing the KZM, and explored the two different types of the kink, discrete and extended, observed in our experiments and presented the role of the quench end-point in configurational change and the survival probability for each type of the kink. Furthermore, we investigated the post-nucleation dynamics of discrete kinks by observing their trajectories in the zigzag structure in a sequence of pictures taken over 0.4 s. The final results demonstrated a behavioral sensitivity on the ion number at the single ion level. A maximum lifetime of  $\geq 1$  s was extracted for the created kinks, implying that further studies of kink dynamics are possible, perhaps even in the quantum regime.

Extending the investigations of the near-transition dynamics to ultra-low temperatures, we presented the outline of an on-going experiment of our group to reach the quantum regime with a smaller string of four  $^{171}\text{Yb}$  ions. The goal of the experiment is to prepare a quantum superposition of the two broken-symmetry states, the zig and zag configurations, and assess the coherence time through tunneling oscillations near the critical point. To assess the feasibility of this measurement, we discussed several possible experimental/technical obstacles of the experiment and estimated the order of required sensitivities for our setup. Compared to the previous experiment in the classical regime, this experiment is more challenging. An awareness of the (possibly limiting) challenges/issues and ways to address them should be generally valuable to similar experiments.

One of the main requirements for the success of the tunneling measurement is an efficient ground-state cooling of the zigzag vibrational mode. In order to achieve an efficient

ground-state cooling in our setup, we demonstrated a 3-D Sisyphus cooling technique as an intermediate step between Doppler cooling and resolved sideband cooling. We provided a complete study of Sisyphus cooling of a single trapped  $^{171}\text{Yb}$  ion in and near the Lamb-Dicke regime by measuring the cooling rate and steady-state  $\bar{n}$  as a function of the cooling beam intensity. The measurement results were shown to agree with molecular dynamics simulations based on semiclassical and quantum models. Moreover, by comparing with the results of simulations under different conditions, we investigated the effects of experimental complications, such as lattice modulation, on the cooling rate and cooling limit. Finally, going back to our original motivation for Sisyphus cooling, we presented the measurement results of a successful ground-state cooling of any given vibrational mode of a four-ion string, in particular of the transverse zigzag mode required for the proposed measurements of tunneling. Based on the technical simplicity of Sisyphus cooling, providing a 3-D simultaneous cooling of all vibration modes to near  $\bar{n} \simeq 1$ , we expect that Sisyphus cooling of trapped ions will be of general use, particularly in experiments involving ion strings of a moderate size.

Beyond the cooling work described in the thesis, we have also worked experimentally on the other challenges listed in Chapter 6 for the tunneling project. We have already demonstrated deterministic preparation of zig or zag state of a four-ion crystal with high efficiency. We have also successfully sideband re-cooled these structures after the ramp to the zigzag side. We have made some preliminary assessment of the residual asymmetry in the four-ion double well by measuring the bias in the creation of the zig or zag (60-40) following a ramp across the transition at sideband-cooled temperatures. The stability of the critical point was assessed using Raman spectroscopy, and we found that drifts likely due to the rf voltage need to be suppressed a further factor 3-10 to reach the desired high stability. Finally, we have made preliminary heating assessments of the local zigzag mode on both sides of the transition near the critical point. On the linear side we find that the heating of the zigzag mode is strongly suppressed, but as can be expected on the zigzag side, the heating rate increases away from the critical point as the zigzag structure grows. We have measured the heating rate of the zigzag mode with a frequency as low as 50 kHz on the zigzag side of the transition (0.6 phonons/ms at  $\nu_{zz}=50$  kHz ) but further measurements closer to the critical point (i.e. at a zigzag mode frequency of about 13 kHz) are still required to determine the level of mode heating to be expected near the tunneling point. The last step would be to assess the net decoherence in the tunneling signal itself.

Looking into the future, if the tunneling signal could be obtained, the next type of experiments one can aim to perform is assessing the decoherence of a zigzag superposition state and its dependence on the size of the system. This could be done by varying the size of the zigzag amplitude or increasing the number of ions in the string. Based on the preliminary heating assessment of our setup, we presume that the latter is probably a more feasible approach for our setup.

# Bibliography

- [1] I. Chuang, R. Durrer, N. Turok, and B. Yurke, “Cosmology in the laboratory: Defect dynamics in liquid crystals,” *Science*, vol. 251, no. 4999, pp. 1336–1342, 1991. [Online]. Available: <http://www.sciencemag.org/content/251/4999/1336.abstract>
- [2] M. J. Bowick, L. Chandar, E. A. Schiff, and A. M. Srivastava, “The cosmological kibble mechanism in the laboratory: String formation in liquid crystals,” *Science*, vol. 263, no. 5149, pp. 943–945, 1994. [Online]. Available: <http://www.sciencemag.org/content/263/5149/943.abstract>
- [3] S. Ducci, P. L. Ramazza, W. González-Viñas, and F. T. Arecchi, “Order parameter fragmentation after a symmetry-breaking transition,” *Phys. Rev. Lett.*, vol. 83, pp. 5210–5213, Dec 1999. [Online]. Available: <http://link.aps.org/doi/10.1103/PhysRevLett.83.5210>
- [4] S. Chae, N. Lee, Y. Horibe, M. Tanimura, S. Mori, B. Gao, S. Carr, and S.-W. Cheong, “Direct observation of the proliferation of ferroelectric loop domains and vortex-antivortex pairs,” *Phys. Rev. Lett.*, vol. 108, p. 167603, Apr 2012. [Online]. Available: <http://link.aps.org/doi/10.1103/PhysRevLett.108.167603>
- [5] S. Griffin, M. Lilienblum, K. Delaney, Y. Kumagai, M. Fiebig, and N. Spaldin, “Scaling behavior and beyond equilibrium in the hexagonal manganites,” *Phys. Rev. X*, vol. 2, p. 041022, Dec 2012. [Online]. Available: <http://link.aps.org/doi/10.1103/PhysRevX.2.041022>
- [6] C. N. Weiler, T. W. Neely, D. R. Scherer, A. S. Bradley, M. J. Davis, and B. P. Anderson, “Spontaneous vortices in the formation of bose-einstein condensates,” *Nature*, vol. 455, p. 948, 10 2008. [Online]. Available: <http://dx.doi.org/10.1038/nature07334>
- [7] G. Lamporesi, S. Donadello, S. Serafini, F. Dalfovo, and G. Ferrari, “Spontaneous creation of kibble-zurek solitons in a bose-einstein condensate,” *Nat Phys*, vol. 9, p. 656, 10 2013. [Online]. Available: <http://dx.doi.org/10.1038/nphys2734>
- [8] K. Pyka, J. Keller, H. L. Partner, R. Nigmatullin, T. Burgermeister, D. M. Meier, K. Kuhlmann, A. Retzker, M. B. Plenio, W. H. Zurek, A. del Campo, and T. E. Mehlstäubler, “Topological defect formation and spontaneous symmetry breaking in ion coulomb crystals,” *Nat Commun*, vol. 4, 08 2013. [Online]. Available: <http://dx.doi.org/10.1038/ncomms3291>
- [9] P. van der Straten, S.-Q. Shang, B. Sheehy, H. Metcalf, and G. Nienhuis, “Laser cooling at low intensity in a strong magnetic field,” *Phys. Rev. A*, vol. 47,

- pp. 4160–4175, May 1993. [Online]. Available: <http://link.aps.org/doi/10.1103/PhysRevA.47.4160>
- [10] R. F. Wuerker, H. Shelton, and R. V. Langmuir, “Electrodynamic containment of charged particles,” *Journal of Applied Physics*, vol. 30, no. 3, pp. 342–349, 1959. [Online]. Available: <http://scitation.aip.org/content/aip/journal/jap/30/3/10.1063/1.1735165>
- [11] G. Werth, V. N. Gheorghe, and F. G. Major, *Charged Particle Traps II Applications*. Springer-Verlag, 2009.
- [12] D. Wineland and H. Dehmelt, “Proposed  $10^{-14}$   $\delta\nu/\nu$  laser fluorescence spectroscopy on  $\text{Ti}^+$  mono-ion oscillator III,” *Bull. Am. Phys. Soc.*, p. 637, 1975.
- [13] T. Hansch and A. Schawlow, “Cooling of gases by laser radiation,” *Optics Communications*, vol. 13, no. 1, pp. 68 – 69, 1975. [Online]. Available: <http://www.sciencedirect.com/science/article/pii/0030401875901595>
- [14] D. J. Wineland, R. E. Drullinger, and F. L. Walls, “Radiation-pressure cooling of bound resonant absorbers,” *Phys. Rev. Lett.*, vol. 40, pp. 1639–1642, Jun 1978. [Online]. Available: <http://link.aps.org/doi/10.1103/PhysRevLett.40.1639>
- [15] W. Neuhauser, M. Hohenstatt, P. Toschek, and H. Dehmelt, “Optical-sideband cooling of visible atom cloud confined in parabolic well,” *Phys. Rev. Lett.*, vol. 41, pp. 233–236, Jul 1978. [Online]. Available: <http://link.aps.org/doi/10.1103/PhysRevLett.41.233>
- [16] W. Neuhauser, M. Hohenstatt, P. E. Toschek, and H. Dehmelt, “Localized visible  $\text{Ba}^+$  mono-ion oscillator,” *Phys. Rev. A*, vol. 22, pp. 1137–1140, Sep 1980. [Online]. Available: <http://link.aps.org/doi/10.1103/PhysRevA.22.1137>
- [17] F. Diedrich, E. Peik, J. M. Chen, W. Quint, and H. Walther, “Observation of a phase transition of stored laser-cooled ions,” *Phys. Rev. Lett.*, vol. 59, pp. 2931–2934, Dec 1987. [Online]. Available: <http://link.aps.org/doi/10.1103/PhysRevLett.59.2931>
- [18] D. J. Wineland, J. C. Bergquist, W. M. Itano, J. J. Bollinger, and C. H. Manney, “Atomic-ion coulomb clusters in an ion trap,” *Phys. Rev. Lett.*, vol. 59, pp. 2935–2938, Dec 1987. [Online]. Available: <http://link.aps.org/doi/10.1103/PhysRevLett.59.2935>
- [19] J. C. Bergquist, W. M. Itano, and D. J. Wineland, “Recoilless optical absorption and doppler sidebands of a single trapped ion,” *Phys. Rev. A*, vol. 36, pp. 428–430, Jul 1987. [Online]. Available: <http://link.aps.org/doi/10.1103/PhysRevA.36.428>
- [20] D. Wineland, C. Monroe, W. M. Itano, D. Leibfried, B. E. King, and D. M. Meekhof, “Experimental issues in coherent quantum-state manipulation of trapped atomic ions,” *J. Res. Natl. Inst. Stand. and Technol.*, vol. 103, no. 3, p. 259, 1998.
- [21] F. Diedrich, J. C. Bergquist, W. M. Itano, and D. J. Wineland, “Laser cooling to the zero-point energy of motion,” *Phys. Rev. Lett.*, vol. 62, pp. 403–406, Jan 1989. [Online]. Available: <http://link.aps.org/doi/10.1103/PhysRevLett.62.403>

- [22] C. Monroe, D. M. Meekhof, B. E. King, S. R. Jefferts, W. M. Itano, D. J. Wineland, and P. Gould, “Resolved-sideband raman cooling of a bound atom to the 3d zero-point energy,” *Phys. Rev. Lett.*, vol. 75, pp. 4011–4014, Nov 1995. [Online]. Available: <http://link.aps.org/doi/10.1103/PhysRevLett.75.4011>
- [23] J. J. Bollinger, J. D. Prestage, W. M. Itano, and D. J. Wineland, “Laser-cooled-atomic frequency standard,” *Phys. Rev. Lett.*, vol. 54, pp. 1000–1003, Mar 1985. [Online]. Available: <http://link.aps.org/doi/10.1103/PhysRevLett.54.1000>
- [24] J. I. Cirac and P. Zoller, “Quantum computations with cold trapped ions,” *Phys. Rev. Lett.*, vol. 74, pp. 4091–4094, May 1995. [Online]. Available: <http://link.aps.org/doi/10.1103/PhysRevLett.74.4091>
- [25] G. Birkl, S. Kassner, and H. Walther, “Multiple-shell structures of laser-cooled  $^{24}\text{Mg}^+$  ions in a quadrupole,” *Nature*, vol. 357, pp. 310–313, 05 1992. [Online]. Available: <http://dx.doi.org/10.1038/357310a0>
- [26] I. Waki, S. Kassner, G. Birkl, and H. Walther, “Observation of ordered structures of laser-cooled ions in a quadrupole storage ring,” *Phys. Rev. Lett.*, vol. 68, pp. 2007–2010, Mar 1992. [Online]. Available: <http://link.aps.org/doi/10.1103/PhysRevLett.68.2007>
- [27] H. Walther, “From a single ion to a mesoscopic system - crystallization of ions in paul traps,” *Physica Scripta*, vol. 1995, no. T59, p. 360, 1995. [Online]. Available: <http://stacks.iop.org/1402-4896/1995/i=T59/a=049>
- [28] W. M. Itano, J. J. Bollinger, J. N. Tan, B. Jelenkovic, X.-P. Huang, and D. J. Wineland, “Bragg diffraction from crystallized ion plasmas,” *Science*, vol. 279, no. 5351, pp. 686–689, 1998. [Online]. Available: <http://www.sciencemag.org/content/279/5351/686.abstract>
- [29] T. B. Mitchell, J. J. Bollinger, D. H. E. Dubin, X.-P. Huang, W. M. Itano, and R. H. Baughman, “Direct observations of structural phase transitions in planar crystallized ion plasmas,” *Science*, vol. 282, no. 5392, pp. 1290–1293, 1998. [Online]. Available: <http://www.sciencemag.org/content/282/5392/1290.abstract>
- [30] T. Mitchell, J. Bollinger, X.-P. Huang, and W. Itano, “Doppler imaging of plasma modes in a penning trap,” *Opt. Express*, vol. 2, no. 8, pp. 314–322, Apr 1998. [Online]. Available: <http://www.opticsexpress.org/abstract.cfm?URI=oe-2-8-314>
- [31] M. Drewsen, C. Brodersen, L. Hornekær, J. S. Hangst, and J. P. Schifffer, “Large ion crystals in a linear paul trap,” *Phys. Rev. Lett.*, vol. 81, pp. 2878–2881, Oct 1998. [Online]. Available: <http://link.aps.org/doi/10.1103/PhysRevLett.81.2878>
- [32] M. J. Jensen, T. Hasegawa, J. J. Bollinger, and D. H. E. Dubin, “Rapid heating of a strongly coupled plasma near the solid-liquid phase transition,” *Phys. Rev. Lett.*, vol. 94, p. 025001, Jan 2005. [Online]. Available: <http://link.aps.org/doi/10.1103/PhysRevLett.94.025001>
- [33] L. Hornekær, N. Kjærgaard, A. M. Thommesen, and M. Drewsen, “Structural properties of two-component coulomb crystals in linear paul traps,” *Phys.*

- Rev. Lett.*, vol. 86, pp. 1994–1997, Mar 2001. [Online]. Available: <http://link.aps.org/doi/10.1103/PhysRevLett.86.1994>
- [34] L. Hornekær and M. Drewsen, “Formation process of large ion coulomb crystals in linear paul traps,” *Phys. Rev. A*, vol. 66, p. 013412, Jul 2002. [Online]. Available: <http://link.aps.org/doi/10.1103/PhysRevA.66.013412>
- [35] A. Mortensen, E. Nielsen, T. Matthey, and M. Drewsen, “Radio frequency field-induced persistent long-range ordered structures in two-species ion coulomb crystals,” *Journal of Physics B: Atomic, Molecular and Optical Physics*, vol. 40, no. 15, p. F223, 2007. [Online]. Available: <http://stacks.iop.org/0953-4075/40/i=15/a=F01>
- [36] A. Dantan, J. P. Marler, M. Albert, D. Guénot, and M. Drewsen, “Noninvasive vibrational mode spectroscopy of ion coulomb crystals through resonant collective coupling to an optical cavity field,” *Phys. Rev. Lett.*, vol. 105, p. 103001, Aug 2010. [Online]. Available: <http://link.aps.org/doi/10.1103/PhysRevLett.105.103001>
- [37] J. Mostowski and M. Gajda, “Light scattering by trapped ions,” *Acta Physica Polonica, A*, vol. 67, pp. 783–802, 1985.
- [38] E. Baklanov and V. Chebotayev, “Resonant light absorption by the ordered structures of ions stored in a trap,” *Applied Physics B*, vol. 39, no. 3, pp. 179–181, 1986. [Online]. Available: <http://dx.doi.org/10.1007/BF00697416>
- [39] R. Casdorff and R. Blatt, “Ordered structures and statistical properties of ion clouds stored in a paul trap,” *Applied Physics B*, vol. 45, pp. 175–182, 1988. [Online]. Available: <http://dx.doi.org/10.1007/BF00695288>
- [40] A. Rahman and J. P. Schiffer, “A condensed state in a system of stored and cooled ions,” *Physica Scripta*, vol. 1988, no. T22, p. 133, 1988. [Online]. Available: <http://stacks.iop.org/1402-4896/1988/i=T22/a=020>
- [41] D. H. E. Dubin and T. M. O’Neil, “Computer simulation of ion clouds in a penning trap,” *Phys. Rev. Lett.*, vol. 60, pp. 511–514, Feb 1988. [Online]. Available: <http://link.aps.org/doi/10.1103/PhysRevLett.60.511>
- [42] R. Hasse and J. Schiffer, “The structure of the cylindrically confined coulomb lattice,” *Annals of Physics*, vol. 203, no. 2, pp. 419 – 448, 1990. [Online]. Available: <http://www.sciencedirect.com/science/article/pii/000349169090177P>
- [43] R. W. Hasse and V. V. Avilov, “Structure and madelung energy of spherical coulomb crystals,” *Phys. Rev. A*, vol. 44, pp. 4506–4515, Oct 1991. [Online]. Available: <http://link.aps.org/doi/10.1103/PhysRevA.44.4506>
- [44] J. P. Schiffer, “Phase transitions in anisotropically confined ionic crystals,” *Phys. Rev. Lett.*, vol. 70, pp. 818–821, Feb 1993. [Online]. Available: <http://link.aps.org/doi/10.1103/PhysRevLett.70.818>
- [45] D. H. E. Dubin, “Theory of structural phase transitions in a trapped coulomb crystal,” *Phys. Rev. Lett.*, vol. 71, pp. 2753–2756, Oct 1993. [Online]. Available: <http://link.aps.org/doi/10.1103/PhysRevLett.71.2753>



- [46] H. Totsuji, T. Kishimoto, C. Totsuji, and K. Tsuruta, “Competition between two forms of ordering in finite coulomb clusters,” *Phys. Rev. Lett.*, vol. 88, p. 125002, Mar 2002. [Online]. Available: <http://link.aps.org/doi/10.1103/PhysRevLett.88.125002>
- [47] D. H. E. Dubin, “Effect of correlations on the thermal equilibrium and normal modes of a non-neutral plasma,” *Phys. Rev. E*, vol. 53, pp. 5268–5290, May 1996. [Online]. Available: <http://link.aps.org/doi/10.1103/PhysRevE.53.5268>
- [48] J. P. Schiffer, M. Drewsen, J. S. Hangst, and L. Hornekær, “Temperature, ordering, and equilibrium with time-dependent confining forces,” *Proceedings of the National Academy of Sciences*, vol. 97, no. 20, pp. 10 697–10 700, 2000. [Online]. Available: <http://www.pnas.org/content/97/20/10697.abstract>
- [49] D. G. Enzer, M. M. Schauer, J. J. Gomez, M. S. Gulley, M. H. Holzscheiter, P. G. Kwiat, S. K. Lamoreaux, C. G. Peterson, V. D. Sandberg, D. Tupa, A. G. White, R. J. Hughes, and D. F. V. James, “Observation of power-law scaling for phase transitions in linear trapped ion crystals,” *Phys. Rev. Lett.*, vol. 85, pp. 2466–2469, Sep 2000. [Online]. Available: <http://link.aps.org/doi/10.1103/PhysRevLett.85.2466>
- [50] E. L. Pollock and J. P. Hansen, “Statistical mechanics of dense ionized matter. ii. equilibrium properties and melting transition of the crystallized one-component plasma,” *Phys. Rev. A*, vol. 8, pp. 3110–3122, Dec 1973. [Online]. Available: <http://link.aps.org/doi/10.1103/PhysRevA.8.3110>
- [51] E. Wigner, “Effects of the electron interaction on the energy levels of electrons in metals,” *Trans. Faraday Soc.*, vol. 34, pp. 678–685, 1938. [Online]. Available: <http://dx.doi.org/10.1039/TF9383400678>
- [52] M. G. Raizen, J. M. Gilligan, J. C. Bergquist, W. M. Itano, and D. J. Wineland, “Ionic crystals in a linear paul trap,” *Phys. Rev. A*, vol. 45, pp. 6493–6501, May 1992. [Online]. Available: <http://link.aps.org/doi/10.1103/PhysRevA.45.6493>
- [53] G. Piacente, I. V. Schweigert, J. J. Betouras, and F. M. Peeters, “Generic properties of a quasi-one-dimensional classical wigner crystal,” *Phys. Rev. B*, vol. 69, p. 045324, Jan 2004. [Online]. Available: <http://link.aps.org/doi/10.1103/PhysRevB.69.045324>
- [54] S. Fishman, G. De Chiara, T. Calarco, and G. Morigi, “Structural phase transitions in low-dimensional ion crystals,” *Phys. Rev. B*, vol. 77, p. 064111, Feb 2008. [Online]. Available: <http://link.aps.org/doi/10.1103/PhysRevB.77.064111>
- [55] E. Shimshoni, G. Morigi, and S. Fishman, “Quantum zigzag transition in ion chains,” *Phys. Rev. Lett.*, vol. 106, p. 010401, Jan 2011. [Online]. Available: <http://link.aps.org/doi/10.1103/PhysRevLett.106.010401>
- [56] P. Silvi, G. De Chiara, T. Calarco, G. Morigi, and S. Montangero, “Full characterization of the quantum linear-zigzag transition in atomic chains,” *Annalen der Physik*, vol. 525, no. 10-11, pp. 827–832, 2013. [Online]. Available: <http://dx.doi.org/10.1002/andp.201300090>
- [57] A. Retzker, R. C. Thompson, D. M. Segal, and M. B. Plenio, “Double well potentials and quantum phase transitions in ion traps,” *Phys. Rev. Lett.*, vol. 101, p. 260504, Dec 2008. [Online]. Available: <http://link.aps.org/doi/10.1103/PhysRevLett.101.260504>

- [58] R. Schmied, T. Roscilde, V. Murg, D. Porrás, and J. I. Cirac, “Quantum phases of trapped ions in an optical lattice,” *New Journal of Physics*, vol. 10, no. 4, p. 045017, 2008. [Online]. Available: <http://stacks.iop.org/1367-2630/10/i=4/a=045017>
- [59] H. Landa, S. Marcovitch, A. Retzker, M. B. Plenio, and B. Reznik, “Quantum coherence of discrete kink solitons in ion traps,” *Phys. Rev. Lett.*, vol. 104, p. 043004, Jan 2010. [Online]. Available: <http://link.aps.org/doi/10.1103/PhysRevLett.104.043004>
- [60] Z.-X. Gong, G.-D. Lin, and L.-M. Duan, “Temperature-driven structural phase transition for trapped ions and a proposal for its experimental detection,” *Phys. Rev. Lett.*, vol. 105, p. 265703, Dec 2010. [Online]. Available: <http://link.aps.org/doi/10.1103/PhysRevLett.105.265703>
- [61] A. del Campo, G. De Chiara, G. Morigi, M. B. Plenio, and A. Retzker, “Structural defects in ion chains by quenching the external potential: The inhomogeneous kibble-zurek mechanism,” *Phys. Rev. Lett.*, vol. 105, p. 075701, Aug 2010. [Online]. Available: <http://link.aps.org/doi/10.1103/PhysRevLett.105.075701>
- [62] J. D. Baltrusch, C. Cormick, G. De Chiara, T. Calarco, and G. Morigi, “Quantum superpositions of crystalline structures,” *Phys. Rev. A*, vol. 84, p. 063821, Dec 2011. [Online]. Available: <http://link.aps.org/doi/10.1103/PhysRevA.84.063821>
- [63] A. Ruiz, D. Alonso, M. B. Plenio, and A. del Campo, “Tuning heat transport in trapped-ion chains across a structural phase transition,” *Phys. Rev. B*, vol. 89, p. 214305, Jun 2014. [Online]. Available: <http://link.aps.org/doi/10.1103/PhysRevB.89.214305>
- [64] M. B. Plenio and A. Retzker, “Ion traps as a testbed of classical and quantum statistical mechanics,” *Annalen der Physik*, vol. 525, no. 10-11, pp. A159–A162, 2013. [Online]. Available: <http://dx.doi.org/10.1002/andp.201300740>
- [65] T. W. B. Kibble, “Topology of cosmic domains and strings,” *Journal of Physics A: Mathematical and General*, vol. 9, no. 8, p. 1387, 1976. [Online]. Available: <http://stacks.iop.org/0305-4470/9/i=8/a=029>
- [66] W. H. Zurek, “Cosmological experiments in superfluid helium?” *Nature*, vol. 317, pp. 505–508, 1985. [Online]. Available: <http://dx.doi.org/10.1038/317505a0>
- [67] J. I. Cirac, R. Blatt, A. S. Parkins, and P. Zoller, “Laser cooling of trapped ions with polarization gradients,” *Phys. Rev. A*, vol. 48, pp. 1434–1445, Aug 1993. [Online]. Available: <http://link.aps.org/doi/10.1103/PhysRevA.48.1434>
- [68] H. J. Metcalf and P. van der Straten, *Laser cooling and trapping*. Springer, 1999.
- [69] P. S. Jessen, C. Gerz, P. D. Lett, W. D. Phillips, S. L. Rolston, R. J. C. Spreeuw, and C. I. Westbrook, “Observation of quantized motion of Rb atoms in an optical field,” *Phys. Rev. Lett.*, vol. 69, pp. 49–52, Jul 1992. [Online]. Available: <http://link.aps.org/doi/10.1103/PhysRevLett.69.49>

- [70] P. Verkerk, B. Lounis, C. Salomon, C. Cohen-Tannoudji, J.-Y. Courtois, and G. Grynberg, “Dynamics and spatial order of cold cesium atoms in a periodic optical potential,” *Phys. Rev. Lett.*, vol. 68, pp. 3861–3864, Jun 1992. [Online]. Available: <http://link.aps.org/doi/10.1103/PhysRevLett.68.3861>
- [71] A. Kastberg, W. D. Phillips, S. L. Rolston, R. J. C. Spreeuw, and P. S. Jessen, “Adiabatic cooling of cesium to 700 nk in an optical lattice,” *Phys. Rev. Lett.*, vol. 74, pp. 1542–1545, Feb 1995. [Online]. Available: <http://link.aps.org/doi/10.1103/PhysRevLett.74.1542>
- [72] S. L. Winoto, M. T. DePue, N. E. Bramall, and D. S. Weiss, “Laser cooling at high density in deep far-detuned optical lattices,” *Phys. Rev. A*, vol. 59, pp. R19–R22, Jan 1999. [Online]. Available: <http://link.aps.org/doi/10.1103/PhysRevA.59.R19>
- [73] A. D. Boozer, A. Boca, R. Miller, T. E. Northup, and H. J. Kimble, “Cooling to the ground state of axial motion for one atom strongly coupled to an optical cavity,” *Phys. Rev. Lett.*, vol. 97, p. 083602, Aug 2006. [Online]. Available: <http://link.aps.org/doi/10.1103/PhysRevLett.97.083602>
- [74] A. M. Kaufman, B. J. Lester, and C. A. Regal, “Cooling a single atom in an optical tweezer to its quantum ground state,” *Phys. Rev. X*, vol. 2, p. 041014, Nov 2012. [Online]. Available: <http://link.aps.org/doi/10.1103/PhysRevX.2.041014>
- [75] S. Nuszmann, K. Murr, M. Hijlkema, B. Weber, A. Kuhn, and G. Rempe, “Vacuum-stimulated cooling of single atoms in three dimensions,” *Nat Phys*, vol. 1, pp. 122–125, 11 2005. [Online]. Available: <http://dx.doi.org/10.1038/nphys120>
- [76] G. Birkl, J. A. Yeazell, R. Ruckerl, and H. Walther, “Polarization gradient cooling of trapped ions,” *EPL (Europhysics Letters)*, vol. 27, no. 3, p. 197, 1994. [Online]. Available: <http://stacks.iop.org/0295-5075/27/i=3/a=005>
- [77] T. Kibble, “Phase-transition dynamics in the lab and the universe,” *Physics Today*, vol. 60, no. 9, pp. 47–52, 2007. [Online]. Available: <http://scitation.aip.org/content/aip/magazine/physicstoday/article/60/9/10.1063/1.2784684>
- [78] W. Zurek, “Cosmological experiments in condensed matter systems,” *Physics Reports*, vol. 276, no. 4, pp. 177 – 221, 1996. [Online]. Available: <http://www.sciencedirect.com/science/article/pii/S0370157396000099>
- [79] A. del Campo and W. H. Zurek, “Universality of phase transition dynamics: Topological defects from symmetry breaking,” *International Journal of Modern Physics A*, vol. 29, no. 08, p. 1430018, 2014. [Online]. Available: <http://www.worldscientific.com/doi/abs/10.1142/S0217751X1430018X>
- [80] Y. B. Zeldovich, I. I. Kobzarev, and L. B. Okun, “Cosmological consequences of a spontaneous breakdown of a discrete symmetry,” *Zhurnal Eksperimental’noi i Teoreticheskoi Fiziki*, vol. 67, pp. 3–11, 1974.
- [81] W. H. Zurek, “Experimental cosmology: strings in superfluid helium,” in *Santa Fe Meeting of the Division of Particles and Fields of APS*, T. Goldman and N. M. M., Eds. Singapore: World Scientific, 1985, p. 479.

- [82] A. D. Linde, “Phase transitions in gauge theories and cosmology,” *Reports on Progress in Physics*, vol. 42, no. 3, p. 389, 1979. [Online]. Available: <http://stacks.iop.org/0034-4885/42/i=3/a=001>
- [83] A. Vilenkin, “Cosmic strings,” *Phys. Rev. D*, vol. 24, pp. 2082–2089, Oct 1981. [Online]. Available: <http://link.aps.org/doi/10.1103/PhysRevD.24.2082>
- [84] P. C. Hendry, N. S. Lawson, R. A. M. Lee, P. V. E. McClintock, and C. D. H. Williams, “Generation of defects in superfluid  $^4\text{He}$  as an analogue of the formation of cosmic strings,” *Nature*, vol. 368, no. 6469, pp. 315–317, 1994. [Online]. Available: <http://dx.doi.org/10.1038/368315a0>
- [85] M. E. Dodd, P. C. Hendry, N. S. Lawson, P. V. E. McClintock, and C. D. H. Williams, “Nonappearance of vortices in fast mechanical expansions of liquid  $^4\text{He}$  through the lambda transition,” *Phys. Rev. Lett.*, vol. 81, pp. 3703–3706, Oct 1998. [Online]. Available: <http://link.aps.org/doi/10.1103/PhysRevLett.81.3703>
- [86] C. Bauerle, Y. M. Bunkov, S. N. Fisher, H. Godfrin, and G. R. Pickett, “Laboratory simulation of cosmic string formation in the early universe using superfluid  $^3\text{He}$ ,” *Nature*, vol. 382, pp. 332–334, 1996. [Online]. Available: <http://dx.doi.org/10.1038/382332a0>
- [87] V. M. H. Ruutu, V. B. Eltsov, A. J. Gill, M. Kibble, T. W. B. and Krusius, Y. G. Makhlin, B. Placais, G. E. Volovik, and W. Xu, “Vortex formation in neutron-irradiated superfluid  $^3\text{He}$  as an analogue of cosmological defect formation,” *Nature*, vol. 382, pp. 334–336, 1996. [Online]. Available: <http://dx.doi.org/10.1038/382334a0>
- [88] R. Carmi and E. Polturak, “Search for spontaneous nucleation of magnetic flux during rapid cooling of  $\text{YBa}_2\text{Cu}_3\text{O}_{7-\delta}$  films through  $T_c$ ,” *Phys. Rev. B*, vol. 60, pp. 7595–7600, Sep 1999. [Online]. Available: <http://link.aps.org/doi/10.1103/PhysRevB.60.7595>
- [89] A. Maniv, E. Polturak, and G. Koren, “Observation of magnetic flux generated spontaneously during a rapid quench of superconducting films,” *Phys. Rev. Lett.*, vol. 91, p. 197001, Nov 2003. [Online]. Available: <http://link.aps.org/doi/10.1103/PhysRevLett.91.197001>
- [90] M. Hindmarsh and A. Rajantie, “Phase transition dynamics in the hot abelian higgs model,” *Phys. Rev. D*, vol. 64, p. 065016, Aug 2001. [Online]. Available: <http://link.aps.org/doi/10.1103/PhysRevD.64.065016>
- [91] G. J. Stephens, L. M. A. Bettencourt, and W. H. Zurek, “Critical dynamics of gauge systems: Spontaneous vortex formation in 2d superconductors,” *Phys. Rev. Lett.*, vol. 88, p. 137004, Mar 2002. [Online]. Available: <http://link.aps.org/doi/10.1103/PhysRevLett.88.137004>
- [92] T. Kibble and A. Rajantie, “Estimation of vortex density after superconducting film quench,” *Phys. Rev. B*, vol. 68, p. 174512, Nov 2003. [Online]. Available: <http://link.aps.org/doi/10.1103/PhysRevB.68.174512>
- [93] J. Kirtley, C. Tsuei, and F. Tafuri, “Thermally activated spontaneous fluxoid formation in superconducting thin film rings,” *Phys. Rev. Lett.*, vol. 90, p. 257001, Jun 2003. [Online]. Available: <http://link.aps.org/doi/10.1103/PhysRevLett.90.257001>

- [94] D. Golubchik, E. Polturak, and G. Koren, “Evidence for long-range correlations within arrays of spontaneously created magnetic vortices in a nb thin-film superconductor,” *Phys. Rev. Lett.*, vol. 104, p. 247002, Jun 2010. [Online]. Available: <http://link.aps.org/doi/10.1103/PhysRevLett.104.247002>
- [95] R. Carmi, E. Polturak, and G. Koren, “Observation of spontaneous flux generation in a multi-josephson-junction loop,” *Phys. Rev. Lett.*, vol. 84, pp. 4966–4969, May 2000. [Online]. Available: <http://link.aps.org/doi/10.1103/PhysRevLett.84.4966>
- [96] R. Monaco, J. Mygind, and R. Rivers, “Zurek-kibble domain structures: The dynamics of spontaneous vortex formation in annular josephson tunnel junctions,” *Phys. Rev. Lett.*, vol. 89, p. 080603, Aug 2002. [Online]. Available: <http://link.aps.org/doi/10.1103/PhysRevLett.89.080603>
- [97] R. Monaco, J. Mygind, and R. J. Rivers, “Spontaneous fluxon formation in annular josephson tunnel junctions,” *Phys. Rev. B*, vol. 67, p. 104506, Mar 2003. [Online]. Available: <http://link.aps.org/doi/10.1103/PhysRevB.67.104506>
- [98] R. Monaco, M. Aaroe, J. Mygind, R. Rivers, and V. Koshelets, “Experiments on spontaneous vortex formation in josephson tunnel junctions,” *Phys. Rev. B*, vol. 74, p. 144513, Oct 2006. [Online]. Available: <http://link.aps.org/doi/10.1103/PhysRevB.74.144513>
- [99] R. Monaco, J. Mygind, M. Aaroe, R. Rivers, and V. Koshelets, “Zurek-kibble mechanism for the spontaneous vortex formation in Nb–Al/al<sub>ox</sub>/Nb josephson tunnel junctions: New theory and experiment,” *Phys. Rev. Lett.*, vol. 96, p. 180604, May 2006. [Online]. Available: <http://link.aps.org/doi/10.1103/PhysRevLett.96.180604>
- [100] R. Monaco, M. Aaroe, J. Mygind, R. Rivers, and V. Koshelets, “Spontaneous fluxon production in annular josephson tunnel junctions in the presence of a magnetic field,” *Phys. Rev. B*, vol. 77, p. 054509, Feb 2008. [Online]. Available: <http://link.aps.org/doi/10.1103/PhysRevB.77.054509>
- [101] R. Monaco, J. Mygind, R. Rivers, and V. Koshelets, “Spontaneous fluxoid formation in superconducting loops,” *Phys. Rev. B*, vol. 80, p. 180501, Nov 2009. [Online]. Available: <http://link.aps.org/doi/10.1103/PhysRevB.80.180501>
- [102] H. Saito, Y. Kawaguchi, and M. Ueda, “Kibble-zurek mechanism in a quenched ferromagnetic bose-einstein condensate,” *Phys. Rev. A*, vol. 76, p. 043613, Oct 2007. [Online]. Available: <http://link.aps.org/doi/10.1103/PhysRevA.76.043613>
- [103] J. Dziarmaga, J. Meisner, and W. Zurek, “Winding up of the wave-function phase by an insulator-to-superfluid transition in a ring of coupled bose-einstein condensates,” *Phys. Rev. Lett.*, vol. 101, p. 115701, Sep 2008. [Online]. Available: <http://link.aps.org/doi/10.1103/PhysRevLett.101.115701>
- [104] H. Wu, L. Li, L.-Z. Liang, S. Liang, Y.-Y. Zhu, and X.-H. Zhu, “Recent progress on the structural characterizations of domain structures in ferroic and multiferroic perovskite oxides: A review,” *Journal of the European Ceramic Society*, vol. 35, no. 2, pp. 411 – 441, 2015. [Online]. Available: <http://www.sciencedirect.com/science/article/pii/S0955221914005305>

- [105] L. Landau, “Zur theorie der energieubertragung.” *Physics of the Soviet Union*, vol. 2, p. 28, 1932.
- [106] C. Zener, “Non-adiabatic crossing of energy levels,” *Proc. Roy. Soc. London Ser. A*, vol. 137, pp. 696–702, 1932.
- [107] E. C. G. Stueckelberg, “Theorie der unelastischen stösse zwischen atomen,” *Helvetica Physica Acta*, vol. 5, 1932.
- [108] E. Majorana, “Atomi orientati in campo magnetico variabile,” *Nuovo Cimento*, vol. 9, pp. 43–50, 1932.
- [109] B. Damski, “The simplest quantum model supporting the kibble-zurek mechanism of topological defect production: Landau-zener transitions from a new perspective,” *Phys. Rev. Lett.*, vol. 95, p. 035701, Jul 2005. [Online]. Available: <http://link.aps.org/doi/10.1103/PhysRevLett.95.035701>
- [110] X.-Y. Xu, Y.-J. Han, K. Sun, J.-S. Xu, J.-S. Tang, C.-F. Li, and G.-C. Guo, “Quantum simulation of landau-zener model dynamics supporting the kibble-zurek mechanism,” *Phys. Rev. Lett.*, vol. 112, p. 035701, Jan 2014. [Online]. Available: <http://link.aps.org/doi/10.1103/PhysRevLett.112.035701>
- [111] L. Wang, C. Zhou, T. Tu, H.-W. Jiang, G.-P. Guo, and G.-C. Guo, “Quantum simulation of the kibble-zurek mechanism using a semiconductor electron charge qubit,” *Phys. Rev. A*, vol. 89, p. 022337, Feb 2014. [Online]. Available: <http://link.aps.org/doi/10.1103/PhysRevA.89.022337>
- [112] L. E. Sadler, J. M. Higbie, S. R. Leslie, M. Vengalattore, and D. M. Stamper-Kurn, “Spontaneous symmetry breaking in a quenched ferromagnetic spinor bose-einstein condensate,” *Nature*, vol. 443, p. 312, 09 2006. [Online]. Available: <http://dx.doi.org/10.1038/nature05094>
- [113] D. R. Scherer, C. N. Weiler, T. W. Neely, and B. P. Anderson, “Vortex formation by merging of multiple trapped bose-einstein condensates,” *Phys. Rev. Lett.*, vol. 98, p. 110402, Mar 2007. [Online]. Available: <http://link.aps.org/doi/10.1103/PhysRevLett.98.110402>
- [114] D. Chen, M. White, C. Borries, and B. DeMarco, “Quantum quench of an atomic mott insulator,” *Phys. Rev. Lett.*, vol. 106, p. 235304, Jun 2011. [Online]. Available: <http://link.aps.org/doi/10.1103/PhysRevLett.106.235304>
- [115] M. P. Kennett, “Out-of-equilibrium dynamics of the bose-hubbard model,” *ISRN Condensed Matter Physics*, vol. 2013, 2013. [Online]. Available: <http://dx.doi.org/10.1155/2013/393616>
- [116] J. Dziarmaga, M. Tylutki, and W. H. Zurek, “Quench from mott insulator to superfluid,” *Phys. Rev. B*, vol. 86, p. 144521, Oct 2012. [Online]. Available: <http://link.aps.org/doi/10.1103/PhysRevB.86.144521>
- [117] W. H. Zurek, “Causality in condensates: Gray solitons as relics of bec formation,” *Phys. Rev. Lett.*, vol. 102, p. 105702, Mar 2009. [Online]. Available: <http://link.aps.org/doi/10.1103/PhysRevLett.102.105702>

- [118] S. Ulm, J. Roßnagel, G. Jacob, C. Degünther, S. T. Dawkins, U. G. Poschinger, R. Nigmatullin, A. Retzker, M. B. Plenio, F. Schmidt-Kaler, and K. Singer, “Observation of the kibble-zurek scaling law for defect formation in ion crystals,” *Nat Commun*, vol. 4, 2013. [Online]. Available: <http://dx.doi.org/10.1038/ncomms3290>
- [119] P. K. Ghosh, *Ion Traps*. Clarendon Press, 1995.
- [120] D. J. Berkeland, J. D. Miller, J. C. Bergquist, W. M. Itano, and D. J. Wineland, “Minimization of ion micromotion in a paul trap,” *Journal of Applied Physics*, vol. 83, no. 10, pp. 5025–5033, 1998. [Online]. Available: <http://scitation.aip.org/content/aip/journal/jap/83/10/10.1063/1.367318>
- [121] D. H. E. Dubin, “Minimum energy state of the one-dimensional coulomb chain,” *Phys. Rev. E*, vol. 55, pp. 4017–4028, Apr 1997. [Online]. Available: <http://link.aps.org/doi/10.1103/PhysRevE.55.4017>
- [122] D. James, “Quantum dynamics of cold trapped ions with application to quantum computation,” *Applied Physics B*, vol. 66, no. 2, pp. 181–190, 1998. [Online]. Available: <http://dx.doi.org/10.1007/s003400050373>
- [123] W. Cochran, “Crystal stability and the theory of ferroelectricity,” *Phys. Rev. Lett.*, vol. 3, pp. 412–414, Nov 1959. [Online]. Available: <http://link.aps.org/doi/10.1103/PhysRevLett.3.412>
- [124] R. Cowley, “Structural phase transitions I. Landau theory,” *Advances in Physics*, vol. 29, no. 1, pp. 1–110, 1980.
- [125] T. Schneider, G. Srinivasan, and C. P. Enz, “Phase transitions and soft modes,” *Phys. Rev. A*, vol. 5, pp. 1528–1536, Mar 1972. [Online]. Available: <http://link.aps.org/doi/10.1103/PhysRevA.5.1528>
- [126] G. Morigi and J. Eschner, “Is an ion string laser-cooled like a single ion?” *Journal of Physics B: Atomic, Molecular and Optical Physics*, vol. 36, no. 5, p. 1041, 2003. [Online]. Available: <http://stacks.iop.org/0953-4075/36/i=5/a=323>
- [127] J. Liang, “Hopping of an impurity defect in ion crystals in linear traps,” Master’s thesis, Simon Fraser University, 2012.
- [128] H. Kaufmann, S. Ulm, G. Jacob, U. Poschinger, H. Landa, A. Retzker, M. B. Plenio, and F. Schmidt-Kaler, “Precise experimental investigation of eigenmodes in a planar ion crystal,” *Phys. Rev. Lett.*, vol. 109, p. 263003, Dec 2012. [Online]. Available: <http://link.aps.org/doi/10.1103/PhysRevLett.109.263003>
- [129] G. D. Chiara, A. del Campo, G. Morigi, M. B. Plenio, and A. Retzker, “Spontaneous nucleation of structural defects in inhomogeneous ion chains,” *New Journal of Physics*, vol. 12, no. 11, p. 115003, 2010. [Online]. Available: <http://stacks.iop.org/1367-2630/12/i=11/a=115003>
- [130] G. Morigi and J. Eschner, “Doppler cooling of a coulomb crystal,” *Phys. Rev. A*, vol. 64, p. 063407, Nov 2001. [Online]. Available: <http://link.aps.org/doi/10.1103/PhysRevA.64.063407>

- [131] P. Laguna and W. H. Zurek, “Critical dynamics of symmetry breaking: Quenches, dissipation, and cosmology,” *Phys. Rev. D*, vol. 58, p. 085021, Sep 1998. [Online]. Available: <http://link.aps.org/doi/10.1103/PhysRevD.58.085021>
- [132] C. Balzer, A. Braun, T. Hannemann, C. Paape, M. Ettlner, W. Neuhauser, and C. Wunderlich, “Electrodynamically trapped  $\text{Yb}^+$  ions for quantum information processing,” *Phys. Rev. A*, vol. 73, p. 041407, Apr 2006. [Online]. Available: <http://link.aps.org/doi/10.1103/PhysRevA.73.041407>
- [133] S. Olmschenk, K. C. Younge, D. L. Moehring, D. N. Matsukevich, P. Maunz, and C. Monroe, “Manipulation and detection of a trapped  $\text{Yb}^+$  hyperfine qubit,” *Phys. Rev. A*, vol. 76, p. 052314, Nov 2007. [Online]. Available: <http://link.aps.org/doi/10.1103/PhysRevA.76.052314>
- [134] A. Friedenauer, H. Schmitz, J. T. Glueckert, D. Porras, and T. Schaetz, “Simulating a quantum magnet with trapped ions,” *Nat Phys*, vol. 4, pp. 757–761, 2008. [Online]. Available: <http://dx.doi.org/10.1038/nphys1032>
- [135] M. Johanning, A. F. Varon, and C. Wunderlich, “Quantum simulations with cold trapped ions,” *Journal of Physics B: Atomic, Molecular and Optical Physics*, vol. 42, no. 15, p. 154009, 2009. [Online]. Available: <http://stacks.iop.org/0953-4075/42/i=15/a=154009>
- [136] B. P. Lanyon, C. Hempel, D. Nigg, M. Müller, R. Gerritsma, F. Zähringer, P. Schindler, J. T. Barreiro, M. Rambach, G. Kirchmair, M. Hennrich, P. Zoller, R. Blatt, and C. F. Roos, “Universal digital quantum simulation with trapped ions,” *Science*, vol. 334, no. 6052, pp. 57–61, 2011. [Online]. Available: <http://www.sciencemag.org/content/334/6052/57.abstract>
- [137] R. Islam, E. Edwards, K. Kim, S. Korenblit, C. Noh, H. Carmichael, G.-D. Lin, L.-M. Duan, C.-C. Joseph Wang, J. Freericks, and C. Monroe, “Onset of a quantum phase transition with a trapped ion quantum simulator,” *Nat Commun*, vol. 2, p. 377, 2011. [Online]. Available: <http://dx.doi.org/10.1038/ncomms1374>
- [138] J. W. Britton, B. C. Sawyer, A. C. Keith, C.-C. J. Wang, J. K. Freericks, H. Uys, M. J. Biercuk, and J. J. Bollinger, “Engineered two-dimensional ising interactions in a trapped-ion quantum simulator with hundreds of spins,” *Nature*, vol. 484, pp. 489–492, 2012. [Online]. Available: <http://dx.doi.org/10.1038/nature10981>
- [139] N. Yu and L. Maleki, “Lifetime measurements of the  $4f^{14}5d$  metastable states in single ytterbium ions,” *Phys. Rev. A*, vol. 61, p. 022507, Jan 2000. [Online]. Available: <http://link.aps.org/doi/10.1103/PhysRevA.61.022507>
- [140] C. Tamm, D. Engelke, and V. Bühner, “Spectroscopy of the electric-quadrupole transition  $^2S_{1/2}(F=0) \rightarrow ^2D_{3/2}(F=2)$  in trapped  $^{171}\text{Yb}^+$ ,” *Phys. Rev. A*, vol. 61, p. 053405, Apr 2000. [Online]. Available: <http://link.aps.org/doi/10.1103/PhysRevA.61.053405>
- [141] T. Schneider, E. Peik, and C. Tamm, “Sub-hertz optical frequency comparisons between two trapped  $^{171}\text{Yb}^+$  ions,” *Phys. Rev. Lett.*, vol. 94, p. 230801, Jun 2005. [Online]. Available: <http://link.aps.org/doi/10.1103/PhysRevLett.94.230801>



- [142] K. Hosaka, S. A. Webster, A. Stannard, B. R. Walton, H. S. Margolis, and P. Gill, “Frequency measurement of the  ${}^2S_{1/2}$ – ${}^2F_{7/2}$  electric octupole transition in a single  ${}^{171}\text{Yb}^+$  ion,” *Phys. Rev. A*, vol. 79, p. 033403, Mar 2009. [Online]. Available: <http://link.aps.org/doi/10.1103/PhysRevA.79.033403>
- [143] A. T. Grier, M. Cetina, F. Oručević, and V. Vuletić, “Observation of cold collisions between trapped ions and trapped atoms,” *Phys. Rev. Lett.*, vol. 102, p. 223201, Jun 2009. [Online]. Available: <http://link.aps.org/doi/10.1103/PhysRevLett.102.223201>
- [144] C. Zipkes, S. Palzer, C. Sias, and M. Kohl, “A trapped single ion inside a bose-einstein condensate,” *Nature*, vol. 464, p. 388, 03 2010. [Online]. Available: <http://dx.doi.org/10.1038/nature08865>
- [145] S. Ejtemaee and P. C. Haljan, “Spontaneous nucleation and dynamics of kink defects in zigzag arrays of trapped ions,” *Phys. Rev. A*, vol. 87, p. 051401, May 2013. [Online]. Available: <http://link.aps.org/doi/10.1103/PhysRevA.87.051401>
- [146] S. Ejtemaee, “A fluorescence study of single trapped ytterbium ions for quantum information applications,” Master’s thesis, Simon Fraser University, 2010.
- [147] S. Ejtemaee, R. Thomas, and P. C. Haljan, “Optimization of  $\text{Yb}^+$  fluorescence and hyperfine-qubit detection,” *Phys. Rev. A*, vol. 82, p. 063419, Dec 2010. [Online]. Available: <http://link.aps.org/doi/10.1103/PhysRevA.82.063419>
- [148] S. Olmschenk, D. Hayes, D. N. Matsukevich, P. Maunz, D. L. Moehring, K. C. Younge, and C. Monroe, “Measurement of the lifetime of the  $6p^2P_{1/2}^o$  level of  $\text{Yb}^+$ ,” *Phys. Rev. A*, vol. 80, p. 022502, Aug 2009. [Online]. Available: <http://link.aps.org/doi/10.1103/PhysRevA.80.022502>
- [149] E. H. Pinnington, G. Rieger, and J. A. Kernahan, “Beam-laser measurements of the lifetimes of the  $6p$  levels in  $\text{yb ii}$ ,” *Phys. Rev. A*, vol. 56, pp. 2421–2423, Sep 1997. [Online]. Available: <http://link.aps.org/doi/10.1103/PhysRevA.56.2421>
- [150] E. Biemont, J.-F. Dutrieux, I. Martin, and P. Quinet, “Lifetime calculations in  $\text{yb ii}$ ,” *Journal of Physics B: Atomic, Molecular and Optical Physics*, vol. 31, no. 15, p. 3321, 1998. [Online]. Available: <http://stacks.iop.org/0953-4075/31/i=15/a=006>
- [151] H. Lehmitz, J. Hattendorf-Ledwoch, R. Blatt, and H. Harde, “Population trapping in excited  $\text{yb ions}$ ,” *Phys. Rev. Lett.*, vol. 62, pp. 2108–2111, May 1989. [Online]. Available: <http://link.aps.org/doi/10.1103/PhysRevLett.62.2108>
- [152] A. Bauch, D. Schnier, and C. Tamm, “Collisional population trapping and optical deexcitation of ytterbium ions in a radiofrequency trap,” *Journal of Modern Optics*, vol. 39, no. 2, pp. 389–401, 1992. [Online]. Available: <http://dx.doi.org/10.1080/09500349214550381>
- [153] M. M. Schauer, J. R. Danielson, A.-T. Nguyen, L.-B. Wang, X. Zhao, and J. R. Torgerson, “Collisional population transfer in trapped  $\text{yb}^+$  ions,” *Phys. Rev. A*, vol. 79, p. 062705, Jun 2009. [Online]. Available: <http://link.aps.org/doi/10.1103/PhysRevA.79.062705>

- [154] J. E. Sansonetti and W. C. Martin, *Handbook of basic atomic spectroscopic data*. National Institute of Standards and Technology, Gaithersburg, MD 20899.
- [155] S. Chang and V. Minogin, “Density-matrix approach to dynamics of multilevel atoms in laser fields,” *Physics Reports*, vol. 365, no. 2, pp. 65 – 143, 2002. [Online]. Available: <http://www.sciencedirect.com/science/article/pii/S0370157302000169>
- [156] W. M. Itano and D. J. Wineland, “Laser cooling of ions stored in harmonic and penning traps,” *Phys. Rev. A*, vol. 25, pp. 35–54, Jan 1982. [Online]. Available: <http://link.aps.org/doi/10.1103/PhysRevA.25.35>
- [157] D. J. Wineland and W. M. Itano, “Laser cooling of atoms,” *Phys. Rev. A*, vol. 20, pp. 1521–1540, Oct 1979. [Online]. Available: <http://link.aps.org/doi/10.1103/PhysRevA.20.1521>
- [158] S. Stenholm, “The semiclassical theory of laser cooling,” *Rev. Mod. Phys.*, vol. 58, pp. 699–739, Jul 1986. [Online]. Available: <http://link.aps.org/doi/10.1103/RevModPhys.58.699>
- [159] M. Mielenz, J. Brox, S. Kahra, G. Leschhorn, M. Albert, T. Schaetz, H. Landa, and B. Reznik, “Trapping of topological-structural defects in coulomb crystals,” *Phys. Rev. Lett.*, vol. 110, p. 133004, Mar 2013. [Online]. Available: <http://link.aps.org/doi/10.1103/PhysRevLett.110.133004>
- [160] O. M. Braun and Y. S. Kivshar, *he Frenkel-Kontorova Model: Concepts, Methods, and Applications*. Springer, New York, 2009.
- [161] T. Schumm, S. Hofferberth, L. M. Andersson, S. Wildermuth, S. Groth, I. Bar-Joseph, J. Schmiedmayer, and P. Kruger, “Matter-wave interferometry in a double well on an atom chip,” *Nat Phys*, vol. 1, pp. 57–62, 2005. [Online]. Available: <http://dx.doi.org/10.1038/nphys125>
- [162] C. Monroe, D. M. Meekhof, B. E. King, and D. J. Wineland, “A schrodinger cat superposition state of an atom,” *Science*, vol. 272, no. 5265, pp. 1131–1136, 1996. [Online]. Available: <http://www.sciencemag.org/content/272/5265/1131.abstract>
- [163] D. Leibfried, E. Knill, S. Seidelin, J. Britton, R. B. Blakestad, J. Chiaverini, D. B. Hume, W. M. Itano, J. D. Jost, C. Langer, R. Ozeri, R. Reichle, and D. J. Wineland, “Creation of a six-atom schrödinger cat state,” *Nature*, vol. 438, pp. 639–642, 2005. [Online]. Available: <http://dx.doi.org/10.1038/nature04251>
- [164] T. Monz, P. Schindler, J. T. Barreiro, M. Chwalla, D. Nigg, W. A. Coish, M. Harlander, W. Hänsel, M. Hennrich, and R. Blatt, “14-qubit entanglement: Creation and coherence,” *Phys. Rev. Lett.*, vol. 106, p. 130506, Mar 2011. [Online]. Available: <http://link.aps.org/doi/10.1103/PhysRevLett.106.130506>
- [165] A. Noguchi, Y. Shikano, K. Toyoda, and S. Urabe, “Aharonov-bohm effect in the tunnelling of a quantum rotor in a linear paul trap,” *Nat Commun*, vol. 5, no. 3868, 2014. [Online]. Available: <http://dx.doi.org/10.1038/ncomms4868>

- [166] V. Jelic and F. Marsiglio, “The double-well potential in quantum mechanics: a simple, numerically exact formulation,” *European Journal of Physics*, vol. 33, no. 6, p. 1651, 2012. [Online]. Available: <http://stacks.iop.org/0143-0807/33/i=6/a=1651>
- [167] N. Kosugi, S. Matsuo, K. Konno, and N. Hatakenaka, “Theory of damped rabi oscillations,” *Phys. Rev. B*, vol. 72, p. 172509, Nov 2005. [Online]. Available: <http://link.aps.org/doi/10.1103/PhysRevB.72.172509>
- [168] F. Diedrich, J. C. Bergquist, W. M. Itano, and D. J. Wineland, “Laser cooling to the zero-point energy of motion,” *Phys. Rev. Lett.*, vol. 62, pp. 403–406, Jan 1989. [Online]. Available: <http://link.aps.org/doi/10.1103/PhysRevLett.62.403>
- [169] B. E. King, C. S. Wood, C. J. Myatt, Q. A. Turchette, D. Leibfried, W. M. Itano, C. Monroe, and D. J. Wineland, “Cooling the collective motion of trapped ions to initialize a quantum register,” *Phys. Rev. Lett.*, vol. 81, pp. 1525–1528, Aug 1998. [Online]. Available: <http://link.aps.org/doi/10.1103/PhysRevLett.81.1525>
- [170] C. F. Roos, D. Leibfried, A. Mundt, F. Schmidt-Kaler, J. Eschner, and R. Blatt, “Experimental demonstration of ground state laser cooling with electromagnetically induced transparency,” *Phys. Rev. Lett.*, vol. 85, pp. 5547–5550, Dec 2000. [Online]. Available: <http://link.aps.org/doi/10.1103/PhysRevLett.85.5547>
- [171] P. D. Lett, R. N. Watts, C. I. Westbrook, W. D. Phillips, P. L. Gould, and H. J. Metcalf, “Observation of atoms laser cooled below the doppler limit,” *Phys. Rev. Lett.*, vol. 61, pp. 169–172, Jul 1988. [Online]. Available: <http://link.aps.org/doi/10.1103/PhysRevLett.61.169>
- [172] J. Dalibard and C. Cohen-Tannoudji, “Laser cooling below the doppler limit by polarization gradients: simple theoretical models,” *J. Opt. Soc. Am. B*, vol. 6, no. 11, pp. 2023–2045, Nov 1989. [Online]. Available: <http://josab.osa.org/abstract.cfm?URI=josab-6-11-2023>
- [173] P. J. Ungar, D. S. Weiss, E. Riis, and S. Chu, “Optical molasses and multilevel atoms: theory,” *J. Opt. Soc. Am. B*, vol. 6, no. 11, pp. 2058–2071, Nov 1989. [Online]. Available: <http://josab.osa.org/abstract.cfm?URI=josab-6-11-2058>
- [174] D. J. Wineland, J. Dalibard, and C. Cohen-Tannoudji, “Sisyphus cooling of a bound atom,” *J. Opt. Soc. Am. B*, vol. 9, no. 1, pp. 32–42, Jan 1992. [Online]. Available: <http://josab.osa.org/abstract.cfm?URI=josab-9-1-32>
- [175] J. I. Cirac, R. Blatt, P. Zoller, and W. D. Phillips, “Laser cooling of trapped ions in a standing wave,” *Phys. Rev. A*, vol. 46, pp. 2668–2681, Sep 1992. [Online]. Available: <http://link.aps.org/doi/10.1103/PhysRevA.46.2668>
- [176] S. M. Yoo and J. Javanainen, “Polarization gradient cooling of a trapped ion,” *Phys. Rev. A*, vol. 48, pp. R30–R33, Jul 1993. [Online]. Available: <http://link.aps.org/doi/10.1103/PhysRevA.48.R30>
- [177] H. Katori, S. Schlipf, and H. Walther, “Anomalous dynamics of a single ion in an optical lattice,” *Phys. Rev. Lett.*, vol. 79, pp. 2221–2224, Sep 1997. [Online]. Available: <http://link.aps.org/doi/10.1103/PhysRevLett.79.2221>

- [178] L. Karpa, A. Bylinskii, D. Gangloff, M. Cetina, and V. Vuletić, “Suppression of ion transport due to long-lived subwavelength localization by an optical lattice,” *Phys. Rev. Lett.*, vol. 111, p. 163002, Oct 2013. [Online]. Available: <http://link.aps.org/doi/10.1103/PhysRevLett.111.163002>
- [179] N. Schlosser, G. Reymond, I. Protsenko, and P. Grangier, “Sub-poissonian loading of single atoms in a microscopic dipole trap,” *Nature*, vol. 411, no. 6841, pp. 1024–1027, Jun. 2001. [Online]. Available: <http://www.nature.com.proxy.lib.sfu.ca/nature/journal/v411/n6841/full/4111024a0.html>
- [180] W. S. Bakr, A. Peng, M. E. Tai, R. Ma, J. Simon, J. I. Gillen, S. Fölling, L. Pollet, and M. Greiner, “Probing the Superfluid-to-Mott Insulator Transition at the Single-Atom Level,” *Science*, vol. 329, no. 5991, pp. 547–550, 2010. [Online]. Available: <http://www.sciencemag.org/content/329/5991/547.abstract>
- [181] M. McGovern, A. J. Hilliard, T. Grünzweig, and M. F. Andersen, “Counting atoms in a deep optical microtrap,” *Opt. Lett.*, vol. 36, no. 7, pp. 1041–1043, Apr 2011. [Online]. Available: <http://ol.osa.org/abstract.cfm?URI=ol-36-7-1041>
- [182] J. Eschner, G. Morigi, F. Schmidt-Kaler, and R. Blatt, “Laser cooling of trapped ions,” *J. Opt. Soc. Am. B*, vol. 20, no. 5, pp. 1003–1015, May 2003. [Online]. Available: <http://josab.osa.org/abstract.cfm?URI=josab-20-5-1003>
- [183] D. Leibfried, R. Blatt, C. Monroe, and D. Wineland, “Quantum dynamics of single trapped ions,” *Rev. Mod. Phys.*, vol. 75, pp. 281–324, Mar 2003. [Online]. Available: <http://link.aps.org/doi/10.1103/RevModPhys.75.281>
- [184] Y. Li and Mølmer, “Sisyphus laser cooling of trapped ions: The transition from optical molasses to the lamb-dicke regime,” *Laser Physics*, vol. 4, p. 829, 1994.
- [185] R. Dum, P. Zoller, and H. Ritsch, “Monte carlo simulation of the atomic master equation for spontaneous emission,” *Phys. Rev. A*, vol. 45, pp. 4879–4887, Apr 1992. [Online]. Available: <http://link.aps.org/doi/10.1103/PhysRevA.45.4879>
- [186] J. Dalibard, Y. Castin, and K. Mølmer, “Wave-function approach to dissipative processes in quantum optics,” *Phys. Rev. Lett.*, vol. 68, pp. 580–583, Feb 1992. [Online]. Available: <http://link.aps.org/doi/10.1103/PhysRevLett.68.580>
- [187] D. J. Berkeland and M. G. Boshier, “Destabilization of dark states and optical spectroscopy in zeeman-degenerate atomic systems,” *Phys. Rev. A*, vol. 65, p. 033413, Feb 2002. [Online]. Available: <http://link.aps.org/doi/10.1103/PhysRevA.65.033413>
- [188] C. Cohen-Tannoudji, *Atomic motion in laser light*, 1992.
- [189] J. P. Gordon and A. Ashkin, “Motion of atoms in a radiation trap,” *Phys. Rev. A*, vol. 21, pp. 1606–1617, May 1980. [Online]. Available: <http://link.aps.org/doi/10.1103/PhysRevA.21.1606>
- [190] G. Nienhuis, P. van der Straten, and S.-Q. Shang, “Operator description of laser cooling below the doppler limit,” *Phys. Rev. A*, vol. 44, pp. 462–474, Jul 1991. [Online]. Available: <http://link.aps.org/doi/10.1103/PhysRevA.44.462>

- [191] M. Lindberg and S. Stenholm, “The master equation for laser cooling of trapped particles,” *Journal of Physics B: Atomic and Molecular Physics*, vol. 17, no. 16, p. 3375, 1984. [Online]. Available: <http://stacks.iop.org/0022-3700/17/i=16/a=019>
- [192] M. Lindberg and J. Javanainen, “Temperature of a laser-cooled trapped three-level ion,” *J. Opt. Soc. Am. B*, vol. 3, no. 7, pp. 1008–1017, Jul 1986. [Online]. Available: <http://josab.osa.org/abstract.cfm?URI=josab-3-7-1008>
- [193] G. Morigi, J. Eschner, and C. H. Keitel, “Ground state laser cooling using electromagnetically induced transparency,” *Phys. Rev. Lett.*, vol. 85, pp. 4458–4461, Nov 2000. [Online]. Available: <http://link.aps.org/doi/10.1103/PhysRevLett.85.4458>
- [194] B. Blinov, D. Leibfried, C. Monroe, and D. Wineland, “Quantum computing with trapped ion hyperfine qubits,” *Quantum Information Processing*, vol. 3, no. 1-5, pp. 45–59, 2004. [Online]. Available: <http://dx.doi.org/10.1007/s11128-004-9417-3>
- [195] C. Ospelkaus, U. Warring, Y. Colombe, K. R. Brown, J. M. Amini, D. Leibfried, and D. J. Wineland, “Microwave quantum logic gates for trapped ions,” *Nature*, vol. 476, p. 181, 2011. [Online]. Available: <http://dx.doi.org/10.1038/nature10290>
- [196] M. Johanning, A. Braun, N. Timoney, V. Elman, W. Neuhauser, and C. Wunderlich, “Individual addressing of trapped ions and coupling of motional and spin states using rf radiation,” *Phys. Rev. Lett.*, vol. 102, p. 073004, Feb 2009. [Online]. Available: <http://link.aps.org/doi/10.1103/PhysRevLett.102.073004>
- [197] N. Timoney, I. Baumgart, M. Johanning, A. F. Varon, M. B. Plenio, A. Retzker, and C. Wunderlich, “Quantum gates and memory using microwave-dressed states,” *Nature*, vol. 476, p. 185, 2011. [Online]. Available: <http://dx.doi.org/10.1038/nature10319>
- [198] S. Ejtemaee and P. C. Haljan, “Detailed study of sisyphus cooling of Yb ions in a linear paul trap: theory and experiment.” *In preparation*.
- [199] P. J. Lee, “Quantum information processing with two trapped cadmium ion,” Ph.D. dissertation, University of Michigan, 2006.
- [200] Y. Lin, J. P. Gaebler, T. R. Tan, R. Bowler, J. D. Jost, D. Leibfried, and D. J. Wineland, “Sympathetic electromagnetically-induced-transparency laser cooling of motional modes in an ion chain,” *Phys. Rev. Lett.*, vol. 110, p. 153002, Apr 2013. [Online]. Available: <http://link.aps.org/doi/10.1103/PhysRevLett.110.153002>
- [201] G.-D. Lin and L.-M. Duan, “Equilibration and temperature distribution in a driven ion chain,” *New Journal of Physics*, vol. 13, no. 7, p. 075015, 2011. [Online]. Available: <http://stacks.iop.org/1367-2630/13/i=7/a=075015>
- [202] T. Pruttivarasin, M. Ramm, I. Talukdar, A. Kreuter, and H. Häffner, “Trapped ions in optical lattices for probing oscillator chain models,” *New Journal of Physics*, vol. 13, no. 7, p. 075012, 2011. [Online]. Available: <http://stacks.iop.org/1367-2630/13/i=7/a=075012>

- [203] A. Bermudez, M. Bruderer, and M. B. Plenio, “Controlling and Measuring Quantum Transport of Heat in Trapped-Ion Crystals,” *Physical Review Letters*, vol. 111, no. 4, p. 040601, Jul. 2013. [Online]. Available: <http://link.aps.org/doi/10.1103/PhysRevLett.111.040601>
- [204] N. Freitas, E. Martinez, and J. P. Paz, “Heat transport through ion crystals,” *arXiv preprint arXiv:1312.6644*, 2013. [Online]. Available: <http://arxiv.org/abs/1312.6644>
- [205] A. Ruiz, D. Alonso, M. B. Plenio, and A. del Campo, “Tuning heat transport in trapped-ion chains across a structural phase transition,” *Physical Review B*, vol. 89, no. 21, p. 214305, Jun. 2014. [Online]. Available: <http://link.aps.org/doi/10.1103/PhysRevB.89.214305>
- [206] C. Ospelkaus, U. Warring, Y. Colombe, K. R. Brown, J. M. Amini, D. Leibfried, and D. J. Wineland, “Microwave quantum logic gates for trapped ions,” *Nature*, vol. 476, no. 7359, p. 181, 2011. [Online]. Available: <http://dx.doi.org/10.1038/nature10290>
- [207] N. Timoney, I. Baumgart, M. Johanning, A. F. Varon, M. B. Plenio, A. Retzker, and C. Wunderlich, “Quantum gates and memory using microwave-dressed states,” *Nature*, vol. 476, no. 7359, p. 185, 2011. [Online]. Available: <http://dx.doi.org/10.1038/nature10319>